Tectonic studies of the lithosphere of Laurentia using magnetotelluric data and the implications for diamond resources

By

Brandon Franklin Werner Chase

A thesis submitted in partial fulfillment of the requirements for the degree of

Doctor of Philosophy

in

Geophysics

Department of Physics
University of Alberta

Abstract

Cratons are the oldest continental landmasses, have a thick lithosphere, preserve important records on the formation and evolution of the continents, and are key repositories of economic minerals and volatiles. The magnetotelluric (MT) method is a useful tool in studying cratons as it can readily image to the base of the lithosphere. Further, the resistivity measurements are sensitive to a number of conductive phases in the lithosphere that are related to tectonic processes and lithosphere modification. In this thesis, the MT method is used to investigate three regions of the Laurentian craton, a composite craton that makes up much of Canada and the continental United States.

The first study area was the Southern Oklahoma Aulacogen (SOA). Long-period MT data were collected across the SOA, and the resulting resistivity model revealed low resistivity anomalies coincident with the SOA in the crust and upper lithospheric mantle which is underlain by a wider conductive lower lithosphere beneath the region. The crustal and upper lithospheric mantle conductor was interpreted to reflect a combination of olivine grain size reduction, graphite, sulfides, and the enrichment of the water content of nominally anhydrous mantle minerals related to metasomatic processes that occurred when the SOA underwent rifting in the Cambrian. This modification likely caused rheological weakening of the lithosphere, which allowed the SOA to be deformed during the later Pennsylvanian-Permian Ancestral Rocky Mountain (ARM) orogeny. This metasomatic weakening model may provide a plausible mechanism for the isolated and dispersed nature of the enigmatic ARM uplifts. The conductive lower lithosphere was interpreted to reflect a water-rich lithosphere that may be related to accretion of the head of

the plume that drove rifting in the Cambrian. The top of this lower lithosphere conductor is coincident with a seismic mid-lithosphere discontinuity and was interpreted to reflect a layer of phlogopite formed along a paleo-lithosphere-asthenosphere boundary during accretion of the plume head.

The next study area was the Trans-Hudson Orogen (THO), located in Saskatchewan, Canada. A grid of long-period MT data were collected over the THO and enigmatic Sask craton to produce the first 3-D resistivity model of the entire lithosphere in the region. The resistivity model showed that a major conductive anomaly was located in the lithospheric mantle beneath the northern Sask craton. This anomaly was interpreted to reflect sulfides formed along the interface between a subducting slab that underwent flat slab subduction and the overriding lithosphere of the northern Sask craton. This implies that much of the lithosphere of the northern Sask craton was added during the THO and that a previously unrecognized episode of west-dipping subduction occurred. A number of conduit-like conductors emanate from this large lithospheric mantle conductor and ascend to the surface, some beneath known mineralization districts. These conductors were interpreted to reflect sulfides that may have formed along pathways for mineralizing fluids. These conductors may then indicate regions of prospective mineralization. Interestingly, kimberlites in the region all erupt along the margin of the main conductor beneath the north Sask craton. This may indicate that kimberlites exploited the terrane boundaries and major trans-lithospheric structures formed during accretion of the flat slab.

The final study area was in northern Alberta over the Birch Mountain and Buffalo Head kimberlite fields. MT stations were collected around the kimberlite fields to provide increased resolution of the provincial resistivity model. The Birch Mountain kimberlite field is underlain by a large conductive anomaly in the lower lithosphere, while the Buffalo Head Hills kimberlite field is among the most resistive lithosphere in the region. Common conductive phases in the lithosphere, including phlogopite, amphibole, water contents, and graphite, cannot explain the low resistivity or slow seismic velocity anomaly observed beneath the Birch Mountains. The nature of this anomaly is currently unknown, but elevated temperature observed in xenoliths from Birch Mountain kimberlites alongside the anomaly connecting with the underlying asthenosphere raises the possibility that it reflects a minor amount of melt and erosion of the diamondiferous lower lithosphere. This erosion may be one of the reasons for the poor diamond contents in the Birch Mountain kimberlites. In comparison, the resistive lithosphere beneath Buffalo Head Hills may indicate an intact diamondiferous lithosphere root, which could explain the good diamond contents in these kimberlites.

Preface

The research presented in this thesis is the original work of Brandon Chase and has been written to fulfill the requirements for the degree of Doctor of Philosophy at the University of Alberta. Dr. Martyn Unsworth supervised this project in the Department of Physics.

Chapter 5 has been published as Chase, B.F.W., Unsworth, M.J., Atekwana, E.A., Evans, R.L. and Zhu, J., (2023). Magnetotelluric Imaging of the Lithospheric Structure of the Southern Oklahoma Aulacogen: Evidence for Long-Term Weakening Caused by Rifting. *Journal of Geophysical Research: Solid Earth*, 128(6), p.e2023JB026555. https://doi.org/10.1029/2023JB026555. Brandon Chase was responsible for the MT fieldwork, MT time series processing, 2-D MT inversion, interpretation, and writing of the manuscript. Martyn Unsworth coordinated the project, provided guidance and training during modelling and interpretation, and helped write the manuscript. Estella Atekwana helped to coordinate the fieldwork while Brandon Chase was a student at Oklahoma State University, and helped write the manuscript. Rob Evans provided equipment, training, and assistance with 2-D modelling of the MT data, and helped with writing the manuscript. Jasmine Zhu helped with initial processing of the MT data. This publication included a "Supplementary Materials" document, which has been included as Appendix A of this thesis.

Chapter 6 has been published as Chase, B.F.W and Unsworth, M.J. (2024). Magnetotelluric evidence for the formation of the layered Sask craton by flat slab subduction. *Earth and Planetary Science Letters.* 647, 119027. https://doi.org/10.1016/j.epsl.2024.119027. Brandon Chase was responsible for the MT data collection, analysis, 3-D inversion, interpretation, and writing of the manuscript. Martyn Unsworth coordinated the project, provided guidance and training during modelling and interpretation, and helped write the manuscript. This publication included a "Supplementary Materials" document, which has been reproduced as Appendix B of this thesis.

Chapter 7 has been published as Chase, B., Unsworth, M.J., Pana, D.I., Wang, E. (2024). Deep Electrical Structure of the Buffalo Head Hills and Birch Mountains, Northern Alberta: Implications for Diamond Exploration. Alberta Energy Regulator / Alberta Geological Survey, *AER/AGS Special Report* 117, 40 p. (link: https://ags.aer.ca/publication/spe-117). Brandon Chase was

responsible for the MT data collection, analysis, 3-D inversion, interpretation, and writing of the manuscript. Martyn Unworth coordinated the project, provided guidance and training during modelling and interpretation, and helped write the manuscript. Dinu Pana helped coordinate and supervise the project with the Alberta Energy Regulatory/Alberta Geological Survey. Enci Wang helped with interpretation and writing the manuscript. Chapter 6 will be submitted to *Journal of Geophysical Research: Solid Earth* in the near future.

While a graduate student at the University of Alberta, Brandon Chase published two additional peer-reviewed scientific journal articles, one as the lead author and the other as a co-author. These articles are not included in this PhD thesis but are mentioned here for completeness. The first was published as Chase, B.F., Kolawole, F., Atekwana, E.A., Carpenter, B.M., Turko, M., Abdelsalam, M. and Finn, C., (2023). The 180-km-long Meers-Willow fault system in the Southern Oklahoma Aulacogen: A potential US mid-continent seismic hazard. *Geological Society of America Bulletin*, 135(3-4), pp.663-677. https://doi.org/10.1130/B36363.1. The second was published as Yu, T.C., Currie, C.A., Unsworth, M.J. and Chase, B.F., (2022). The structure and dynamics of the uppermost mantle of southwestern Canada from a joint analysis of geophysical observations. Journal of Geophysical Research: Solid Earth, 127(10), p. e2022JB024130. https://doi.org/10.1029/2022JB024130.

Acknowledgments

I would like to thank my supervisor, Dr. Martyn Unsworth, for teaching me most of what I know about the MT method and interpretation. While my own field work was not in exciting locations, I was trusted to plan and conduct surveys that spanned many days to weeks in remote locations and to install MT stations by truck and helicopter. We were able to work together on data collection in British Columbia via helicopter and truck in the Coast Mountains, a dramatic departure from the flat land and farm fields I was used to collecting data in. I learned a lot about MT during this time. I am grateful for these experiences and the knowledge that I gained from both the fieldwork and his supervision.

I would also like to thank my supervisory committee members, Dr. Thomas Stachel and Dr. Graham Pearson. They provided valuable support and insight into the geology relevant to my graduate studies. I would also like to thank my PhD thesis examiners, Richard Smith, Thomas Chacko, and Alexander Penin, for their helpful comments and suggestions. I would also like to thank Dr. Estella Atekwana and Dr. Folarin Kolawole as both prior advisors and long-time collaborators for helping me write and publish my first peer-reviewed scientific article.

During my graduate studies, I took part in more than 150 days of fieldwork doing MT and other geophysical methods. Much of this work was conducted in locations, often remote, that I would have never otherwise been able to see, and for this I am grateful. During my studies, I have exchanged knowledge and ideas with other students that have ultimately helped my project move forward. I have also called upon a number of them for assistance in the field to get projects done and data collected. Often, this was much to their disinclination, as driving around Saskatchewan, Manitoba, and Oklahoma is not exactly the most exciting fieldwork. Regardless, I am thankful for their time and assistance, as these projects were ultimately made possible by their help. I would like to thank the following: Zoë Vestrum, Theron Finley, Andrew Williamson, Erich Slobodian, Javier Gonzalez, Keytash Moshtaghian, Megan Caston, Dr. Benjamin Lee, Dr. Darcy Cordell, Dr. Folarin Kolawole, Dr. Micah Mayle, David Beckendorff, Curt Carter, Allyson Shewchuk, and Keeya Beausoleil.

I would also like to thank a variety of funding agencies that provided support for this research: Society of Economic Geologists, Society of Exploration Geophysicists, Geological Society of America, Alberta Energy Regulator/Alberta Geological Survey, Manitoba Geological Survey, and Saskatchewan Geological Survey. Jason Marks and Alicia Maki of the Manitoba Geological Survey are thanked for their assistance in the field.

I would like to thank the variety of landowners who so graciously allowed us access to their lands and farms in order to install MT sites. A special thanks to Ken and Marion Laroque for allowing the field crew to use their farm in Saskatchewan to stage equipment and as lodging on multiple occasions in 2021 and 2022.

Briefly, I would like to thank my former high school teacher, David Ward. A geologist by training, you were so excited to teach the first ever geology class at Chaparral High School, it pushed me to major in it. The following 12 years that have led to me to pursuing a PhD were ultimately set in motion because of your effort and enthusiasm for this subject as a teacher.

I would like to recognize my MSc advisor, Dr. Mohamed Gamal Abdelsalam, who passed away in 2024 before I was able to finish my PhD and thank him for his support over the years. I will always fondly remember listening to your stories for hours in your office and your good humor about everything. You will be forever remembered and missed.

Finally, I would like to wholeheartedly thank my parents, Terry and Richard Chase, for their much-needed advice and support throughout my entire academic career. I know it has not been easy to be living so far apart for these past few years. Your love, support, and belief in me through my educational career have always been appreciated. The sacrifices you both made to ensure my success both growing up and as an adult are also appreciated. Our families are ultimately chosen for us, by fate or chance, and I am glad that I was chosen to be with you both. I could not have asked for better parents.

Table of Contents

List of Tables

List of Figures

List of Common Symbols and Abbreviations

1-D	One-dimensional
2-D	Two-dimensional
3-D	Three-dimensional
AMT	audio magnetotellurics
BBMT	broadband magnetotellurics
BHH	Buffalo Head Hills
BM	Birch Mountains
EM	Electromagnetics
FALC	Fort à la Corne
Hz	Hertz
LPMT	long-period magnetotellurics
Ma	Mega-annum (million years)
MT	Magnetotelluric(s)
NAB	Northern Alberta
NSC	North Sask craton
R.M.S.	Root-mean-square
SOA	Southern Oklahoma Aulacogen
THO	Trans-Hudson Orogen
vol. %	Volume percent
WCSB	Western Canadian Sedimentary Basin
wt %	Weight percent
Ωm	ohm-meter
σ	siemens per mete

CHAPTER 1. INTRODUCTION

The research presented in this thesis is motivated by a desire to understand the formation and evolution of cratons. The crystalline basement rocks of much of Canada and the United States consist of amalgamated cratonic lithosphere that together form Laurentia, also referred to as the Laurentian craton. Cratons also contain a plurality of critical mineral resources vital to the transition from hydrocarbon to more sustainable energy sources. The efficient development of these resources also requires an understanding of the structure and evolution of cratonic regions. In this introduction, the concept of a craton is introduced in addition to the processes by which they are formed, modified, and destroyed. The importance of cratons for mineral and metal resources within Canada will also be discussed with a focus on kimberlites, which are the primary source of the gemstone diamond. Finally, the research that will be presented in Chapters 5-7 will also be introduced.

1.1 Cratons, their formation, and evolution

Cratons are among the oldest parts of the continental lithosphere, with the nuclei of many having formed during the Archean (>2.5 Ga). Cratons are regions of thick lithosphere in excess of 150 km and today comprise over 60% of the continental landmass (Pearson et al., 2021) (Fig. 1.1). Unlike other parts of the continents, cratons appear to be more resistant to tectonic modification due to their refractory (i.e., chemically depleted and water depleted) mantle lithosphere, which yields high viscosities, low density, and rheological stability (Peslier et al., 2010). In recent years, it has been shown that cratons are often structurally complex features created by protracted and multi-phased tectonic processes (e.g., Aulbach et al., 2012; Liu et al., 2021). Figure 1.2 shows some of the tectonic processes that have been suggested to be responsible for craton formation. Each of these processes can also destroy cratons. For example, plume-craton interactions or similar mantle upwelling processes may metasomatize the overlying lithosphere, resulting in increased density and reduced viscosity, and could lead to lithosphere delamination (Tang et al., 2013; Liu et al., 2021). Subduction-accretion and orogenic tectonics may also remove lithosphere directly through mechanical processes, such as the so-called flat slab “continental bulldozer” (e.g., Kapp et al., 2023). Such processes are thought to have been instrumental in the destruction of the Sahara

and North China cratons (Abdelsalam et al., 2002; Tang et al., 2013). Any of these tectonic processes may also lead to preconditioning (i.e., initial partial destabilization or rheologic weakening resulting from metasomatism) effects in the overlying craton. In this case, the initial tectonic episode may modify and weaken but not destroy the craton and a later tectonic event may partially remove the previously weakened lithospheric mantle (e.g., Liu et al., 2021).

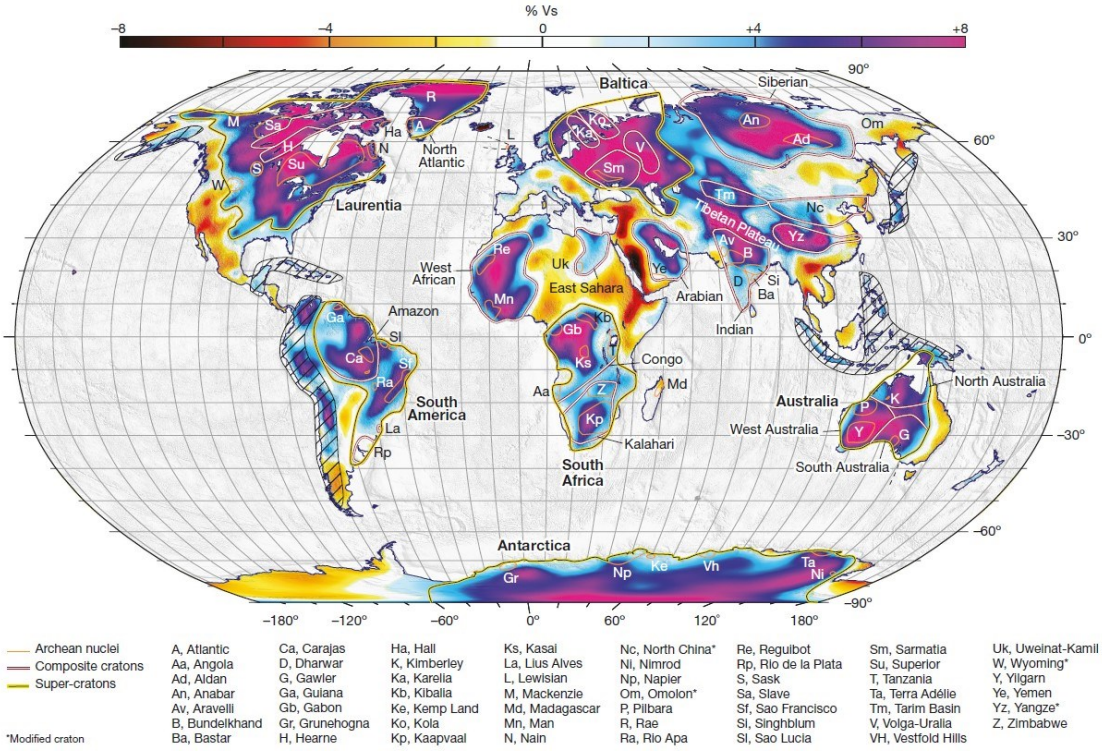

Figure 1.1: *Global craton map from Pearson et al. (2021). Laurentia is shown in the upper left as a super-craton composed of 6 Archean craton nuclei. Note that the definition of cratons in this thesis refers to terranes with crust that has been stable since at least 1 Gyr ago with a lithosphere thickness greater than 150 km.*

The evolutionary history of a craton may include phases of growth, modification, destruction, and reformation, which leads to a complex lithospheric structure. Many of these processes appear to act preferentially along cratonic margins, in regions with significant lithosphere topography, or where pre-existing weaknesses are located (Foley, 2008). Studies of cratonic lithosphere are complicated by their size and depth and are often limited by a paucity of data. In many cases, the majority of our understanding comes from insights obtained from the study of kimberlites. These small-volume volatile-rich melts traverse the lithosphere and entrain mantle xenoliths, ultimately

bringing them to the surface for study by geologists (Russell et al., 2019). However, by virtue of their association with kimberlites, these xenoliths may represent anomalous samples of the mantle and may not be representative of the lithosphere of the craton as a whole. Similarly, the spatial distribution of kimberlites is not uniform, showing a tendency to cluster in specific regions often associated with major structural features (Jelsma et al., 2009; Tappe et al., 2018a, and references therein). This can leave entire regions of a craton and its lithosphere under sampled and poorly understood. Finally, due to the fact that kimberlites ascend directly upwards, they functionally offer a 1-D sample of the lithosphere (i.e., a vertical sample of the lithospheric mantle directly below the kimberlite). However, despite these limitations, they are currently the only way to directly sample the mantle lithosphere.

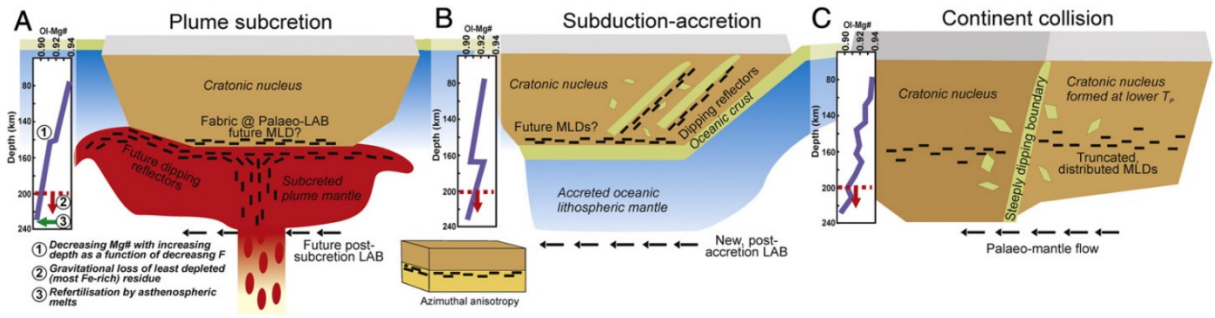

Figure 1.2: *Tectonic processes that may be involved in craton formation. (A) Subcretion of a residual plume head to the base of the original cratonic nuclei. (B) Subduction-accretion, where subducted slabs are added to the sides or bottom of the craton (i.e., flat slab subduction). (C) Continent collision or orogenic formation, where a craton is created as a result of terranes colliding and suturing together. Figure from Aulbach et al. (2017). MLD, Mid-lithosphere discontinuity; LAB, lithosphere-asthenosphere boundary.*

These limitations have resulted in an incomplete understanding of craton evolution. The study of cratons can provide insights into past tectonic episodes, the tectonic evolution of regions, and preserved examples of lithosphere modification. This type of study can also offer constraints on volatile fluxes and storage as well as the formation of significant economic mineral deposits critical to the energy transition from hydrocarbons to renewables, as cratons are key hosts for both (Foley and Fischer, 2017; Frezzotti and Ferrando, 2018; Aulbach, 2018; Selway 2018; Hoggard et al., 2020; Pearson et al., 2021). In order to better investigate cratons and expand analysis into the 2-D and 3-D space, geophysical data can be used alongside xenolith data to provide robust interpretations of the whole lithosphere. Geophysical data well-suited for this type of task include

seismic, potential field, and electromagnetic methods capable of imagining deep structures and covering large regions.

1.2 Kimberlites and diamonds resources

Kimberlites occur globally but are restricted to cratons or terranes directly adjacent to cratons (Tappe et al., 2018b). The origin and composition of kimberlite magmas is the subject of considerable debate, but it is generally agreed they originate at depths >150 km in the asthenosphere or deeper under pressure and temperature conditions restricted to cratons or peri-cratonic regions (Stamm and Schmidt, 2017; Russell et al., 2019; Giuliani and Pearson, 2019). Kimberlites are the primary host of diamonds (>70% by value), which are xenocrysts entrained by kimberlite magmas, and cratons host almost 100% of diamonds (Pearson et al., 2021). Originally, diamonds were associated mainly with Archean cratons due to the strong historical association of these terranes with diamondiferous (i.e., diamond bearing) kimberlites, and this became known as "Clifford's rule" (Clifford, 1966). In recent years, diamondiferous kimberlites have been increasingly found in in association with Proterozoic-aged cratons (e.g., Banas et al., 2007; Czas et al., 2018; 2020). This has motivated diamond exploration in new regions (Kjarsgaard et al., 2022).

Canada is a major producer of diamonds, which are mined from a number of kimberlites on a number of cratons (Fig. 1.3). The first diamond mines opened in the late 1990s (Kjarsgaard and Levinson, 2002) and until 2019, Canada was the third largest supplier of rough diamonds globally (NRCAN, 2019). Many mines, such as Diavik, Ekati, and Gahco Kué are also scheduled to be decommissioned in the near future (Clinton, 2024). Compounding these issues has been a lack of new kimberlite discoveries. Ultimately, this threatens the position of Canada within the global diamond market alongside a significant revenue source within the Canadian mining sector. The economic impact of the continued reduction in diamond mining will be especially acute in the regions of Canada where production occurs. For example, the loss of the three aforementioned diamond mines in the Northwest Territories could reduce own source taxation for the territorial government by nearly 30%, reduce revenue from the mining sector by nearly three quarters in a territory that derives 25% of its GDP from this sector, and eliminate nearly 3,400 jobs in a territory

with a population of only ~45,000 people (Bauer, 2017; Clinton, 2023). For the diamond industry to continue exploration is necessary to find new resources.

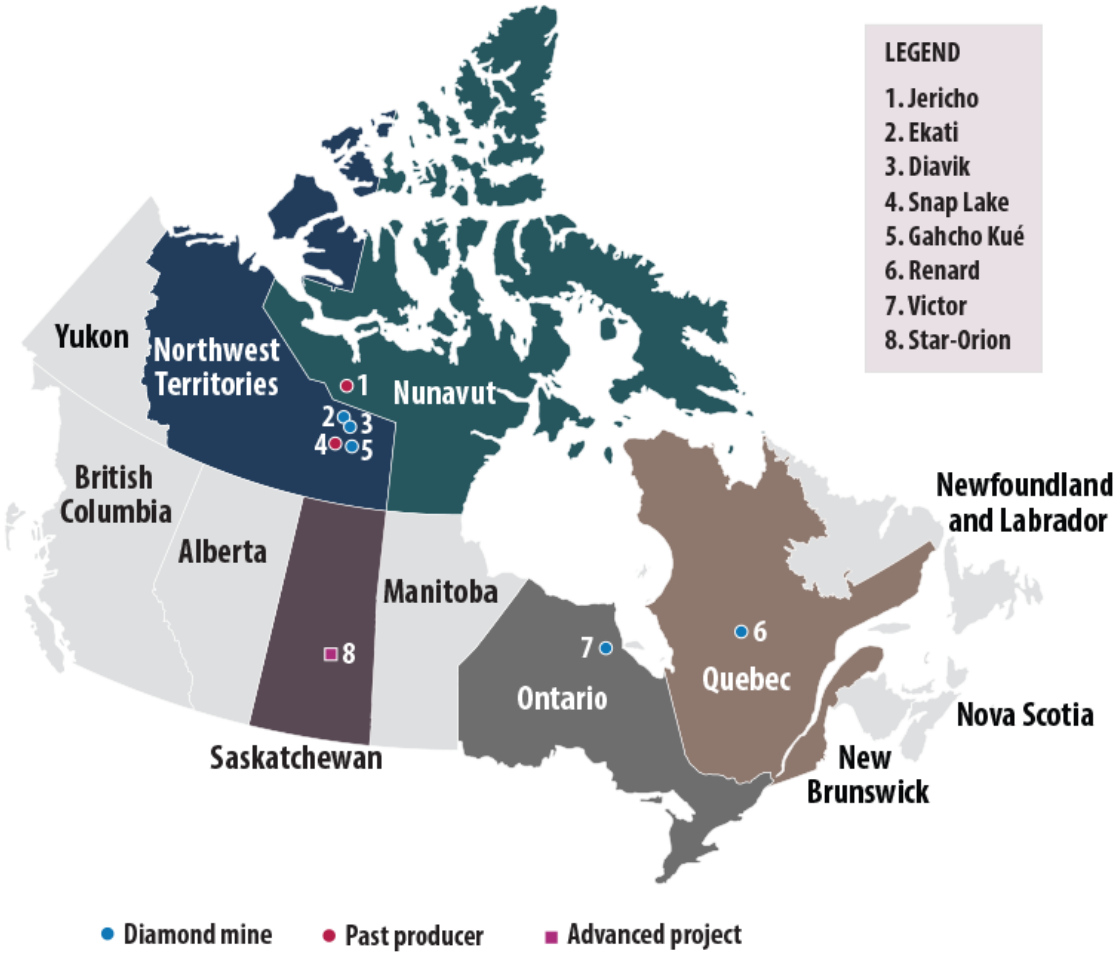

***Figure 1.3**: The location of diamond mines in Canada. Figure © NRCan (2019).*

1.3 Exploration for diamondiferous kimberlites

Exploration for kimberlites is a difficult endeavor. The prospective regions can cover entire cratons, tens of thousands of square kilometers in size, while the kimberlites themselves are usually less than 1 km in diameter (Kjarsgaard et al., 2019). This raises exploration costs and, correspondingly, investment risk. Exploration is further complicated by the fact that not all kimberlites contain economic quantities of diamonds. More than 3,500 kimberlites have been

discovered to date, but less than 3% are significantly diamondiferous, and less than 100 have been commercially developed (de Wit, 2010; Giuliani and Pearson, 2019). Geologic exploration primarily relies on the detection of kimberlite indicator minerals (KIMs). KIMs are mantle xenocrysts brought to the surface by the kimberlites and are recovered from sediment sampling. Obtaining samples from a number of locations ideally allows the sediment samples and KIMs to be traced back to their source kimberlites (Kjarsgaard et al., 2019). Given the role of sediments, it becomes necessary to clearly understand transport processes (e.g., the direction of glacial or alluvial movements) and paleodrainage (e.g., de Wit, 2018) in the region of exploration. The type of KIMs recovered allows determination of the composition of the lithospheric mantle (e.g., lherzolite, harzburgite, eclogite). Thermobarometry methods can be used on KIMs to determine the paleogeotherm at the time of kimberlite eruption. The intersection of the paleogeotherm with the graphite-diamond transition (Day, 2012) and the mantle adiabat is used to determine the "diamond window" (Kjarsgaard et al., 2019). Higher numbers of KIMs within the diamond window provide a first-pass assessment of the "diamond potential" of a kimberlite. Complicating this type of analysis is that kimberlites are often located in clusters, making it difficult to prioritize targets. Geophysical data can be used to complement geologic data during kimberlite exploration and are particularly useful in regions where sedimentary cover may prevent direct observations of the kimberlites.

1.3.1 Pipe-scale kimberlite exploration

Geophysical exploration methods typically rely on direct detection of kimberlites at the pipe-scale (Fig. 1.4). The small volumes of kimberlite melts mean they typically occur as small, isolated, and short spatial wavelength anomalies, usually less than 1 km in diameter. The typical shape of a kimberlite is as a carrot-shaped pipe (Fig. 1.4E). Typically, airborne and ground-based magnetics, gravity, electromagnetic and electrical resistivity methods are used (e.g., Smith et al., 1996; Jansen and Witherly, 2004; Reed and Witherly, 2007). The improvements made in airborne geophysical data acquisition and processing in the last few decades have allowed for rapid identification of kimberlites over large regions at relatively low cost compared to ground data collection (Power et al., 2004; Reed and Witherly, 2007). However, the detection of kimberlites is not straightforward as the geophysical responses are inherently non-unique and kimberlites can have a variable

geophysical response that may not be distinct from the country rock (Fig. 1.4) (Reed and Witherly, 2007). For example, in aeromagnetic data, the ultramafic composition of kimberlites means that they can exhibit both induced and remnant magnetization (Fig. 1.4B). Magnetization is primarily due to the content of ferromagnetic minerals in the rock, predominately magnetite and pyrrhotite. Induced magnetization is always parallel to the present day geomagnetic field. In a location where the magnetic field is close to vertical, the induced magnetic field will result in a positive anomaly. A common filtering technique applied to magnetic data is the reduction to pole or reduction to equator correction, which simplifies anomalies so that they appear as positive anomalies as if they were located directly above the magnetic poles. In comparison, remnant magnetization is formed when the kimberlite erupts and cools below the Currie Point, and the magnetic minerals acquire a remnant magnetic component usually parallel to the prevailing geomagnetic field at the time. Since the geomagnetic field undergoes regular reversals, this remnant magnetization can be negative or positive. In a period where the magnetic field had a reverse polarity, kimberlites will have a negative remnant magnetization, and vice versa. To determine the type of magnetic anomaly, the induced magnetization and remnant magnetization must be combined. Figure 1.5 is a conceptual model demonstrating the concept of induced and remnant magnetization. The model has been simplified by assuming a high inclination for the geomagnetic field so that anomalies appear directly above the magnetic source. In the model, a negative anomaly is observed above the source with remnant magnetization because the magnetic remanence is stronger than the inducing field and at a significantly different orientation (opposite here). This may not always be the case, and the interpretation of remnant magnetization is often not straightforward. Additionally, false positive anomalies can also be caused by other intrusions (i.e., dikes) or regions with thick succession of sediment (i.e., lakes) (Power et al., 2004).

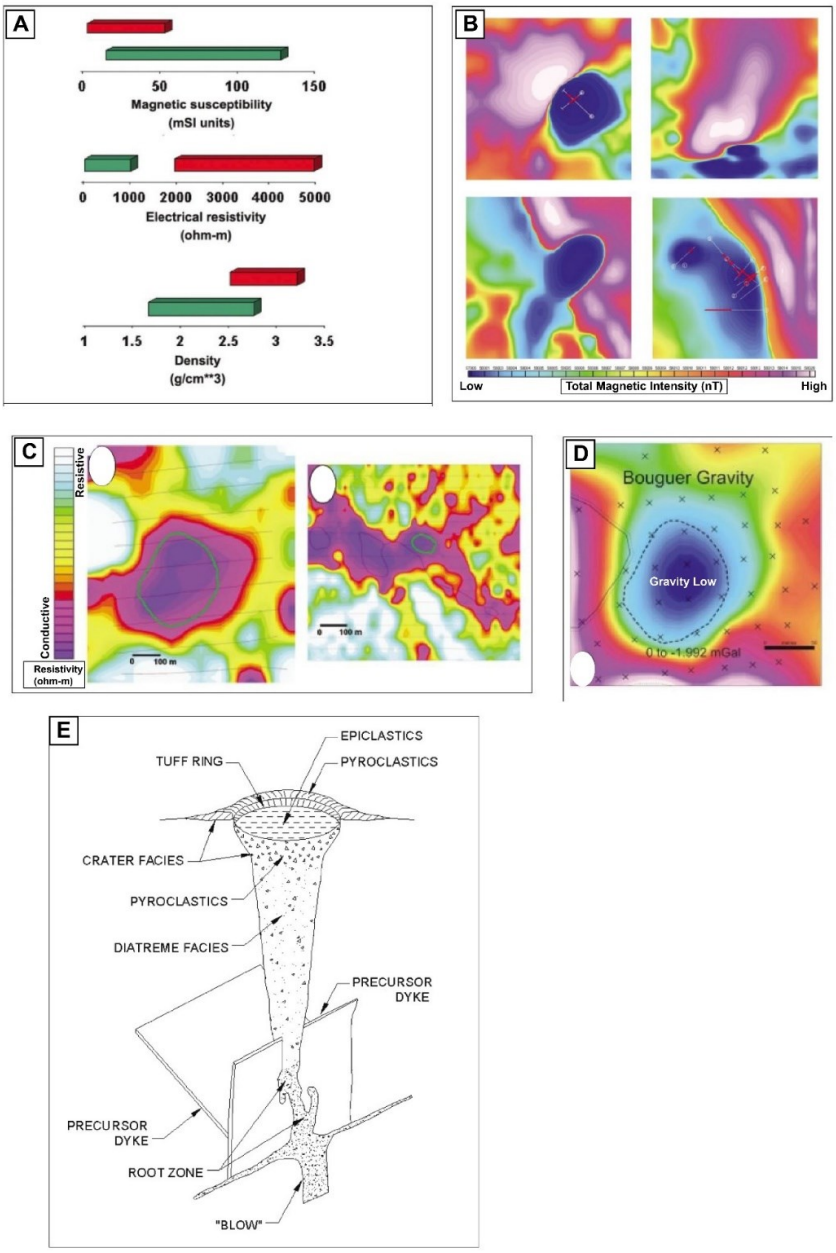

Figure 1.4: *(A) Physical properties of kimberlites (green) and granitic rocks (red). (B) Aeromagnetic responses of some kimberlites. (Top left) Dipole response, (top right) a kimberlite corresponding to a direct magnetic high, (lower left) a kimberlite as a magnetic low (i.e., reverse magnetization due to remnant magnetization), (lower right) kimberlite as a magnetic low intruded next to a pre-existing dike. (C) Kimberlites as they may appear in electromagnetic data. (Left) a pipe beneath a lake, (right) a kimberlite beneath sedimentary overburden. Note how the conductive lake water and sediments obscure the kimberlite. (D) Gravity anomaly above a kimberlite showing a distinct gravity low. (E) cross-section of a typical kimberlite pipe that could be responsible for the distinctive circle-shaped anomalies in B, C, and D. Note that kimberlite intrusions can take other forms, but these pipe-like structures appear to be the most common. Images adapted form Power et al. (2004).*

Gravity data will often show kimberlites as Bouguer lows (Fig. 1.4D), though this may not be the case with hypabyssal sections where density may be similar to crystalline basement rocks, and false positives can be generated by anomalously thick sedimentary sections or low-density igneous rocks (Power et al., 2004; Reed and Witherly, 2007).

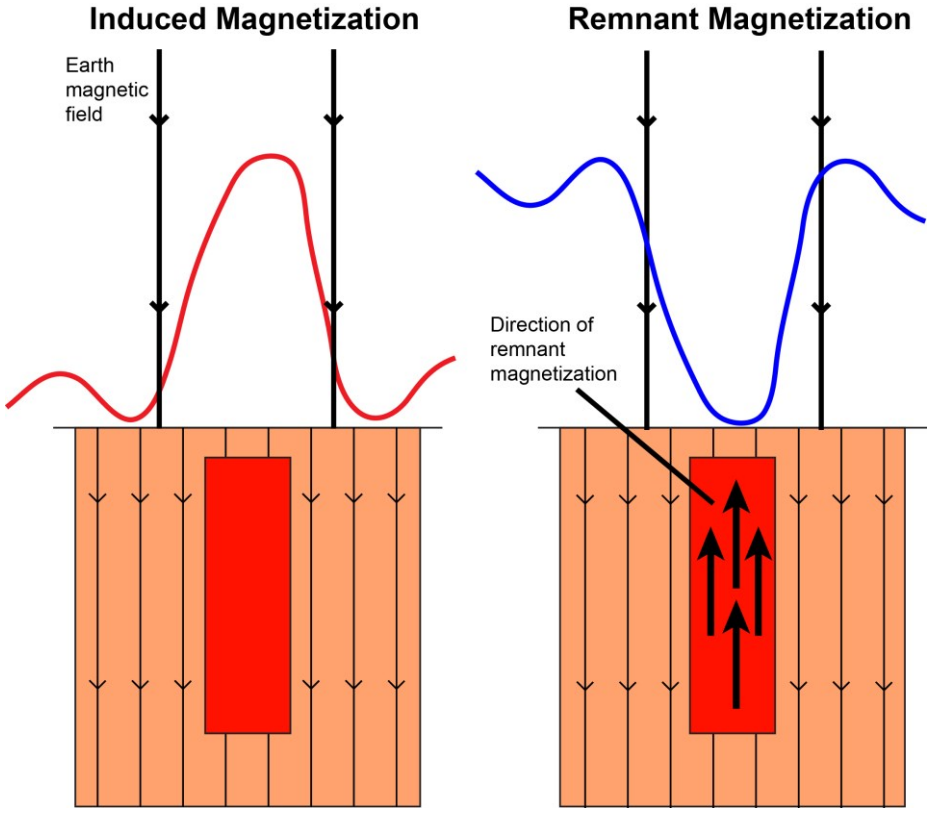

Figure 1.5: *Conceptual model of induced and remnant magnetization at high field inclinations (i.e., polar regions). Induced magnetic fields will produce relatively high amplitude positive anomalies. The remnant magnetization will produce low-amplitude negative anomalies. The negative anomaly generated by the remnant example assumes that the magnetic remanence is sufficiently strong to overcome the induced field and produce a negative anomaly.*

With electromagnetic methods, there are a number of processes that form characteristic resistivity anomalies that contrast with the country rock and allow pipes to be detected (Fournier et al., 2017). A strong contrast arises when the top of kimberlites weathers to form clay minerals that have a prominent low resistivity (5-100 Ω·m) (Smith et al., 1996). In some cases, the kimberlite itself may be electrically conductive (Fournier et al., 2017). However, these signatures can also be masked by sedimentary overburden or water bodies, which may also be conductive (Fig. 1.4C) (Power et al., 2004). Conversely, if parts of the kimberlite have not weathered significantly, it may

show up as an electrically resistive body in a conductive background, which can be useful for delineating the edge of a kimberlite body or field (Janssen and Witherly, 2004). In order to overcome the inherent non-uniqueness of geophysical data and the variable geophysical responses of kimberlite, it is often necessary to collect multiple complementary datasets during kimberlite exploration.

1.3.2 Regional-scale kimberlite investigations

In more recent years, there has been an effort to conduct regional-scale studies focused on kimberlites and cratonic structures. This has been motivated by earlier observations of the tendency of kimberlites to cluster in specific regions (e.g., Jelsma et al., 2009; Tappe et al., 2018, and references therein). In the Slave craton in northern Canada (Fig. 1.1.) both magnetotelluric and teleseismic studies have shown resistivity and velocity anomalies, respectively, associated with productive kimberlites (e.g., Chen et al., 2009; Bettac et al., 2023). Magnetotelluric results from South Africa have demonstrated an association between diamondiferous kimberlites and moderately metasomatized lithosphere (Özaydın et al., 2021; Özaydın and Selway, 2022). These observations suggest a spatial relationship may exist between kimberlites and anomalous cratonic lithosphere. This type of observation can be integrated into the mineral systems (section 1.5) concept to narrow down the exploration space for kimberlites, particularly at the regional level.

1.4 Other mineral resources found within cratons

In addition to diamonds, cratons are also well endowed with other mineral resources. For example, cratons account for over 90% of global gold and platinum production (Pearson et al., 2021). A variety of mineral deposit types and systems are associated with cratons or lithosphere with thick mantle lithosphere roots (Groves and Santosh, 2021). Many of the minerals found in these deposits are critical to meet global energy transition goals (Fortier et al., 2022). However, the distribution of these metals is not uniform, and certain cratons may be more prospective than others. Further, certain sub-regions (i.e., provinces, terranes, and districts) can contain the majority of a specific mineral, while others are comparatively barren (Jaireth and Huston, 2010 and references therein). The variability of both inter-craton and intra-craton mineral potential is the result of multiple

factors. These include the presence of major structures that guide and permit the ascent of mineralizing fluids, the duration and intensity of fluid and energy flux, and the ability to trap mineralization to a sufficient degree that economically viable deposits can develop (Jarieth and Huston, 2010; Groves and Santosh, 2021).

In recent years, the spatial relationship between cratons and mineralization in adjacent terranes has also commanded attention (e.g., Kirkby et al., 2020). As detailed models about the location and extent of the thick lithosphere of cratons have become available, continued research has observed the presence of mineralization in the terranes along cratonic margins (e.g., Hoggard et al., 2020; Groves and Santosh, 2021). In this context, the rheological stability and longevity of cratons influence the development of conduit structures, the movement of mineralizing fluids, and the development of suitable host rocks for mineralization and fluid generation (Groves and Santosh, 2021). Conversely, the destruction of cratonic lithosphere may also play a major role in mineralization. For example, study of the North China craton suggests that the same fluids responsible for lithosphere destruction here also played a role in concentrating gold mineralization in the remnant continental lithosphere (Zhu et al., 2017). These observations highlight the importance of studying regions of cratonic lithosphere in order to better access and develop critical mineral resources. Observations from these studies can ultimately be used in mineral systems models (McCuaig et al., 2010; McCuaig and Hronsky, 2014) to guide and develop better exploration practices.

1.5 The mineral systems concept

Traditionally, mineral exploration has focused on locating deposits or evidence of mineralization at the surface, determining the size and geometry of the deposit, and then evaluating how to exploit the deposit and the viability of mining. In this approach, exploration is focused heavily on relatively small-scale deposits, and this has led to a wealth of deposit models. These deposit models can then be used to better predict the behaviour or detection of similar analogous deposits during the early stages of exploration, ultimately saving costs and permitting easier exploitation. However, this approach has not produced increased exploration success in recent years. In fact, trends in recent decades indicate that exploration expenditures are outpacing returns, and that the

exploration industry has become an industry where expenses are greater than revenue (Fig. 1.6A). While this increase in exploration expenditures (Fig. 1.6A) has led to the discovery of increasingly more deposits, most of these deposits are of poor quality (i.e., low ore grade) or a small size (Fig. 1.6B) and are not worth developing. Critically, the discovery and development of tier 1 and 2 deposits, the largest deposit types that account for <8% of discoveries but are where 68% of the value is created, have become less frequent (Fig. 1.6; Schodde, 2019). A widespread perception is that the "low-hanging fruit" is now gone and that explorers of today will have to literally and figuratively dig deeper to be successful (Koch et al., 2015). The reasons for declining exploration success are multi-faceted and include more challenging and/or isolated environments, burial under overburden, and social and environmental concerns (Okada, 2022). This trend is especially evident in greenfield regions, areas new to mineral exploration where little is known, institutional knowledge is limited, and risks can be high, which is a trend that must be reversed due to the projected increase in the demand for minerals (Davies et al., 2021). These challenges indicate that there is a disconnection between the traditional exploration approach and successful exploration outcomes (McCuaig and Hronsky, 2014).

In recent years, the mineral systems framework has been developed to address these trends with the goal of improving exploration outcomes (McCuaig et al., 2010; McCuaig and Hronsky, 2014). The mineral systems framework treats the individual deposits as the expression of larger geodynamic processes. It seeks to understand these larger processes in order to better determine where mineralization and deposits might form. . Key features of the mineral systems framework include:

(1) Increasing the spatial scope of mineral exploration in an effort to understand the generation, movement, and trapping (or deposition) of mineralizing fluids from the tectonic-regional scale to the deposit scale (i.e., the lithosphere architecture associated with mineralizing fluids).

(2) Emphasizing that deposits are the endmembers of common large-scale ore-forming processes that should be understood.

(3) Seeking to understand this larger context in order to link disparate deposits to primary Earth processes and generate models to aid mineral assessments and exploration outcomes (McCuaig et al., 2010; McCuaig and Hronsky, 2014; Hofstra and Kreiner, 2020).

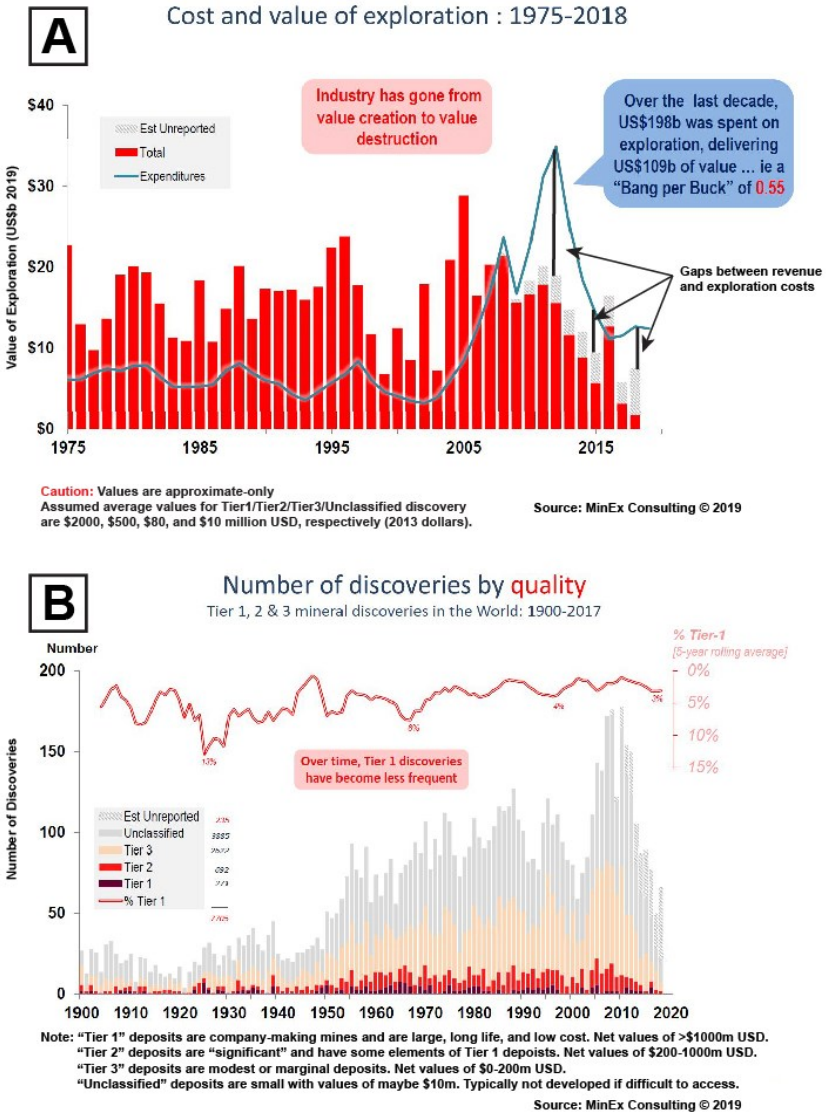

***Figure 1.6**: (A) Trends in expenditures as a function of the value returned for the mineral exploration industry from 1975-2018. Note that years when the blue line is greater than the red bars represent years is where the industry has lost money. (B) Trends in discoveries of new mineral deposits from 1900-2020. Note the decline of tier 1 and 2 deposits in the 21st century. While these Tier 1 and Tier 2 deposits are not common, they account for the overwhelming majority of value for the industry. Figure adapted from Schodde (2019).*

A major focus of the mineral systems framework is on determining the movement and storage of mineralizing fluids and the geometry and location of associated structures such as major trans-lithospheric faults, terrane boundaries, major crustal deformation zones, magma or plutonic bodies, among others (Heinson et al., 2018; Comeau et al., 2022; Groves et al., 2022). Geophysical methods, and in particular electromagnetic and potential fields methods, are well-suited to address these challenges given their combined sensitivity to major tectonic structures and faults, and the presence of fluids and melts in the lithosphere.

Figure 1.7 provides an example of the mineral systems framework as applied to porphyry deposit exploration at the regional, camp, and deposit scale. It also shows the geophysical methods relevant to exploration at each spatial scale, as well as diagrams illustrating each method and their typical depth of exploration. Figure 1. 8 identifies critical elements at each of the three spatial scales of the mineral systems framework relevant to geophysics.

- At the regional scale (Fig. 1.7A), the entire lithosphere may be examined, and emphasis is placed on understanding the geodynamic setting, regions of fluid or melt movement and corresponding metasomatic modification of the lithosphere, and the location of large structural boundaries that can act as fluid or melt conduits (Fig. 1.7A). Datasets at this scale focus on attaining coverage over large regions (i.e., provinces, states, etc.) and providing imaging of the majority of the lithosphere (Fig. 1.8A).

- The camp scale is largely restricted to the crust and upper crust, and emphasis is placed on regions where melts and fluid congregate and in determining the location of key structures that control major deposits or a series of deposits in a region (Fig. 1.7B). At this scale, datasets are focused on providing higher-resolution imaging than the regional scale (Fig. 1.8B).

- The deposit scale commands most of the attention in exploration endeavors as it is ultimately the most relevant scale for economic activity. Here, emphasis is placed on determining alteration halos from ore zones and determining the size, scale, and grade of

ore bodies of economic interest. Datasets on this scale are usually very high-resolution as they are often used to help guide and adapt drilling campaigns.

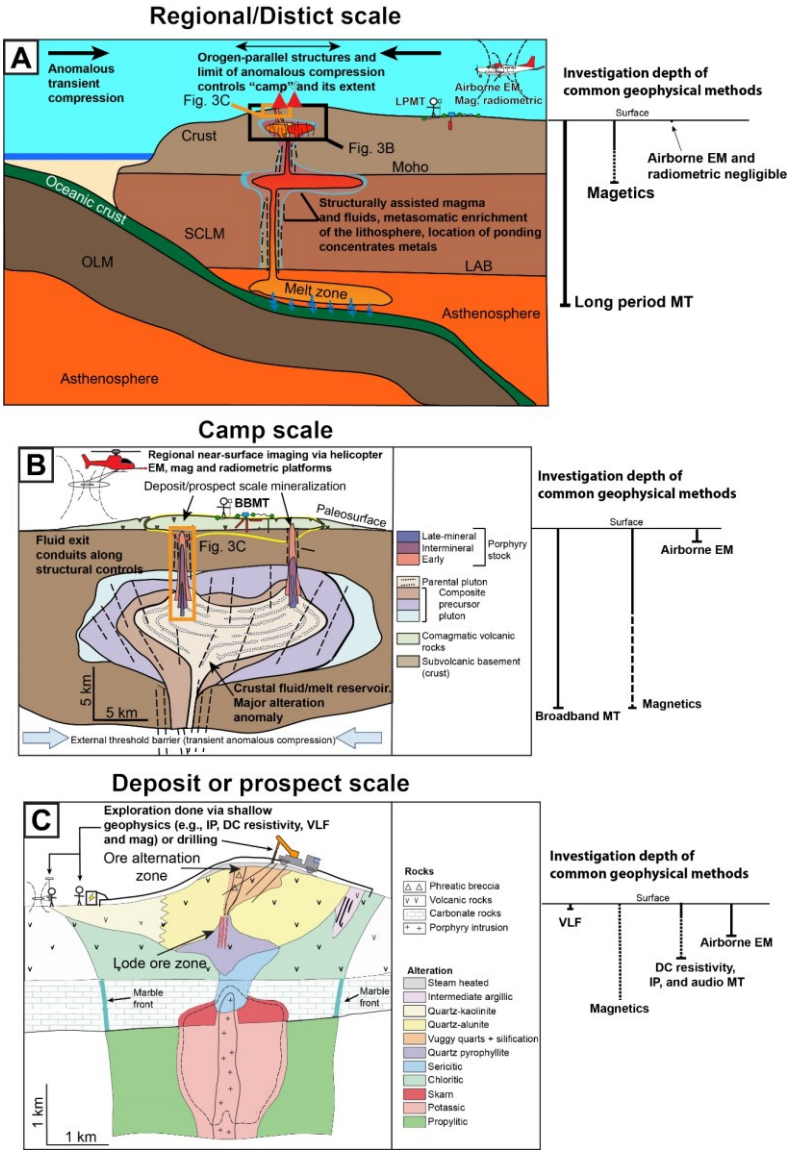

Figure 1.7*: A potential mineral system model for porphyry deposits showing the movement of mineralizing fluids. The geophysical methods most applicable for imaging the subsurface at each spatial scale are also shown. (A) The tectonic-regional (state to multi-state) scale shows how mineralizing fluids are initially generated during subduction, traverse and modify the overlying lithosphere, and organize and concentrate in discrete regions at the camp-district scale. (B) The camp-district (county to multi-county) scale shows the structure, alteration, and mineral zonation within a hypothetical mineral-rich pluton. (C) The deposit scale shows how a hypothetical porphyry deposit can be hosted. This scale occupies the overwhelming majority of private sector activity and the majority of expenditures as it is critical for determining resource size, mine viability and planning. Adapted from McCuaig and Hronsky (2014). LPMT, long-period MT; BBMT, broadband MT; SCLM, subcontinental lithosphere mantle; OLM, oceanic lithosphere mantle; IP, induced polarization; DC, direct current; VLF, very low frequency.*

While the Mineral systems framework has largely been applied to exploration for precious and semi-precious metallic deposits, it is also relevant to kimberlite exploration. By virtue of their generation in the asthenosphere and ascent through the entire lithosphere to the surface (Stamm and Schmidt, 2017; Russell et al., 2019), kimberlites move through all the spatial scales of the mineral systems framework. Their well-established tendency to form in clusters or in well-defined regions (Jelsma et al., 2009; Tappe et al., 2018, and references therein) illustrates that major structures influence their distribution. Diamond formation is also associated with fluid or melt metasomatism (Luth and Stachel, 2014; Stachel and Luth, 2015), and the hydrogen content of these fluids can often be electrically conductive in the lithosphere (Gardes et al., 2014). While kimberlite melts occur in volumes that are too small to be detected directly, these related elements can be investigated and used to create a kimberlite mineral systems models. As exploration for diamond and kimberlites expands into more unconventional settings further away from Archean cratons (Banas et al., 2007; Czas et al., 2018; 2020; Pearson et al., 2021), the mineral systems concept can help to reduce the exploration space and improve area selection for kimberlite exploration.

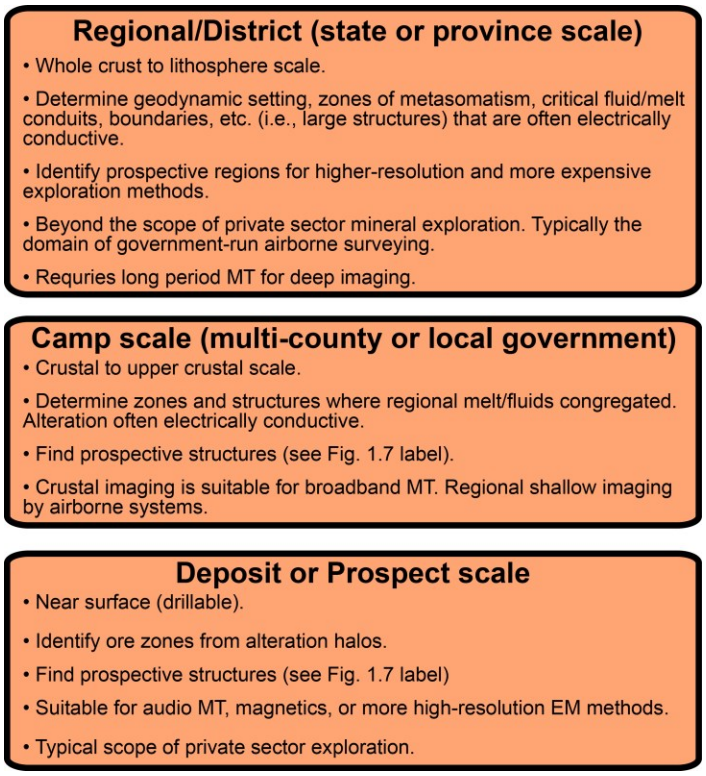

Figure 1.8*: Diagram showing critical elements of the Mineral Systems concept that are relevant to geophysical data at each scale.*

1.6 Thesis objectives

Additional studies of cratons are needed to develop a better understanding of their formation and evolution. The focus on studying cratons will also allow for the investigation of elements of a kimberlite mineral system. This thesis uses geophysical data to assess craton structure and evolution as well as components of the kimberlite mineral system within the Laurentian craton. The research in this thesis is centered on three study areas: (1) The Southern Oklahoma Aulacogen (Chapter 5), (2) The Sask craton (Chapter 6), and the Buffalo Head terrane and Taltson magmatic arc in northern Alberta (Chapter 7).

The research objectives of these three studies are:

1) Chapter 5:

- Determine the resistivity structure of the lithosphere of the Southern Oklahoma Aulacogen from MT data.

- Determine and understand how the tectothermal history of the Southern Oklahoma Aulacogen has modified the margin of the Laurentian craton and influenced future tectonic deformation.

- Determine how the present-day lithosphere exists along this southern margin of the Laurentian craton.

2) Chapter 6:

- Determine the resistivity structure of the Sask craton with MT.

- Determine the role of the Sask craton during the formation of the Trans-Hudson Orogen during the Paleoproterozoic.

- Determine how the lithosphere structure and tectonic evolution of the Sask craton influenced regional mineralization and kimberlite emplacement.

3) Chapter 7:

- Refine the resistivity model derived from MT data and the lithosphere structure beneath the Taltson magmatic arc and Buffalo Head terrane.

- Use this to determine how the lithosphere structure is different between the two terranes.

- Relate this lithosphere structure to the regional tectonic history.

- Investigate how this lithosphere structure influenced the variable diamond potential found between the two terranes.

1.7 Thesis outline

The geology and tectonic setting within the Laurentian craton for each of the study areas is discussed in Chapter 2. Chapter 3 discusses the resistivity of the lithosphere. Chapter 4 discusses electromagnetic geophysical methods with a specific focus on the MT method used for this thesis. Chapters 3 and 4 will provide a foundation detailing the methods used in the research presented in Chapter 5-7.

Chapter 5 presents and discusses the resistivity model obtained for the Southern Oklahoma Aulacogen. This chapter was published in the *Journal of Geophysical Research: Solid Earth* (Chase et al., 2023). The associated supplemental materials for this article can be found in Appendix A.

Chapter 6 presents and discusses the resistivity model centered over the Sask craton and Trans-Hudson Orogen. This chapter was published in *Earth and Planetary Science Letters* (Chase and

Unsworth, 2024). The associated supplemental materials for this article can be found in Appendix B.

Chapter 7 presents and discusses the resistivity model centered over the Buffalo Head and Taltson magmatic arc terranes in Northern Alberta. This chapter was published as a Special Report with the Alberta Energy Regulator (Chase et al., 2024a) and an updated version with additional interpretations will be submitted to *Journal of Geophysical Research: Solid Earth* in the near future. The version included in this thesis is the version published with the Alberta Energy Regulator. The supplemental material that will accompany this submission can be found in Appendix C.

Chapter 8 provides a summary of the investigations in this thesis and suggestions for future research.

CHAPTER 2. TECTONIC SETTING AND GEOLOGY

2.1 The Laurentian craton

The Laurentian craton, also called the North America Craton or Laurentia, makes up the majority of the landmass of Canada and the United States (Fig. 2.1). The core or nuclei of the Laurentian craton is comprised of a number of Archean cratons which include the Slave, Superior, Hearne, Rae, Mackenzie, Sask and Wyoming cratons (Pearson et al., 2021). During the Proterozoic these cratons were sutured together, forming much of what is now northern Canada while additional terranes were added largely along the margins, predominantly the southern margin (Whitmeyer and Karlstrom, 2007). In the areas with Archean cratonic nuclei, the lithosphere thicknesses can be greater than 200 km (Czas et al., 2018; 2020; Bettac et al., 2023). Along the margins the lithosphere is thinner in the range of 140-200 km, but these regions have been largely tectonically inactive since the Proterozoic (Fig. 2.1). This is not always the case as, for example, many of the juvenile arc terranes along the western margin of Laurentia in Alberta have lithosphere thicknesses in excess of 200 km (Wang and Unsworth, 2022). The internal heterogeneity of the Laurentia has led to its classification as a composite or super craton, the size of which is defined by the extent of relatively thick (>150 km) and tectonically inactive lithosphere (Pearson et al., 2021).

The processes responsible for the assembly and evolution of Laurentia were complex and highly variable by location. For simplicity, the discussion of Laurentian tectonics will be restricted to the individual study areas in Oklahoma, the Sask craton, and northern Alberta.

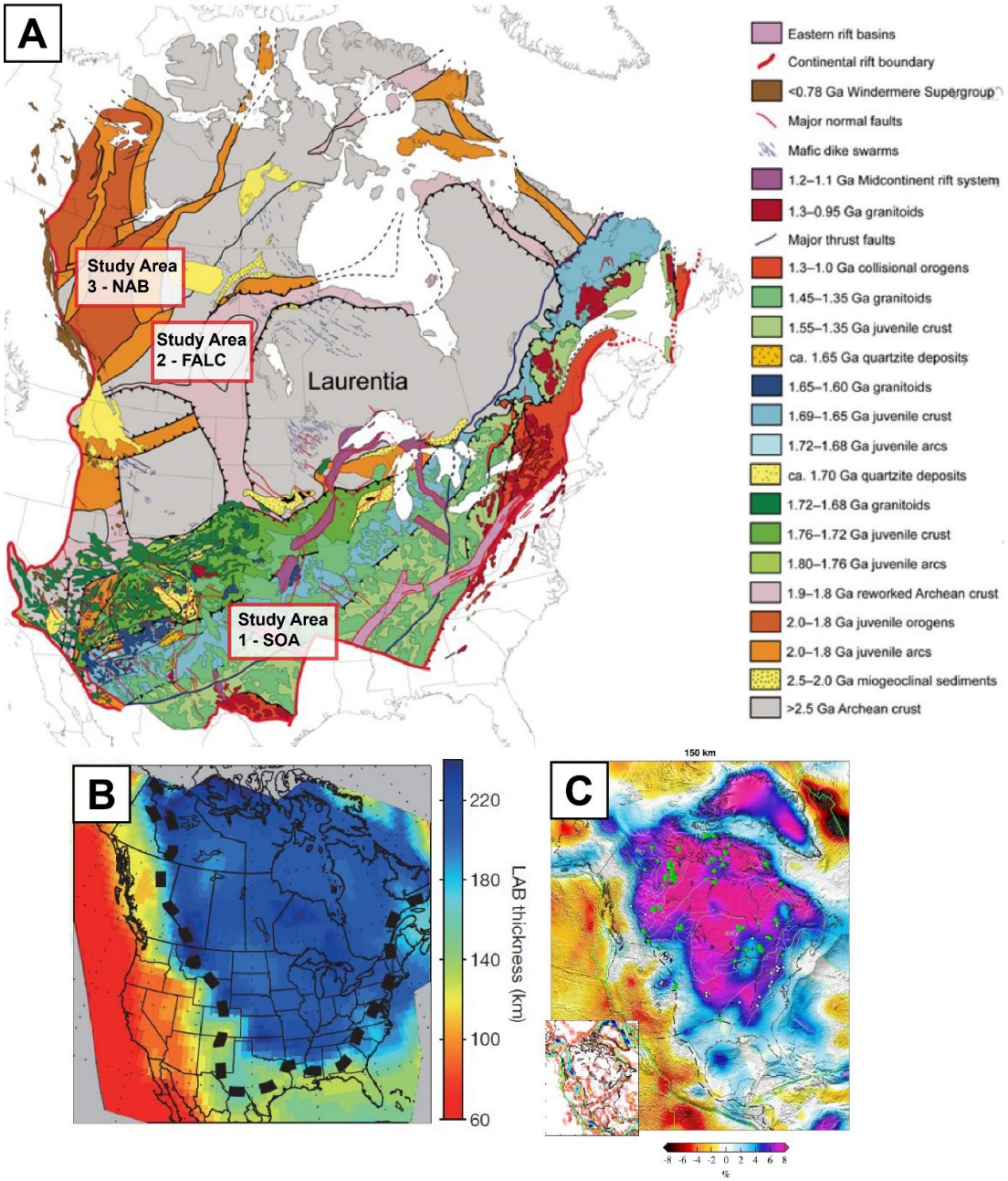

Figure 2.1*: (A) Tectonic map showing the terranes that form the Laurentian craton, and the study areas described in this thesis. Note that the map shows the evolution of the Laurentian craton up to the Cambrian. Additions to the North American after this date are typically associated with thinner lithosphere and are not included in the Laurentian craton. Figure adapted from Whitmeyer and Karlstrom (2007). (B) Lithosphere-asthenosphere boundary (LAB) depth map created from seismic data that shows the extent of the thick lithosphere of the Laurentian craton (black dashed line). Figure adapted from Yuan and Romanowicz (2010). (C) Updated seismic model at 150 km showing the extent of seismically slow and thick lithosphere corresponding to the Laurentian craton (purple and blue colors). Figure adapted from Schaeffer and Lebedev (2014). SOA, Southern Oklahoma Aulacogen; FALC, Fort à la Corne; NAB, northern Alberta.*

2.2 The Southern Oklahoma Aulacogen (SOA)

The SOA is a failed rift located on the southern margin of the Laurentian craton (study area 1 in Fig. 2.1). To the north of the SOA is the Mazatzal Province, which was accreted to the southeastern margin of the Laurentian craton from 1.65-1.60 Ga (Fig. 2.2). Later, from 1.55-1.35 Ga, the Granite-Rhyolite Province was accreted to the southeast margin of the Mazatzal (Fig. 2.2). The development of the SOA has routinely been suggested to have occurred along an arcuate suture zone boundary located between the Granite-Rhyolite and Mazatzal provinces (Budnik, 1986; Keller and Stephenson, 2007). Seismic datasets have repeatedly observed anomalies in the mantle lithosphere that are interpreted to suggest the presence of a terrane suture (e.g. Yuan et al., 2014; Porritt et al., 2014). However, it is impossible to determine if these features represent a pre-existing Mazatzal-Granite-Rhyolite suture or a secondary modification related to SOA tectonics. Subsequent to terrane suturing, both terranes saw widespread granitoid intrusions from 1.48-1.35 Ga (Whitmeyer and Karlstrom, 2007) (Fig. 2.2). Assembly of the Laurentian craton continued along the southern and eastern margins of the Granite-Rhyolite Province through the Proterozoic. However, the SOA region remained tectonically inactive at this time.

Renewed tectonism in the Mazatzal and Granite-Rhyolite provinces occurred around 1.1 Ga with the development of the western arm of the Midcontinent Rift. Geophysical data indicates the presence of a southward extension of the Midcontinent Rift into northern Oklahoma (Stein et al., 2018). However, there is no evidence that this extension interacted directly with the region of the SOA. The SOA underwent direct tectonism during the Cambrian disassembly of Rodinia, when it was part of a plume-driven rift-rift-rift triple junction alongside the Reelfoot Rift further east (Hoffman et al., 1974; Wall et al., 2021; Fig. 2.2). The SOA was the unsuccessful arm of this triple junction. The successful arms ultimately removed a block of the Granite-Rhyolite Province southeast of the SOA, which is now present in the Argentine Precordillera (Thomas et al., 2012). The majority of magmatism occurred in an ~2 Myr period from 532-530 Ma (Wall et al., 2021; Fig. 2.3). Magmatism was initially mafic and later followed by a felsic stage (Hanson et al., 2013; Brueseke et al., 2016). The total magmatic package is suggested to have a volume in excess of 250,000 km^3, leading Hanson et al. (2013) to suggest that the SOA was a Large Igneous Province

and the only one present along the southern margin of the Laurentian craton during the disassembly of Rodinia during the Cambrian.

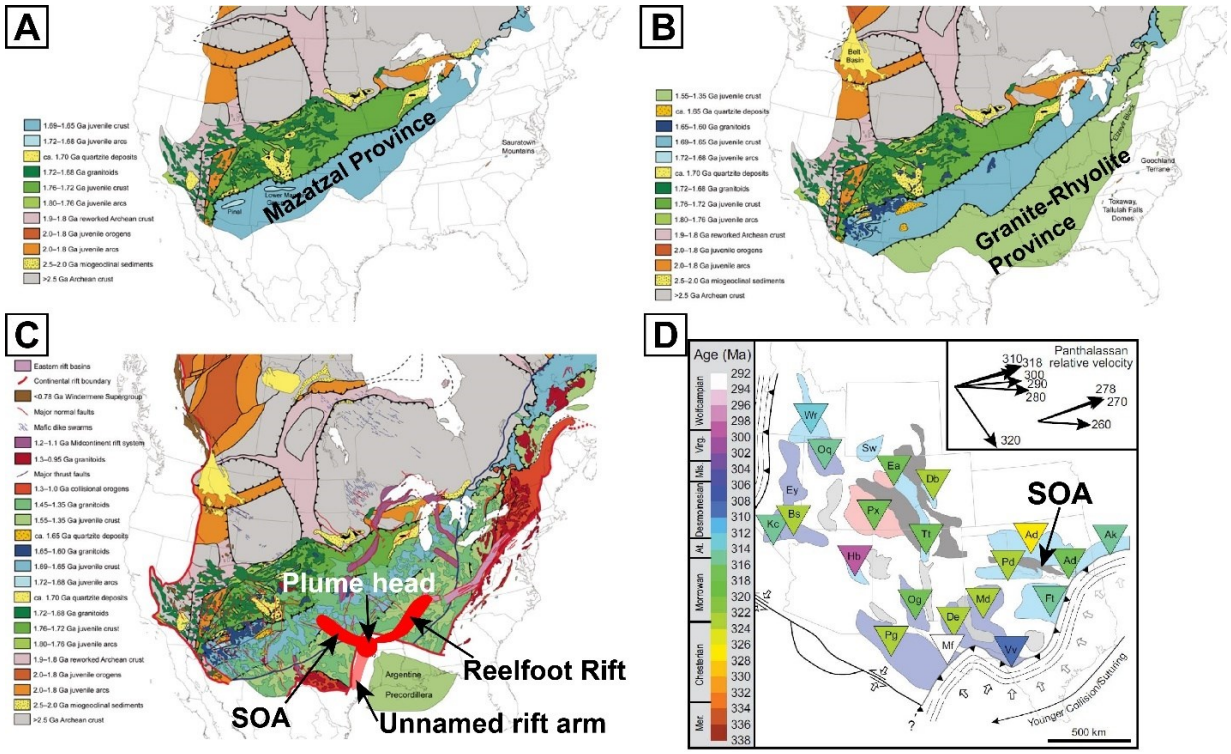

Figure 2.2*: Tectonic evolution of the SOA region. (A) Terrane assembly of the Mazatzal Provine and (B) Granite-Rhyolite Province. Figures adapted from Whitmeyer and Karlstrom (2007). (C) Cambriantriple junction rifting. Figure adapted from Whitmeyer and Karlstrom (2007). (D) Structural inversion and deformation associated with the formation of the Ancestral Rocky Mountains. Figure adapted from Leary et al. (2017).*

After Cambrian rifting, the SOA experienced minimal tectonic activity beyond phases of broad upwarping during the Devonian (Amsden, 1982; Fig. 2.3). Post-rifting subsidence and sedimentation buried the SOA beneath 4-5 km of sedimentary rock during this time (Gilbert, 1983). Starting in the Pennsylvanian and continuing into the Permian, the SOA was the first block to undergo uplift as part of the Ancestral Rocky Mountain Orogeny (Fig. 2.2) (Leary et al., 2017). This deformation resulted in 12-15 km of vertical uplift and upwards of 40 km of horizontal offset along left lateral strike-slip faults (Chase et al., 2022a, and references therein). Subsequent erosion and sedimentation resulted in the oil-rich Holis-Hardeman and Anadarko basins to the south and north, respectively. The SOA has been tectonically inactive since this time but is a notable intraplate-seismic hazard capable of producing earthquakes up to M_w 7.0 (Hornsby et al., 2020,

and references therein). Today, the SOA is located on the southern margin of the Laurentian craton where the lithosphere begins to rapidly thin beneath the terranes located further south (Yuan and Romanowicz, 2010; Schaeffer and Lebedev, 2014).

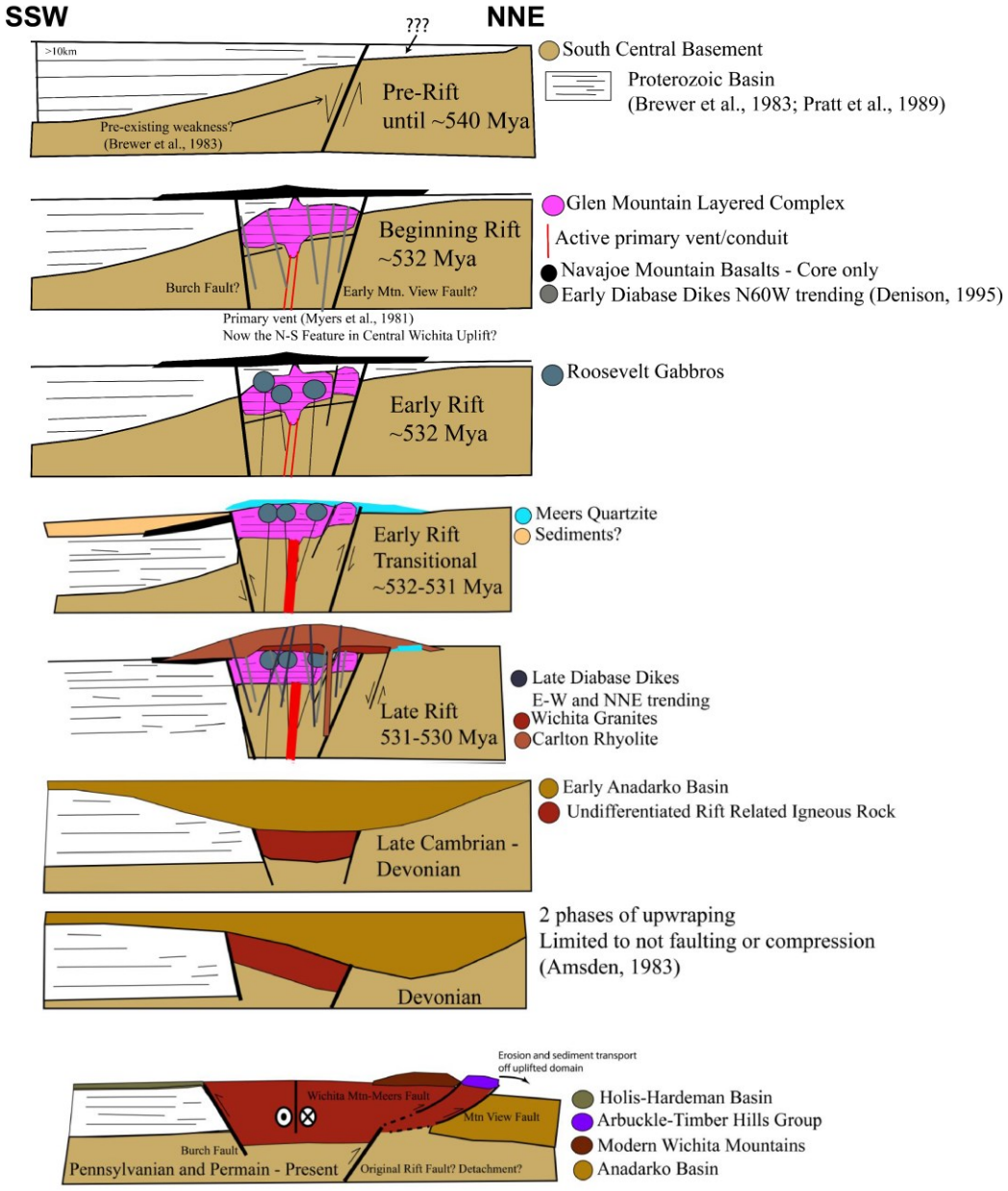

Figure 2.3*: A cross section view of the tectonic evolution of the SOA from the Cambrian through the Permian. Figure adapted from Gilbert (1983) but updated with observations from Hogan and Gilbert (1998); McConnell and Gilbert (1990), Keller and Stephenson (2007), Hanson et al. (2013), Wall et al. (2021), Cullen et al. (2016), and Chase et al. (2022).*

2.3 Sask craton, Trans-Hudson Orogen, and Fort à la Corne (FALC)

The Sask craton is a small Archean craton found within one of the fundamental tectonic features of the Laurentian craton, the Trans-Hudson Orogen (THO). This feature was formed around 1.9-1.8 Ga by the closure of the Manikewan Ocean and joined the Superior craton with the amalgamated Rae-Hearne-Slave cratons (Fig. 2.4). The location and structure of the Sask craton during this time remains enigmatic. It has a similar geochemical signature to the Wyoming craton located further south (Bickford et al., 2005). This observation has been used to suggest that the Sask craton was originally located to the south and was translated northward during THO tectonics (e.g., Bickford et al., 2005; Bedrosian and Finn, 2021). Independent evidence for this northward translation comes from folding consistent with north-south translation along the eastern edge of the Wyoming craton (Redden et al., 1990). However, Ansdell (2005) points out that no paleomagnetic data supports this suggestion.

The polarity and location of the subduction systems during the closure of the Manikewan ocean are also controversial. Early models developed from the LITHOPROBE datasets suggest that west-dipping subduction zones along the Superior and Hearne margins consumed most of the oceanic lithosphere (Ansdell, 2005 and references therein). However, other LITHOPROBE geophysical data suggest the possibility of an east-dipping subduction zone along the western margin of the Sask craton (Jones et al., 2005). After terminal ocean closure, the region underwent continued orogenic deformation with metamorphism reaching the amphibolite and granulite grade (Crocker et al., 1993; Ansdell, 2005). The collision, orogenesis, and resulting sedimentation and metamorphism have left the Sask craton largely buried beneath the internide (internal region) of the THO called the Reindeer zone (Ansdell, 2005). Subsequent deposition of the Western Canadian Sedimentary Basin since the Phanerozoic has also further buried much of both the THO and Sask craton, further complicating investigations. Ultimately, this has made it difficult to interpret the structure of the THO as well as the position, size, geometry, and role of the Sask craton during tectonism.

The highly complex structure and geology introduced during terminal collision and orogenesis occasionally may have resulted in reversals in crustal structure orientation that have led to

difficulty in interpreting subduction polarity (e.g., Bleeker, 1990; White et al., 2002; Bedrosian and Finn, 2021). Much of the geophysical data used for early interpretations was limited to the crustal depths (e.g., Lewry et al., 1994). Deeper imaging geophysical methods have suggested that some of the structures interpreted from these datasets reflect relatively thin-skinned secondary features related to overprinting during the terminal orogenic phase, which has led to incorrect interpretations about subduction polarity, but that these pre-collision structures are still preserved in the deeper lithosphere (Bedrosian and Finn, 2021). However, these datasets are largely limited to the United States, and the structure of the THO in Canada has not been investigated by similar datasets.

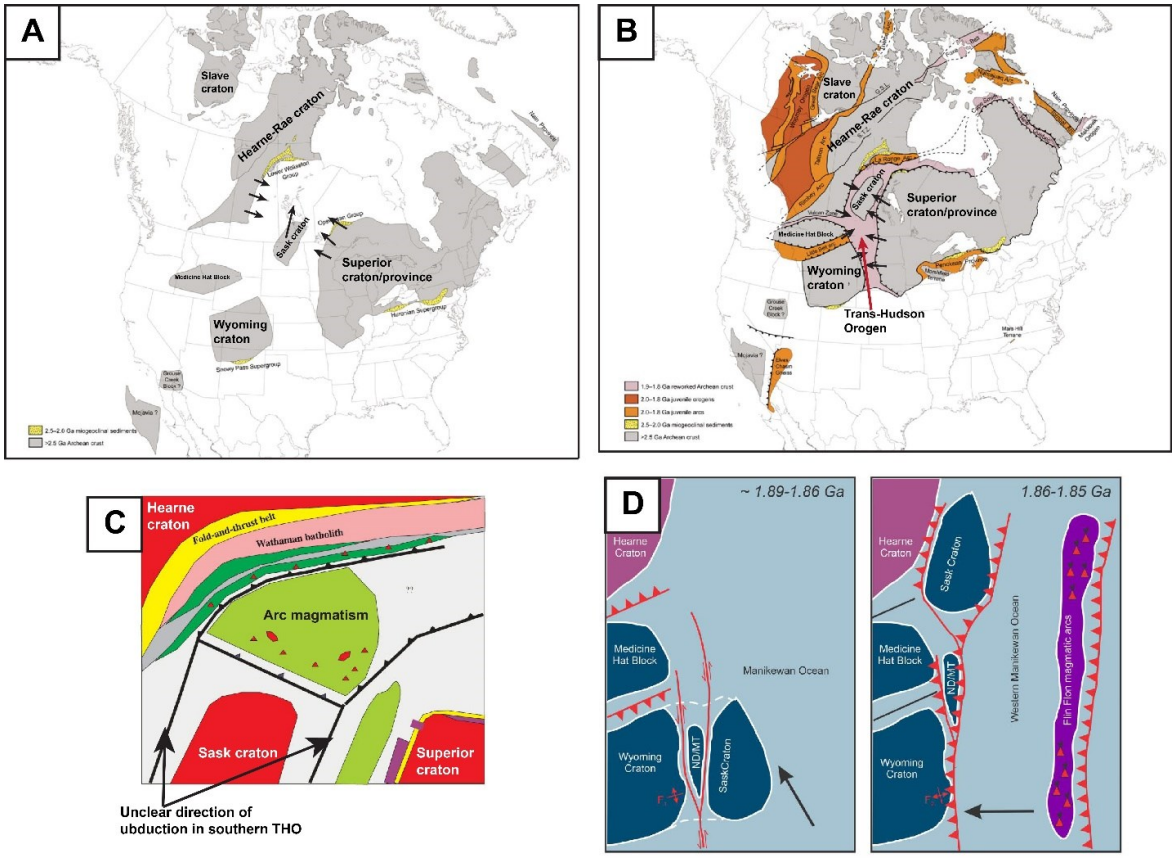

Figure 2.4*: Summary of the terranes that formed the THO. (A) The initial position of the major cratonic segments of the Laurentian craton at the beginning of Manikewan Ocean closure. (B) The position of the major cratonic segments during terminal ocean closure and formation of the THO. Arrows show the directions of motion of the various terranes. (A) and (B) adapted from Whitmeyer and Karlstrom (2007). Subduction systems in the THO as suggested by (C) Ansdell (2005), produced from a summary of LITHOPROBE data, and (D) as suggested by Bedrosian and Finn (2021), produced from more modern deep-imaging geophysical data. Note the variability between subduction polarity along the margin of the Sask craton between C and D. Also, note the variability between subduction polarity between C and B.*

The Sask craton is intruded by kimberlites at Fort à la Corne (FALC), Pikoo, and Candle Lake. Two distinct episodes of kimberlite magmatism are documented (1) at Pikoo at 417 ± 14 Ma and (2) at FALC at 115-92.5 Ma, respectively (Kjarsgaard et al., 2017; Smyth, 2020). The Candle Lake kimberlite remains undated but is thought to be a satellite cluster of the FALC kimberlites (Pezzera et al., 2024). The FALC kimberlite field and Candle Lake kimberlite indicate that lherzolite and eclogite are present in the lithospheric mantle of the Sask craton and that part of the lithosphere was added during the formation of the THO (Czas et al., 2018; 2020; Pezzera et al., 2024). The presence of eclogite alongside the role of organic carbon in diamond formation (Milne, 2024) shows that subduction may have played a critical role in the formation of the Sask craton. The formation and stabilization of the lithosphere in this location during the Paleoproterozoic is significant from a diamond exploration perspective. This is because it represents a departure from the typical association of diamond potential with Archean lithosphere (Czas et al., 2020; Milne et al., 2024). As a result, the Sask craton represents an ideal location to study the diamond potential of Paleoproterozoic cratons, which could represent regions of untapped economic potential.

In addition to regional diamond potential, the region of the THO around the Sask craton also hosts world-class orogenic and volcanogenic massive sulfide mineral deposits (Morelli and MacLachlan, 2012). Exploration and production have occurred in this region for over 100 years. The majority of these deposits are found within thrust-imbricated or major orogenic structures (Syme et al., 1999; Rubingh et al., 2024). Key regions associated with mineralization have been around Flin Flon and Snow Lake, Manitoba and La Ronge, Saskatchewan. While extensive exploration activity has taken place in the region, little attention has been paid to regional mineralization (Fig. 2.5) on spatial scales greater than the individual deposit. It remains unclear what, if any, larger structures may control mineralization and how these relate to THO tectonics.

A major low resistivity anomaly within the THO was first reported on the basis of geophysical data collected during the 1970s (Reitzel et al., 1970; Camfield et al., 1970; Rankin and Reddy, 1973). This feature was named the North American Central Plains (NACP) conductor and has been observed in deep imaging electromagnetic geophysical surveys from Saskatchewan in Canada to Wyoming in the United States (Jones et al., 2005; Bedrosian and Finn, 2021). A similar low

resistivity anomaly has been interpreted from magnetometer stations in western Manitoba (Gupta et al., 1985; Jones et al., 2005). These observations have been used to suggest that the NACP conductor is over 2,200 km long, potentially as long as the entire >3,000 km long THO, and that THO tectonics were surprisingly uniform along its entire length (Jones et al., 2005). In the southern THO, the continuity of the NACP conductor can be readily observed in resistivity models derived from MT data collected during the EarthScope project, and conductance maps of the crust seem to suggest it may be part of an en-echelon series of paleo-subduction and suture zones (Bedrosian and Finn, 2021). In Canada, the north-south continuity of the NACP conductor is less clear. While it appears in multiple LITHOPROBE MT profiles across Saskatchewan, these MT data were collected on 2-D profiles spaced hundreds of kilometers apart and are largely broadband MT data. This limits their ability to resolve the regions between profiles and constrains the 3-D structure necessary to map the NACP conductor as a continuous feature in the province.

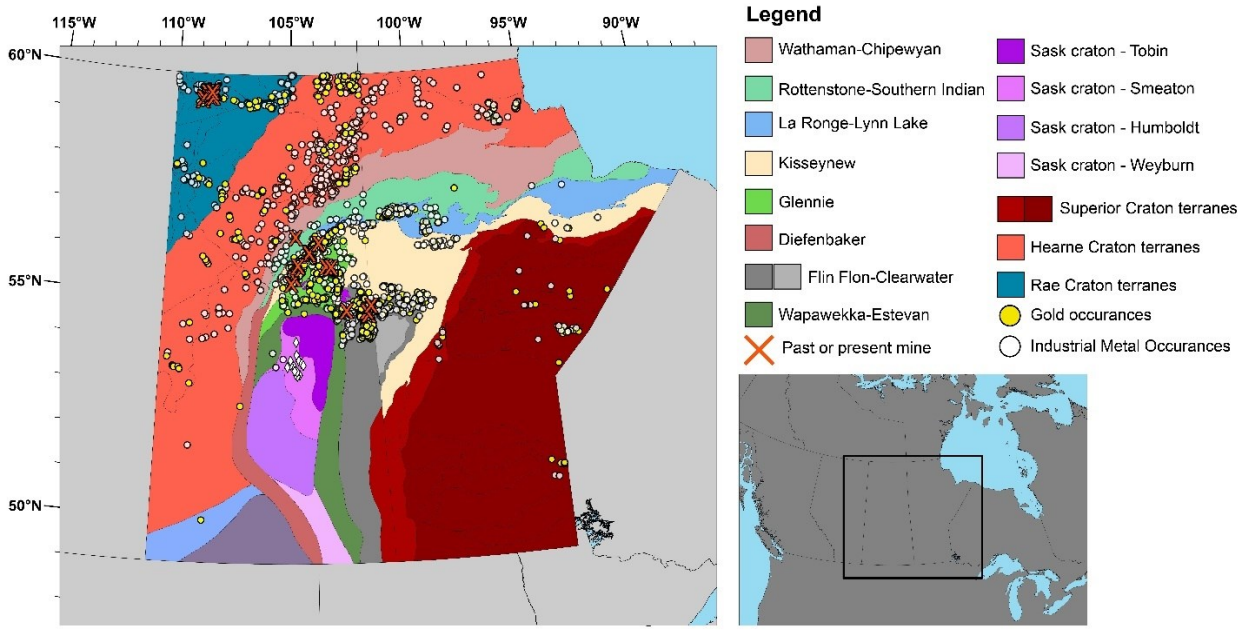

Figure 2.5*: Map showing mineral (precious and industrial metals), kimberlites, and previous and present mining within the THO in Manitoba and Saskatchewan. Tectonic terranes taken from the Saskatchewan and Manitoba Geological Surveys.*

The continuing difficulty in determining the structure of the THO and the tectonic processes that formed it are the result of two key challenges. The first is the inherent difficulty of reconstructing tectonic events that occurred in the Paleoproterozoic, because most of the geological evidence for

these events has been eroded, buried, or modified by glaciation. The other challenge is a lack of deep imaging geophysical data, particularly along the THO in Canada.

2.4 Taltson magmatic zone and Buffalo Head terranes in northern Alberta (NAB)

The third study area encompasses the Taltson and Buffalo Head terranes along the western margin of the Laurentian craton (Fig. 2.1). The Taltson magmatic arc (or Taltson-Thelon orogenic belt) and Buffalo Head terranes were accreted to the western margin of the Hearne-Rae craton around 1.96-1.86 Ga (Whitmeyer and Karlstrom, 2007). The Taltson magmatic arc terrane is characterized by abundant granitoids emplaced over two phases from 1.99-1.93 Ga into a lithologically diverse metaplutonic and paragneissess basement aged 2.4-2.1 Ga, though some slices of older Archean units are also present (McNicoll et al., 2000). The Buffalo Head terrane has an age of 2.3-2.0 Ga (Ross et al., 1994). Controversy exists regarding the tectonic evolution of the Taltson magmatic arc and Buffalo Head terranes and the genesis of the granitoids, and two tectonics models have been proposed. The first model was summarized by Ross (2002) and Ross and Eaton (2002) and is shown in Figure 2.6. This model views the Taltson magmatic arc terrane as a plate margin with oceanic lithosphere separating it from the Buffalo Head terrane. The Chinchaga terrane was accreted to the Buffalo Head terrain through east-dipping subduction, which produced magmatic rocks unique to the Buffalo Head terrane from 1.99-1.93 Ma. The combined continental block was isolated in the ocean until west-dipping and east-dipping subduction occurred along its western and eastern margins, respectively from 1.98-1.90. This process accreted the Buffalo Head-Chinchaga landmass to the larger Taltson-Rae continent and produced the granitoids found in the Taltson.

The second model is summarized by Chacko et al. (2000) and shown in Figure 2.7. This model is largely focused on the evolution of the Taltson magmatic zone terrane. It notes that the 1.99-1.93 granitoid suite lacks the mantle signature expected for continental-margin arc rocks derived from subduction. Instead, it suggests that these rocks are intra-crustal in origin and formed in the continental hinterland of a convergent plate margin. The model suggests that the Taltson magmatic zone terrane was a plate-interior region, and that magmatism occurred in response to the orogenic thickening of the continental interior similar to the Tian Shan region in the modern India-Asia

collision system in China, Kyrgyzstan, Kazakhstan, and Uzbekistan. This model also suggests that regional continental assembly occurred between 2.5-2.0 Ga, earlier than the prior model. This earlier terrane assembly may have been responsible for 2.44-2.27 Ga granitoids observed in the Taltson magmatic zone (McNicoll et al., 1994), and the suture zone formed during this phase may have been reactivated by the younger 1.99-1.93 granitoids. Critically, this model implies that subduction only occurred west of the Buffalo Head terrane.

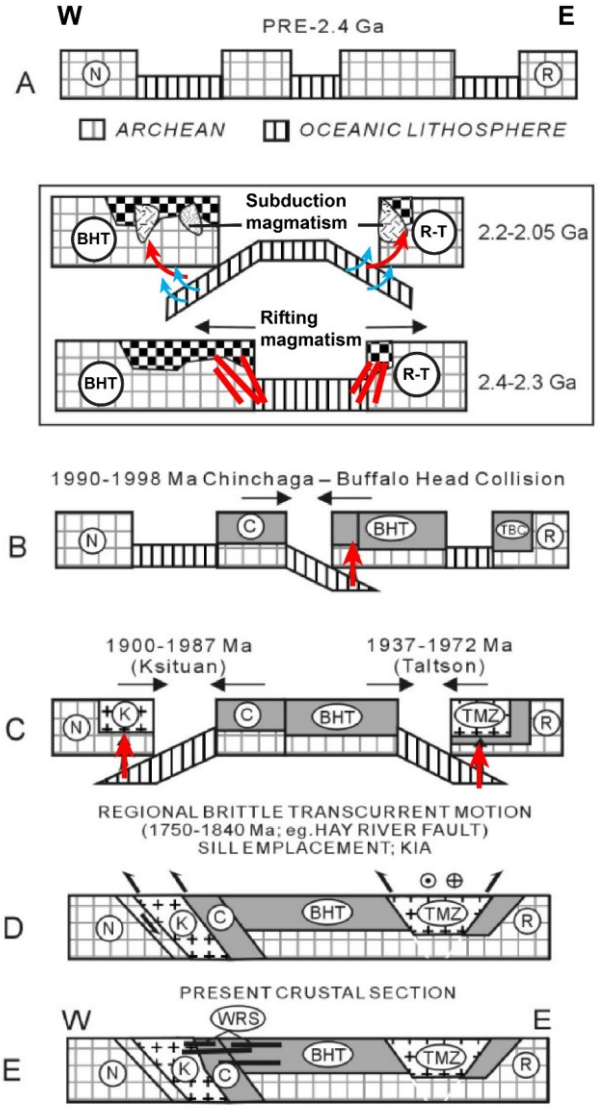

***Figure 2.6**: The subduction model of Ross and Eaton (2002) for the Buffalo Head and Taltson terranes. Figure adapted from Ross and Eaton (2002). Abbreviations: N, Nova domain; R, Rae province; BHT, Buffalo Head terrane; R-T, Rae-Taltson terrane; C, Chinchaga domain; TBC, Taltson basement complex, K, Ksituan domain; WRS, Winagami reflection sequence. Note that the use of R and R-T in this figure discusses similar terranes. The R-T distinction is added to accommodate the possibility that the Taltson terrane was a segment of the larger Rae province.*

After terrane assembly, it is believed that the Taltson magmatic arc and Buffalo Head terranes were tectonically inactive until the assembly of the Canadian Cordillera in the Cretaceous. While Cordillera formation occurred further west in modern British Columbia, during this time, kimberlite and other alkaline intrusions formed within the Taltson magmatic arc, Buffalo Head, and Chinchaga terranes. These intrusions are aged 88-60 Ma, occur in three distinct clusters over a distance of 400 km, and are named the Mountain Lake intrusion, Buffalo Head kimberlite field, and Birch Mountains kimberlite field (Fig. 2.8). A number of tectonic models have been invoked to explain the formation and localization of these intrusions, and these are examined in detail in Chapter 7. Curiously, the diamond potential between the fields is highly variable. The Buffalo Head field has the best diamond grades and potential, while the Birch Mountain field has limited potential and poor diamond grades (Banas et al., 2007; Eccles, 2011). At the same time, the Birch Mountain field is underlain by a major lithosphere low resistivity anomaly of unknown origin, while the Buffalo Head field is highly electrically resistive (Wang and Unsworth, 2022). At present, the Mountain Lake intrusion does not have any known diamond potential and does not appear to be a kimberlite, largely precluding it from carrying diamonds at all.

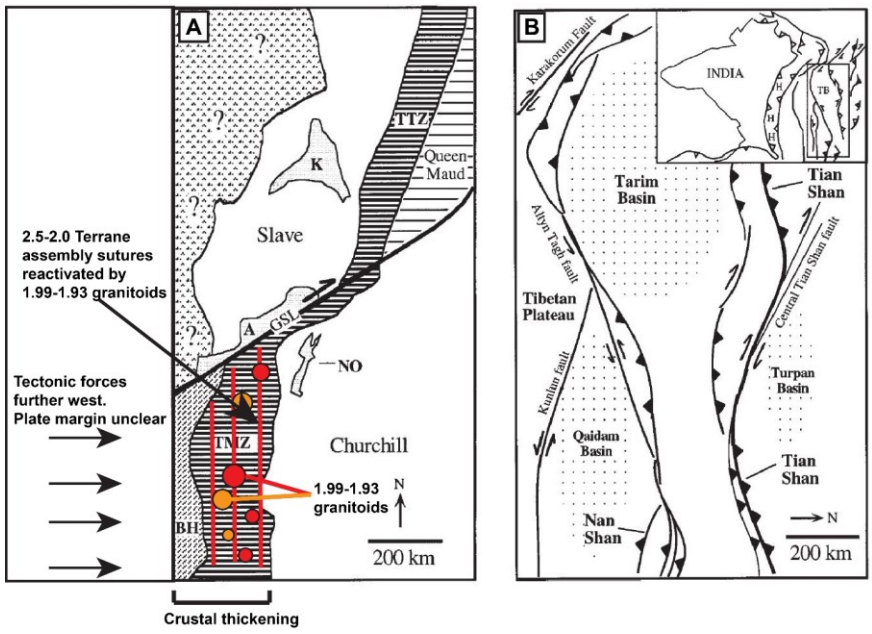

Figure 2.7*: The plate-interior model of Chacko et al. (2000) for the Taltson magmatic arc terrane, and Buffalo Head terrane, by extension. Figure adapted from Chacko et al. (2000). Abbreviations: TMZ – Taltson magmatic zone.*

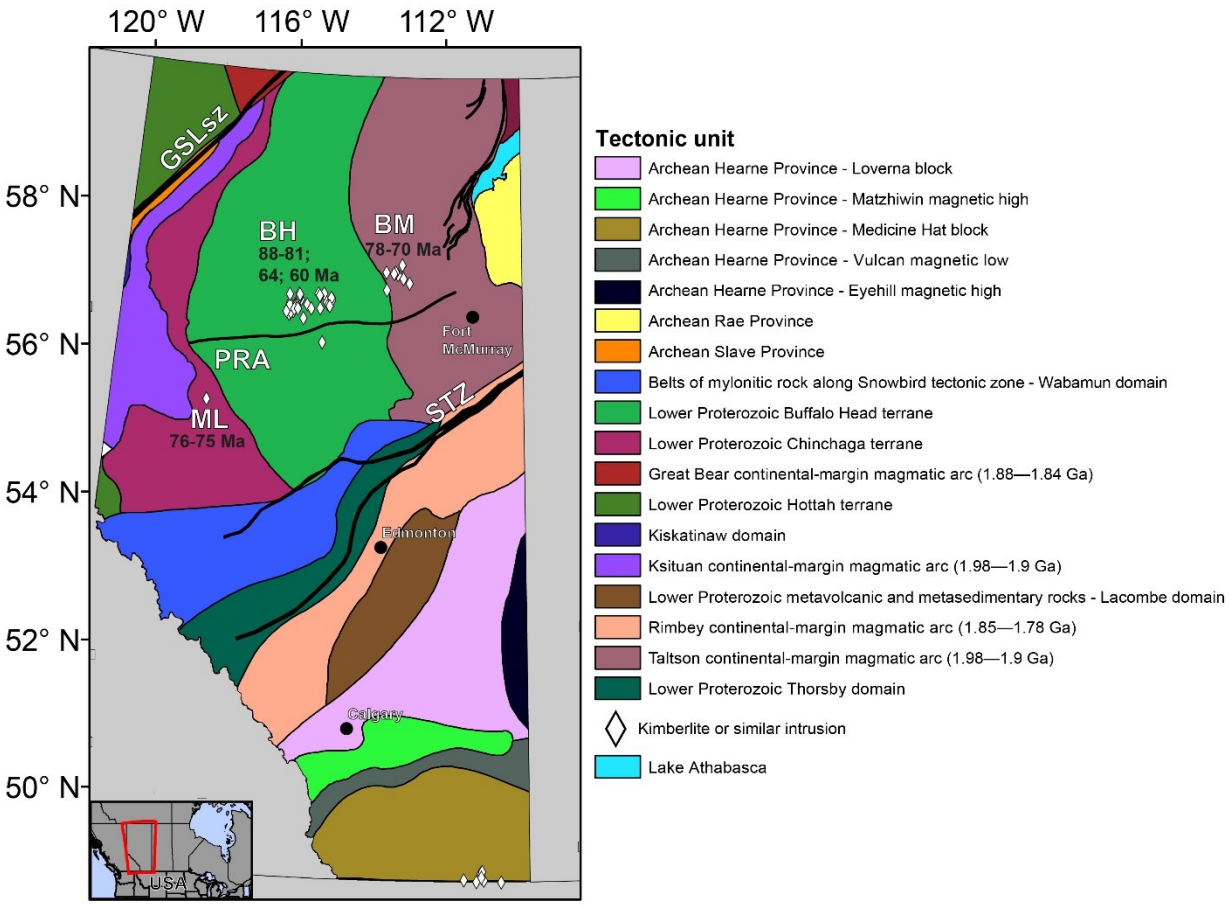

***Figure 2.8**: Tectonic terrane map from Ross et al. (2008) derived from potential field data. Kimberlites and similar intrusions are shown as white diamonds. Age dates for the kimberlites and similar intrusions are from Eccles (2011). Abbreviations: BH, Buffalo Head Hills kimberlite field; BM, Birch Mountain kimberlite field; ML, Mountain Lake intrusion; PRA, Peace River Arch; GSLsz, Great Slave Lake shear zone; STZ, Snowbird tectonic zone.*

2.5 Summary

The three study areas investigated in this thesis are located in diverse regions of the Laurentian craton and were involved in key episodes of its tectonic evolution. The SOA is located along the poorly understood southern margin of the Laurentian craton and was involved in two episodes of tectonism. The first was rifting in the Cambrian, and the second was the enigmatic Ancestral Rocky Mountain orogeny. The Sask craton is located within the Trans-Hudson Orogen, arguably the most important tectonic feature responsible for the formation of the Laurentian craton. The Taltson and Buffalo Head terranes in northern Alberta are located along the western margin of the Laurentian

craton, a region where little is known about the growth and evolution of the craton. Both northern Alberta and the Sask craton host diamondiferous kimberlites. Investigations in these regions can provide insights into the ascent and localization of diamond resources within the craton

CHAPTER 3. ELECTROMAGNETIC GEOPHYSICAL METHODS AND THE ELECTRICAL RESISTIVITY OF THE DEEP LITHOSPHERE

Electrical resistivity is an important rock property that is often measured in studies of the lithosphere in both tectonically active and inactive regions. Resistivity values in the Earth can vary by orders of magnitude from 10^{-7} to 10^{12} Ωm (Fig. 3.1; Simpson and Bahr, 2005). Additionally, many conductive minerals and phases (e.g., amphibole, fluids, melt, etc.) can be restricted to certain depth intervals or specific tectonic processes and environments (Fig. 3.2; Selway, 2014). This means that electrical resistivity can be used to investigate past or present tectonic episodes and to investigate how they interacted with the lithosphere.

This chapter introduces the concept of electrical resistivity and describes how it varies among common Earth materials and in the lithosphere. This provides the necessary background to the research presented in Chapters 5, 6, and 7, where resistivity models of the lithosphere mantle are interpreted in terms of (a) present-day structure and (b) tectonic history.

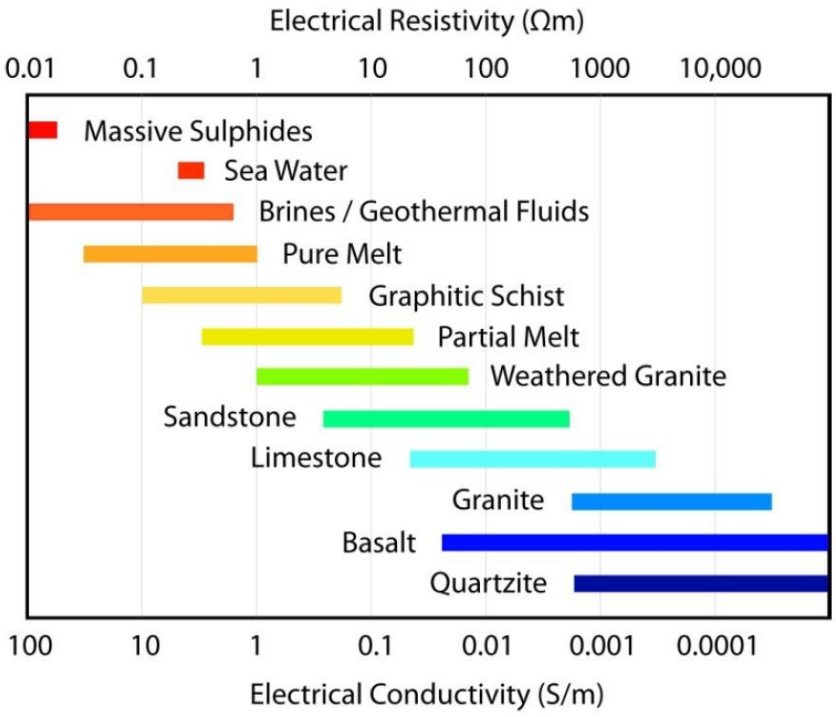

Figure 3.1: *The electrical resistivity and electrical conductivity of some common Earth materials. From Comeau (2015), values taken from Simpson and Bahr (2005).*

The resistivity of the lithosphere can be measured with a range of geophysical methods. These include electromagnetic (EM) methods using natural EM signals, such as magnetotellurics (MT), and controlled-source EM methods in which the signals are generated with a transmitter. Controlled source methods are used in a wide range of configurations, and systems operate in both the time domain and frequency domain (Nabighian, 1987). These systems can operate on the ground or on airborne platforms depending on the survey requirements (e.g., Smith et al., 1996). However, controlled-source EM methods are typically limited in their depth of exploration to no greater than 1-2 km. This is because controlled source EM methods operate in a relatively high frequency range, which does not penetrate into the Earth as deeply as lower frequency natural EM signals (see section 3.2.3). Additionally, controlled source EM methods rely on human-generated EM signals, which are inherently weaker than the EM signals associated with natural sources that come from either lightning strikes or interactions of the magnetosphere with the solar wind. However, these depths are often sufficient for mineral exploration activities, and so the use of controlled-source EM methods and systems has become widespread. For exploration or scientific investigations at depths greater than 1-2 km, the MT method is used due to the relatively low frequencies and greater signal strengths.

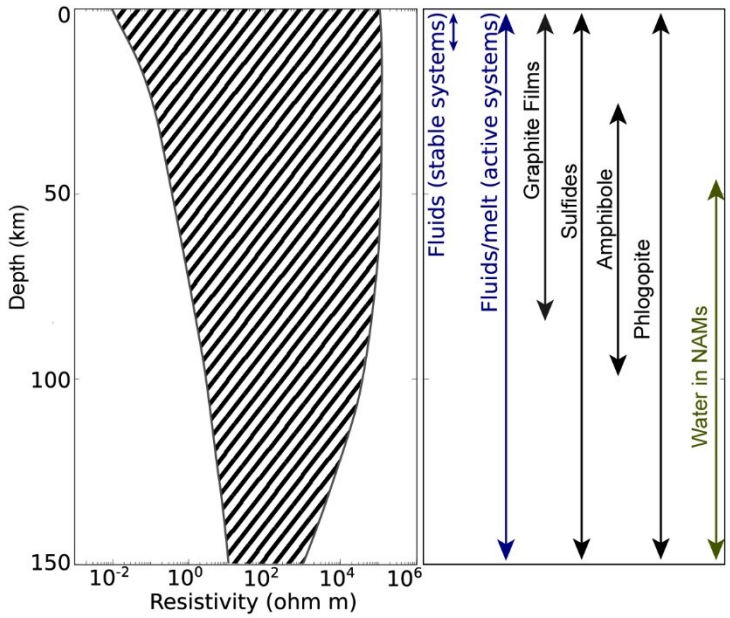

Figure 3.2*: A plot showing the range of resistivity values commonly observed in the continental lithosphere as a function of depth. The plot also shows the depth intervals over which common conductive mechanisms operate in the lithosphere. This diagram can be used to determine the origin of low resistivity anomalies. Adapted from Selway (2018). NAM = Nominally Anhydrous Minerals.*

3.1 Definition of electrical resistivity

Electrical conductivity is an inherent physical property of a material and determines its ability to permit the flow of electrical current. The material properties relevant to electrical conductivity can be related to it as follows:

$$\sigma = \frac{ne^2\tau}{m} \tag{3.1}$$

where σ is the electrical conductivity in Siemens per meter (S/m), m is the mass of an electron, n is the number of electrons per unit volume, and τ is the relaxation time (s). This equation describes how electrical conductivity is related to the inherent physical properties of a material.
The electrical conductivity can be related to electrical resistivity by:

$$\sigma = \frac{1}{\rho} \tag{3.2}$$

where ρ electrical resistivity in ohm meters (Ωm). The reciprocal:

$$\rho = \frac{1}{\sigma} \tag{3.3}$$

electrically resistivity is more commonly used in MT studies to display data. The electrical resistivity should not be confused with electrical resistance. If we consider the case of a sample of a conductor, the resistance is defined by:

$$\rho = \frac{RA}{L} \tag{3.4}$$

where R is the material resistance, A is the cross-sectional area (m^2), and L is the length (m). The resistance is clearly dependent on the length (L) and cross-sectional area (A) of the sample. The electrical resistivity (or conductivity), however, is an inherent property of the material (Equation 3.1). In the remainder of this chapter, the resistance is not generally important. Instead, it is the electrical resistivity (or conductivity) that is of interest.

The terms electrical resistivity or electrical conductivity are both used when discussing the anomalies investigated by EM methods. This is a standard practice in EM geophysical studies, as it helps simplify the discussion of anomalies by allowing them to be categorized as conductors and resistors that can then be linked with their respective electrical properties. The terms conductor and resistor are relative terms when used to discuss anomalies. They do not refer to absolute

resistivity or conductivity values. Rather, they are generally used to discuss regions where the electrical properties of the subsurface deviate from the background values. For example, a cratonic region of the Earth could be generally electrically resistive with values >1,000 Ωm but host a few low-resistivity anomalies of various magnitudes <50 Ωm. These low resistivity anomalies would all be referred to as conductors. In some cases, adjectives such as highly, major, moderate, very low, etc., may be added to a conductor or resistor to differentiate anomalies by conductivity or resistivity magnitudes. For example, to differentiate between a 50 Ωm anomaly (i.e., moderate conductor) and a 1 Ωm anomaly (i.e., major conductor).

3.2 Mixing laws, multi-phase systems, and bulk resistivity in the crust and mantle lithosphere

The subsurface of the Earth is almost always a mixture of several materials or mineral phases with different resistivity values. To accurately model the bulk resistivity of the subsurface, it is important to consider the electrical resistivity of each phase. This is because the subsurface is almost always a mixture of two or more phases, be that minerals, rocks, or fluids. In the crust, it is usually sufficient to model the bulk resistivity as a mixture of two or three phases at most. Traditionally, the solid minerals and rocks of the crust are assigned a high resistivity (e.g., 1000 Ωm or greater). Conductive phases, typically sulfides, graphite, aqueous fluids, or melt, are then modeled as additional phases as needed. One of the most popular models for determining the bulk conductivity of a two phase is Archie's Law (Archie, 1942):

$$\sigma_b = \sigma_f \phi^m \tag{3.5}$$

where σ_b is the bulk conductivity, σ_f is the fluid, melt, or other conductive phase conductivity, ϕ is the porosity or fraction of the conductive phase (e.g., melt), and m is the cementation exponent. The cementation exponent is typically in the range 1 and 2 and is a measure of the interconnectivity of the conductive phase, with lower numbers representing increased interconnection. The more interconnected a conductive phase is, the more it is able to influence the bulk conductivity. Archie's Law assumes that the matrix has a very low conductivity. In practice, this is not true, but it usually does not matter due to the significant differences in conductivity between rocks at crustal depths and the various conductive phases (Fig. 3.1). Archie's Law also assumes that surface conduction on the surface of the mineral grains is not significant. As a result, using Archie's Law

will underestimate the bulk conductivity where clays are present, as surface conduction can be a significant process in these minerals. This can impose limits on the application of Archie's Law in clay-rich rocks in sedimentary basins or where clay rock rocks have been buried by tectonic processes.

To model the conductivity of more complex systems, a two-phase modified Archie's Law has been developed by Glover et al. (2000). This approach can be used when it is necessary to incorporate the conductivity of the host rock. The equation is written as:

$$\sigma_b = \sigma_h(1-\phi)^p + \sigma_f\phi^m \tag{3.6}$$

where σ_h is the host rock (matrix) conductivity and p is:

$$p = \frac{\log(1-\phi^m)}{\log(1-\phi)} \tag{3.7}$$

The two-phase mixing model is a better approximation than the standard Archie's Law in the elevated temperature and pressure conditions of the deeper lithosphere, where the matrix can be moderately conductive.

In the case of n-phases, the multi-phase or generalized Archie's Law of Glover (2010) can be used and is written as:

$$\sigma = \sum_{i}^{n} \sigma_i \phi_i^{m_i} \tag{3.8}$$

where σ_i, ϕ_i, m^i are the conductivity, porosity (or fraction), and cementation exponent (or phase exponent), respectively, for each of the various phases in the matrix. This equation is an intuitive extension of Equation 3.5 and described by Glover (2010). This equation is often used in multi-phase systems, particularly in the mantle lithosphere, where it represents the best available model. This is because conduction often occurs in multiple minerals simultaneously (usually 3 or more for peridotite lithosphere) due to the elevated P-T conditions in the mantle. As a result, the conductivity effects of mineral needs to be accounted for alongside any additional conductive minerals of interest to the interpreter. Figure 3.3 is a conceptual model demonstrating this and showing how Equation 3.8 can be applied to a mantle peridotite. The four main mantle minerals

are olivine, orthopyroxene, clinopyroxene, and garnet and they can be considered conductive phases as shown in Figure 3.8A. The conductivity of each mineral phase can be enhanced by water content as described in Sections 3.3 and 3.4. This water content itself does not act as another phase but acts to increase the conductivity of each mineral (sections 3.4 and 3.5). Figure 3.3B shows the same peridotite with the introduction of a sulfide vein that acts as an additional conductive phase. This increases the number of phases to be considered in Equation 3.8 to five. In this conceptual model, the conductive phase is well-connected and dispersed throughout the model and would have a major effect on the bulk resistivity, even in small amounts.

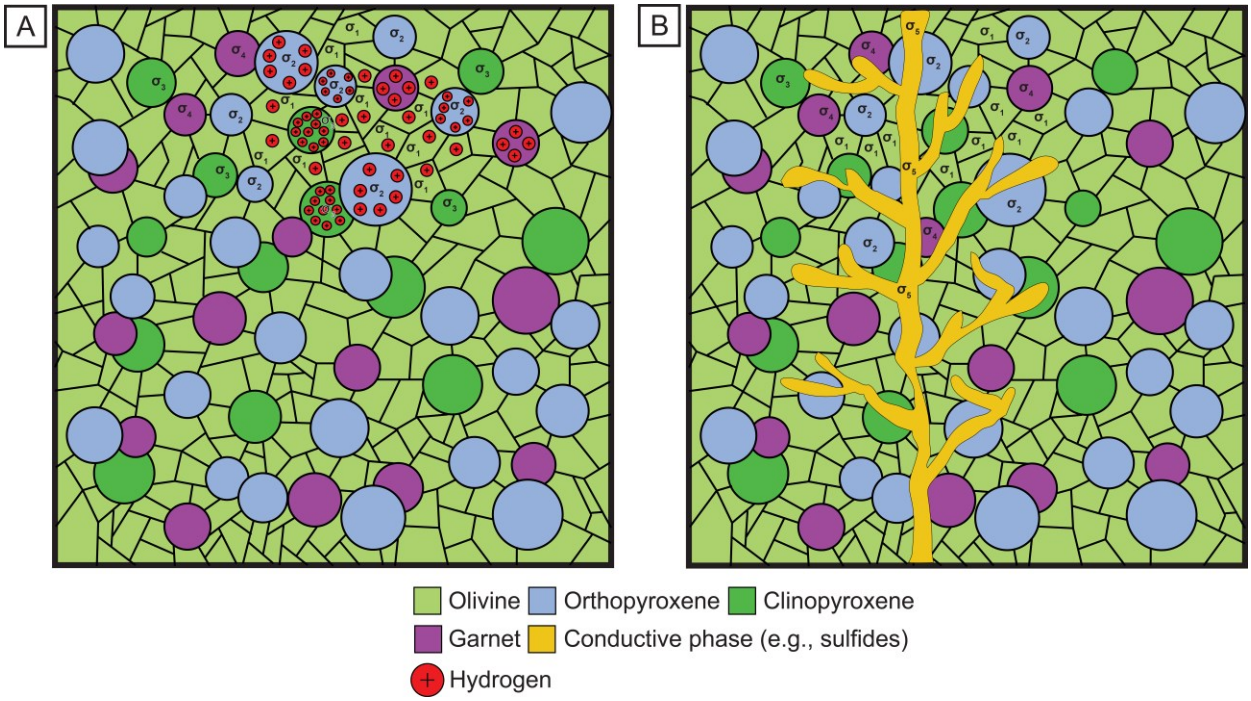

Figure 3.3*: (A) A schematic cartoon of a multi-phase system. In this case, it is a hypothetical lherzolite with the four main mineral assemblages to show how each is an independent conductive phase that would need to be modeled with Equation 3.8 in the lithospheric mantle. The added hydrogen atoms H+ would enhance the conductivity of each mineral separately. The number of hydrogen atoms in each mineral reflects the general difference in storage capacity for each mineral. (B) The same schematic cartoon, but this time it shows how a well-connected conductive phase (e.g., phlogopite or sulfides) could be distributed in a peridotite. In this case, the conductive phase is a separate phase that must be incorporated into Equation 3.8.*

When conductive melts or fluids are present in both the crust and mantle lithosphere, the concept of the dihedral angle becomes important. The dihedral angle, or wetting angle, determines if fluid or melt will be interconnected. The critical value for the dihedral angle is 60°. A dihedral angle

larger than 60° will mean that the fluid or melt phase will form blebs, or isolated pockets that are not interconnected. A dihedral angle less than 60° will mean that the fluid or melt phase will be interconnected. The dihedral angle has important complications for bulk resistivity. For example, if the dihedral angle of a melt is greater than 60°, the bulk resistivity might be relatively unchanged despite the presence of an otherwise conductive fluid or melt.

Another way to calculate bulk conductivity is to use the Hashin-Shtrikman upper and lower bounds, which are:

$$\sigma_+ = \sigma_2 \left(1 - \frac{3(1-\phi_2)(\sigma_2 - \sigma_1)}{3\sigma_2 - \phi_2(\sigma_2 - \sigma_1)}\right) \tag{3.9}$$

and

$$\sigma_- = \sigma_1 \left(1 + \frac{3\phi_2(\sigma_2 - \sigma_1)}{3\sigma_1 + (1-\phi_2)(\sigma_2 - \sigma_2)}\right) \tag{3.10}$$

respectively (Hashin and Shtrikman, 1962; Glover, 2010). The ϕ denotes the volume fraction (or porosity) and σ_1 and σ_2 are the conductivities of the two different phases. The upper bound (Equation 3.9) is denoted as the HS+ and is comparable to isolated resistors in a conductive matrix i.e., a good conductor or region with low resistivity. The lower bound (Equation 3.10) is denoted HS- and is comparable to isolated conductors in a resistive matrix i.e., a poor conductor or region of high resistivity. A conceptual model of the Hashin-Shtrikman bounds is shown in Figure 3.4. Figure 3.5 compares the calculated resistivity of conductive graphite in a resistive crystalline basement using Archie's Law and the Hashin-Shtrikman bounds. It shows that as the cementation exponent used in Archie's Law increases the calculated resistivity slowly approaches the Hashin-Shtrikman lower bound. that A deeper overview of mixing models is given by Glover (2010) and Cai et al. (2017).

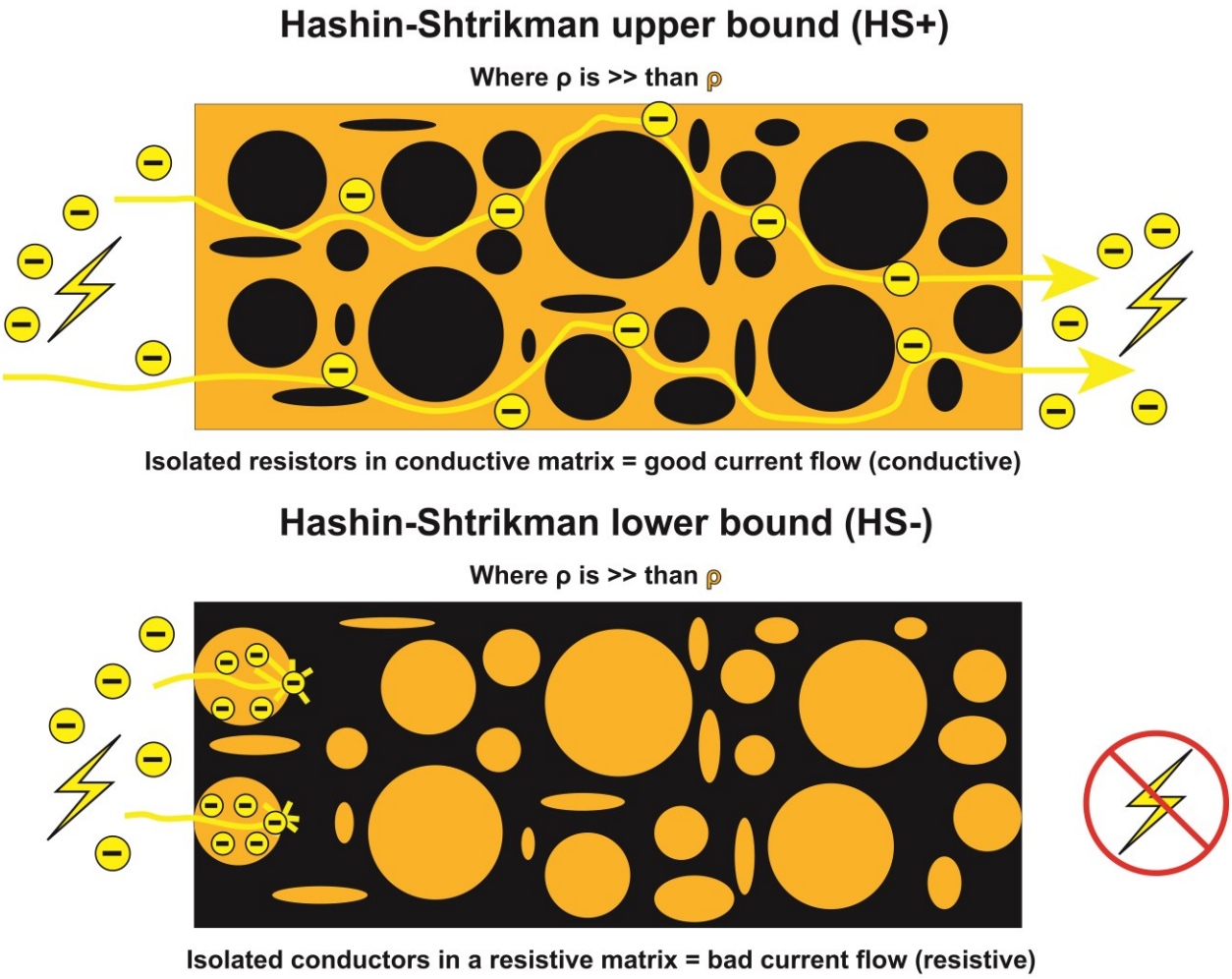

Figure 3.4: *Conceptual model demonstrating the Hashin-Shtrikman upper and lower bounds and how they relate to the movement of electrical charges. ρ denotes the resistivity of the two materials (gold and black).*

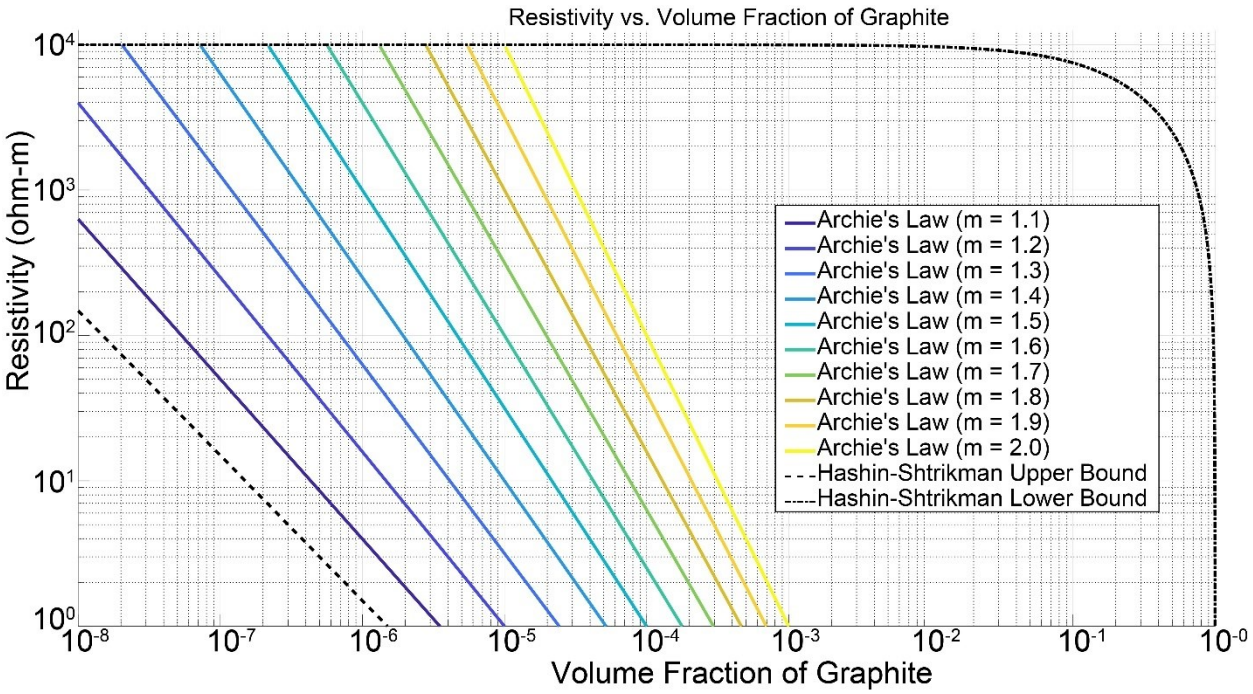

Figure 3.5: *Plot comparing the calculated electrical resistivity as a function of graphite volume fraction for Archie's Law and the Hashin-Shtrikman upper and lower bounds. Resistivity values of 10-6 and 104 ohm-m were used for graphite and a hypothetical crystalline crust, respectively.*

3.3 Resistivity of minerals in the crust and near surface

The Earth is composed of an assemblage of different materials that are present on a variety of spatial scales. These ranges from the pore scale to entire geologic terranes. These Earth materials can be broadly subdivided into minerals and fluids. Fluids in the Earth generally refer to water, hydrocarbons, or melts. Minerals are solid, inorganic, naturally occurring, and have a well-defined chemical and crystallographic structure. Different Earth materials conduct electricity differently (Fig. 3.1), with some acting as resistors and others as conductors. Thus, in the Earth, electrical current will flow more easily through some materials than others.

The majority of minerals at the surface or near the surface in the crust are silicates, have high a high electrical resistivity. This is because there is no ability for charge carriers such as electrons or ions to move through the rigid crystalline lattice. As seen in Figure 3.1, common crustal rocks such as granite, basalt, and quartzite composed of these silicate minerals and have resistivity values greater than 100 Ωm and often significantly higher. In contrast, a number of Earth materials and minerals exhibit very low resistivity values, and these include pure metals, graphite, sulfide

minerals, and clay minerals. The presence of these phases can cause low resistivity anomalies in EM data. Pure metals have low resistivity because they contain excess free electrons, which allows electrical currents to flow easily. Minerals such as sulfides and graphite behave as semiconductors. Sulfides can be electrically resistive due to a combination of abundant metallic bonds, overlapping electron energy bands, and structural defects that permit the flow of free electrons. Compared to metals, charge carriers are less mobile and fewer in number in sulfides. Graphite is conductive because the carbon atoms form planar sheets that allow free electrons to move freely through it (Frost et al., 1989). Clay minerals are conductive when hydrated, as they attract ions and provide electrical current pathways for current flow through surface conduction (Revil, 2013). These minerals and rocks can be quite conductive and often make these minerals specific targets during exploration activities or regional studies. For example, sulfides and metals are of particular interest to mining and mineral exploration, and their low electrical resistivity is exploited when attempting to find deposits or ore zones (Palacky, 1987). The low resistivity of graphite can be exploited in the same way. Graphite also occurs frequently as a result of aqueous fluid and melt movements related to tectonic processes, and so the resulting low resistivity anomalies can inform on the location of past tectonics and associated structures (e.g., DeLucia et al., 2019; Murphy et al., 2022). For example, in the Athabasca Basin, graphite bodies formed by fault-assisted fluid flow are associated with the uranium ore that was of economic interest, and this allowed exploration to find ore zones by targeting locations with graphite (Tuncer et al., 2006). Finally, clays often form because of the hydrothermal circulation and alteration associated with geothermal systems (Samrock et al., 2015), and so zones of clay in the subsurface may offer information on where geothermal resources are located.

Many of the aforementioned low resistivity materials are only found in the crust (Fig. 3.2). Graphite film interconnection appears to break down over relatively short timescales at temperature conditions found at depths as shallow as the lower crust (Yoshino and Noritake, 2011; Zhang and Yoshino, 2017). While the lower temperatures inherent to cratons may somewhat increase the depth of graphite film stability, this is unlikely to extend its stability significantly into the elevated temperatures of the lithospheric mantle. Graphite films that attain sufficient thickness may be able to resist breaking down and persist over geologic timescales (Yoshino and Noritake, 2011; Zhang and Yoshino, 2017), though the exact thickness required remains unclear. This has

led to models that suggest sufficiently thick films could be formed and survive by exploiting pre-existing weaknesses such as faults, particularly in the crust (e.g., Murphy et al., 2022). The viability of graphite films continues to be the subject of ongoing debate. However, the graphite-diamond transition, which is typically located at ~130 km depth in cratons (Day, 2012), but will vary based on the geotherm, provides a maximum depth of graphite stability and its ability to be invoked to explain low resistivity anomalies. Compared to graphite, sulfide phases are readily stable and present throughout the lithosphere, are commonly observed in xenoliths at all depths of the lithospheric mantle, and are associated with pervasive metasomatic processes (e.g., Alard et al., 2002; Giuliani et al., 2016; Czas et al., 2020; Burness et al., 2021). In the crust, sulfide minerals can concentrate and occupy a large portion of the rock matrix, but this typically occurs over very small spatial scales and in association with mineral deposits. It is unclear if concentrations of sulfides could be a widespread enough feature to produce low resistivity anomalies in the lithospheric mantle. Finally, clays can be effectively discounted below the upper crust, given that the intrinsic increasing pressure and temperature conditions with depth would metamorphose them into resistive rocks. Outside of these exceptions, the majority of the crust is composed of silicate minerals, which behave as resistors.

3.4 Resistivity of minerals in the mantle lithosphere

At the surface and upper crust, silicate minerals will behave as resistors. However, at the pressure and temperature conditions found in the lower crust and lithospheric mantle, they can behave as semiconductors. The charge carriers for semiconducting silicates are diffusing ionic particles (Chakraborty, 2008), and the conductivity obeys the Nernst-Einstein equation:

$$\sigma = Nze\mu \tag{3.11}$$

where z is the charge number, N is the number of electric charge carriers per unit volume, μ is the particle mobility, and e is the charge of an electron. The Arrhenius relation:

$$\sigma = \sigma_0 \cdot e^{\left(\frac{-\Delta H}{RT}\right)} \tag{3.12}$$

defines the conductions of diffusing species. Here σ_0 is the pre-exponential factor, ΔH is activation enthalpy, T is the absolute temperature, and R is the gas constant (Selway, 2014). This relationship demonstrates that the two most important factors controlling the conductivity of silicates are temperature and composition, with the composition controlling the number of species available to

diffuse. Experiments have shown that proton diffusion of hydrogen (H+) is the most important compositional factor affecting the conductivity of nominally anhydrous mantle minerals such as olivine, orthopyroxene, clinopyroxene, and garnet (Karato, 1990; Yoshino et al., 2008; Yoshino, 2010; Yang et al., 2012; Gardes et al., 2014, Selway, 2018). In the literature, hydrogen content is often referred to as water content for simplicity. With increasing depth, the water storage capacity of these mantle minerals increases dramatically (e.g., Ardia et al., 2012; Padrón-Navarta and Hermann, 2017). In turn, this increases the conductivity-enhancing effects of water with depth.

Water is primarily introduced or reintroduced into the mantle lithosphere as a result of fluxes of C-O-H fluids and melts during metasomatic processes (O'Reilly and Griffin, 2013). Metasomatism can occur in relation to both tectonic events acting over a large region (e.g., subduction and rifting; Fig. 1.1) and smaller events occurring at a more local scale (e.g., kimberlite infiltration). Water behaves as an incompatible component in the mantle (Hauri et al., 2006) and will be extracted during mantle melting. As a result, metasomatism can also remove water if it generates melting in the lithosphere. Melt extraction can also occur as a result of terrane stabilization. Generally, a younger terrane is enriched in incompatible elements that are then extracted, or depleted, through melting and plutonism during stabilization (O'Reilly and Griffin, 2013, and references therein). As a result, water content should decrease as a terrane or craton ages. This is critical process in the cratonization process, as water content plays a vital role in driving many geodynamic processes, including craton rheologic stability and longevity (Peslier et al., 2010; 2017). The content of the element titanium may also exert a similar control on the rheology (Fei et al., 2013; Faul et al., 2016). However, titanium content is also thought to be incompatible during melting (Padrón-Navarta and Hermann, 2017). It follows that the titanium contents are likely high in regions of elevated water content, and so a distinction between the two may not be needed in most cases.

Terranes and cratons are formed by a complex history of melt depletion and metasomatic enrichment events. This can result in lithosphere water contents that are highly variable (e.g., Yang et al., 2021; Munch and Grayver, 2022; Özaydın and Selway, 2022). However, this also means that water content can be seen as a proxy for the tectonic formation, modification, and evolution of the lithosphere in a region (Hirth and Kohlstedt, 1996). Electrical resistivity data can then be used to map the distribution of water content in the mantle with implications for regional tectonic

evolution, mineralization, kimberlites, and volatile cycling and storage (Yang et al., 2021; Munch and Grayver, 2022; Özaydın and Selway, 2022). In many cases, variations in water content can account for the majority of resistivity deviations from a dry peridotite mantle in cratonic regions (Özaydın and Selway, 2022, and references therein). As a result, determining the P-T conditions and evaluating mantle water content are often key first steps to perform when investigating any resistivity anomaly.

Additional effects on resistivity can result from variations in iron content and magnesium number, but these are largely secondary effects (Dai and Karato, 2009c; Dai et al., 2012). Iron content can produce polaron diffusion that is dependent on iron content and involves electron diffusion between ferrous (Fe^{2+}) and ferric (Fe^{3+}) ions. The role of magnesium content focuses on ion diffusion between iron and magnesium ions with a site vacancy. These two mechanisms have higher activation enthalpies than proton diffusion. However, they should be considered because temperature increases in certain systems may overcome the required activation enthalpy and change the most efficient diffusion regime (Chakraborty, 2008; Yoshino, 2008).

To understand the variability in the resistivity of olivine, orthopyroxene, clinopyroxene, and garnet in relation to P-T conditions and water contents, the MATE program (Özaydın and Selway, 2020) is used below. The analysis below is restricted to sub-solidus conditions that are typical of regions with cratonic or stable lithosphere. The parameters used during this modeling follow the work outlined in Chapters 5, 6, and 7 and their respective appendices. This analysis is done in order to demonstrate the range of resistivity values typical of the stable lithosphere and to better understand which resistivity anomalies may be explained by these factors alone and which may require additional low resistivity phases (e.g., graphite, sulfides, etc.).

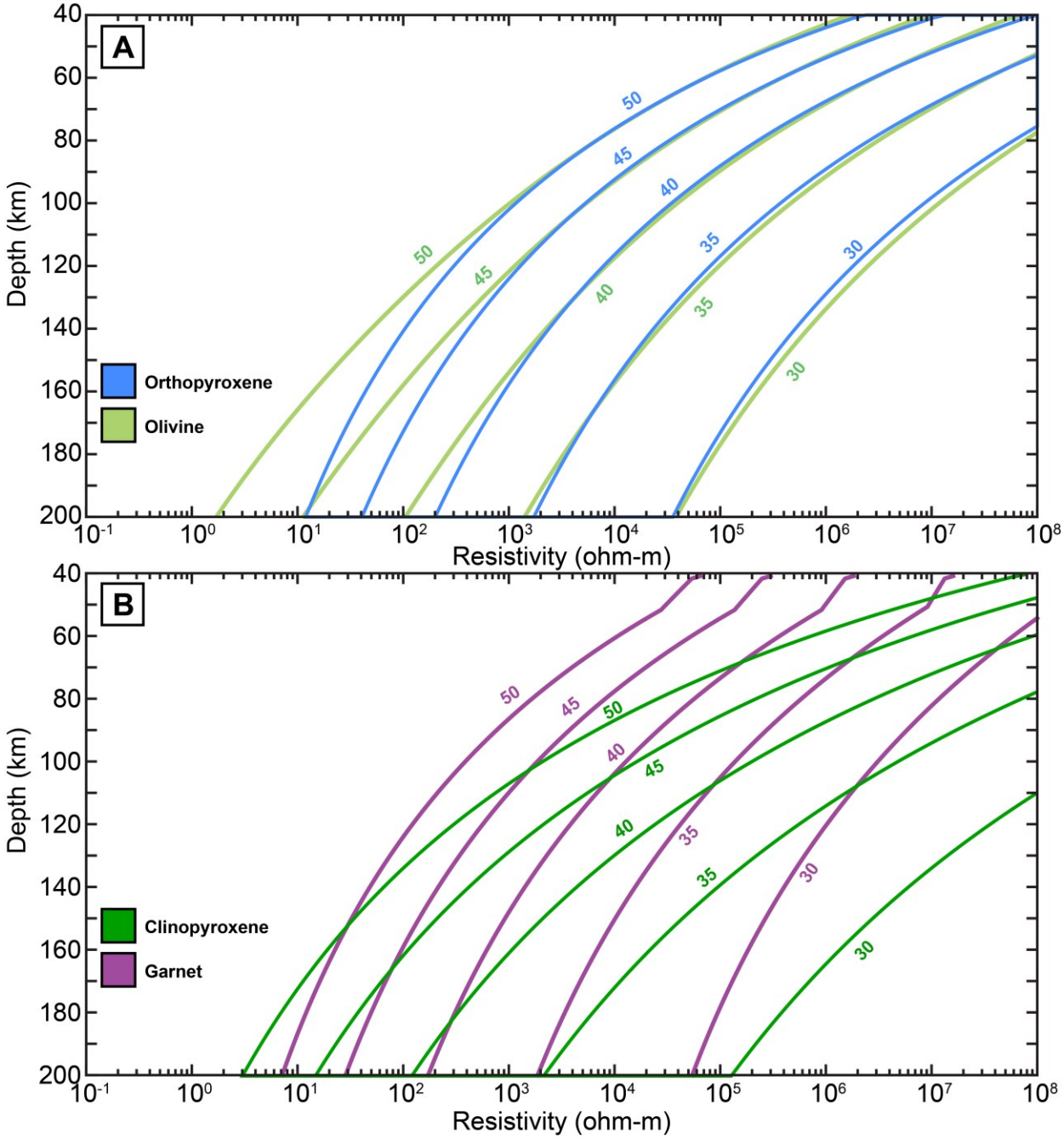

Figure 3.6: *Resistivity versus depth for olivine (green), orthopyroxene (blue), clinopyroxene (gray), and garnet (purple) as a function of depth at various geotherms. The numbers on each line correspond to geotherms in mW/m^2. A 40 mW/m^2 geotherm is used for further calculations, as it represents an approximate average geotherm for Precambrian terranes based on the results of Hasterok and Chapman (2011).*

Figure 3.6 shows the resistivity of each of the common minerals found in the lithosphere under dry conditions for a range of geotherms. Typical cratonic geotherms are calculated from mantle

heat flows that range from 35–45 mW/m^2 with a 40 mW/m^2 often used as an average geotherm estimate for cratonic and Precambrian terranes (Hasterok and Chapman, 2011). There is not a significant difference in resistivity for each of the minerals at the same temperature conditions (Fig. 3.6). Additionally, under temperature conditions typical of Precambrian terranes, it is unlikely that the resistivity of any of these minerals to be less than 10 Ω (Fig. 3.6). Figure 3.7 shows that the resistivity of each of the common lithospheric minerals from dry to saturated conditions based on the sub-solidus water solubility model of Padrón-Navarta and Hermann (2017) with 40 mW/m^2 geotherm. In comparison to dry conditions, where olivine is slightly less resistive than the other minerals (Fig. 3.3), garnet and clinopyroxene become the least resistive (most conductive) mineral phases with increasing saturation and depth. The dashed curves in Figure 3.7 also show the resistivity values expected at the upper range of water contents that have been observed in each mineral from xenolith measurements from samples across multiple regions (Table 3.1). At certain depths, the resistivity values for these water contents (dashed curves) are in excess of those calculated from the saturation limit of Padrón-Navarta and Hermann (2017). In theory, this means that the xenolith samples contain a free fluid phase, but this is highly unlikely in a tectonically inactive region. Similarly, at certain depths, the dashed curves are far below the saturation limit (e.g., Fig 3.7B for clinopyroxene at depths greater than 120 km). Many of these xenolith water measurements lack depth constraints from thermobarometry, so it is difficult to compare them to calculations derived from saturation limit data directly. These limitations demonstrate the limits between current laboratory solubility models and real-world conditions in the mantle.

Measuring the water content of xenoliths is not currently a standard analytical practice. As a result, knowledge on the average values, variability, and maximum water contents of the lithosphere remains uncertain. Additionally, all xenoliths have undergone transport to the surface and may have been altered by this process and thus not reflect in situ conditions in the mantle. For example, water contents obtained from xenoliths found in kimberlites could have been increased or decreased during interaction with the kimberlite melts. However, using the current xenolith water contents (Table 3.1), the lowest resistivity values in cratons on a typical mantle geotherm are likely to be in the range 1–10 Ωm (Fig. 3.7). However, these values are restricted to the base of the lithosphere, where temperatures are highest.

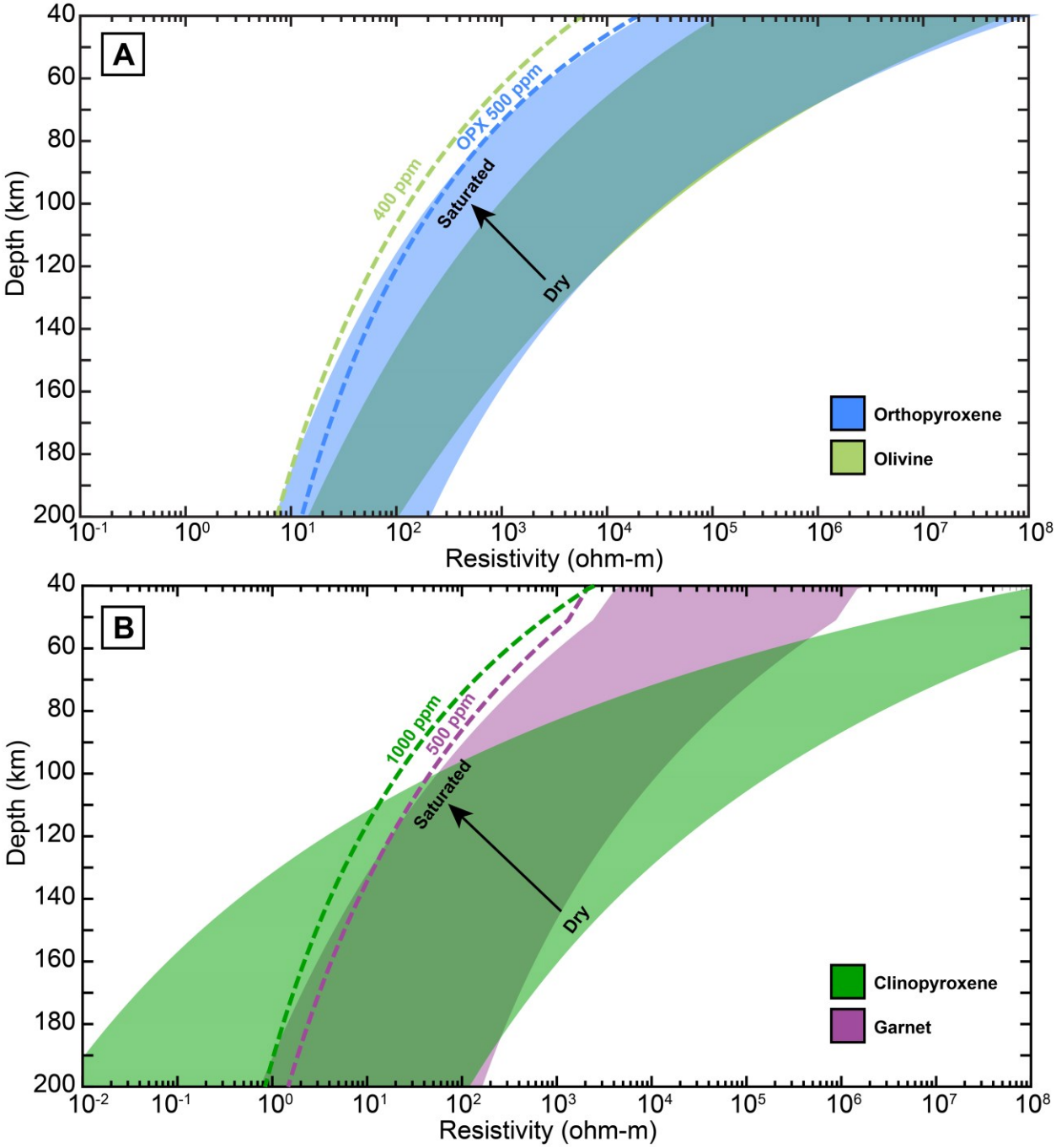

Figure 3.7: *Resistivity versus depth as a function of water content for (A) olivine (light green) and orthopyroxene (blue) and for (B) garnet (purple) and clinopyroxene (dark green). Note the change in the resistivity axis for (B). The shaded polygons reflect the range of resistivity values for each mineral, spanning from dry to fully saturated conditions. Dashed lines show the resistivity values for each mineral at the upper range of water contents observed in xenolith samples (Table. 3.1). Where the dashed lines are to the left of the shaded polygons reflects where water contents exceed the saturation limits of the sub-solidus water solubility model of Padrón-Navarta and Hermann (2017) used here. A geotherm of 40 mW/m^2 was used.*

Table 3.1: *Water contents for olivine, orthopyroxene, clinopyroxene, and garnet from a series of sources. All values shown are in ppm.*

Locality	Olivine	Orthopyroxene	Clinopyroxene	Garnet	Reference
Colorado Plateau	2–45	53–402	171-957	N/A	Li et al. (2008)
Siberian craton	6-323	28-301	100-272	0-23	Doucet et al (2014)
Kimberley	10-370	20-370	30-550	Up to 340	Katayama et al (2011)
Kaapvaal	0-86	40-250	150-400	0-20	Peslier et al (2012), and references therein

3.5 Resistivity of common rocks in the mantle lithosphere

The study of the resistivity of these individual minerals in the mantle gives important background. However, it is essential to be able to calculate the bulk resistivity of the mantle since it is an aggregate of a number of minerals. In addition, the composition of the lithosphere evolves over time and will change as a result of tectonothermal events and age. Metasomatism is again a key process in this temporal evolution. O'Reilly and Griffin (2013) define three types of metasomatism that can affect composition. The first is modal metasomatism, which involves the introduction of new minerals that were not previously present. For example, the creation of a lherzolite occurs when clinopyroxene and orthopyroxene are added to a dunite. The second is cryptic metasomatism, which involves changes in the compositions of pre-existing minerals in the lithosphere without the formation of new phases. An example of this would be the enrichment of trace elements in mantle minerals. The third is stealth metasomatism, which involves the addition of new minerals such as olivine or orthopyroxene, but since these minerals are already common in mantle peridotites, their addition can go unnoticed.

As with water content discussed in Section 3.4, the composition of the lithosphere is expected to become increasingly depleted due to partial melting related to lithosphere stabilization or tectothermal events (Griffin et al., 2009). For example, if rocks of the peridotite group have undergone 20% melt depletion, clinopyroxene will have been removed, and the dominant mineralogy will become harzburgitic. After 50% melt depletion, orthopyroxene will have been removed, and the dominant mineralogy becomes dunitic, which is a pyroxene-free rock dominantly made up of olivine (Stachel, 2021—EAS 561 course notes). Melt depletion plays a critical role in developing the chemical buoyancy and rheological strength necessary for craton stabilization and longevity (Sleep, 2003; O'Neill et al., 2008). In addition to metasomatism and melt depletion, the lithosphere can be compositionally changed as a result of mechanical processes related to tectonics. For example, subduction or orogenic processes can accrete new material laterally or horizontally (see Fig. 1.2).

Modern cratons and regions of stable lithosphere are often the result of multiple episodes of metasomatism, tectonic addition and removal, and melt depletion related to stabilization, formation, and tectothermal events (e.g., Czas et al., 2018; 2020; Liu et al., 2021). Despite this complexity, the most common and overwhelmingly abundant mineralogy for the mantle lithosphere are the peridotite-group rocks lherzolite and harzburgite (Griffin et al., 2009).The interpretation of geophysical data is simplified if xenoliths are available as it will allow independent and direct constraints on the mantle composition. In the absence of xenoliths, the Tecton, Proton, and Archon lithosphere compositions of Griffin et al. (2009) (Table 3.2) can be used. These compositions can be thought of as average lithosphere compositions that are based on the time elapsed since the last tectothermal event to affect the area. Archon compositions were last affected >2.5 Ga, Proton compositions from 2.5–1.0 Ga, and Tecton compositions formed or were last modified at <1 Ga. The trend from Tecton to Proton to Archon reflects the effects of melt depletion on the composition of the lithosphere and is categorized by decreasing garnet and clinopyroxene content and increasing orthopyroxene and olivine content (Griffin et al., 2009). These compositions can serve as proxies for age and melt depletion in regions where xenolith constraints are unavailable.

Additional rocks that may be present in small amounts in the mantle lithosphere include eclogites, pyroxenites, and the glimmerite group. Eclogites are broadly composed of garnet and omphacitic clinopyroxene, usually in similar proportions, and are typically formed by subduction. They form at most ~5% of the lithosphere by volume (Schulze, 1989). The pyroxenite group is subdivided into websterites, olivine-websterites, clinopyroxenites, and orthopyroxenites. Pyroxenite group rocks may locally account for up to 5 % of the lithosphere by volume and are associated with dikes and subduction processes (Stachel, 2021). The glimmerite group subdivides into MARID (mica, amphibole, rutile, ilmenite, and diopside) and PIC (phlogopite, ilmenite, and clinopyroxene) categories (Dawson and Smith, 1977; Gregoire et al., 2002). These rocks are rich in mica-group minerals and are associated with melt-rock interactions associated with kimberlite volcanism but have historically been largely associated with the Kaapvaal craton in southern Africa (Fitzpayne et al., 2018; Silva et al., 2022).

Figure 3.8 shows the resistivity of various lithosphere compositions at dry conditions for a 40 mW/m^2 geotherm. Table 3.2 provides the compositions used for this modeling. All the compositions converge to a resistivity of approximately 100 Ωm at the base of the lithosphere, where the temperatures are highest, and resistivity is expected to be lowest. This value is similar to the resistivity values produced by the individual minerals (Fig. 3.6), as expected since these compositions are aggregates of the individual minerals. The majority of mantle compositions also exhibit similar resistivity values throughout the lithosphere (Fig. 3.8), despite dramatic differences in mineralogy (Table 3.2). This is because the most dominant mineral phase in these compositions is olivine (Griffin et al., 2009; Table 3.2), and so it is the most interconnected and thus controls the bulk resistivity. To illustrate this point further, an almost pure olivine dunite composition is included in Figure 3.8. Despite the total absence of clinopyroxene and most of the orthopyroxene and garnet from this composition, it has a resistivity value that is indistinguishable from the other compositions. This also means that regardless of age or melt depletion, differences in mineralogical composition in dry cratonic lithosphere do not generally result in a resistivity signature that can be detected by MT methods.

The only composition with resistivity values that are notably different is eclogite (Fig. 3.8). This is because olivine is absent in eclogite (Table 3.2), and so it cannot control bulk resistivity.

Additionally, eclogite does not contain the least most resistive mineral, orthopyroxene (Fig. 3.6). Instead, the bulk resistivity is controlled by garnet and clinopyroxene, and garnet is notably less resistive than the other mineral phases in the mid-lithosphere (Fig. 3.6). However, this deviation is only present in the mid-lithosphere, where garnet resistivity values are lower than olivine (Fig. 3.6). As a result, eclogite also converges to a resistivity of 100 Ωm at the base of the lithosphere (Fig. 3.8), where olivine becomes the least resistive (most conductive) dry mineral (Fig. 3.6). In the lithosphere, the slightly lower resistivity values of eclogite are unlikely to have a major effect on bulk lithosphere resistivity. This is because, as stated previously, eclogite is not usually a volumetrically significant fraction of the bulk lithosphere (Schulze, 1989; Griffin et al., 2009). Eclogite may make up locally significant volume fractions in certain tectonic settings such as subduction zones or via melt interactions (Schulze, 1989; Griffin et al., 2009). If present in a significant volume fraction, eclogite can cause gravitational instabilities due to its high density. However, Schulze (1989) estimated that only up to 5% of the mantle by volume could be eclogite in certain locations. As part of the research in Chapter 6, the resistivity of a lithospheric mantle composed of (a) 100% lherzolite and (b) 95% lherzolite and 5% eclogite was modeled. The resulting change in resistivity was negligible. Finally, these eclogite caveats also apply to pyroxenites, which are modeled in Figure 3.8 with a websterite composition but do not have appreciably lower resistivity values relative to the peridotite compositions.

Table 3.2: *Mantle compositions used for the lithosphere modelling shown in Figures 3.8-3.10. All values shown are volume fractions (i.e. modal percentages).*

Composition	Olivine	Orthopyroxene	Clinopyroxene	Garnet	Reference
Archon	68.7	25.8	1.9	3.6	Griffin et al. (2009)
Proton	67.9	19	5.8	7.3	Griffin et al. (2009)
Tecton	62.1	13.6	10.5	13.8	Griffin et al. (2009)
Harzburgite	78.5	18	1.3	2.2	Griffin et al. (2009)
Lherzolite	60	15	10.7	14.3	Griffin et al. (2009)
Dunite	95.7	2.5	1.1	0.7	Griffin et al. (2009)
Websterite	0	50	50	0	N/A
Eclogite	0	0	50	50	N/A

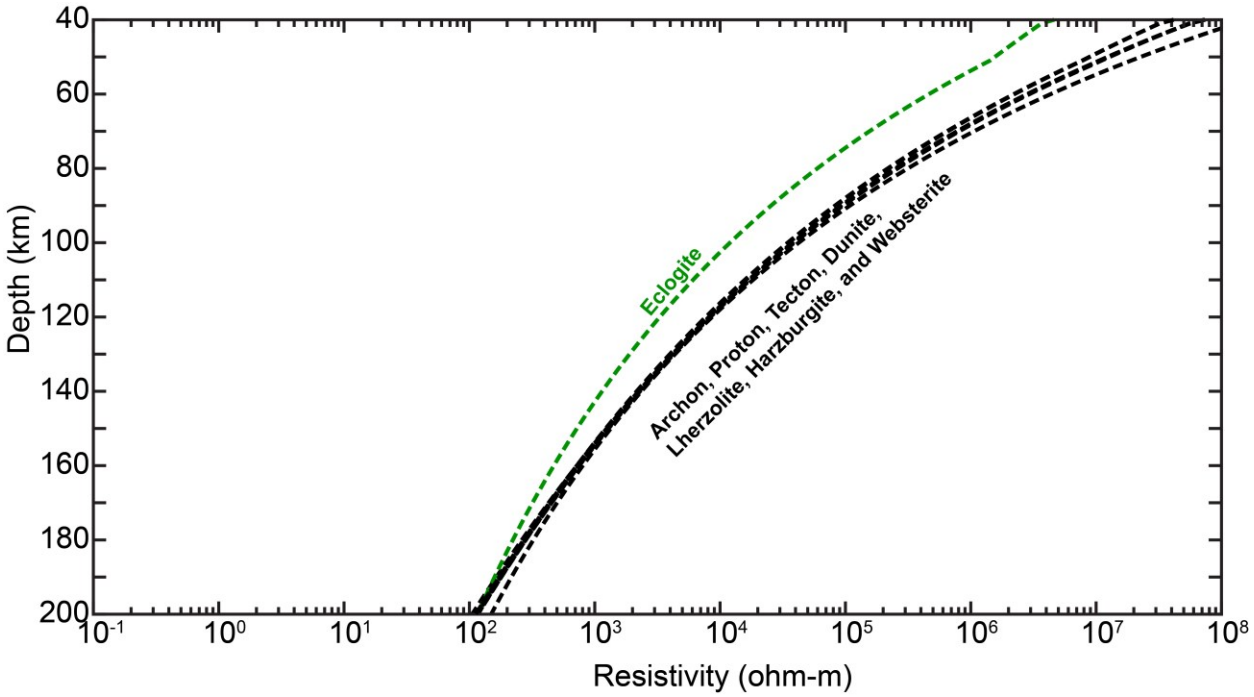

Figure 3.8: *Resistivity as a function of depth for common mantle composition along a 40 mW/m^2 geotherm. Also plotted are the general age-related Archon, Proton, and Tecton compositions of Griffin et al. (2009) that can be used in regions where the age of tectonics is known but xenolith constraints on mantle composition are unavailable.*

As with the individual minerals described in Section 3.4, the presence of water can lower the bulk resistivity of mantle rocks. The resistivity values for the most common peridotite compositions, lherzolite, and harzburgite, at dry and fully saturated conditions (i.e., the solubility limits of the various minerals) are shown in Figure 3.9. Figure 3.10 is the same but for the Archon, Proton, and Tecton mantle compositions. There is little difference in the resistivity values between these compositions. Again, this reflects the dominance of olivine in controlling the bulk resistivity, as well as the generally small changes in composition (Table 3.1). However, the resistivity values for these compositions fall at lower values than those of pure olivine (Fig. 3.6A). Instead, the resistivity values are closer to those of garnet and clinopyroxene (Fig. 3.6B), which have considerably higher water solubility limits compared to orthopyroxene and olivine. Despite the comparatively small percentages of these minerals in these compositions (Table 3.2), this demonstrates the effect that small but highly conductive phases can have on bulk resistivity. Overall, since these peridotite compositions dominate the composition of the mantle lithosphere, this means that MT is unlikely to be able to detect compositional differences at both wet and dry conditions.

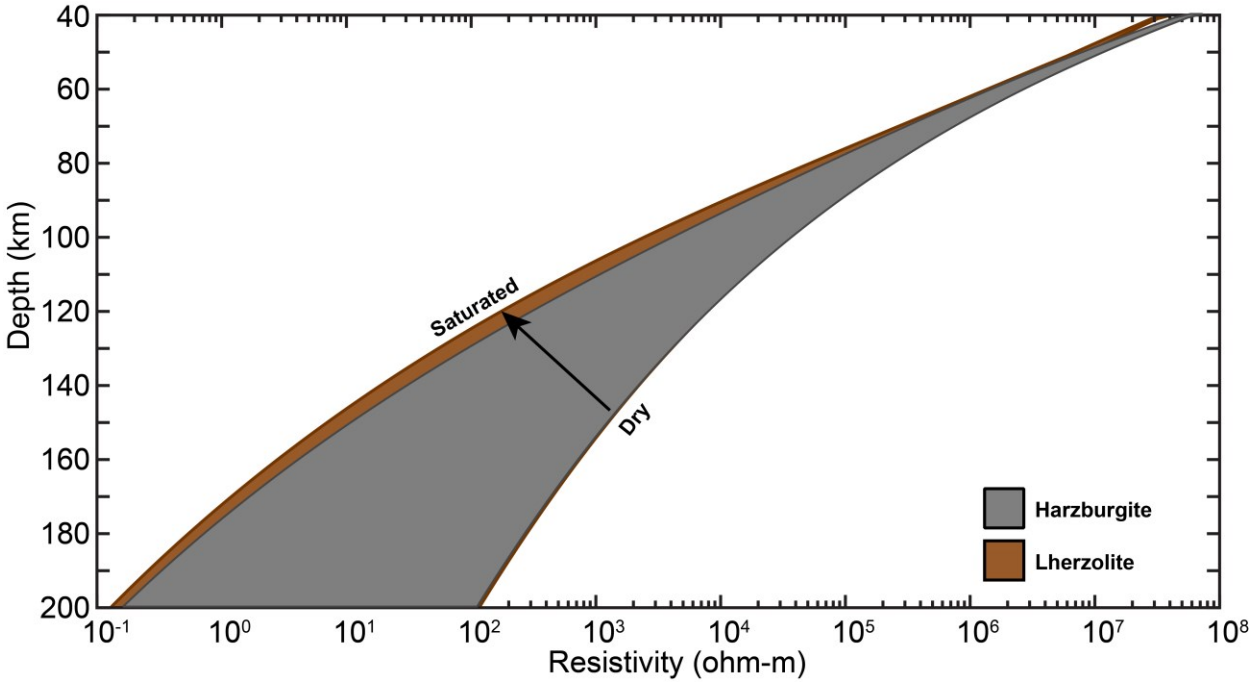

Figure 3.9: *Resistivity as a function of depth at the range of water contents for the most common peridotite mantle compositions. The water sub-solidus water solubility model of Padrón-Navarta and Hearmann (2017) was used here. A geotherm calculated from a heatflow of 40 mW/m^2 was used.*

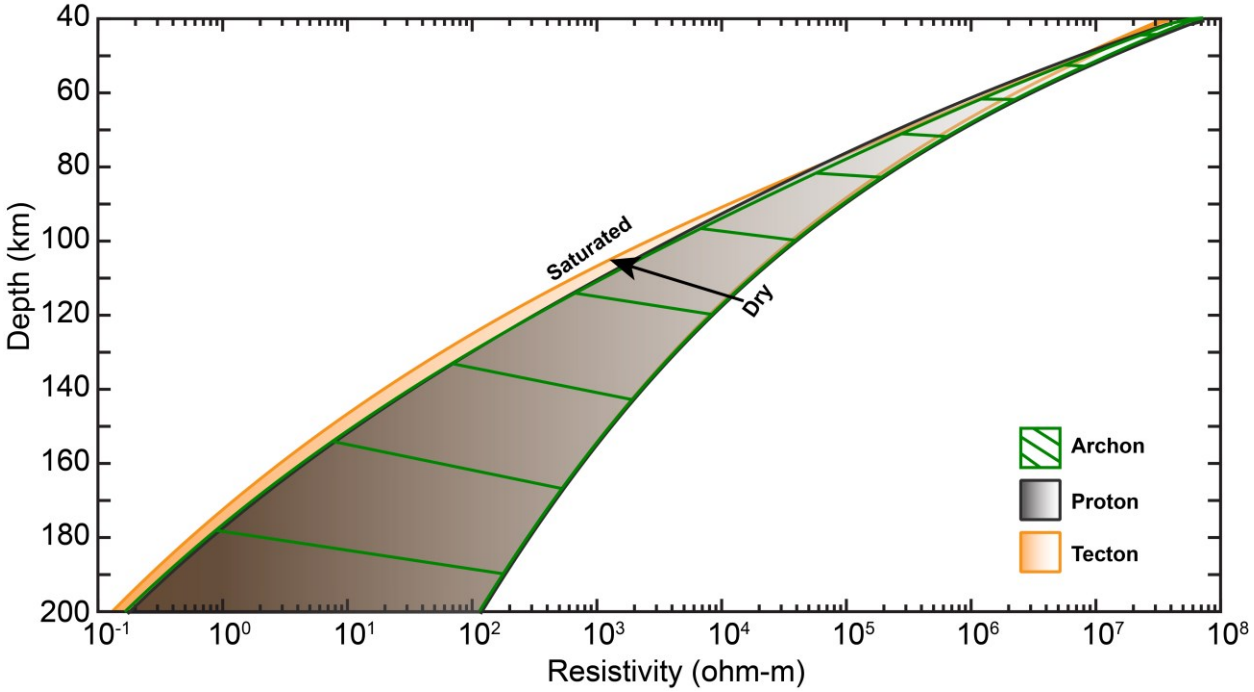

Figure 3.10: *Resistivity as a function of depth with respect to water content for the Archon, Proton, and Tecton compositions of Griffin et al. (2009). The water sub-solidus water solubility model of Padrón-Navarta and Hearmann (2017) was used here. A geotherm calculated from a heatflow of 40 mW/m^2 was used.*

3.6 Resistivity of hydrous minerals in the lithosphere

The prior sections showed that elevated water contents can produce low resistivity anomalies, especially towards the base of cratons. However, the ability of water to lower resistivity is greatly reduced at shallower levels in the Earth (Figs. 3.6-3.10). If the resistivity values are too low to be explained by water content and P-T conditions, then other low resistivity phases must be considered as possible explanations. Two possible low resistivity phases are the hydrous minerals amphibole and phlogopite (Fig. 3.2). Both minerals are stable throughout the lithospheric mantle (Konzett et al., 1997; Frost, 2006). In xenolith samples, these minerals often form interconnected veins or dikes (Ionov et al., 2005; Tappe et al., 2008; Foley and Fischer, 2017), permitting electrical conduction. Compared to the effects of water contents on the resistivity of olivine, little is known about the conductivity mechanisms that occur in amphibole and phlogopite, and few laboratory experiments have been performed. The effects of water content are described by Li et al., (2016) and Hu et al., (2018). However, experimental data suggests that fluorine may be the primary charge carrier in both minerals (Li et al., 2017). In this case, electrical resistivity measurements where these minerals are present may provide insights into the halogen cycling and storage within the Earth (Luth, 2014). Critically, amphibole has been examined only at the temperature and pressure conditions of the upper lithospheric mantle (e.g., Hu et al., 2018, and references therein), and the majority of these studies have considered only the pargasite amphibole phase.

These hydrous minerals also have low seismic velocities, making them a particularly attractive explanation for coincident seismic and electrical anomalies (Rader et al., 2015; Selway, 2018). Mid-lithosphere seismic discontinuities have been observed on multiple continents in the depth range of 60-160 km, but most have been reported between 80-100 km (Selway et al., 2015, and references therein). Seismic velocity reductions range from 3-10% (Wölbern et al., 2012; Sodoudi et al., 2013; Lekić and Fischer, 2014), which corresponds to 5-20% phlogopite by volume and 5 to >20% amphibole by volume (Rader et al., 2015). A marked increase in the solidus of peridotites occurs at pressures around 3 GPa (100 km depth), which could force ascending melts to stall and deposit hydrous minerals roughly at the depth of most mid-lithosphere discontinuities (Hansen et al., 2015). However, both minerals are usually accessory phases in xenoliths, and only in uncommon wehrlite, pyroxenite, and glimmerite-group rocks do they reach modally relevant

amounts (Ionov et al., 2005; Fitzpayne et al., 2018). It is unclear if hydrous minerals could be both modally and spatially abundant enough to explain mid-lithosphere discontinuities, but it remains an attractive explanation.

3.7 Resistivity of aqueous fluids and melts

In tectonically active systems, melt and aqueous fluids can both explain low resistivity anomalies provided they are interconnected, which is dependent on their respective dihedral angles (Section 3.2). In active systems, melt and aqueous fluids may pond at boundaries such as the Moho or lithosphere-asthenosphere boundary. They can also ascend through conduit structures towards magmatic centers (e.g., Naif et al., 2013, 2021; Li et al., 2021). Given their relationship to volcanic hazards and geothermal resources, crustal fluids and melts are better understood than their mantle counterparts. The resistivity of melts is dependent on a variety of factors, including temperature, pressure, water content, and composition (Yoshino et al., 2010; Pommier, 2014). The compositional spectrum for melts in the mantle ranges from silicate to carbonatite melts (i.e., carbon-rich melts). Most laboratory experiments have focused on systems where the lithosphere-asthenosphere boundary (LAB) is relatively shallow, particularly beneath the oceanic plates at and close to mid-ocean ridges. As a result, the majority of laboratory experiments have been conducted at pressures at or less than 3 GPa in accordance with typical plate thicknesses in these regions that are less than 100 km (e.g., Yoshino et al., 2010; Sifré et al., 2014). The nature of melts in the deeper lithosphere found beneath cratons has commanded less attention. However, some experimental studies at pressures greater than 3 GPa indicate that silicate melt interconnectivity decreases with increasing pressures. As melt interconnectivity decreases, this means that even small volumes of silicate melts can produce low resistivity anomalies (Yoshino et al., 2009; 2010). Similar experiments at pressures greater than 3 GPa have not been conducted for carbon-rich melts. However, carbon-rich melts have lower dihedral angles, increased mobility, and lower viscosities than basaltic melts by several orders of magnitude (Hunter and McKenzie, 1989; Hammouda and Laporte, 2000). Carbon-rich melts are also more conductive than silicate melts (Gaillard et al., 2008). This would suggest that even smaller amounts of carbon-rich melts would be necessary to explain low resistivity anomalies (Yoshino et al., 2009).

A number of experiments have been conducted on silicate melts (Laumonier et al., 2017, and references therein), and the conductivity generally follows the Arrhenius law:

$$\sigma = \sigma_0 e^{-\left(E_a + \frac{P\Delta V}{RT}\right)} \tag{3.13}$$

where σ_0, E_a, P, ΔV, R, and T are the experimentally derived pre-exponential term (S/m), the activation energy (J/mol), the pressure (bars), the empirically derived activation volume (cm^3/mol), R is the gas constant (J K^{-1} mol^{-1}), and temperature (kelvin), respectively. In silicate melts, the concentration and mobility of ions is the primary control on resistivity, with Na^+ ions having the highest mobility and exerting the greatest control, particularly in dry melts; Mg^{2+}, K^+, and Ca^{2+} ions have an increased role in hydrous melts where their mobility is increased (Zhang et al., 2021). The typical conductivity range for silicate melts is 0.01–10 S/m, and the conductivity for a wide range of compositions has been inferred due to fractionation processes that largely occur in the crust (Gaillard et al., 2008; Laumonier et al., 2017). Carbon-rich melts have been studied less, but conductivity generally follows an Arrhenius law of the form:

$$\sigma = \sigma_0 e^{-\frac{E_a}{RT}} \tag{3.14}$$

where the terms are the same as in Equation 3.13 (Gilliard et al., 2008). Critically, pressure is not accounted for in the carbon-rich melt equation, but pressure effects are expected to be minimal (Genge et al., 1995; Dobson et al., 1996; Gaillard et al., 2008). In silicate melts, increased pressure will decrease conductivity, but this is often a small effect (Zhang et al., 2021) that is probably offset by the increase in silicate melt interconnectivity with increasing pressure (Yoshino et al., 2009). Compositional effects in carbon-rich melts appear to have less effect on conductivity than in silicate melts (Gilliard et al., 2008; Laumonier et al., 2017). The typical conductivity range for carbon-rich melts is 10^2–$10^{2.5}$ (S/m) (Gaillard et al., 2008).

Aqueous fluids, commonly referred to as brines, are common in the upper lithosphere and relevant to studies of sedimentary basins, volcanic systems, subduction zones, and geothermal resources. Ions are the primary charge carriers in aqueous fluid systems, with the salts NaCl and KCl being the most relevant species while also having similar behavior (Nesbitt, 1993). Sinmyo and Keppler (2017) and Guo and Keppler (2019) derived equations for the electrical resistivity of NaCl-bearing aqueous fluids that are likely also applicable to KCl. Two different equations were derived for both low- and high-pressure systems, and these are:

$$\log(\sigma) = -1.7060 - \frac{93.78}{T} + 0.8075\log(c) + 3.0781\log(d) + \log(\Lambda_0) \quad (3.15)$$

And:

$$\log(\sigma) = -0.919 - \frac{872.5}{T} + 0.852\log(c) + 7.61\log(d) + \log(\Lambda_0) \quad (3.16)$$

where Λ_0 is the molar conductivity of NaCl in water at infinite dilution (S cm^2/mol) and is defined as:

$$\Lambda_0 = 1573 - 1212d + \frac{537062}{T} + \frac{208122721}{T^2} \quad (3.17)$$

where σ is the conductivity (S/m), T is the temperature (Kelvin), c is the concentration of NaCl in wt %, and d is the density of water (g/cm^3) at a given temperatures and pressure, respectively. Equation 3.15 is the low-pressure equation and is valid for temperatures 100–800 °C, pressures less than 1 GPa, and densities in the range of 0.3–1.3 g/cm^3. Equation 3.16 is the high-pressure equation and is valid for the range 300-900 °C, pressures in the range 1–5 GPa, and densities in the range of 0.3–1.4 g/cm^3. Resistivity is then a function of temperature, salinity, pressure, and density. These equations are then applicable to the crust and uppermost mantle lithosphere, which span the depth interval aqueous fluids are thought to be relevant before hydrogen proton diffusion becomes the primary water-related conductivity-enhancing mechanism.

In general, the ability of melt or aqueous fluid circulation to explain low resistivity anomalies is usually restricted to tectonically active or recently active regions. Due to the long timescales since tectonism, it is usually assumed that aqueous fluid circulation as well as the heat necessary to produce melting have long since dissipated.

3.8 Summary of resistivity in the lithosphere

In the crust, silicate minerals generally exhibit a high resistivity with typical values in the range of 1,000–10,000 Ωm. In tectonically inactive regions, low resistivity anomalies are predominantly due to the presence of low resistivity minerals such as sulfides, graphite, or clays. However, to produce low resistivity anomalies, these low resistivity minerals must be interconnected. These low resistivity minerals are often associated with past fluid and melt movements linked to tectonic processes (e.g., Murphy et al., 2022). As a result, conductors in the crust can offer insights into

volatile cycling, the location of structures such as faults and terrane boundaries, and mineral deposits. In tectonically active regions, low resistivity anomalies are predominately related to the movement of fluid and melt. As a result, these conductors will offer insights into the plumping of volcanic centers, geothermal resources, and fluid and melt movements during active tectonics. Due to the high resistivity of silicate minerals in the crust, it is often sufficient to model low resistivity anomalies with simple two-phase mixing laws, such as Archie's Law (equation 3.5).

In the mantle lithosphere, silicate minerals can begin to behave as semiconductors due to the elevated temperatures and pressures. The main mantle lithosphere minerals are olivine, orthopyroxene, clinopyroxene, and harzburgite. With increasing depth, these minerals become more less resistivity and begin to contribute to the bulk resistivity to a degree they can no longer be ignored in mixing models as in the crust. Mineral resistivities can be lowered by elevated water contents, and this effect increases dramatically with depth as mineral solubility limits increase. Compositionally, rocks in the mantle lithosphere have a diverse mineralogy, often reflecting a protracted and multi-phase tectonic evolution. The variability in water content can be similarly diverse. Regardless, the overwhelming majority of the mantle lithosphere is predominantly composed of the peridotite-group rocks lherzolite and harzburgite. When both the individual minerals and the variety of rock compositions in the mantle lithosphere are modeled, the results (Figs. 3.6-3.10) show that differences in mineralogy cannot be detected by methods like MT. However, since water contents serve as a proxy for enrichment or depletion in the mantle lithosphere, they can be used as a proxy for the tectonic evolution of the lithosphere.

While increased water content can produce elevated low resistivity anomalies towards the base of the lithosphere, these effects decrease dramatically at shallower depths. As a result, low resistivity anomalies in the mid-lithosphere may require additional low resistivity phases to explain. These low resistivity phases can consist of the hydrous minerals phlogopite and amphibole, sulfides, and in some cases graphite. As in the crust, these phases are emplaced by and melt movements during past episodes of terrorism, and resulting resistivity anomalies can offer insights into these episodes. In tectonically active regions, melt-related anomalies may be relevant, with both silicate and carbon-rich melts have low resistivity values. All of these low resistivity phases can have dramatic influences on bulk resistivity, even if they are only present in small amounts, assuming they are

well-connected over large areas. Unlike in the crust, because silicate minerals are moderately resistive in the mantle lithosphere, they and all other phases of interest need to be modeled as separate resistivity phases in mixing laws. Multi-phase mixing laws such as Equation 3.8, are useful in this regard.

The fact that the bulk electrical resistivity of the lithosphere can be dominated by minor low resistivity phases, assuming these phases are interconnected, contrasts EM methods with the seismic methods that are also used to study the lithosphere, that are primarily sensitive bulk compositional changes. This means that seismic methods can miss details in the structure of the lithosphere if the modification is not volumetrically significant over a large region or if the modifications do not introduce appreciable velocity variations. This contrasts with EM methods, which may be able to detect these smaller-scale features, again assuming the low resistivity phases are interconnected. Conversely, EM methods may not be able to detect changes in lithosphere structure if a significant resistivity contrast is not present. EM and seismic methods often complement each other (e.g., Jones, 1987), and it has become increasingly common to use both when investigating the structure of the lithosphere.

CHAPTER 4. ELECTROMAGNETIC GEOPHYSICAL METHODS AND THE ELECTRICAL RESISTIVITY OF THE DEEP LITHOSPHERE

The previous chapter showed that there are major spatial variations in the resistivity of the lithosphere. These variations contain information about composition and related tectonic processes. Measuring the resistivity can determine important information about subsurface composition and structure. These measurements can be made in a number of ways. One approach is to us electrical resistivity logs when drilling, which can provide direct measurements of the subsurface. However, drilling has a limited depth, is often the most expensive way to acquire information, and can only provide information in the immediate vicinity of the drill hole. In regions where little is known about the subsurface, drilling would be a logistically and cost-prohibitive method of investigation. Direct current resistivity methods can also be used to measure subsurface resistivity, but the depth of investigation is proportional to the dipole length and is usually less than 500 m. To overcome these limitation and image deeper, electromagnetic (EM) geophysical methods have been developed that have the advantage of imaging the subsurface remotely using instruments deployed at the surface at lower costs than drilling. All EM methods rely on the movement of electric current within a continuous medium (i.e., the subsurface), which is described by Ohm's Law and can be written as:

$$\boldsymbol{J} = \sigma \boldsymbol{E} \tag{4.1}$$

which is one of the three constitutive relations. Here $\boldsymbol{J}$ is the current density (A/m^2), $\boldsymbol{E}$ is the strength of the electric field (V/m) as a function of position and time, and σ is the electrical conductivity in Siemens per meter (S/m).

EM methods provide a way to measure the subsurface resistivity remotely. This chapter will discuss EM methods, with a focus on describing the MT method, as it was the key method used for the investigations presented in Chapters 5, 6, and 7. This chapter concludes with a brief description of geophysical inverse theory and non-uniqueness, which is an important concept to understand when developing a resistivity model from MT data, as these models are used to produce geologic interpretations.

Understanding how EM geophysical methods work first requires an understanding of how EM signals travel in the Earth. Maxwell's equations describe how electric and magnetic fields are related, and these equations govern the MT method. The unified set of four equations described by Maxwell (1873) is shown below.

The first is Gauss's Law which can be written as:

$$\nabla \cdot \boldsymbol{E} = \frac{Q}{\epsilon_o} \tag{4.2}$$

which quantifies how electric charges generate electric fields. Again, $\boldsymbol{E}$ is the strength of the electric field in V/m as a function of position and time, Q is the charge density (C/m^3), and ϵ_o is the dielectric permittivity of free space (8.85 x 10^{-12} F/m).

The first equation is Gauss' Law of Magnetism that is written as:

$$\nabla \cdot \boldsymbol{B} = 0 \tag{4.3}$$

and requires that magnetic monopoles do not exist in isolation. Rather north and south magnetic poles exist only as dipoles. Here $\boldsymbol{B}$ is the magnetic flux density in tesla (T) as a function of time and position, and t is time in seconds (s).

The third equation is Faraday's Law that is written as:

$$\nabla \, x \, \boldsymbol{E} = - \frac{\partial \boldsymbol{B}}{\partial t} \tag{4.4}$$

and quantifies how a time-varying magnetic field will generate an electric field.

The final equation is Ampere's Law:

$$\nabla \, x \, \boldsymbol{B} = \mu_o \left(\boldsymbol{J} + \epsilon_o \frac{\partial \boldsymbol{E}}{\partial t} \right) \tag{4.5}$$

and describes how moving electric charges (i.e., current) generate magnetic fields. Here μ_o is the magnetic permeability of free space (4π x 10^{-7} H/m) and $\boldsymbol{J}$ is again the current density (A/m^2). This form is Ampere's Law with the displacement current of Maxwell (1873) added. The addition of the displacement current was necessary to couple Ampere's Law with Faraday's Law, make

Ampere's Law consistent with charge conservation, and explain the existence of electromagnetic waves.

Substituting Equation 4.1 into Equation 4.5 yield the equation:

$$\nabla \wedge \boldsymbol{B} = \mu_o \sigma \boldsymbol{E} + \mu_o \epsilon_o \frac{\partial \boldsymbol{E}}{\partial t} \tag{4.6}$$

the first and second terms again represent the conduction and displacement currents, respectively.

4.1 Propagation of electromagnetic fields in the Earth

To understand how EM fields propagate in the Earth, it is necessary to consider a simple case. Consider a homogenous, isotropic, and conductive medium with dielectric permittivity and magnetic permeability equal to the free space values that were defined in above. If we assume these properties are time-invariant and that there are no free electric charges (i.e., Q = 0), we can begin by using Equation 4.4 to derive an expression for **E** by eliminating **B**. This can be done by taking the curl of Equation 4.4 (Faraday's Law) to get:

$$\nabla \wedge (\nabla \wedge \boldsymbol{E}) = -\frac{\partial}{\partial t}(\nabla \, x \, \boldsymbol{B}) \tag{4.7}$$

The vector identity below is then useful:

$$\nabla \wedge (\nabla \wedge \boldsymbol{E}) = \nabla(\nabla \cdot \boldsymbol{E}) - \nabla^2 \boldsymbol{E} \tag{4.8}$$

we can use this vector identity, substitute Equation 4.6 into Equation 4.7, and with the prior assumptions in mind, we can show that:

$$(\nabla \cdot \boldsymbol{E}) - \nabla^2 \boldsymbol{E} = -\frac{\partial}{\partial t}\left(\mu_o \sigma \boldsymbol{E} + \mu_o \epsilon_o \frac{\partial \boldsymbol{E}}{\partial t}\right) \tag{4.9}$$

Which can be simplified to:

$$(\nabla \cdot \boldsymbol{E}) - \nabla^2 \boldsymbol{E} = -\mu_o \sigma \frac{\partial \boldsymbol{E}}{\partial t} - \mu_o \epsilon_o \frac{\partial^2 \boldsymbol{E}}{\partial t^2} \tag{4.10}$$

The assumption of no free electric charges means that Gauss' Law (Equation 4.3) can be rewritten as:

$$\nabla \cdot \boldsymbol{E} = 0 \tag{4.11}$$

Then Equation 4.10 simplifies to:

$$\nabla^2 \boldsymbol{E} = \mu_o \sigma \frac{\partial \boldsymbol{E}}{\partial t} + \mu_o \epsilon_o \frac{\partial^2 \boldsymbol{E}}{\partial t^2} \tag{4.12}$$

which produces a second-order differential for **E**(x,y,z,t) where the time variation can be assumed to be general and which describes EM signals in the time domain. As in Equation 4.6, the first term is the conduction current, and the second term is the displacement current. If either term is much larger than the other, the equation can be simplified by removing one of them.

To determine which current term is more important for EM signals in the earth, we can transform Equation 4.12 into the frequency domain. Here we assume that electric and magnetic fields have a harmonic time variation at an angular frequency represented by ω, where $\omega = 2\pi f$. This allows the separation of the variables to be written as:

$$\boldsymbol{E}(x,y,z,t) = \boldsymbol{E_o}(x,y,z)e^{-i\omega t} \tag{4.13}$$

Where $i=\sqrt{-1}$. If Equation 4.13 is substituted into Equation 4.12 this produces:

$$\nabla^2 \boldsymbol{E_o} = -i\omega\mu_o\sigma\boldsymbol{E_o} - \omega^2\mu_o\epsilon_o\boldsymbol{E_o} \tag{4.14}$$

The two terms on the right represent the conduction and displacement current as before. The relationship between the displacement and conduction current can be written as:

$$R = \frac{\omega\epsilon_o}{\sigma} \tag{4.15}$$

MT uses low-frequency EM signals typically in the bandwidth 1000–0.0001 Hz. At these frequencies and considering the range of resistivity of Earth materials (Fig. 3.1), R will be very small, thus the conduction current will dominate, and EM signals will propagate by diffusion. Essentially, due to the low frequencies of the MT method, we assume that displacement currents can be ignored. Equation 4.14 then becomes:

$$\nabla^2 \boldsymbol{E_o}(x,y,z) = -i\omega\mu_o\sigma\boldsymbol{E_o}(x,y,z) \tag{4.16}$$

The left side of Equation 4.16 can be expressed in its component form if we recall the Laplace Equation for three dimensions in Cartesian coordinates. If we assume that the electric field is polarized in the x-direction, meaning $\mathbf{E_o}= (E_x, 0, 0)$ where y and z = 0, Equation 4.16 becomes:

$$\frac{\partial^2 E_x}{\partial^2 x^2} + \frac{\partial^2 E_x}{\partial^2 y^2} + \frac{\partial^2 E_x}{\partial^2 z^2} + i\omega\mu_o\sigma E_x = 0 \tag{4.17}$$

Now if the EM wave is assumed to be planar and amplitude does not change in the x or y directions, the partial derivatives for these components can be set to zero, and Equation 4.17 becomes:

$$\frac{d^2 E_x(z)}{dz^2} + i\omega\mu_o\sigma E_x(z) = 0 \tag{4.18}$$

A trial solution of the form $E_x(z) = Ae^{kz}$ where A and k are constants that needs to be determined. Substituting this into Equation 4.18 yields:

$$k^2A + i\omega\mu_o\sigma A = 0 \tag{4.19}$$

This requires that:

$$k^2 = -i\omega\mu_o\sigma \tag{4.20}$$

Equation 4.20 yields two possible solutions:

$$k = \pm(1-i)\sqrt{\frac{\omega\mu_o\sigma}{2}} \tag{4.21}$$

A general form of the solution is then:

$$E_x(z) = A_1e^{(1-i)\sqrt{\frac{\omega\mu_o\sigma}{2}}z} + A_2e^{-(1-i)\sqrt{\frac{\omega\mu_o\sigma}{2}}z} \tag{4.22}$$

which can be expanded as:

$$E_x(z) = A_1e^{\sqrt{\frac{\omega\mu_o\sigma}{2}}z}e^{(-i)\sqrt{\frac{\omega\mu_o\sigma}{2}}z} + A_2e^{-\sqrt{\frac{\omega\mu_o\sigma}{2}}z}e^{(i)\sqrt{\frac{\omega\mu_o\sigma}{2}}z} \tag{4.23}$$

and consists of both an exponential function and an oscillatory function. A_1 and A_2 can be determined by applying appropriate boundary conditions. The first boundary condition is that the solution must remain bounded as z approaches infinity, which is only possible if $A_1 = 0$. The second boundary condition is that at the surface (z = 0), $E_x(0) = E_x^s$ has a defined value. This requires that $A_2 = E_x^s$ and so Equation 4.23 can be rewritten:

$$E_x(z) = E_x^se^{-\sqrt{\frac{\omega\mu_o\sigma}{2}}z}e^{(i)\sqrt{\frac{\omega\mu_o\sigma}{2}}z} = E_x^se^{-\sqrt{\frac{\omega\mu_o\sigma}{2}}z}\left[\cos\left(\sqrt{\frac{\omega\mu_o\sigma}{2}}z\right) + isin\left(\sqrt{\frac{\omega\mu_o\sigma}{2}}z\right)\right] \tag{4.24}$$

which contains both real and imaginary parts, and both are parts of the solution. Figure 4.1 shows Equation 4.24 in graphical form and demonstrates how the attenuation of the EM wave in the subsurface is controlled by frequency and resistivity.

4.2 The electromagnetic skin depth

The solution for the horizontal electric field in Equation 4.23 behaves as a damped oscillation (i.e., amplitude oscillates and decays with depth). Physically, this is due to energy loss from the electric field as current is converted into heat. It is useful to then have an estimate of the distance that the signal will travel. The modulus of the electric field is defined as:

$$|E_x^s(z)| = |E_x^s(z)|e^{-\sqrt{\frac{\omega\mu_o\sigma}{2}}z} \tag{4.25}$$

and decreases monotonically with increasing z (depth). The skin depth (δ) is defined as the depth at which the electric field magnitude has decreased by a factor of 1/e from the surface (in meters). Rewriting Equation 4.25 gives:

$$\frac{|E_x^s(z=\delta)|}{|E_x^s|} = \frac{1}{e} = e^{\sqrt{\frac{\omega\mu_o\sigma}{2}}\delta} \tag{4.26}$$

and therefore:

$$\delta = \sqrt{\frac{2}{\omega\mu_o\sigma}} \tag{4.27}$$

using $\mu_o = 4\pi$ x 10^{-7}, and recalling that $\omega = 2\pi f$, the skin depth in meters can be shown to be equal to:

$$\delta = \frac{503}{\sqrt{\sigma f}} \tag{4.28}$$

or:

$$\delta = 503\sqrt{\rho T} \tag{4.29}$$

this is considered the typical depth of penetration for the MT method at the specific frequency and ground conductivity (Equation 4.28) or period and ground resistivity (Equation 4.29) of interest.

The behavior of the magnetic field under the above assumptions is similar. Consider the example of an electric field in the x-direction incident between the air (resistor) and the Earth (a halfspace conductor). From Faraday's law (Equation 4.4) and the relationship $B = \mu_o H$ where H is the magnetic field strength, it can be shown that:

$$H_y(z,t) = \frac{1}{i\omega\mu_o}\frac{\partial E_x(z,t)}{\partial t} \tag{4.30}$$

The electric field transmitted into the Earth is given by:

$$E_x^t(z,t) = E_x^t e^{-k_1 z} e^{-i\omega t} \tag{4.31}$$

and the magnetic field transmitted into the Earth is given by:

$$H_y^t(z,t) = \frac{1}{i\omega\mu_o} E_x^t(-k) e^{-k_1 z} e^{-i\omega t} \tag{4.32}$$

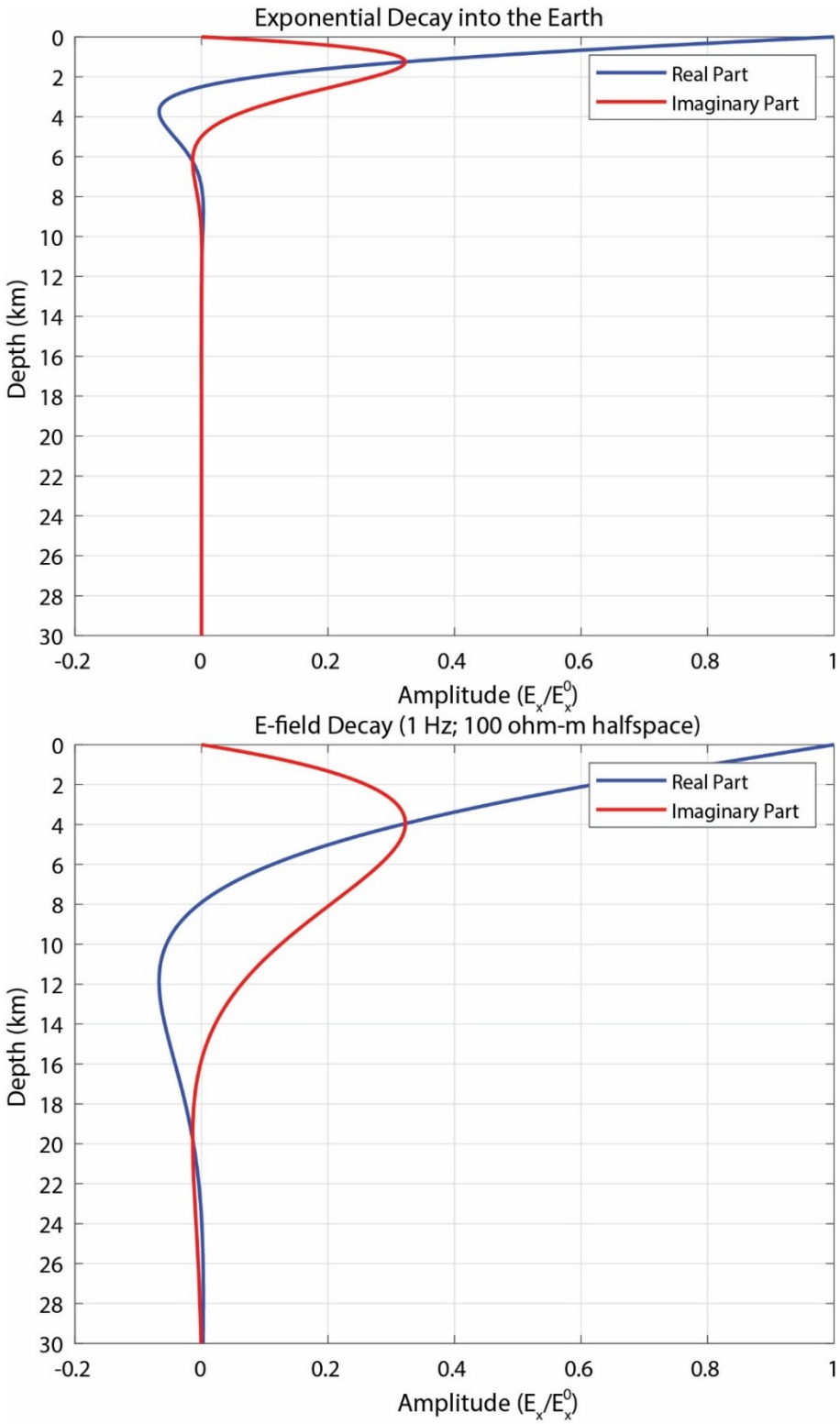

Figure 4.1: *Attenuation of a plane EM wave in the subsurface at two different resistivity values. Where the two lines converge to an amplitude of zero is roughly the depth of penetration of the signals. Complex numbers are used to simplify the derivation, and both real and imaginary parts are solution.*

4.3 The magnetotelluric method

Equations 4.31 and 4.32 can be used to define the impedance as:

$$Z_{xy} = \frac{E_x(\omega)}{H_y(\omega)} \tag{4.33}$$

It can be shown that:

$$Z_{xy} = \frac{(1-i)}{\sqrt{2}}\sqrt{\frac{\omega\mu_o}{\sigma_i}} \tag{4.34}$$

It is important to note that Equations 4.33 and 4.34 depend only on the properties of the Earth, not the air. This is because by defining the ratio in Equations 4.33 and 4.34 information about the amplitude of the transmitted electric field is removed. Taking the magnitude of the impedance, Equation 4.34 can be rearranged to determine the conductivity of the Earth:

$$\sigma_i(\omega) = \frac{\omega\mu_o}{\left|Z_{xy}\right|^2} = \frac{\omega\mu_o}{\left|\frac{E_x(\omega)}{H_y(\omega)}\right|^2} \tag{4.35}$$

or resistivity:

$$\rho_i(\omega) = \frac{1}{\omega\mu_o}\left|Z_{xy}\right|^2 = \frac{1}{\omega\mu_o}\left|\frac{E_x(\omega)}{H_y(\omega)}\right|^2 \tag{4.36}$$

Note that all terms on the right side of Equations 4.35 and 4.36 can be measured. It is also important to note that due to the skin depth equation (Equation 4.29), the EM fields attenuate in a hemisphere with a radius of δ around the measurement location. It should also be noted that the Earth is unlikely to have a constant resistivity over a hemisphere. Thus, the resistivity in Equation 4.36 is usually referred to as the apparent resistivity, and it can be considered an average resistivity over the hemisphere. These measurements also allow us to calculate the phase with the equation:

$$\phi(\omega) = \tan^{-1}\left[Z_{xy}\right] = \tan^{-1}\left[\frac{E_x(\omega)}{H_y(\omega)}\right] \tag{4.37}$$

which is typically between 0–90 °. For a halfspace and a uniform Earth, the phase will be equal to π/4 (45°). When resistivity increases with depth, the phase will decrease and become less than 45°. When resistivity decreases with depth, the phase is greater than 45° (Simpson and Bahr, 2005).

4.3.1 1-D, 2-D, and 3-D Earth resistivity structure

The impedance varies depending on the resistivity structure of the Earth. In the 1-D case, the impedance will have the same magnitude for any pair of orthogonal horizontal direction electrical and magnetic field components and can be written as:

$$\boldsymbol{Z}(\omega) = \begin{bmatrix} 0 & Z(\omega) \\ -Z(\omega) & 0 \end{bmatrix} \tag{4.38}$$

In this case, the apparent resistivity becomes a scalar quantity. With a 1-D resistivity structure, the Earth at a select depth can be considered uniform in all cardinal directions and only variable with depth (Fig. 4.2). This type of structure is a reasonable approximation in areas such as sedimentary basins. Figure 4.3 demonstrates apparent resistivity and phase responses for hypothetical MT stations located over a 1-D structure.

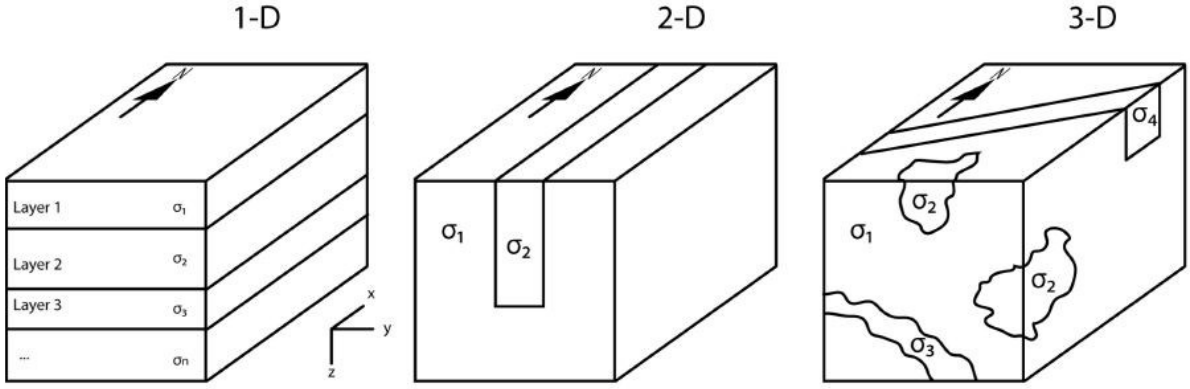

Figure 4.2: *Schematic cartoons of 1-D, 2-D, and 3-D conductivity structures in the Earth. In the 2-D and 3-D examples* σ_2 *would be the electrically conductive targets. From Cordell (2020).*

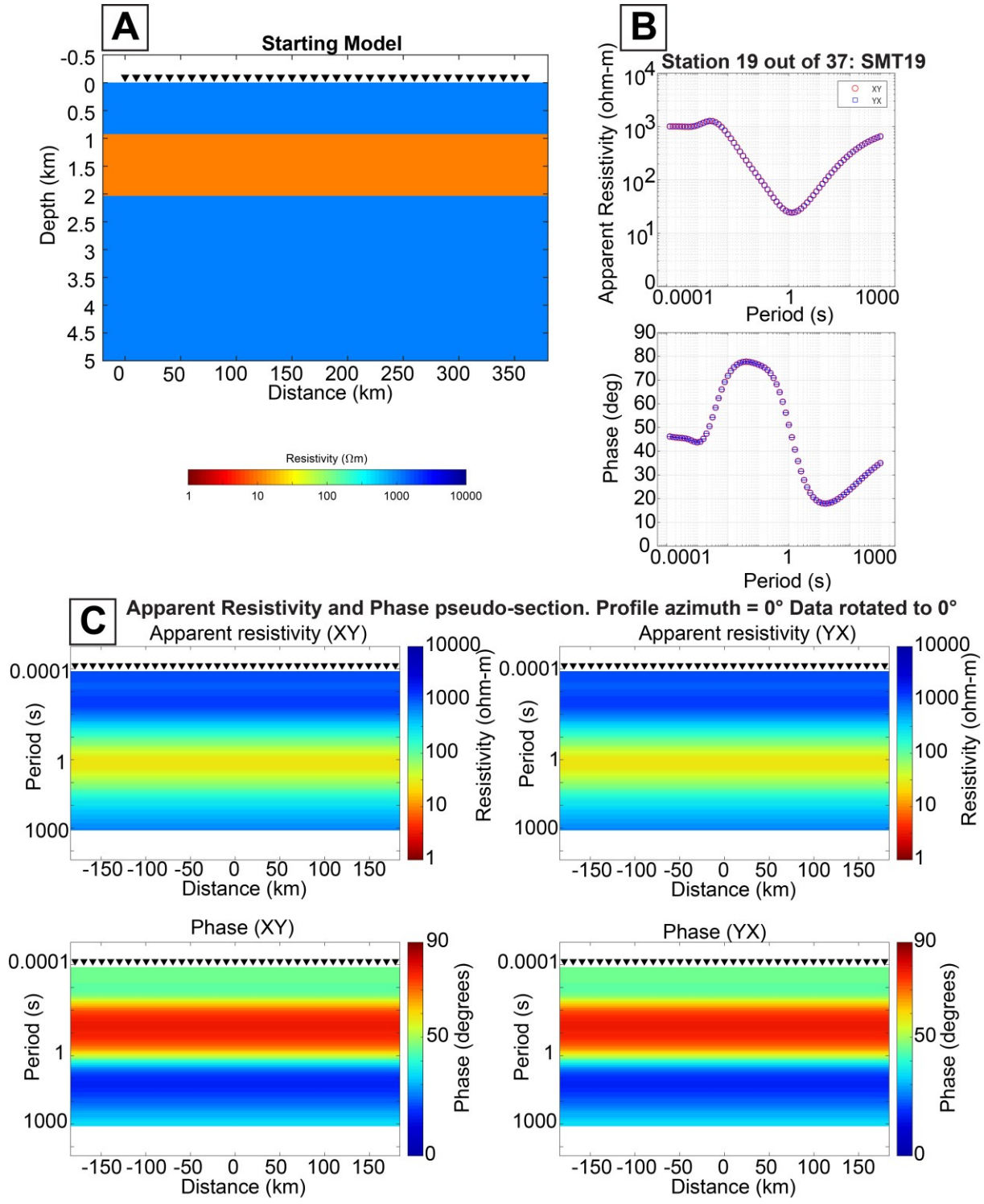

Figure 4.3: *A forward model of MT data over 1-D structure. (A) The starting model contains a low resistivity layer from 1000–2000 m that extends across the entire model space. (B) The apparent resistivity and phase curves are shown for one MT station (triangles) but are the same at all stations. Note that the XY and YX components overlap perfectly. (C) The pseudosections show the apparent resistivity and phase data beneath all stations; note the uniformity.*

In the 2-D case (Fig. 4.2) the impedance can be written as:

$$\boldsymbol{Z}(\omega) = \begin{bmatrix} 0 & Z_{xy}(\omega) \\ Z_{yx}(\omega) & 0 \end{bmatrix} \tag{4.39}$$

and relates the orthogonal and electric and magnetic fields in two directions (e.g., Fig 4.4). In practice, these are called (a) the transverse electric (TE) mode, or E-polarization, and (b) the transverse magnetic (TM) mode, or B-polarization. Figure 4.5 demonstrates the response of the TE and TM modes in the presence of a 2-D structure with an infinite strike in and out of the page. The low resistivity feature in Figure 4.5 is conceptually equivalent to the structure in Figure 4.4. The strike of the low resistivity features is defined as the direction in which there is no change in resistivity structure. In the ideal 2-D case in this example, there is no resistivity variation in the x-direction. This would correspond to a geologic strike that trends geographic north-south. Instead, resistivity variations are confined to the y-direction only, or in the geographic east-west direction. In this example, in the TE mode, the electric field would be polarized parallel to the strike direction, and the magnetic field is polarized to the plane orthogonal to the strike direction. In comparison, in the TM mode, the magnetic field is polarized in the strike direction while the electric field is polarized in the plane orthogonal to the strike direction.

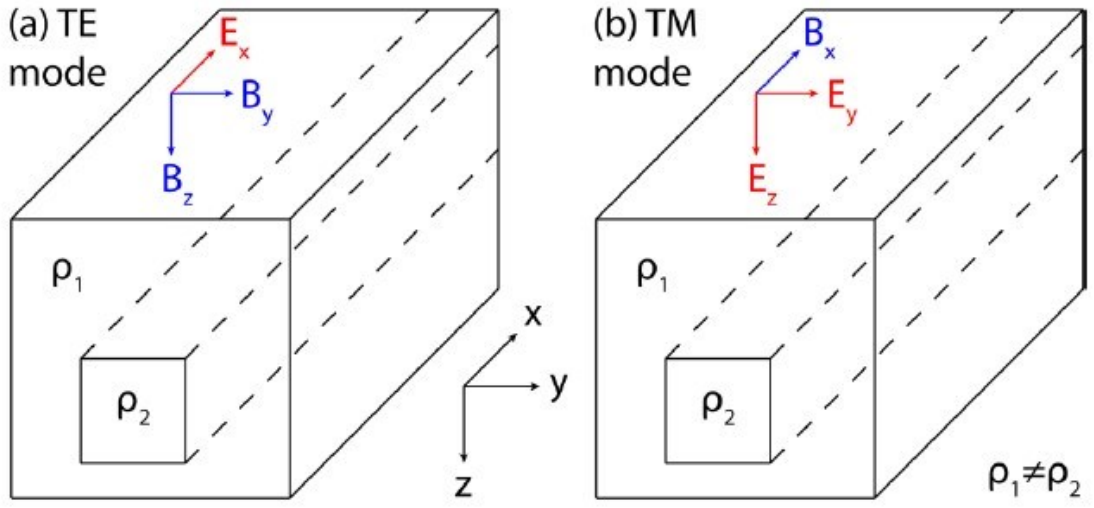

Figure 4.4: *2-D resistivity structure and field components associated with the (a) TE and (b) TM MT modes.*

When structure is not 1-D, electric charges may develop on the surface of resistivity contrasts due to electric currents flowing orthogonal (across) to the strike. This produces galvanic effects in the

TM mode and violates the initial assumption of no free electric changes (Section 4.1). The TM mode includes both inductive and galvanic effects and can resolve both conductors and resistors. The TE mode induces electrical currents parallel to the strike and so does not have galvanic effects. The TE mode is then very good at resolving conductors, but not resistors.

In the 3-D case, the impedance tensor becomes a full matrix with the form:

$$\boldsymbol{Z}(\omega) = \begin{bmatrix} Z_{xx}(\omega) & Z_{xy}(\omega) \\ Z_{yx}(\omega) & Z_{yy}(\omega) \end{bmatrix} \tag{4.40}$$

$Z_{xy}$and Z_{yx} are referred to as the off-diagonal components while $Z_{xx}$and Z_{yy} are referred to as the diagonal components. If large diagonal components are observed in the data, this may indicate a 3-D structure. However, it could also indicate that the data was collected in a coordinate system different from the regional geoelectric strike (see Section 4.4). Figure 4.5 demonstrates the response of the TE and TM modes in the presence of a structure that is geometrically similar to the one modelled in Figure 4.5 but is made 3-D with the inclusion of finite dimensions in the X and Y directions. Generally, the apparent resistivity and phase curves alongside the pseudosections are similar to the 2-D example. However, subtle differences can be observed, such as the diverging curves at long periods at station SMT19 in the 2-D case that plot nearly on top of each other in the 3-D case. Similarly, the amplitudes of the response curves as well as anomalies in the pseudosections show subtle differences between the two. The subtlety of these differences makes it difficult to intuitively interpret 3-D MT data compared to 1-D or 2-D data. This makes it necessary to use 3-D algorithms to accurately model the subsurface in the presence of 3-D data.

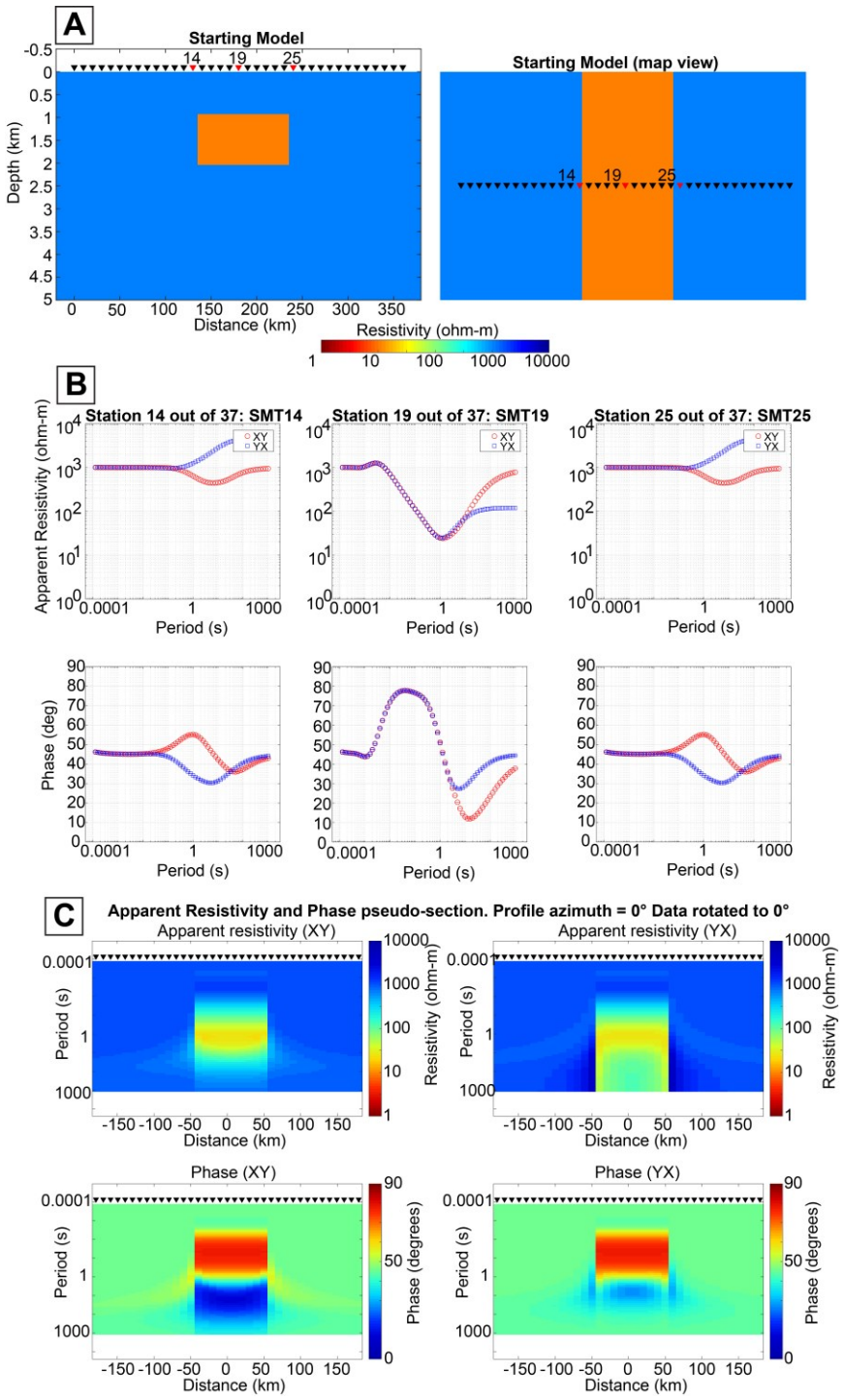

Figure 4.5: *A forward model of MT data over 2-D resistivity model. (A) The starting model contains a low resistivity layer from 1000–2000 m that extends across the entire model space. (B) The apparent resistivity and phase curves are shown for three MT station (triangles) but are the same at all stations. Note that the XY and YX components overlap perfectly. (C) The pseudosections show the apparent resistivity and phase data beneath all stations; note the change in apparent resistivity and phase as the stations approach the low resistivity layer. The NLCG code of Rodi and Mackie (2001) was used to produce the model responses.*

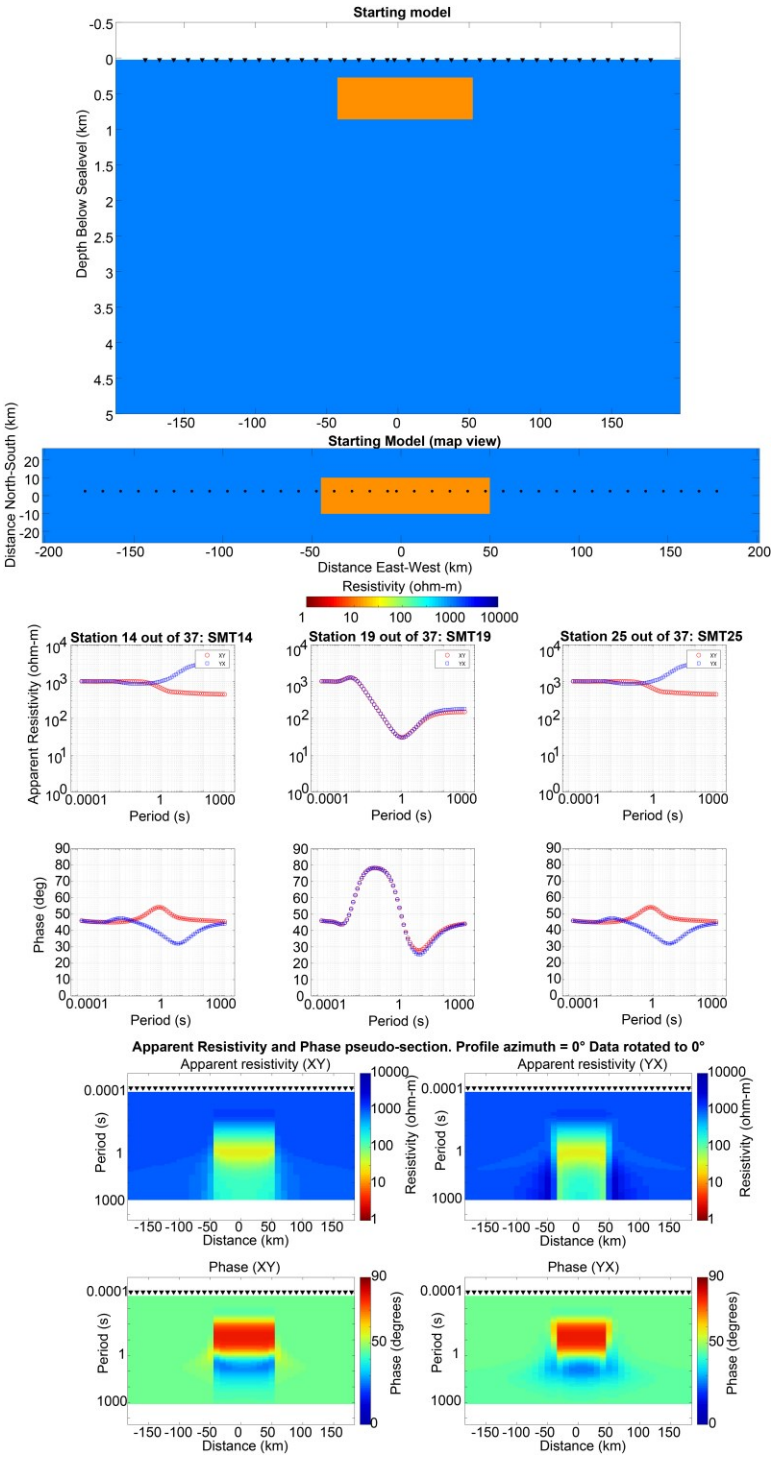

Figure 4.6: *A forward model of MT data over 3-D resistivity model. (A) The starting model contains a low resistivity layer from 1000–2000 m that extends across the entire model space. (B) The apparent resistivity and phase curves are shown for three MT station (triangles) but are the same at all stations. Note that the XY and YX components overlap perfectly. (C) The pseudosections show the apparent resistivity and phase data beneath all stations; note the change in apparent resistivity and phase as the stations approach the low resistivity layer. The NLCG code of Rodi and Mackie (2001) was used to produce the model responses.*

4.4 Directionality, distortion, and dimensionality magnetotelluric impedance data

The impedance tensor defined in Section 4.3 relates the horizontal components of the electric and magnetic fields. Additional information about subsurface resistivity can also be obtained by analysis of the vertical component of the magnetic field. The vertical electric field is not often recorded due to it being logistically difficult to measure (see Section 4.5.1). The vertical magnetic field transfer function is typically referred to as the tipper (T) and relates the vertical magnetic field to the horizontal magnetic field components as follows:

$$T(\omega) = \left[T_{zy}(\omega)\, T_{zx}(\omega)\right] = \left[\frac{H_z(\omega)}{H_x(\omega)}\, \frac{H_z(\omega)}{H_y(\omega)}\right] \tag{4.41}$$

The tipper components T_{zy} and T_{zx} are dimensionless and are ratios of the magnetic field. H_z is zero if resistivity varies only in the vertical direction (i.e., 1-D, Fig 4.2). Tipper data is non-zero in 2-D and 3-D scenarios. It is common to plot the real component of the tipper in map view, and these are called induction vectors. The induction vectors will align parallel to resistivity gradients or, in other words, orthogonal to low resistivity features in the subsurface. The direction of the arrow is arbitrary. In the Parkinson convention, arrows point toward conductors, while in the Wiese convention, they point away (Simpson and Bahr, 2005). Since the location of low-resistivity features of interest is not usually known beforehand, plotting the tipper in map view can provide a quick way to detect anomalies and alter station placement accordingly.

Distortion in MT data can be caused by a number of factors. The first is local inhomogeneities in resistivity in the subsurface, which can occur if an MT site is located near a region of anomalously low or high resistivity that is beyond the ability of the highest frequency (or shortest period) to detect. This can result in galvanic distortions in the data (Wannamaker et al., 1984; Groom and Bailey, 1991). This shows up as a frequency-independent shift, called a static shift, in the data due to the excess electric current density near the small inhomogeneity (Jones, 1988). A second source of distortion stems from the assumption that MT measurements are made at a point. Data collection requires setting up electric dipoles that are 50–100 m in length, and this may result in electrodes being located in different materials with different electrical properties. In turn, this result is distortion in estimates of the impedance tensor (Jones, 1988). In practice, this can be occasionally

mitigated by careful site selection. A third source of distortion is topography. At both the local and regional scales, electric currents may be weaker or stronger in the presence of topographic highs or lows, respectively (Wannamaker et al., 1986). At the regional scale, current channeling can take place along valleys or coastlines and distort the electric fields to flow in a particular direction (Jones, 1983). Mitigating these issues usually involves modeling the topography or bathymetry as closely as possible within the limits of available computational power. Finally, the majority of MT analysis assumes the Earth is isotropic, where resistivity measurements are scalars independent of direction. The reality is that many rocks can have an anisotropic resistivity (e.g., Pommier, 2014; Liddell et al., 2016). The assumption of isotropy in the presence of anisotropy can lead to erroneous interpretation. To adequately model electrical anisotropy would require making the resistivity a 9-component tensor. While anisotropic inversions for MT data do exist (e.g., Cao et al., 2018; Kong et al., 2021), they are relatively new, not widely used, and require significantly more computational resources than isotropic inversions. Only a few studies have attempted to apply these codes to field data (e.g., Lee et al., 2024).

In an ideal world, these distortion effects might be accounted for with very fine inversion meshes capable of replicating topography, small-scale anisotropy, or local inhomogeneities. However, current memory and computational power do not permit this, and meshes must be coarser than desired. As a result, MT fieldwork, analysis, inversion, and interpretation need to be done with the knowledge that distortion can be minimized but cannot be completely removed.

A number of approaches have been developed to overcome distortion and assess dimensionality. More exhaustive analyses of each method can be found in Simpson and Bahr (2005) and Chave and Jones (2012). Those relevant to this thesis will be discussed here. These methods are tensor decomposition and the phase tensor. D+ editing can also be used, but it is generally more relevant to data processing, and so it is discussed in section 4.5.2.

The tensor decomposition approach was originally developed by Groom and Bailey (1989, 1991). The tensor decomposition identifies that any impedance tensor will have some amount of distortion present and that the observed tensor can be decomposed into a distortion tensor and an “un-distorted tensor” as follows:

$$Z_{obs} = R(\theta_r) C Z_t R^T(\theta_r) \tag{4.42}$$

where Z_{obs} is the observed impedance tensor, R is a rotation matrix, C is the distortion tensor, Z_t is the undistorted impedance tensor, and θ_r is the regional geoelectric strike angle. Unlike simple tensor rotation, which assumes a quasi-2-D structure once the diagonal elements are minimized, the tensor decomposition approach recognizes that the true geoelectric strike may still not be recovered due to additional galvanic distortions warping the regional electric field (Groom and Bailey, 1989). The goal of this approach is to decompose the distortion tensor into determinable and indeterminable parts. These parts are called the twist angle (the local strike of a distorting inhomogeneity that departs from the regional strike), shear angle (the distortion of the various EM fields from orthogonality), multiplicative gain (usually called a static shift), and anisotropy factor (the ellipticity of local inhomogeneities present). Groom and Bailey (1989) show that the multiplicative gain is indeterminable while the other parts can be determined, and thus an undistorted tensor can be recovered. In the case of 1-D or 2-D inversion, it is advantageous to invert the undistorted tensor as it excludes the galvanic effects of small-scale 3-D inhomogeneities. McNeice and Jones (2001) further developed this approach, introducing statistical methods to fit a general twist, shear, anisotropy, and regional strike for multiple periods and sites. Their approach allows for a geoelectric strike to be found for all periods over an entire survey area. Since MT data is rarely collected with the regional geoelectric strike known (i.e., most sites are arranged with the magnetic and electric channels oriented magnetic north-south and east-west), this approach allows rotation of the MT sites and alignment of the TM and TE modes to regional structure. This is an especially useful step prior to 2-D inversion. Determining the gain parameter, or static shift, is often done separately using approaches such as regional averaging (Jones, 1988), using transient EM soundings taken in the area, or fitting static shifts during inversion. With the increasing use of 3-D inversions, static shifts are usually accounted for by the inversion routine placing small-scale resistivity anomalies in the near-surface near stations. If near-surface interpretations are being performed, these anomalies need to be kept in mind.

The phase tensor approach is another form of the tensor decomposition introduced by Caldwell et al. (2004). The phase tensor is also unaffected by local distortions, and so it provides an unbiased measurement of the regional geoelectric strike. It can also be decomposed into a geoelectric strike angle and skew angle. The strike angle is conceptually the same as the geoelectric strike

determined from other methods (e.g., tensor decomposition). The skew angle is a measure of the tensor asymmetry with minimum and maximum components. The phase tensor is represented graphically in Figure 4.6 as an ellipse. The minimum and maximum components can be plotted as minimum (short) and maximum (long) axes of an ellipse. If the structure is 1-D, the phase tensor is a circle, and the skew angle is zero. If the structure is 2-D, the phase tensor becomes an ellipse with the minimum and maximum axes. The maximum axis is parallel to the strike angle, and the skew is still zero. If the structure is 3-D, the skew angle is nonzero, and the major axis is equal to the skew angle minus the strike angle, this becomes the inferred geoelectric strike. In general, if the skew parameter is greater than 3°, it can be assumed that 3-D inductive effects dominate (Booker, 2014). In recent years, the phase tensor has increasingly become the first and primary method used when assessing the dimensionality of MT data.

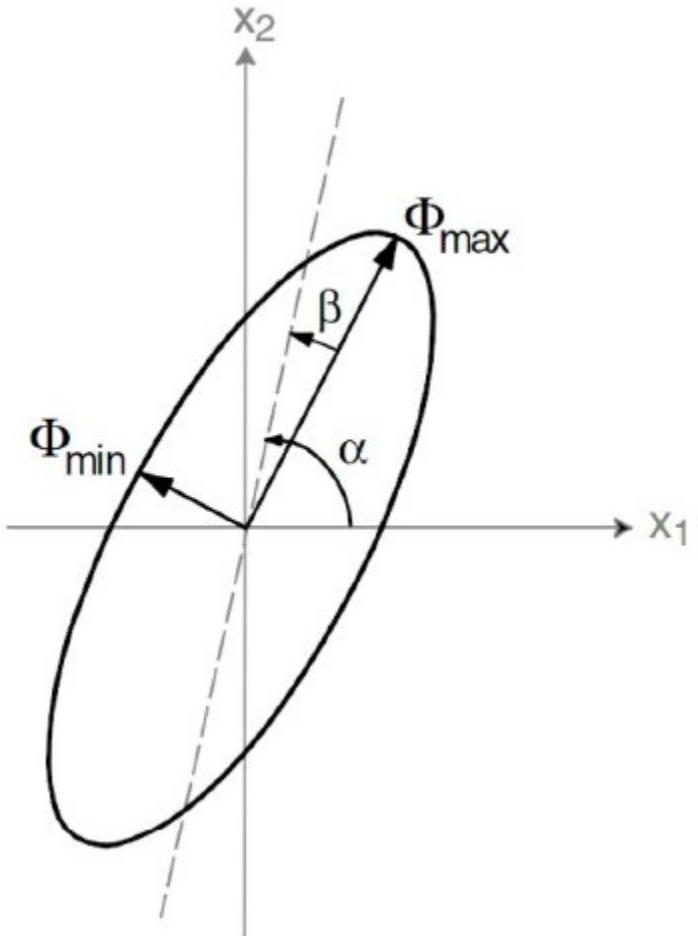

Figure 4.6: *Schematic diagram of the phase tensor ellipse. The variables Φ_{min} and Φ_{max} are the minimum and maximum values of the phase tensor. The skew angle is β. α is the strike angle. Image from Caldwell et al. (2004).*

4.5 Practical aspects of the magnetotelluric methods

4.5.1 Instrumentation and data collection

Magnetotelluric data collection can be split into three distinct configurations. The typical specifications for each configuration and their associated frequency bands are shown in Table 4.1. The configuration chosen is a function of the skin depth and the depth of the target of interest in a study and are as follows:

- The shallowest approach is audio magnetotellurics (AMT) and is typically used to image the relatively shallow near surface, often at drillable depths.
- Broadband magnetotellurics (BBMT) is the next deeper imaging option, and it is typically used in crustal studies, but it may reach depths of the upper lithospheric mantle under certain conditions.
- Long-period MT (LMT) is the final method, and it is capable of imaging the entire lithosphere and is typically used in regional or tectonic-scale studies. While LMT can image structure at the greatest depths, its highest frequencies are much less than AMT and BBMT. Thus, it is often unable to resolve structure in the upper crust.

As frequencies decrease, the recording time for an MT measurement gets longer. At least 20 samples of a specific period should be measured to get a reliable estimate of the apparent resistivity, phase, and tipper at a selected period. For example, to get an estimate at 5,000 seconds, this would require recording data for at least 100,000 seconds, or ~28 hours. However, MT data quality is highly variable and depends on the presence of signal, anthropogenic noise such as powerlines, and surface conditions such as temperature variations, rain, etc. As a result, longer recording durations are often necessary in real-world conditions. In practice, a typical recording duration is usually a few hours for AMT, a day or two for BBTM, and 1-2 weeks for LMT (Table 4.1).

LMT data typically records at a fixed sampling rate, usually no greater than 10 Hz. Based on the Nyquist frequency, LMT should be able to recover signals at 5 Hz. However, a sampling rate that is an order of magnitude higher than the highest desired frequency is usually better. This means

that LMT is usually limited to frequencies no greater than 1 Hz. In comparison, broadband and audio MT typically have variable sampling rates depending on the machine chosen. Due to the higher frequency bands involved, broadband and audio MT often use a discontinuous high-frequency sampling scheme for the highest range of their respective frequency bands (e.g., recording high-frequency signals for only a few minutes every hour). This has the advantage of keeping data volumes low while reserving most of the recording duration for longer-period (lower frequency) signals.

Table 4.1**:** *Specifications of the various MT systems.*

MT System	Frequency Band	Typical Recording Time	Depth of Investigation	Electrode Spacing	Magnetometer Type
Long-period MT (LMT)	1–0.0001 Hz	1-3 weeks	200 + km	100 m	3-component fluxgate
Broadband MT (BBMT)	1000 Hz–0.001 Hz	1-2 days	<40 km	50–100 m	Induction Coil x3
Audio MT (AMT)	10 kHz–1 Hz	A few hours at most	1-2 km	<50 m. Sometimes 25m	Induction Coil x3

Due to the short recording duration and high frequencies desired, AMT often uses metal stakes as electrodes for their efficiency in installation. For the longer recordings of broadband MT and LMT, metal stakes are not used as they will begin to corrode and generate electrical noise. Instead, porous pot non-polarizing electrodes are used. These electrodes are usually composed of some type of metal-salt solution and have low noise and low temporal drift. The electrodes are typically spaced 50-100 m apart in the shape of either an L, T, or plus sign depending on site constraints (Fig. 4.7). However, in AMT, electrodes may be spaced closer than this. The electric field is measured as the potential difference between the two electrodes divided by their distance. The dipoles are usually

oriented magnetic north-south (X-direction) and east-west (Y-direction) unless they need to be rotated due to site constraints. The vertical electric field is usually not measured, as this would require drilling a borehole to attain an adequate dipole. Daily temperature variations can affect the electrodes and produce drift due to the thermoelectric effect. Burial of at least 30 centimeters wherever possible is usually sought to minimize these temperature effects. Bentonite or other highly absorbent clays may be placed around the electrode to increase the electrical connection with the ground and to avoid the possibility of the electrode drying out and failing. The preferred method of deploying electrodes for this thesis involves tying cord to the electrode housing, surrounding the porous end with bentonite, and placing this in a porous canvas anode bag that was then placed in the ground. The entire bag-bentonite-electrode system could then be easily recovered by pulling on the rope and then reused at a different recording site as needed.

Different types of magnetometers are used in the three types of MT system described above. LMT uses a fluxgate magnetometer due to higher signal-to-noise ratios at long periods. In the fluxgate magnetometer, all three magnetic fields (two horizontal and one vertical) are housed in a single container, and only one hole needs to be dug (Fig. 4.7). A fluxgate magnetometer operates by saturating a magnetic core material with an induced magnetic field and measuring how it is affected by the presence of an external magnetic field. In comparison, AMT and BBMT use three induction coil magnetometers. These are aligned north-south, east-west, and vertically. This requires digging one vertical hole and two trenches. It is often difficult to fully bury the vertical search coil, and so a mound is built around it to minimize disturbances. Induction coils operate by measuring voltages within a metal coil that is wound around a magnetic core material that are induced by time-varying magnetic fields.

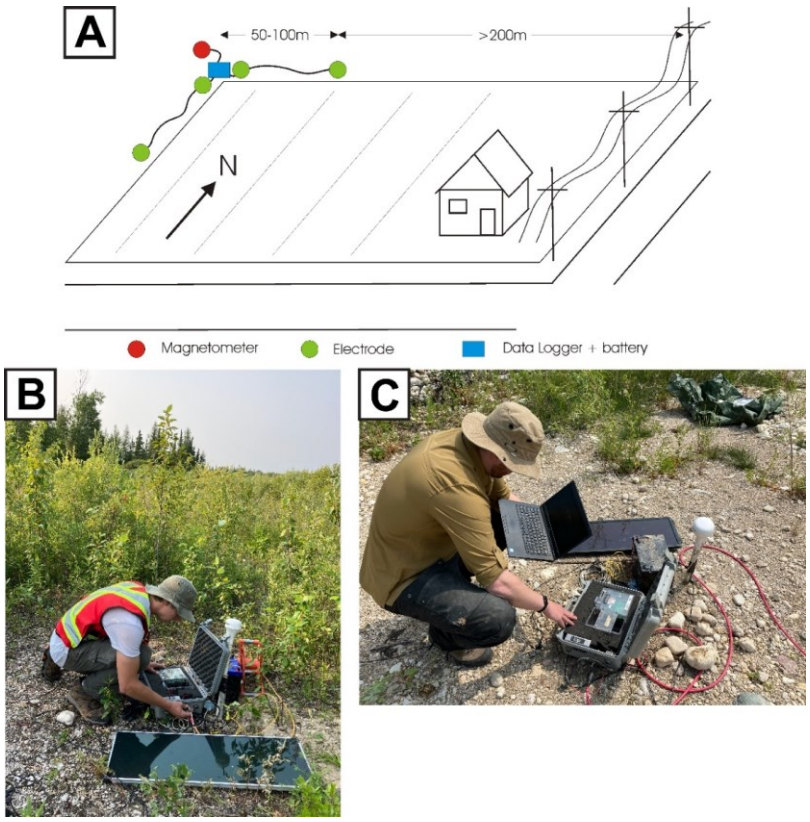

Figure 4.7: *(A) Layout of an LMT station. Installation only requires digging 4-6 holes in the ground to a depth of 30 cm. The station typically occupies an area that is up to 100 x 100 m in size. Note that for a BBMT or MT station, the magnetic fields are measured by 3 separate induction coils. (B) and (C) are examples of the Narod Geophysics Ltd's NIMS (Narod Intelligent Magnetotelluric System) LMT system being deployed in the field in Manitoba. Figure from Chase et al. (2024b).*

4.5.2 Magnetotelluric time series processing

This section discusses MT time series processing at a very high level in order to introduce the main concepts and procedures. For a more in-depth understanding, the reader is directed towards the work of Chave and Jones (2012) and Simpson and Bahr (2005).

MT data are collected in the time domain as a time series (e.g., Fig. 4.8), but they are typically viewed and interpreted in the frequency domain. The time series data are typically converted into the frequency domain using a Fast-Fourier transform. Early solutions for the calculation of the impedance tensor involved a least-squares method to average multiple estimates of the impedance at each measurement frequency (Sims et al., 1971). This method assumed that the noise in the electric and magnetic fields was incoherent between channels and Gaussian (Chave et al., 1987;

Chave and Thomson, 1989). Some types of electric and magnetic field noise satisfy these requirements, but others do not. Manually editing the data to remove noisy sections can be very time consuming, and so automated processing tools using statistically robust methods are typically used to make this task simpler for the user. A range of techniques have been developed, but most identify outliers that do not match a predicted statistical model and then remove them so that a Gaussian distribution is obtained (Egbert and Booker, 1986; Jones et al., 1989; Simpson and Bahr, 2005; Chave, 2017). Additional updates to this method include coherency sorting (Egbert and Livelybrooks, 1996) and imposing smoothness on the estimated transfer functions (Larsen et al., 1996). Remote reference techniques were developed have also been introduced as a way to separate noise and signal. This method uses electric and magnetic field data that have been recorded simultaneously at two locations. It is assumed that the same signal will be present at both locations, but that the noise will be different (Gamble et al., 1979). This method was extended to use data recorded at multiple stations in an array by Egbert (1997). Data analysis in this thesis uses this remote reference approach which produced valuable response curves when noise was present. Data processing is often an iterative process and can involve multiple attempts at editing the time series, using different sites to conduct remote referencing, etc. The final output is generally curves of the apparent resistivity, phase, and tipper plotted against frequency or period (e.g., Figure 4.9).

\

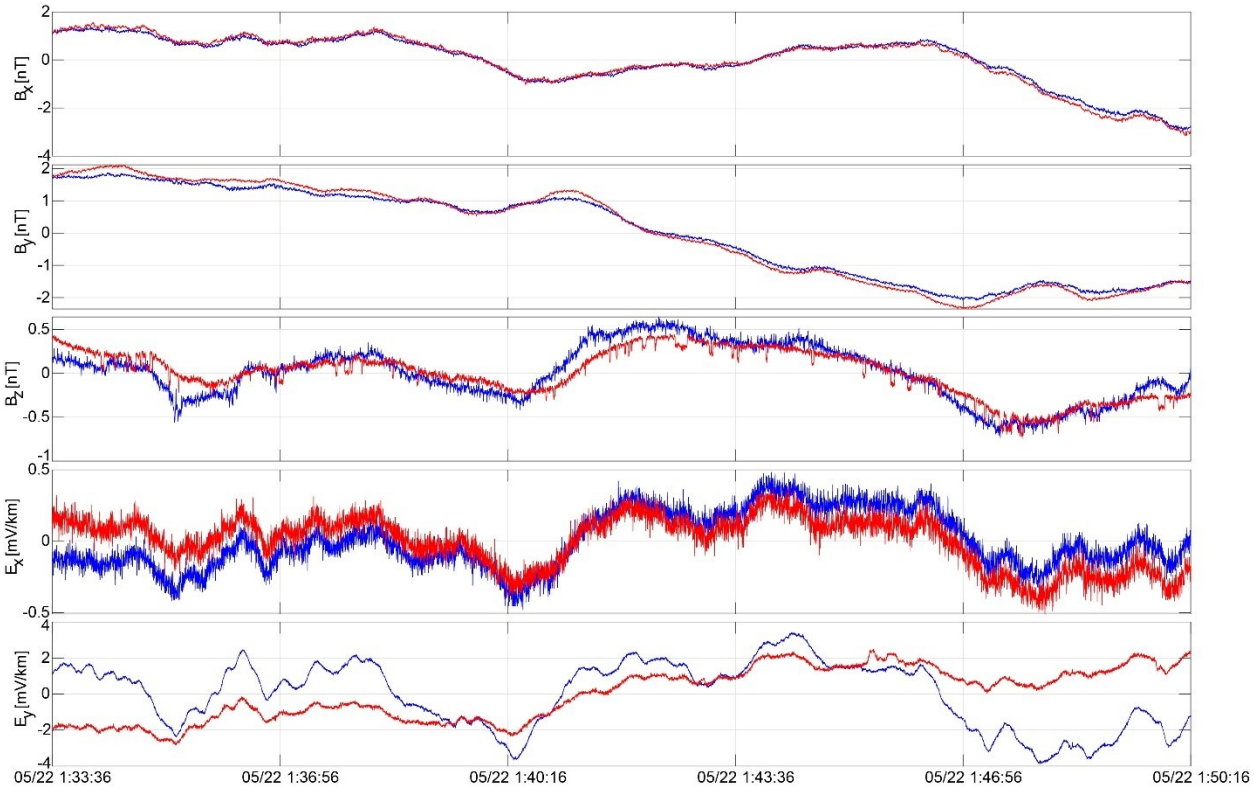

Figure 4.8: *A plot showing a typical times series for two MT stations (red and blue) that were collected at the same time. The three magnetic field components are on top and the two electric field components are on the bottom.*

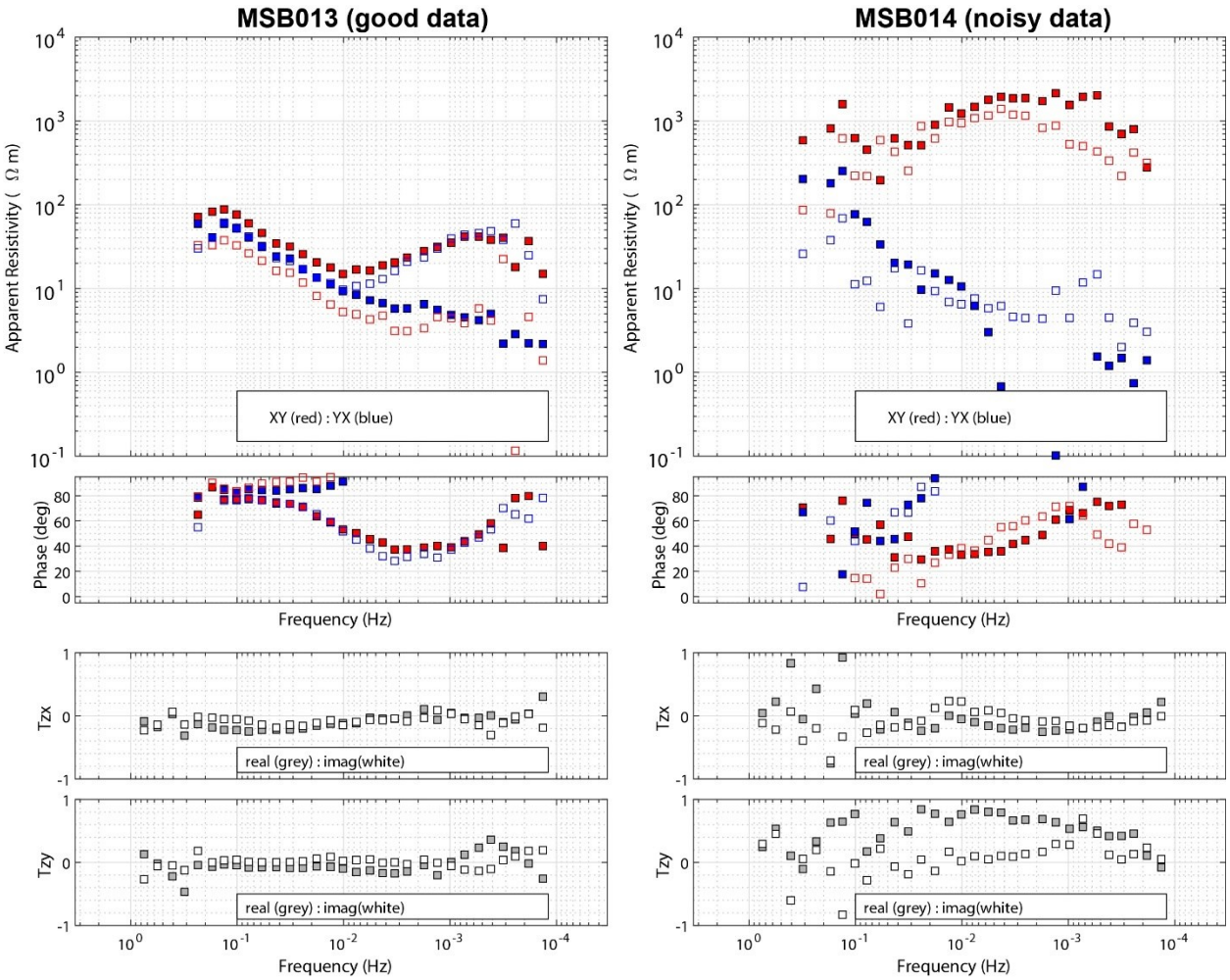

Figure 4.9**:** *Data from two different MT stations showing examples of quiet and noisy data. The main difference is the smooth curve in the quiet data and the ragged curve in the noisy data. In the top two panels, the solid red boxes are show the XY component of the impedance tensor, solid blue boxes are the YX component, open red boxes are the XX component, and open blue boxes are the YY component. In the bottom two panels, the grey and white boxes are the real (in-phase) and the imaginary (imag; out-of-phase) components of the tipper (T), respectively.*

The above provides a high-level summary of the methods and steps involved in MT time-series data processing, which are summarized in Figure 4.10. One additional step used in the work here during the final stages of editing the transfer function was the D+ approach. The D+ editing method can be used as a first-pass technique to ensure a dataset is consistent and reliable (Parker and Booker, 1996). If an MT sounding cannot fit a D+ model, this implies the site needs careful evaluation to ensure channels were connected properly or for other errors in the field procedures. It is also a useful technique for removing outlier points that do not conform to the smoother dispersive physics of MT. However, poor D+ fit may also indicate that unique local or regional

geology is causing significant 3-D effects, galvanic distortions, electrical anisotropy, etc. (Cordell, 2020).

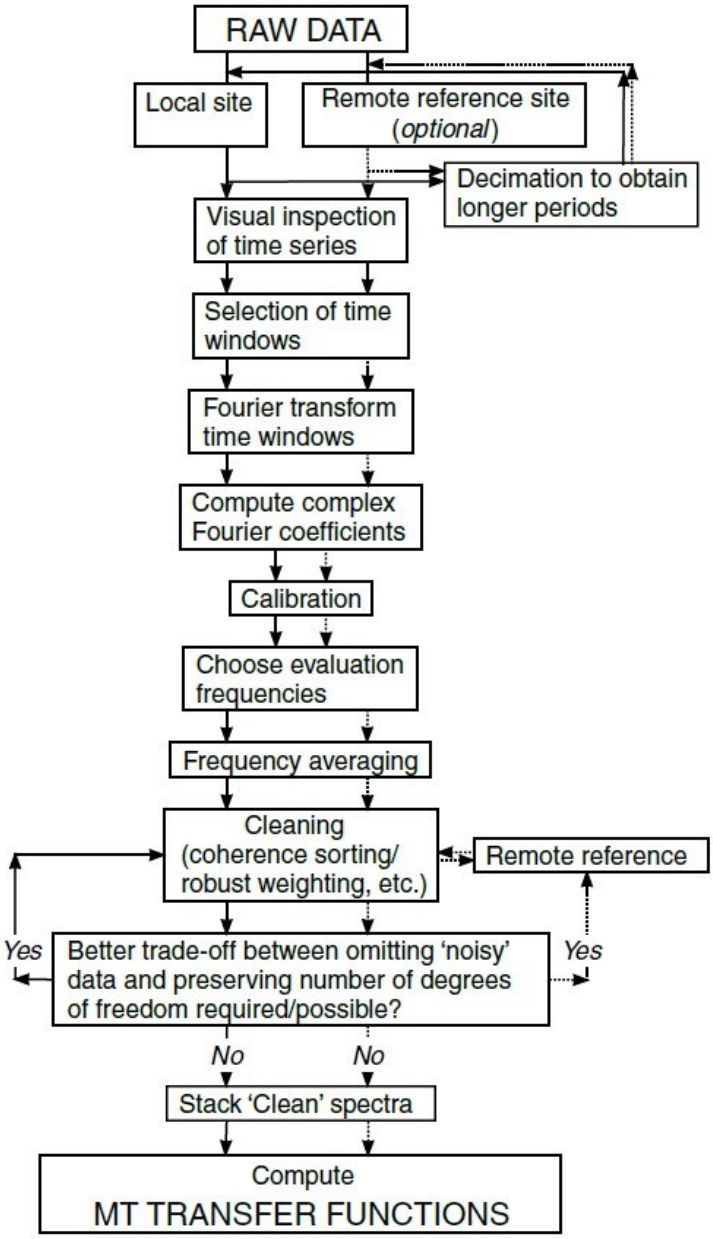

Figure 4.10: *Flowchart that summarizes the steps in processing MT data. Figure from Simpson and Bahr (2005).*

4.6 Geophysical inverse theory and non-uniqueness

The apparent resistivity, phase, and tipper curves derived from the MT time series data are functions of frequency, which is a proxy for depth in the Earth through the skin depth equation (Equation 4.27). To be interpreted in terms of subsurface structure, these frequency domain data need to be converted into a resistivity model as a function of depth and horizontal position. Forward and inverse approaches are often used in conjunction to accomplish this task.

The apparent resistivity, phase, and tipper curves derived from the MT time series data are functions of frequency, which is a proxy for depth in the Earth through the skin depth equation (Equation 4.27). To be interpreted in terms of subsurface structure, these frequency domain data need to be converted into a resistivity model as a function of depth and horizontal position. Forward and inverse approaches are often used in conjunction to accomplish this task.

4.6.1 Forward problems

Forward solutions provide the predicted responses for a specified resistivity model (Fig. 4.11), and these are often called synthetic data (Fig. 4.11). This synthetic data can be compared to the measured data to see if the forward model accurately reproduced the real data. Most approaches seek to get data misfit, usually expressed as root mean square (R.M.S.) misfit, between the measured and calculated data close to a value of one. In practice, this is difficult to achieve due to issues with noise in real data, and so R.M.S misfit values of 1-1.5 are usually acceptable. The forward model can be updated repeatedly in a trail-and-error approach until the measured data agrees with the predicted data to a specified misfit level. Forward modeling is often used to evaluate model non-uniqueness, data sensitivity, and hypotheses about subsurface structure (e.g., Chapters 5 and 6). For example, one may suspect that measured data is not sensitive to a deep conductor. The conductor could be removed from the model, a forward calculation run, and the resulting synthetic data compared to the observed data to see if the removal of the conductor had an appreciable effect on data misfit. Similarly, given that MT physics is diffusive, it might be suspected that the vertical extent of a conductor might be artificial as a result of smoothing

constraints imposed by an inversion algorithm. A hypothesis then might be to see if a relatively thin low resistivity layer accurately fits the data, and a forward solution modeling this could be conducted. The synthetic data could also be inverted separately to see if a model reasonably similar to the original inverse solution is obtained. Critically, forward solutions provide unique analytical solutions, and the resulting model or data fit should be the same every time the same forward model is used as an input. In practice, the trail-and-error approach can be time consuming and is really only practical in 1-D cases with a limited number of stations.

As the number of stations increases or problems become 2- and 3-D, the increasing complexity makes it impractical to perform forward calculation. Instead, it becomes much more efficient to automate this process using numerical inverse approaches (Simpson and Bahr, 2005).

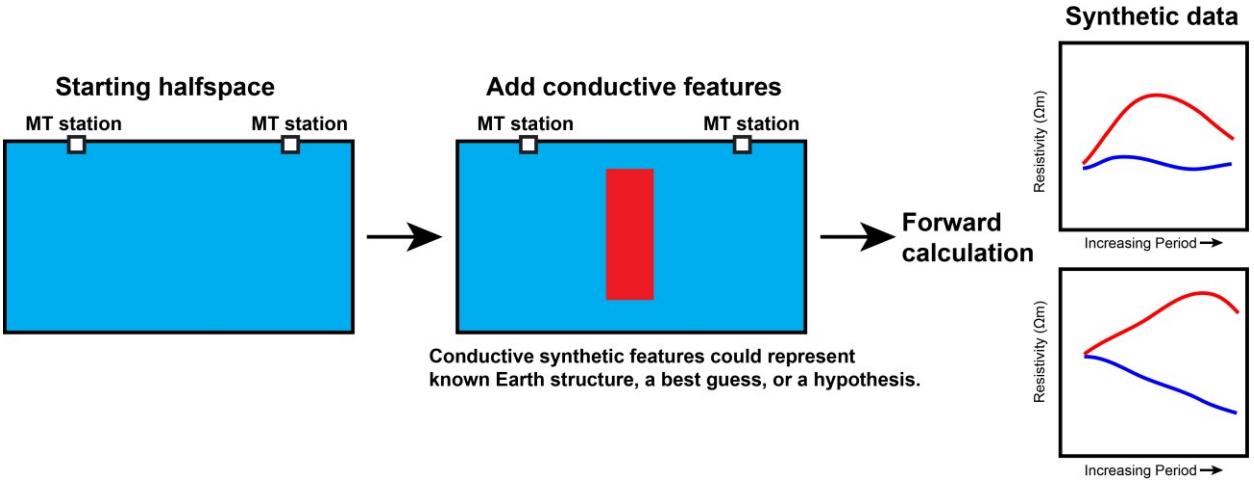

Figure 4.11: *Conceptual model of the forward calculation. The forward calculation is simpler and less computationally intensive than the inverse calculation. The red and blue curves correspond to the XY and YX apparent resistivity curves, respectively.*

4.6.2 Basics of inverse problems

The opposite process to forward modelling is called inversion. Inversion routines determine a resistivity model that satisfies a set of observed data to a specified statistical level. Inversion algorithms seek to minimize an objective function. The objective function is usually a combination of a data misfit and regularization parameters linked with forward modelling operation. The data misfit, usually root mean square (R.M.S.) misfit, is again often used in these algorithms as a measure of the difference between the observed (measured) data and the calculated data from the

inversion model. The model smoothness is imposed due to the diffuse physics of the MT method and to maintain stability of the inversion algorithm. The regularization parameter weighs the relative importance of the misfit vs. model smoothness. A low regularization will give greater weight to minimizing data misfit but produce a rougher model. A large regularization will prioritize model smoothness at the expense of data misfit. The inverse problem is non-unique as there is usually far less data than model parameters. This leaves the inverse problem underdetermined, and, as a result, an infinite number of solutions exist. Additional uncertainty can be introduced by noise and regularization (i.e., smoothing) constraints. Figure 4.12 shows a conceptual model demonstrating the inversion process. In addition to the collected data, inversion schemes first require a starting model to begin. A reference model, usually a half-space, is chosen to define model smoothness such that the final model is smooth relative to the reference model. The starting model is then perturbed, and predicated data are calculated and handled by the forward modeling operator. If the predicted data agree favorably with the observed data, usually determined by a reduction in R.M.S. misfit, the model perturbations are maintained (Fig. 4.12). If the perturbations do not agree favorably, they are discarded (Fig. 4.12). This process then repeats until an acceptable model is created with respect to data misfit and model smoothness.

Inversion routines can be divided into either deterministic or stochastic methods. Deterministic methods start from an initial guess, such as a 1-D, 2-D or 3-D input resistivity model (usually a halfspace), and then iteratively improve the model to minimize data misfit. Deterministic methods are iterative because the problem is non-linear and will require iterative refinement to converge on a solution that minimizes the misfit between the measured data and the predicted data. The final model obtained by deterministic inversion can be dependent on the initial starting model, and this means the inversion can get stuck in local minima (a potentially incorrect model that the routine cannot escape from).

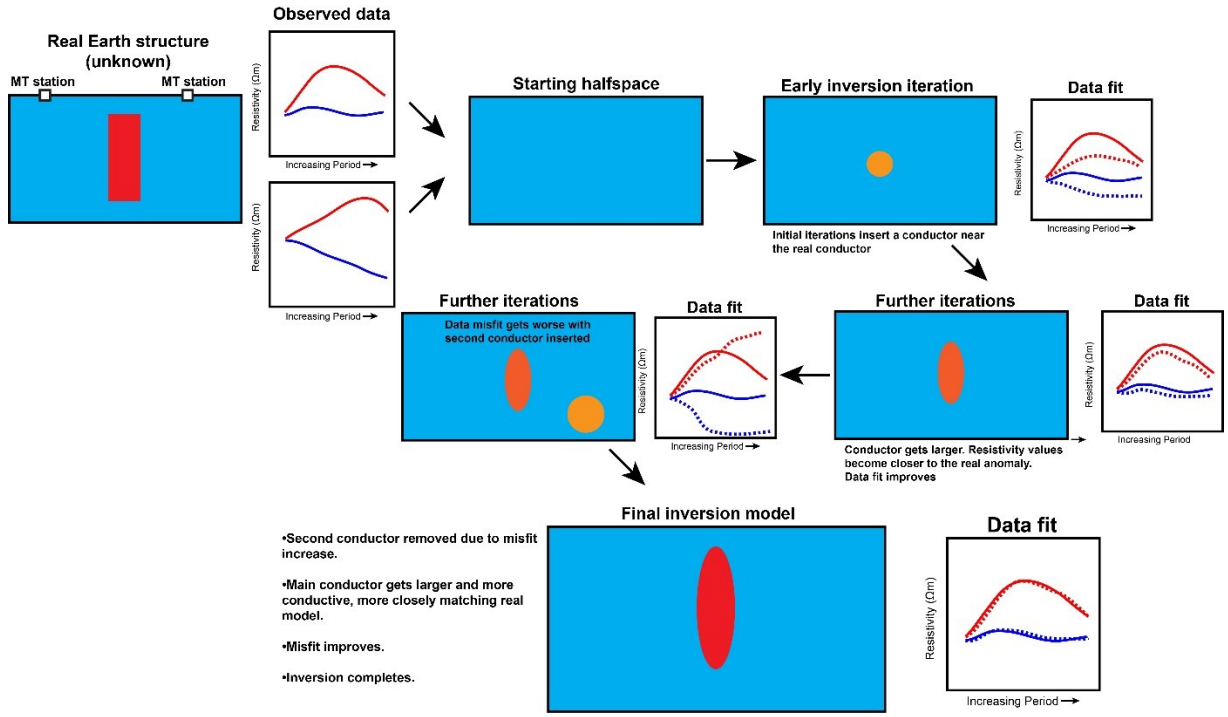

Figure 4.12: *Conceptual model of the inverse calculation (i.e., inversion). Earth structure, usually unknown, is measured by MT stations in the field. The resulting apparent resistivity data, alongside a halfspace, are then used as inputs for the inversion algorithm. The algorithm begins by attempting to locate a conductor in the halfspace (orange circle). If data fit is improved, this change is kept. The conductor may then be perturbed (i.e., changed) to more closely match the anomaly in the real Earth structure model (larger, darker orange oval). If data fit continues to improve, this change is kept. However, the inversion algorithm may introduce additional structure, and data fit worsens (second orange circle). In this case, the change is likely to be rejected. The inversion continues until, ideally, a reasonable approximation of the real Earth structure is obtained (final red oval). Critically, since the MT method relies on diffusive physics and the inversion routine on regularization (i.e., smoothing), it is unlikely the algorithm will produce a conductor that is an exact match to the real Earth structure. This is especially true if the low resistivity feature in the real Earth has sharp boundaries, as is the case here (red rectangle).*

The other approach is stochastic inverse methods, which generate a range of forward models and evaluate how well each fits the measured data. Typically, these models are generated through random or probabilistic process and then modified using misfit as a selection criterion (e.g., Monte Carlo vs Markov Chain Monte Carlo methods). Instead of directly seeking to minimize an objective function like deterministic methods, stochastic methods will generate a wide distribution of models and balance data fit and prior knowledge to better understand model variability and uncertainty. In the past, stochastic inversions have largely been used to obtain 1-D solutions where the computational cost of the forward problem is relatively low. In 2-D and 3-D cases the forward

problem gets considerably more computationally expensive and time consuming, and the process of evaluating hundreds or thousands of models in stochastic methods is less feasible. As a result, deterministic methods have been favored for 2-D and 3-D problems in recent decades. However, in recent years, progress has been made in applying stochastic inverse methods for 3-D problems (e.g., Manassero et al., 2020).

To minimize uncertainty and improve interpretation, a priori information is often introduced into the starting model prior to inversion. This a priori information may come from geologic or other geophysical data. For example, in regions with sedimentary overburden, it is common to approximate the effects of these sediments during modeling by creating a low resistivity layer at the surface of the model. Geospatial data, such as bathymetric maps, may also be used to introduce a priori information like electrically conductive seawater into the model.

A number of inversion algorithms have been developed to convert MT data to resistivity models. In the past, computational limits meant most of these algorithms were 1-D and 2-D. However, as access to high-performance computing clusters has improves the use of 3-D inversion algorithms has become increasingly standard. In this thesis, the 2-D algorithm of Rodi and Mackie (2001) was used for Chapter 4, and the 3-D ModEM algorithm of Kelbert et al. (2014) was used for Chapter 5 and Chapter 6. Both algorithms are examples of deterministic inverse and use the non-linear conjugate gradient method to fit the model response to the measured MT data within a user-specified statistical tolerance.

Figure 4.13 displays two apparent resistivity and phase curves from two MT stations used in the inversion to create the resistivity model for Chapter 5. For both, the inversion response curves (shown by colored solid lines) are smooth, which reflects the diffuse physics of the MT method and the effects of the regularization parameter. In this case, the inversion fit site SAS028 well as the R.M.S. misfit is low, and the response curve fits all data points within their error bars (the colored vertical lines at each point). However, the fit was less than ideal for SAS044 as the R.M.S. misfit was high, and the response curve do not fit multiple long-period XY data. A lower regularization parameter (i.e., less smooth) might have been able to fit the sharp increase in resistivity at ~200 seconds in the XY data of SAS04. However, this would have produced an unrealistically rough model.

The above was a very high-level introduction to inverse problems. Readers interested in additional details are directed to the work of Simpson and Bahr (2005), Chave and Jones (2012), and Zhdanov (2015).

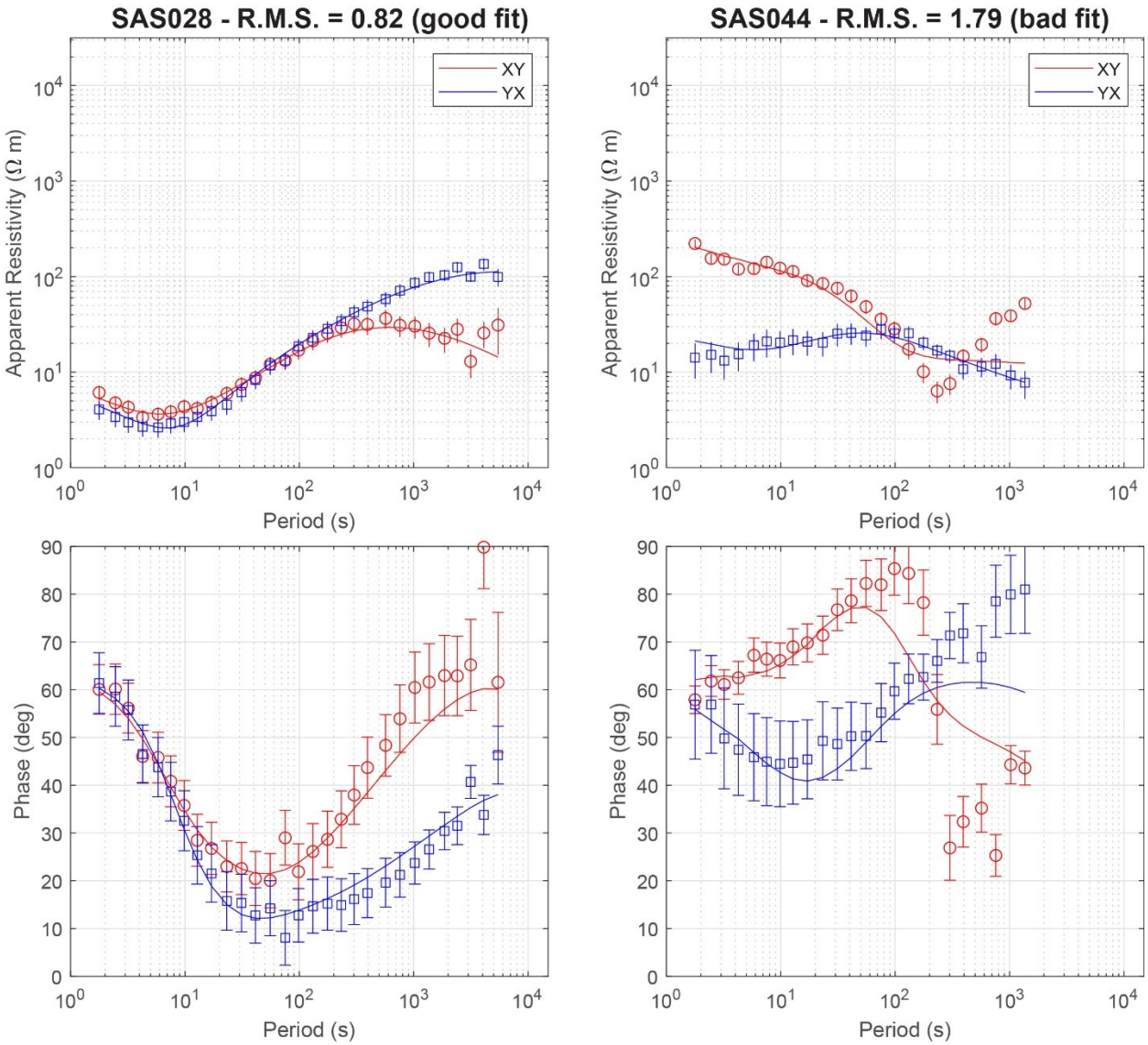

Figure 4.13: *Example apparent resistivity curves demonstrating a low (good) R.M.S. misfit (left) and high (bad) R.M.S. misfit (right) for the inversion model produced in Chapter 6. Note the smooth inversion response curves (solid-colored lines), which are typical of the diffusive physics of MT and regularization imposed by the inversion algorithms.*

CHAPTER 5. MAGNETOTELLURIC IMAGING OF THE LITHOSPHERIC STRUCTURE OF THE SOUTHERN OKLAHOMA AULACOGEN: EVIDENCE FOR LONG-TERM WEAKENING CAUSED BY RIFTING

Chase, B.F.W., Unsworth, M.J., Atekwana, E.A., Evans, R.L. and Zhu, J., 2023.
Journal of Geophysical Research: Solid Earth, Volume 28, Issue 6, e2023JB026555

Abstract

Magnetotelluric (MT) data were used to study the lithosphere structure of the Southern Oklahoma Aulacogen (SOA). Inversion of the data revealed two low resistivity anomalies beneath the SOA. The first is located in the depth range 0-90 km in the crust and upper lithospheric mantle. The second extends from a depth 100 km to the base of the lithospheric mantle and extends away from the SOA to the ends of the profile. The cause of low resistivity anomalies is discussed in relation to the tectonic evolution of the region and recent laboratory experiments on rock conductivity. The first anomaly is attributed to the combination of (1) water present in mantle minerals, and (2) the formation of hydrous mineral phases by interactions between a plume and the lithosphere during rifting. Grain size reduction and fabric alignment from deformation during the Ancestral Rocky Mountain (ARM) orogeny may have also contributed to the low resistivity. This enrichment phase may have mechanically weakened the lithosphere and allowed deformation to occur during the ARM orogeny. The low resistivity of the deeper anomaly is attributed to a fluorine-enriched phlogopite layer that is also coincident with an observed seismic mid-lithosphere discontinuity (MLD). A lithosphere keel of mantle minerals enriched in water underlies this layer and may have formed by accretion of the plume head to the lower lithosphere after rifting, which also rethickened the lithosphere to its present-day depths. The MLD may then reflect a melt layer along a paleo lithosphere-asthenosphere boundary entombed during the accretion.

5.1 Introduction

Cratonic regions are areas characterized by long-term lithospheric stability that often persists through a significant amount of earth history. However, many studies have shown that cratons can be modified by later tectonic events and in some cases destroyed (e.g., Abdelsalam et al., 2002; Tang et al., 2013, Liu et al., 2021). The study of the deep lithosphere beneath and along craton margins offers the opportunity to understand the processes that can modify and potentially destroy cratons, and to connect these processes with evolution of the lithosphere on the regional scale. This type of study can also offer constraints on volatile fluxes and storage, rheology, and long-term survivability of the subcontinental lithosphere mantle (SCLM), as well as the formation of economically significant mineral deposits within the cratonic lithosphere (O' Reilly and Griffin, 2013; Griffin et al., 2013; Foley and Fischer, 2017; Selway, 2018; Aulbach, 2018; Fezzotti and Ferrando, 2018).

The southern midcontinent of the United States is located on the margin of the Laurentian craton. This region records geologic events that extend from the initial assembly of Laurentia to its breakup from Pangea. Many of these features have escaped later tectonic reworking, offering a valuable window into the evolution of the continent. Since the breakup of Pangea, regional tectonic activity has ceased, and Phanerozoic sedimentary rocks up to 12 km thick have covered most of the region. This has complicated investigation of regional basement rocks critical for tectonic studies, making geophysical imaging necessary. Notably, the EarthScope seismic array has defined variations in seismic velocity, Moho depths, lithosphere structure, and the lithosphere-asthenosphere boundary (LAB), offering valuable insights into regional terrane assembly and tectonic evolution, as well as how these processes modified and are preserved in the lithosphere (e.g., Kumar et al., 2012; Shen et al., 2015; Nyamwandha et al., 2016). The complimentary EarthScope MT array has offered additional insights by defining regions of lithosphere enrichment and modification resulting from regional tectonic processes (e.g., Yang et al., 2015; Bedrosian, 2016; DeLucia et al., 2019).

This paper presents an investigation of the Southern Oklahoma Aulacogen, which is a failed, structurally inverted rift located in Oklahoma and Texas (Fig. 5.1). The SOA was involved in two

episodes of Laurentian evolution. The first was as a failed rift arm during the Cambrian breakup of Rodinia, and the second was as an uplift in the Pennsylvanian-Permian Ancestral Rocky Mountain (ARM) orogeny during the assembly of Pangea (Kluth and Coney, 1981; Whitmeyer and Karlstrom, 2007; Leary et al., 2017). Study of the SOA provides the opportunity to understand (a) how Cambrian rifting modified the lithosphere, (b) if this modification is still preserved, and (c) how this modification may have influenced the evolution of the SOA during the ARM orogeny. Relative to the much of the regional basement the SOA is buried at shallow depths (100s of meters to <1 km) which has allowed it to be subjected to a wide variety of geochemical, geophysical, and structural studies (e.g., Brewer et al., 1983; Hanson et al., 2013; Chase et al., 2022a). However, geophysical imaging of sufficient resolution at depths greater than the mid-crust is lacking. Further, while the EarthScope seismic array extended over the region the resolution is limited due to the large 70 km site spacing (Evanzia et al., 2014). The EarthScope MT array did not extend to the region.

In this paper, the first modern MT study of the SOA itself is described. The only other MT data in the region was a study of the adjacent Anadarko basin (Vozoff, 1972). A profile of 13 long period MT stations was collected from 2018-2019 and inverted to give a two-dimensional (2D) lithosphere-scale resistivity model. Details of the resistivity model are discussed to investigate the cause of the low resistivity zones observed and relate them to past tectonic processes. The implications of the electrical resistivity structure in relation to the evolution of Laurentia, particularly how they may relate to ARM tectonics and Rodinian rifting are discussed. It should be noted that the terms resistivity and conductivity, mathematical inverses of each other, are both used in this paper.

5.2 Geologic and tectonic Framework

5.2.1 Geologic and tectonic history

The SOA is located on the inferred terrane boundary between the Mazatzal and Granite-Rhyolite provinces (Whitmeyer and Karlstrom, 2007) (inset, Fig. 5.1). Following terrane collision in the mid-Proterozoic, widespread granitoid intrusion occurred across both terranes around ~1.4 Ga

(Whitmeyer and Karlstrom, 2007). After this, there is no recorded activity until the early Cambrian during the breakup of Rodinia when the region rifted as the failed arm of a plume-driven rift-rift-rift triple junction centered near the present-day Oklahoma-Texas border (Hoffman et al., 1974; inset Fig. 5.1). The original suture between the two terranes may have been a region of pre-existing weakness that aided rifting localization and development (Budnik, 1986; Keller and Stephenson, 2007; Yuan et al., 2015). An alternate interpretation was proposed by Thomas (2011; 2014), who suggested that the SOA was a leaky transform fault that is associated with pronounced lateral offset. This interpretation and rifting are not mutually exclusive (Hanson et al., 2013), but generally leaky transforms do not exhibit the extensive magmatism and produce magmas of different composition that are observed in the SOA (Skulski et al., 1991; 1992 Brueseke et al., 2016). Based on this analysis, the SOA is referred to as a rift in this paper.

Initial volcanism during rifting was mafic, of largely subalkaline tholeiitic affinity with another, smaller component of alkaline-transitional affinity, and produced the extensive Glen Mountain Layered Complex, gabbros, and ultramafic rocks at depth (Powell and Phelps, 1997; Brueseke et al., 2016). A later felsic stage emplaced mostly fluorine-rich, water-poor A-type magmas between and on top of the mafic units (Hogan and Gilbert, 1998; Hanson et al., 2013; Price et al., 2014). Numerous diabase dikes and sills intruding all other units were emplaced throughout rifting and mark the final stage of volcanism (Gilbert, 1983; Hanson et al., 2013). Some intermediate igneous rocks occur in the subsurface, with these units often intercalated with the rhyolitic units (Hanson et al., 2013). No calderas or volcanic centers have been reported, and feeder dikes are inferred to have produced most of the volcanism (McConnell and Gilbert, 1990), which can be defined in aeromagnetic data (Chase et al., 2022a). Volcanism lasted from 539-529 Mya, was largely bimodal with limited breaks between phases, and most of the magmatism occurred in a ~2 My timeframe from 532-530 Mya (Hogan and Gilbert, 1988; Wall et al., 2020). Geochemistry results point to (1) the derivation of felsic magmas by the partial melting of plume-derived mafic units or of a mafic underplate, (2) the derivation of mafic units from a plume of ocean island basalt (OIB) affinity, and (3) most units appear to have been generated with limited interaction and partial melting of the existing lithosphere (Hanson et al., 2013; Price et al., 2014; Brueseke et al., 2016; Wall et al., 2020). The total volume of igneous rock emplaced by the SOA was estimated by Hanson et al.,

(2013) to be at >250,000 km^3, which led the authors to argue the SOA was a Large Igneous Province, the only one reported along the southern margin of Rodinia during the Cambrian.

After rifting, the SOA experienced subsidence, with tectonic activity limited to pulses of broad crustal flexure from the Ordovician to the Devonian, occurring at the same time as the deposition of ~4-5 km of sedimentary rock (Amsden, 1982; Gilbert, 1983). During the assembly of Pangea in the Pennsylvanian, the SOA was the first block to be uplifted as part of the larger ARM orogeny that occurred from Oklahoma to Colorado and New Mexico (Leary et al., 2017). Deformation in the SOA occurred in two phases. The first saw compressional NE-SW-directed stresses and a small amount of sinistral strike-slip movement, leading to structural inversion via thrust faulting. The first phase and thrust faulting ceased by the Atokan (~311-308 Ma). A second phase, dominated by sinistral strike-slip movement, continued until sometime into the Permian (Brewer et al., 1983; Granath, 1989; Turko and Mitra, 2021; Chase et al., 2022a). Overall, transpressional tectonics was the primary mechanism for SOA ARM deformation which resulted in ~12-15 km of vertical uplift, ~ 15 ± 5 km of crustal shortening, and sinistral strike slip deformation ranging from <1 km to as much as 40 km (Granath, 1989; McConnell, 1989; Perry, 1989; Keller and Stephenson, 2007; Turko and Mitra, 2021; Chase et al., 2022a). Continued sedimentary deposition would occur in the newly created basins yielding the 12-15 km deep Anadarko and 2-4 km deep Holis-Hardeman basins to the north and south of the SOA, respectively. The SOA has been tectonically inactive since the ARM but is a notable intraplate-seismic hazard capable of producing earthquake up to M_w 7.0 (Hornsby et al., 2020 and references therein).

5.2.2 Prior geophysical studies

Several geophysical surveys have studied the SOA, revealing that the upper to mid crust contains an extensive, high-density volcanic package (e.g., Chang et al., 1989; Keller and Baldridge, 2006). However, few surveys have imaged to depths greater than 15-25 km. The EarthScope seismic array is the only exception and revealed several seismic anomalies in the SCLM. These include a 2-4% slow shear wave velocity anomaly at depths >75 km (Evanzia et al., 2014), a seismic mid-lithosphere discontinuity (MLD) at depths of 100-120 km (Kumar et al., 2012), and a southwest-dipping, high-angle slow seismic anomaly extending deep into the upper mantle (Neeto and

Pulliam, 2020). Other anomalies present are as follow. The first is a lithosphere-scale negative radial anisotropy anomaly interpreted as a terrain boundary (Yuan et al., 2014). The next is a velocity anomaly interpreted similarly as evidence of a paleo-suture terrane boundary zone (Porritt et al., 2014). There is a final seismic anisotropy anomaly with the fast direction parallel to the SOA that was interpreted as relict lithosphere fabrics or dikes (Comiskey, 2013; Refayee et al., 2014). In the crust, the products of SOA magmatism have been studied by the analysis of gravity data, which detected both a dense core of mafic units that extend downward into the mid-crust and the Moho at a depth of 40-45 km, deepening beneath the rift itself (Keller and Stephenson, 2007; Tave, 2013). Aeromagnetic data have revealed that the SOA is heavily deformed, with numerous NW to EW oriented faults (Chase et al., 2022a). Additional geophysical data that is sensitive to the entire lithosphere and has closer site spacing to improve resolution are necessary to improve upon these prior observations and constrain the lithospheric structure of the SOA. Long-period MT data are suitable for this given their sensitivity to the entire lithosphere and to the presence of various electrically conductive mantle phases associated with tectonic modification (e.g., Bedrosian, 2016; DeLucia et al., 2019).

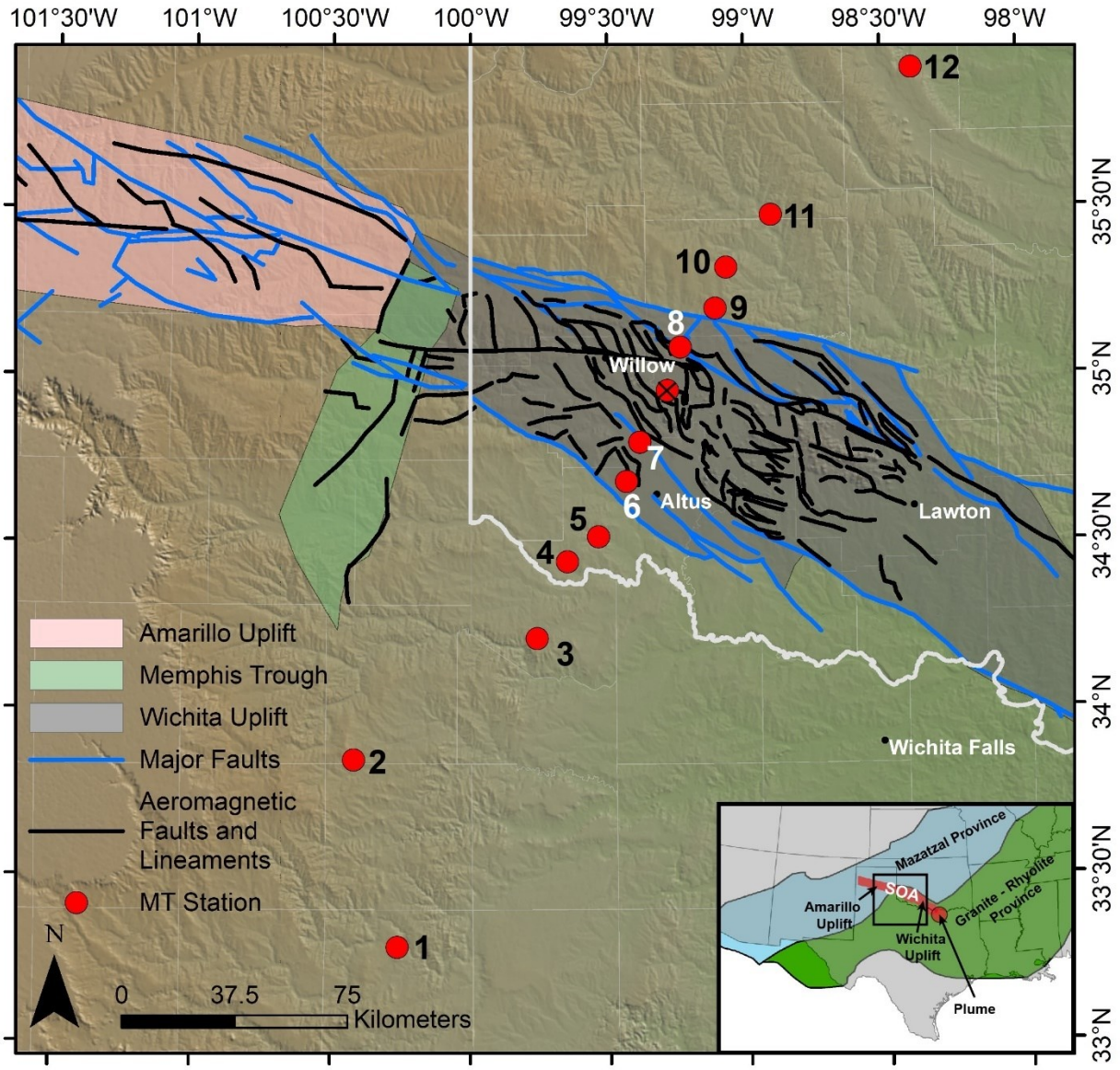

Figure 5.1: *Map of the SOA in Oklahoma and Texas, where it breaks down into locally named uplifts (see inset). The station, station 8, with the black X was ultimately removed from the final inversion model. See text for details. Major faults from Marsh and Holland (2016). Aeromagnetic faults and lineaments from Chase et al. (2022). Tectonic terranes in the inset are from Whitmeyer and Karlstrom (2007).*

5.3 Data analysis

5.3.1 Magnetotelluric data collection

From 2017 to 2019 long-period MT stations were collected at 13 stations along a NE-SW striking profile oriented perpendicular to the N60°W strike of the SOA (Fig 5.1). Stations were spaced ~20 km within the SOA and recorded data for 2-3 weeks. The 3 stations outside of the rift were spaced at ~50 km and recorded data for 6 weeks (Fig. 5.1). Data were collected with LEMI-417M instruments using a fluxgate magnetometer and non-polarizable silver chloride electrodes. Reliable transfer functions were obtained at 26 periods in the range of 4 – 25000 s using the bounded influence code, BIRRP (Chave & Thomson, 2004). Time series data at each site were remote referenced to other synchronously recording sites to remove noise and improve data quality. The resulting apparent resistivity and phase curves for all sites are included in the Supplementary Materials (Fig. A.1) and show low resistivity values at short periods, high resistivity values at mid periods, and a final trend towards low resistivity values at long periods.

5.3.2 Dimensionality of data

The dimensionality of the data was evaluated using the induction vectors and phase tensors. Induction vectors are computed from the vertical and horizontal components of the magnetic field and in the convention of Parkinson (1959) point to concentrations of currents (i.e., conductive zones). The phase tensor displays the azimuthal variation of the impedance and gives a graphical way to determine if the subsurface has a 1-D, 2-D, or 3-D resistivity structure. (Caldwell et al., 2004). The direction of the major axis is either parallel or perpendicular to the geoelectric strike. A parameter called the skew angle is also calculated and indicates the dimensionality (Booker, 2012). A circular phase tensor with zero skew reflects 1-D resistivity structure, an elliptical tensor with zero skew indicates 2-D resistivity structure, and an elliptical tensor with non-zero skew indicates 3-D resistivity structure (Caldwell et al., 2004; Booker, 2012). An important aspect of the phase tensor is that it is not affected by near surface galvanic distortions (Booker, 2012).

Information about dimensionality comes from both the induction vectors and phase tensors. The phase tensors exhibit significantly 3-D behavior at the three periods less than 10 seconds with (a) skew angles ranging from 5° to -5° and (b) scattered ellipse orientations (Fig. 5.2B). This is likely due to the complexity of the conductivity structure associated with the Anadarko and Holis-Hardeman sedimentary basins. Deeper resistivity structure is sensed by longer periods. At periods greater than 400 s, the phase tensor axes align in a direction ~N60°W, roughly parallel to the strike of the SOA, and exhibit more 2-D behavior with skew values ranging from -3° to 2° (Fig. 5.2). This suggests a conductive feature is located beneath the SOA. The induction vectors at the same period as Figure 5.2 are shown in Figure A.2 and also indicate a geoelectric strike parallel to the SOA.

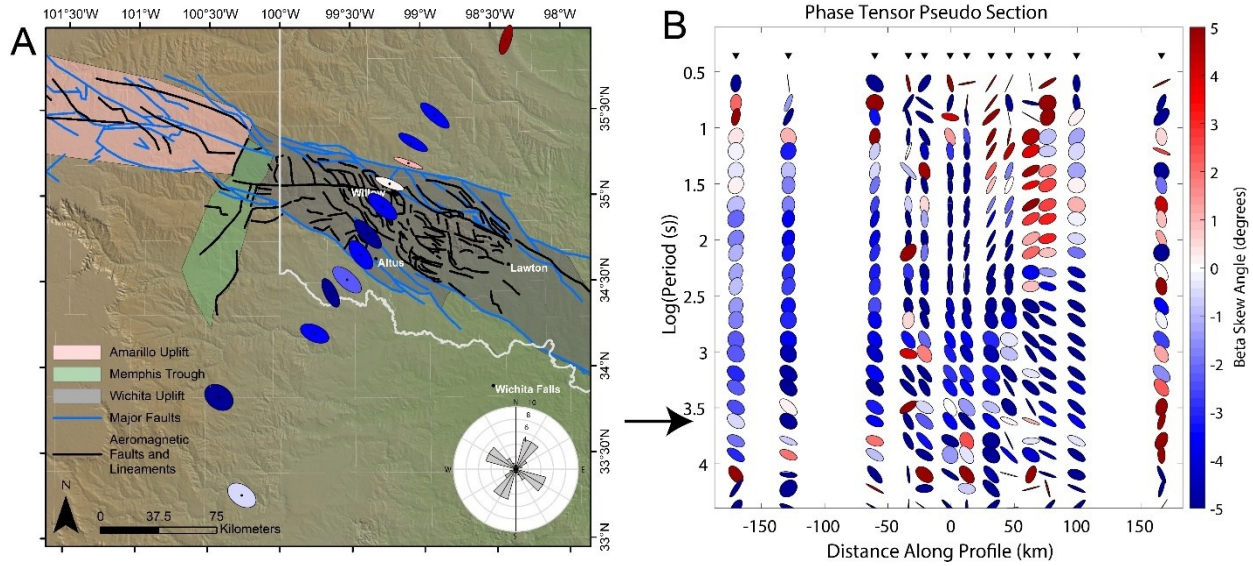

Figure 5.2: *A) phase tensors and induction vector map of the stations over the SOA (red and grey polygons) at 4000 seconds, where the geoelectic strike of the SOA is most obvious. The rose diagram in the lower right show the orientations of the phase tensors in grey. B) phase tensors plot showing the dimensionality of the data as a function of period.*

Since this study is focused on the deep lithosphere structure of the SOA the first 3 periods were removed to simplify the inversion. This left the data at 23 periods over a range of 12-25000 s for inversion. The longest three periods also show the possible influence of 3-D effects. An inversion was undertaken with these periods excluded and the resulting model was very similar to the one shown in Figure 5.4A. The N60°W orientation of the phase tensor provides an estimate of the geoelectric strike direction necessary for 2-D inversion, so the data was rotated to this orientation. The pseudosections in Figure 5.3A display the transverse electric (TE) and transverse magnetic

(TM) modes for the data and inversion model. The TE mode is computed from electric currents flowing along strike of the SOA and the physics is dominated by inductive effects, making it good at detecting conductors. The TM mode is computed from currents flowing across strike and includes both inductive and galvanic effects, making it capable of detecting more moderate conductors and resistors. At the shortest periods along the entire profile low apparent resistivity values are observed in both modes, reflecting the presence of low resistivity sedimentary rocks at the surface. At periods greater than 100 s the apparent resistivity and phase vary along the profile in both modes, indicating a 2-D structure for the crystalline basement. There is a marked change in both the TE and TM modes at ~200 km along the profile, coincident with the SOA. Here, the TM mode detects the SOA as a region of slightly higher apparent resistivity values relative to the low resistivity of the surrounding region. The TE mode has a similar apparent resistivity response, but the phase data at the SOA is slightly elevated at mid periods, indicating the presence of a conductor in the region.

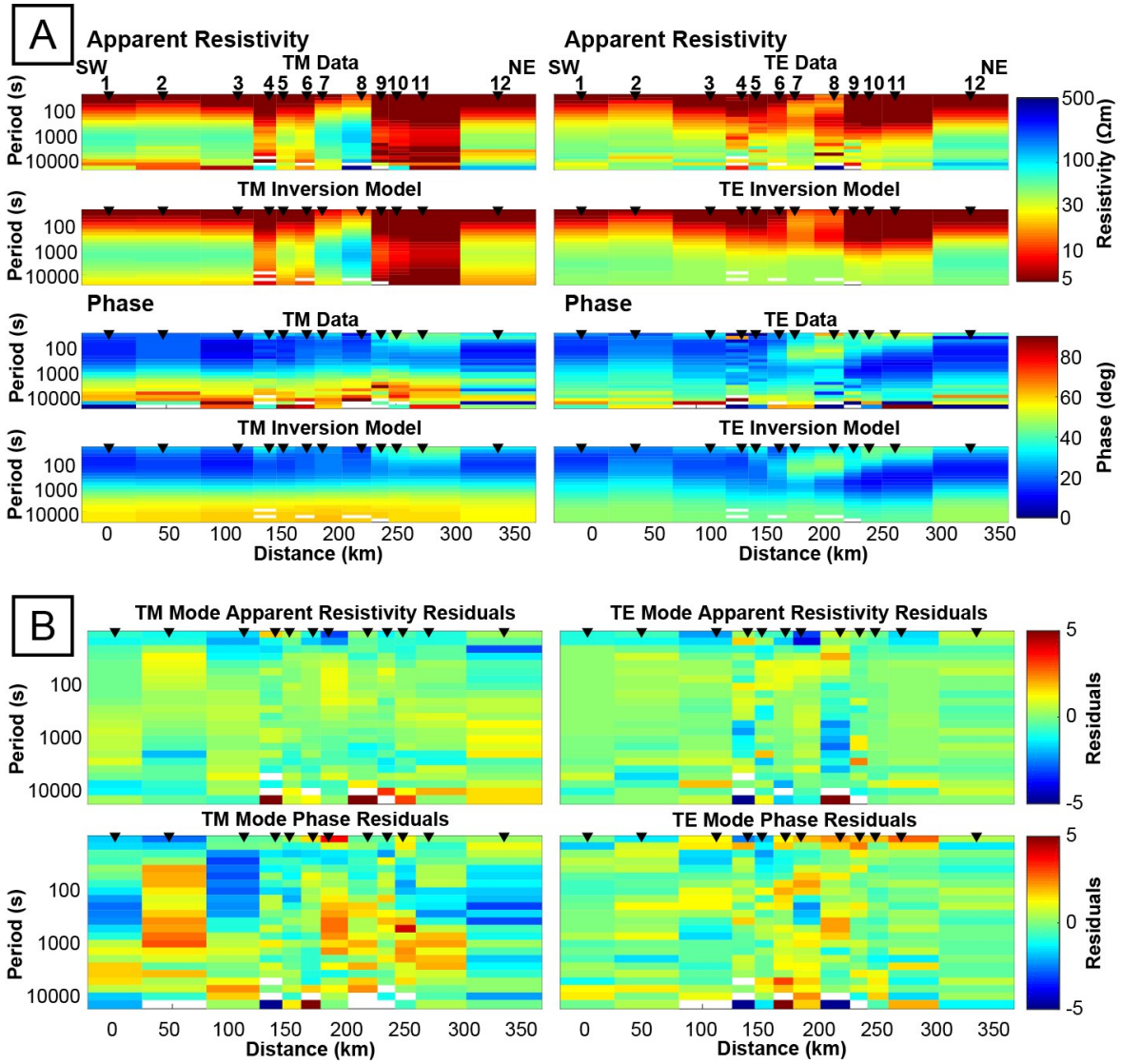

Figure 5.3: *A) Pseudosections comparing the apparent resistivity and phase for the TM and TE modes between the data and the inversion model in Figure 5.4. B) Pseudosections of the error residuals for the apparent resistivity and phase for the TM and TE modes after inversion.*

5.3.3 Inversion of MT data

The data were inverted using the 2-D isotropic non-linear conjugate gradient code of Rodi and Mackie (2001) to produce a 2-D resistivity model. A 3-D modelling approach was not used due to the 2-D survey geometry and because preliminary 3-D inversions showed they were biased to the initial starting model. Error floors of 20% and 5% were applied to the apparent resistivity and phase data, respectively. To account for static shifts in the data, the inversion routine was allowed to invert for them using a 20% error floor. The tipper data was not used in the inversion as the

induction vectors showed sensitivity to either the adjacent basins or features SSE of the study area. Station 8 had large static shifts and was ultimately excluded from the inversion (site with a black x in Fig. 5.1). Given that relatively few MT sites were collected for this study, the model obtained with an inversion that included station 8 is included in the Supplementary Material for completeness (Fig. A.3B). Additional attempts to correct for the static shift at Station 8 before inverting the data involved both manually estimating the static shift and only allowing the inversion algorithm to correct for static shifts at Station 8 (Fig. A.3). Both attempts resulted in increases in RMS misfit (Fig. A.3). Further, manually estimating the static shift for Station 8 is difficult due to the nearest sites being located 20 km away, a distance over which the structure could change considerably given the area is within the SOA. The inversion used a grid with a horizontal cell size of 5 km, which provided a suitable tradeoff between computation time and imaging of interstation resistivity features. In the vertical direction, the first layer had a spacing of 500 m and the thickness of rows increased geometrically downward with a factor of 1.1. The inversion algorithm seeks the smoothest resistivity model that fits the measured MT data within a specific tolerance, and a range of models can be found depending on the degree of smoothing applied. The degree of spatial smoothing can be varied with the trade-off parameter τ. A range of inversions were undertaken using values of τ ranging from 0.01-300. The RMS misfit and roughness results are plotted as an L-curve in Figure A.4, and the smoothing factor was set to 10 based on L-curve search criteria.

An initial inversion started from a model that was a 100 Ωm half-space. The RMS misfit started at 3.75 and the inversion converged to an RMS misfit of 1.49 after 96 iterations. The data fit is illustrated in Figures A.5 and A.6, and shows a good fit to the measured data, but a general overestimation of apparent resistivity values at short periods. The resulting model (Fig. A.7A) shows a low resistivity surface layer that can be identified as the sedimentary basins. However, they extend to unrealistic depths in excess of 10-20 km, which is greater than the known sedimentary basin structure and depths (Perry, 1989). This is due to the smoothing imposed by the 2-D inversion on the resistivity model. This problem can be overcome by using knowledge of basin depth to impose constraints on the inversion. A second inversion allowed the resistivity model to have a discontinuity at the base of the sedimentary basin where the requirement for resistivity model smoothness was not imposed i.e., a tear. Smoothness was imposed on the

remainder of the resistivity model. This starting model incorporated the sedimentary basin as a 4Ωm layer with a 100 Ωm basement layer below. The resistivity of both layers was permitted to vary as the inversion proceeded (Fig. A.7B). The basin depths were taken from seismic, drilling and isopach data from Laske et al. (2013), Perry (1989), Davis and Northcutt (1988), and Brewer et al. (1983). The resulting inversion model is shown in Figure 5.5. It started with an RMS misfit of 3.75 which was reduced to 1.19 after 102 iterations. The fit between the measured MT data and inversion model response is shown in Figures 5.3 and A.8. Comparison of the residual errors in pseudosection format in Figures 5.3B and A.8B shows that allowing the tear gives a better fit particularly in the shorter periods. A reference model was not used in the inversion, and the sensitivity of the model was instead evaluated using the process outlined in section 5.4.

The final model (Fig. 5.4) contains the following resistivity features:

- A 1-10 Ωm conductor extending from the surface to a depth of 3-12 km, corresponding to the Holis-Hardeman and Anadarko sedimentary basins, respectively. This low resistivity is due to the presence of sedimentary rocks and associated pore fluids found in these basins.

- An underlying 200-400 Ωm resistive layer stretching over most of the study area in the depth range 5-100 km. Given the relative insensitivity of MT to high resistivity regions, and possible downward smoothing of overlying conductors, the resistivity values of this layer may be underestimated.

- An interruption of this resistive region below the SOA is observed where resistivity values decrease to 40-60 Ω-m. This feature is referred to as the Southern Oklahoma Aulacogen Conductor (SOAC).

- Below a depth of 100 km, the resistivity again decreases to 20-30 Ω-m over a broad region, which continues through the bottom of the model and is referred to as the Lower Lithosphere Conductor (LLC).

Both conductors (SOAC and LLC) are significant because they have resistivity values much lower than the high values (100-10,000 Ωm) typically observed in basement rocks found within the crust and mantle of stable lithosphere (Selway, 2014).

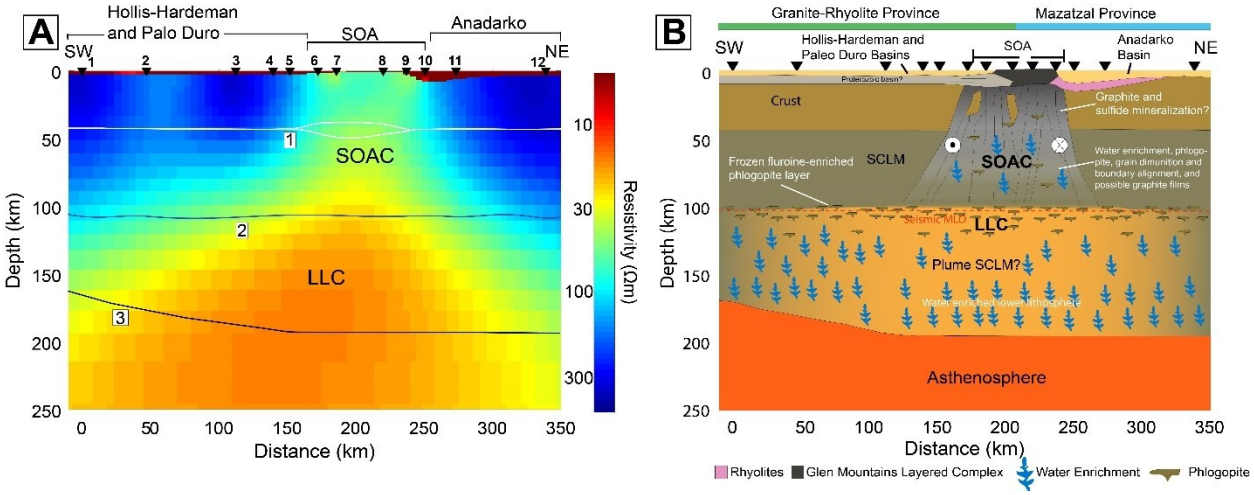

Figure 5.4: *A) Preferred inversion model of the remaining 12 stations. Various drawn lines are as follows. 1) Moho and rift pillow beneath the SOA (Tave, 2013); 2) MLD (Kumar et al., 2012); 3) Lithosphere-Asthenosphere Boundary (Yuan and Romanowicz, 2010). B) Schematic summary cross section of interpretations for the SOA beneath the profile. The analysis leading up to this model will be done in Section 4.4. Blue shapes represent hydrogen enrichment, green-brown shapes represent the frozen melt phlogopite-MLD layer. Seismic MLD from Kumar et al. (2012). Proterozoic basin is from Brewer et al. (1983) and Pratt et al. (1992). Sense of strike-slip movement during ARM deformation is from Chase et al. (2022). Note that the boundary between the Granite-Rhyolite and Mazatzal province is speculative and should not be taken as a definitive marker.*

5.3.4 Sensitivity analysis

To evaluate the sensitivity of the measured MT data to the features present in the preferred model, a variety of tests were performed. This included both synthetic inversions and forward modelling.

A synthetic inversion approach was investigated and is illustrated in the Supplemental material. A model was developed with a low resistivity feature to represent the LLC (Fig. A.9A), SOAC (Fig. A.9B), and the more resistive basement region (Fig. A.9C). Resistivity values were selected so that they matched those observed in Figure 5.4A. The LLC was modelled as a 20 Ω-m main block that extended to a depth of 300 km with a 50 Ω-m layer above. Both features extended flat to the edge of the space. A forward calculation was used to generate synthetic MT data, and noise at 5%

was then added. These data were then inverted using the same approach as for the field data. The synthetic inversion model obtained showed that this layer could be imaged (Fig. A.9A). It also showed that the resistivity of this layer was lowest beneath the center of the profile. The true model had a flat geometry, but the inversion produced a model where the layer deepens at the ends of the profile (Fig. A.9A). The SOAC was represented as a 50 Ω-m block, and the synthetic inversion model shows that this feature can be imaged within the surrounding 100 Ω-m half-space (Fig. A.9B). Finally, the resistive basement was included as a 275 Ω-m halfspace. This value was chosen as a median value of this layer below MT sites located away from the SOAC. Including the resistive feature further centralizes the lowest resistivity values in the LLC beneath the center of the profile (Fig. A.9C). It also has the effect of making the deepening of the LLC on the flanks of the profile more pronounced. A further test evaluated how the model in Figure A.9C varied with the amount of added noise and error floors applied to the inversion. To simulate the measured MT data, 20% and 5% noise were added to the apparent resistivity and phase, respectively. The error floors in the inversion were assigned similar values and the resulting inversion model is shown in Figure A.9D, and here the SOAC anomaly is not recovered by the inversion. This suggests that the 20% noise added to the apparent resistivity is greater than the subtle response of the SOAC anomaly. This suggests that a noise level of 20% was likely an overestimation of the noise level in the measured MT data at period ranges sensitive to the SOAC anomaly. Additional tests not included in this paper showed that the extent of this deepening on either side of the SOA were heavily influenced by the depth extent and geometry of the tear region used to model the Anadarko and Holis-Hardeman basins.

To evaluate if the SOAC and LLC are robust and required by the MT data, the preferred inversion model in Figure 5.4A was modified to remove these resistivity features. This modified model was then used as the starting model for a new inversion. This was done as follows:

- The SOAC was modified by replacing it with a 275 Ω-m resistivity. A forward calculation was performed for this model, and it was found that the editing increased the RMS misfit from 1.19 to 2.426. The inversion was then allowed to run, and it converged to 1.262 after 88 iterations which was close to the original misfit (Figs. A.10; A.12).

- The LLC was modified by replacing it with a 100 Ω-m resistive feature in the depth range from 100-300 km. A forward calculation was performed, and it was found that editing the model increased the RMS misfit from 1.19 to 2.587. The inversion converged to an RMS misfit of 1.440 after 112 iterations (Figs. A.11; A.12).

The significant increase in RMS misfit for both the edited models shows that the SOAC and LLC are well resolved by the measured MT data.

5.4 Resistivity model interpretation

Zones of low resistivity have been frequently reported in regions of stable lithosphere globally (Selway, 2014; 2018; Aulbach, 2018). These anomalies may be due to several factors that include elevated temperature conditions, lithosphere grain boundary alignments alongside grainsize reduction, enrichment of nominally anhydrous minerals (NAMs) in water as OH^- ions dissolved in the mineral lattice, and the presence of fluids, melts, exotic minerals such as sulphides and graphite, or hydrous minerals such as phlogopite and amphibole. It is important to determine the cause of these low resistivity anomalies because they can address important questions about tectonic assembly, lithospheric evolution and survival, and mineral exploration. This section will explore the causes of the low resistivity features observed in Figure A5.4A in relation to the mechanisms listed above. The interpretations will build into the final schematic summary presented in Figure 5.4B.

5.4.1 Temperature, fluid, and melt conditions

The temperature at depth is a key parameter controlling mantle resistivity and can determine if certain conduction mechanisms can occur. A geotherm was constructed using the surface heat flow and temperature estimates from xenoliths. A key challenge in this task is that heat flow represents present day conditions, while xenoliths represent temperature conditions in the past. Garnet xenocrysts from kimberlite pipes with an age of 106 Ma in nearby Arkansas support a relatively cool geotherm, consistent with a heat flow of 35-40 mW/m2 (Griffin et al., 2004; 2011). This region of Arkansas has experienced the same tectonic history as the SOA making the Arkansas

geotherm a useful analog, and available xenocrysts postdate the major heat-producing tectonic episodes. While earlier rifting or orogenesis could have perturbed and increased temperatures, the rifting occurred too far into the past for perturbations to remain today (Kaminski and Jaupart, 2000). Further, the temperature effects of orogenesis would have rapidly re-equilibrated due to the narrowness (~100 km) of the SOA (Guademer et al., 1988). As a result, we use the geotherm consistent with a heat flow of 40 mW/m^2 from Hasterok and Chapman (2011) for modelling. Other geotherm estimates in the region are derived from boreholes drilled into the sedimentary basins and may overestimate the subsurface temperatures as a result of the lower thermal conductivity of the sedimentary units (Blackwell et al., 2007). Figures 5.5A and 5.6A show temperatures that are far below the dry peridotite solidus with this geotherm. Sections 5.2.1 and 5.3.2 below examine the possibility of peridotite being enriched in water content due to tectonism. This enrichment would lower the peridotite solidus curve, potentially resulting in melt generation. However, this melt would have to somehow survive past the post-tectonic thermal re-equilibration previously mentioned and well as remain in the lithosphere far longer than estimated residence times (Mackenzie, 1985). Further, if melt were present, we would expect seismic velocity reductions far greater than those observed beneath the SOA today (Evanzia et al., 2014). Given this, it is unlikely that the anomalies present in the resistivity model (Fig. 5.4) reflect relict high temperatures related to either past tectonic episodes or the presence of partial melt. It is also unlikely that these anomalies reflect the presence of relict aqueous fluids since porosity is very low at these depths and fluids will have migrated out of the system since the cessation of tectonic activity (Selway, 2014, and references therein). Given that neither melt or aqueous fluids phases are unlikely explanation, assessing the viability of additional conductivity phases for explaining the SOAC and LLC will be done independently.

5.4.2 Origin of Southern Oklahoma Aulacogen Conductor (SOAC)

The MATE program of Özaydın and Selway (2020) integrates decades of mantle mineral physics experiments in order to interpret MT data and was used here to determine which conductivity phases could explain the 40-60 ohm-m resistivity of the SOAC anomaly. Given the lack of xenolith constraints for the composition of the SOA SCLM, the generic composition model for Proterozoic aged lithosphere of Griffin et al. (2004; 2011) was used. MATE also requires estimates of

additional parameters such as mineral solubility limits, water partitioning, Al_2O_3 content in orthopyroxene, and mineral conductivity models. Most parameter choices have a minimal impact on conductivity results, and the choices for these parameters and justifications are provided in the Supplementary Materials[1]. The final bulk resistivity value for each model produced by MATE was calculated using the multi-phase Archie's Law of Glover (2010).

5.4.2.1 Water enrichment in nominally anhydrous minerals (NAMs)

The enrichment of nominally anhydrous mantle minerals (NAMs) with water has been proposed as an explanation for low resistivity in the depth range from the mid-crust to the base of the lithosphere (see Selway, 2014, and references therein). Since olivine is the dominant, most interconnected mineral phase in the SCLM it exerts a primary control on the bulk resistivity. As a result, MATE parameters related to its solubility limit and enrichment conductivity model are among the most important to define. Here, the olivine conductivity model of Gardes et al. (2014) was used as it incorporates the errors and uncertainties of previous laboratory studies. The solubility limit of Padrón-Navarta and Hermann (2017) was used as it avoids super solidus temperatures, supercritical fluid phase condition issues, and used a multi-grained natural peridotite.

Figure 5.5A displays the variation of bulk resistivity as a function of water content in NAMs using MATE. It shows that the observed resistivity of 40-60 ohm-m would require a concentration of 3000-10000 ppm of bulk water (i.e., total water content in clinopyroxene, orthopyroxene, garnet, and olivine), or 600-1300 ppm in olivine, decreasing with depth. This far exceeds the saturation limit of NAMs at these depths (Padron-Navarta and Hermann, 2017), which range from 0-100 ppm of bulk water, with 0-30 ppm in olivine (Fig. 5.5B). To explain the resistivity of the SOAC anomaly in terms of water enrichment would require a combination of water in the NAMS in addition to some free fluids. As mentioned above, the significant time since tectonism makes it is unlikely that free fluid phases are still present.

While water enrichment in NAMs is not capable of explaining the entire anomaly of the SOAC it may still partially contribute to it, particularly in lithosphere mantle regions. The viability of water

as a conductivity enhancing mechanism in the context of the tectonic history of the SOA then deserves consideration. Water enrichment occurs when tectonothermal events such as rifting introduce metasomatic fluid fluxes into the lithosphere (Bell and Rossman, 1993; Hoffman, 1997; Martin, 2006). Since water is incompatible during partial melting (Arth, 1976; Salters et al., 2002; Aulbaud et al., 2004), to avoid depletion requires either limited partial melting or enrichment during the final stages of tectonism. At all stages of SOA rifting the genesis of magmatic products appears to have produced limited or no partial melting of the lithosphere (Hanson et al., 2013; Price et al., 2014; Lidiak et al., 2014; Brueseke et al., 2016; Wall et al., 2020), allowing any enrichment to escape subsequent depletion. The abundant A-type felsic and tholeiitic subalkaline mafic units in the SOA argue that the water content of magmas were 2-5 wt % (Clemens et al., 1986; Frost and Lindsay, 1992; Hogan et al., 1995; Dall-Agnol et al., 1999; Klimm et al., 2003; Martin, 2006; Bonin, 2007; Hanson et al., 2013; Brueseke et al., 2016).

While the low resistivity of the SOAC anomaly cannot be explained by water enrichment alone, the chemistry and evolution of the SOA during rifting argues that water content likely contributes to the lower resistivity values.

5.4.2.2 Hydrous minerals

Metasomatic processes in the lithosphere often produce hydrous mineral phases such as phlogopite and amphibole (O' Reilly and Griffin, 2013). These minerals often have lower resistivity values than surrounding mantle peridotite (Selway, 2014; 2018). Both amphibole and phlogopite are often deposited as veins or dikes (Foley, 1992; Foley and Fischer, 2017) which means that they are likely to form well-connected systems in the mantle and can have a large effect on bulk resistivity at small volumes. The conductivity of phlogopite can be further enhanced through enrichment in the primary charge carrier fluorine (Li et al., 2016; 2017). In the SOA, fluorine could have been supplied by the same phases that ultimately produced the fluorine-rich A-type magmatism during rifting (Hogan et al., 1995; Price et al., 1999; Martin, 2006; Bonin, 2007; Hanson et al., 2013).

The effect of phlogopite on resistivity was modeled in MATE and is shown in Figure 5.5C. We modelled both amphibole and phlogopite with cementation factors of m = 1.3, reflecting a well-

connected system. No xenolith data were available to constrain the fluorine content, so a value of 2 wt % was used. No xenolith data were available to constrain the fluorine content, so a value of 2 wt % were used. The upper value is an approximate average value for phlogopite xenoliths collected by Li et al (2016). The results in Figure 5.5C show that phlogopite concentrations in the range 10-50% can explain the bulk resistivity of the SOAC.

Phlogopite is often produced by metasomatic processes associated with alkaline fluids (Grégoire et al., 2002; O'Reilly and Griffin, 2013; Safonov et al., 2019). These fluid species are associated with the genesis of A-type felsic rock (Martin, 2006) common to the SOA (Hanson et al., 2013; Brueseke et al., 2016). Hydrous minerals are also seismically slower than surrounding lithosphere, and so seismic data can be used to confirm their presence. The minimum concentration of phlogopite required by the resistivity is 10% and would produce a corresponding ~4% reduction in seismic shear wave velocities (Rader et al., 2015). The larger amounts of amphibole necessary would produce considerably higher seismic anomalies. At 75 km beneath the SOA a reduction in shear wave velocities on the order of 2-4% has been reported (Evanzia et al., 2014), requiring a 5-10% concentration of phlogopite (Rader et al., 2015). These values are generally below the percentages necessary to produce the observed resistivity of the SOAC (Fig. 5.5C). As a result, while phlogopite is not capable of explaining the observed resistivity values alone, it may contribute to both the resistivity and seismic anomalies, and its presence is possible based on the tectonic history.

Amphibole cannot explain the bulk resistivity of the SOAC, even if the rock was composed of pure amphibole (Fig. 5.5C). However, it has been proposed that amphibole is also a main carrier of fluorine in the mantle (Smith, 1981; Aiuppa et al., 2009). This could enhance the conductivity of amphibole by a similar mechanism to that which occurs in phlogopite (Li et al., 2017). Evidence from xenolith data shows that amphibole occurrences are widespread at pressures < 3 GPa (~100 km) (Selway et al., 2015 and references therein) making it a viable conduction mechanism in the upper lithospheric mantle. However, the mineral physics experiments critical in evaluating the fluorine and amphibole conductivity relationship have not yet been performed. This data is needed in order to accurately evaluate the role of amphibole in producing low resistivity anomalies in the mantle.

5.4.2.3 Graphite

Graphite films are stable in the lithosphere and are often invoked to explain low resistivity features. Experiments show that if the films are thick enough, they will be interconnected up to a temperature of 1000 °C (~130 km beneath the SOA) (Yoshino and Noritake, 2011; Zhang and Yoshino, 2017). However, xenoliths have only shown graphite film stability to ~600-900 °C (~65-115 km) (Mathez et al., 1984; Mathez, 1987; Pineau and Mathez, 1990). Additionally, even at lower temperatures graphite film stability may be transient feature, becoming disconnected over just a few tens of thousands of years (Yoshino and Noritake, 2011). With this background, the MATE software was used to investigate if the bulk conductivity of the SOAC could be explained by graphite films. The results show that with a cementation factor of m = 2, graphite concentrations of 300-500 ppm can produce the observed resistivity of the SOAC (Fig. 5.5D). The amount of graphite required is highly sensitive to the cementation factor. For example, producing SOAC resistivity values can require as much as 1750 ppm when m = 2.5 or as little as 35 ppm if m = 1.5 (Fig. 5.5D).

What would be the source of the carbon? The enriched OIB source for SOA rift magmatism can have carbon concentration for 50-500 ppm (Dasgupta and Hirschmann, 2010), meeting the ~100 ppm concentrations necessary for lowering mantle resistivity (Duba and Shankland, 1982). The reducing conditions responsible for SOA tholeiitic magmatism also promote graphite stability (Frost and Lindsay, 1992; Stagno and Frost, 2010). Graphite formation and deposition could have been accomplished by a reduction of a CO_2 fluid phase common for rift zones (Brune et al., 2017; Foley and Fisher, 2017) and in the genesis of A-type granitic magmas (Martin 2006). However, the nephelinitic and carbonatitic volcanic units associated with this phase (Martin, 2006) have not been reported in the SOA. Further, chemical reduction of CO_2 appears incapable of wetting silicate grain boundaries, producing graphite that would be isolated and poorly conducting (Watson and Brenan, 1987; Yoshino and Noritake, 2011; Zhang and Yoshino, 2017). Oxidation of CH_4-rich fluid species could also result in the formation of graphite films (Stachel and Luth, 2015), but the SOA magmatic units leave the role of this fluid species unclear and argue for reducing conditions. As a result, the viability and stability of graphite films produced by fluids in a rifting environment

appears unlikely for the part of the SOAC located in the SCLM. Previous authors have argued this conduction mechanism system could be stable in the crust (e.g., Murphy et al., 2022), but few laboratory observations have been made for this type of system.

Another factor relevant to the discussion of graphite is the secondary deformation and shearing that occurred during the later-stage ARM (Granath, 1989; Chase et al., 2022). This could have potentially mobilized, smeared, and interconnected previously deposited and isolated graphite (Glover and Adam, 2008; Puelles et al., 2014). This is similar to interpretations of graphite-related low-resistivity anomalies in both orogenic and shear zones systems (e.g., Jones et al., 2005; DeLucia et al., 2019). The caveat to this interpretation is that grain boundary films could still become disconnected over time, as observed in typical mantle olivine aggregates (e.g., Zhang and Yoshino, 2017). However, if interconnection was accomplished along zones of structure weakness like those created during rifting, these can be longstanding features that are resistant to healing (Bercovici and Ricard, 2012), which may provide for long-term graphite film stability.

Despite the difficulty to initially establish grain boundary graphite films, the tectonic and magmatic history of the SOA appears favorable for both introducing graphite and establishing interconnection sufficient to produce the resistivity values observed in the SOAC. However, the volcanic history of the SOA does not suggest the prominence of carbon-bearing fluids or the conditions necessary to form graphite. Additionally, the long-term stability of these films appears tenuous (Yoshino and Noritake, 2011). Given that it is a prominent phase to explain low resistivity anomalies elsewhere we do not rule it out, but suggest it is unlikely to explain the SOAC.

5.4.2.4 Sulfide minerals

Sulfides minerals are another viable candidate to explain low resistivity and are stable throughout the mantle lithosphere (Selway, 2018). Sulfides have conductivity values similar to graphite (Saxena et al., 2021), and resistivity calculations give results similar to those for graphite. Prior studies have suggested that large igneous provinces such as the SOA can host significant amounts of sulfide minerals (Jones et al., 2015), and layered complexes such as the Glen Mountain Layered Complex of the SOA can host large quantities of sulfides phases (Godel et al., 2006; Zientek,

2012). However, occurrences of sulfides in drill core from the SOA are few, and largely limited to the diabase dikes (Ham et al., 1964; Hanson et al., 2013; Puckett et al., 2014; Lidiak et al., 2014; Brueseke et al., 2016). The sulfide concentrations necessary to significantly reduce resistivity are high, >6 vol.%, (Saxena et al., 2021), and at these concentrations we would expect to see the presence of sulfides noted far more often in geologic studies of SOA rock units. Given these constraints, it is unlikely the low resistivity of the entire SOAC can be explained by the presence of sulfides minerals. However, if present, sulfides may be a plausible mechanism in the shallow to mid crust, particularly along volcanic conduits.

It should be noted that this study uses long-period MT data, which has generally poor sensitivity to the upper crust. As a result, resistivity values in the upper crustal portion of the SOAC are likely to be poorly constrained.

5.4.2.5 Grain size reduction

The conductivity of olivine in the upper mantle can be enhanced by a reduction of average grain size and the alignment of grain boundaries, which provide better pathways and more surface area per unit volume for conduction (ten Grotenhuis et al., 2004; Pommier et al., 2018). With increasing shear strain from 1.3-7.3 and temperatures from 800-1200 °C, resistivity values of olivine can range from 1000-10 Ωm (Pommier et al., 2018).

Given the pronounced vertical uplift, crustal shortening and strike-slip deformation that occurred along the SOA during the ARM, a corresponding reduction in the olivine grain size is plausible. However, post-tectonic annealing would have increased the grain size and lowered the conductivity over time (Pommier et al., 2018). However, in a polycrystalline lithosphere assemblage, this process is suggested to have a timescale of hundreds of millions of years (Bercovici and Ricard, 2012). Deformation in the SOA occurred ~300 million years ago, which supports the idea that deformation effects could persist to the present day.

Strain related to the ARM is estimated to be approximately 3.6 from the analysis of sedimentary basins located near the SOA (Craddock et al., 1993). If these estimates are also representative of

the conditions experienced by the SOA lithosphere, this could produce resistivity anomalies in the range 900 - 1100 Ωm in the SOAC SCLM (Pommier et al., 2018). These resistivity values are far higher than those observed in the SOAC. As a result, while grain size reduction and boundary alignment cannot explain the SOAC alone, based on the tectonic history it could still contribute to the observed resistivity anomaly.

5.4.2.6 Summary of SOAC conductivity mechanisms

Given the tectonic and magmatic history of the SOA it is proposed that the low resistivity of the SOAC is due to a combination of mechanisms that includes the presence of hydrous minerals such as phlogopite, (2) elevated water content in NAMs, and (3) a reduction of olivine grain size. Graphite and sulfide films are also capable of explaining the low resistivity of the anomaly, but are unlikely candidates given the reasons above.

However, in the crust at depths less than 30 km, many of the mechanisms listed above will have minimal impact on resistivity values with the exception of graphite and sulfides. While we discount these conductive phases due to their paucity in regional geologic data, we acknowledge that the low resistivity of the crustal portion of the SOAC is likely to be better explained by them. Additional study of the shallow subsurface in the SOA would be useful in evaluating these mechanisms.

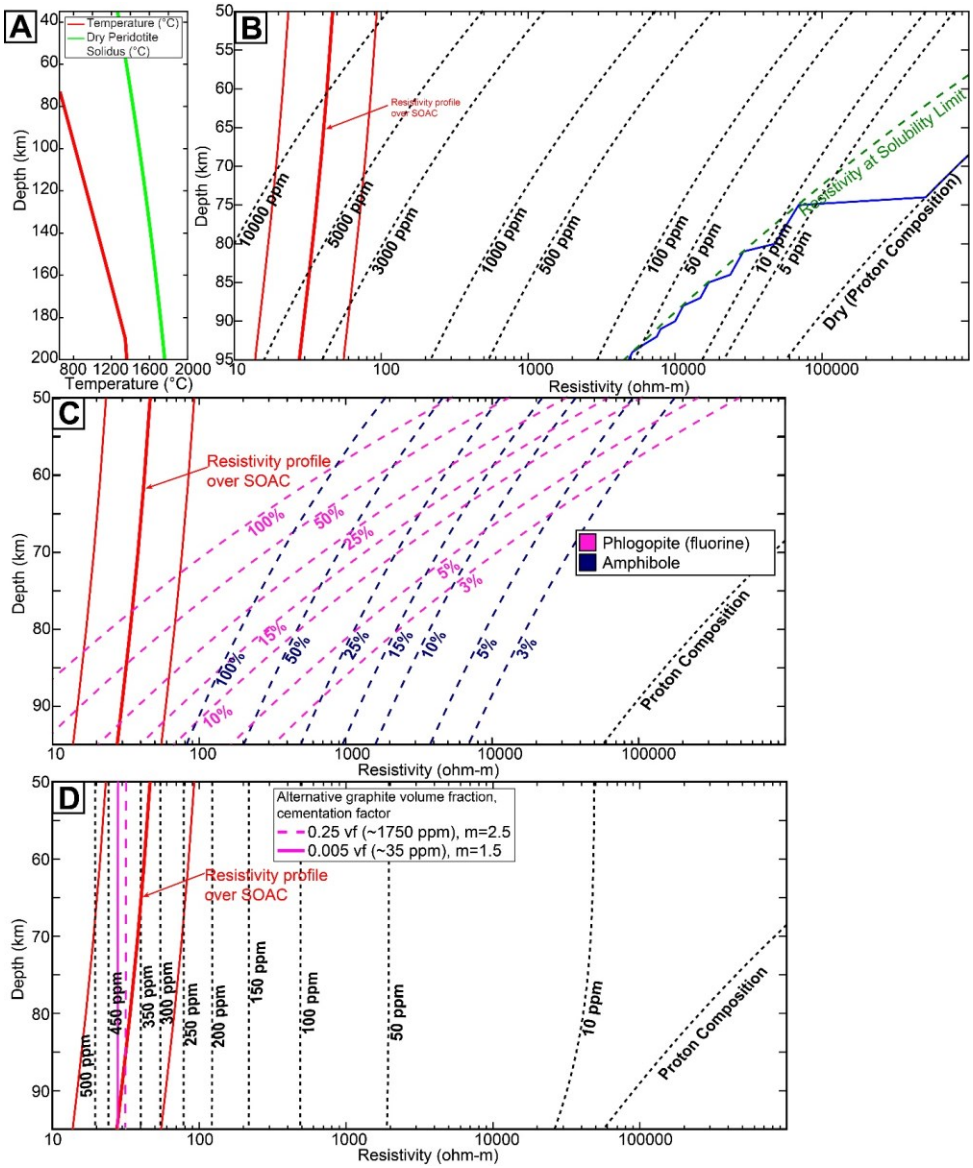

Figure 5.5: *A) Red line, 40 mW/m2 geotherm from Hasterok and Chapman (2011) used for the region; green line, Dry Peridotite Solidus from Hirschmann et al. (2009). Note that the temperature does not cross the solidus, suggesting melt is not found in the region. B-D, results of MATE analysis for the SOAC. The thick red line in each image is the resistivity profile central to the SOAC station. The outer thinner red lines are the resistivity values within the error range of the data. B) Analysis of resistivity as a function of different ppm bulk water content in peridotite (black dashed lines). The green line is resistivity at the solubility limit for peridotite from Padrón-Navarta and Hermann (2017). Note that black lines left of the green line are over the storage capacities of the minerals. C) Resistivity as a function of different percentages of the matrix being made up of amphibole (blue) or phlogopite with 2 wt % fluorine (pink). D) Resistivity as a function of moderately well connected (m=2) ppm graphite in the matrix (black dashed lines). The pink lines are calculations of resistivity as a function of graphite content with different cementation factors and ppm.*

5.4.3 Origin of lower lithosphere conductor (LLC)

The LLC begins at a depth of around 100 km as a 20-30 Ω-m horizontal layer that extends laterally and downward over the profile. At 100 km depth temperatures exceed 800 °C (Fig. 5.6A) and pressures are greater than 3 GPa. Under these mantle conditions graphite films cannot explain the low resistivity of the LLC anomaly due to film instability over geologic timescales (Yoshino and Noritake, 2011; Yoshino and Zhang, 2017). Similarly, sulfides cannot explain the LLC anomaly as they are unlikely to be present over such a large area (Selway, 2018). The remaining phases viable to explain the low resistivity of the LLC are either hydrous mineral phases such as phlogopite (Li et al., 2016; Li et al., 2017), or enrichment of NAMs in water. The viability of each of these mechanisms is examined below.

5.4.3.1 Hydrous mineral phases

Due to its stability in the lower lithosphere, phlogopite is the hydrous mineral most likely responsible for the low resistivity of the LLC (Frost, 2006; Safonov et al., 2019). Extending the modelling of phlogopite from section 5.2.2 shows that a phlogopite concentration in the range 1-15 %, and which decreases with depth, could produce the resistivity values observed (Fig. 5.6B). These would produce a corresponding reduction in seismic velocity in the range from 0.5-7% (Rader et al., 2015). Coincident with the start of the LLC at 100 km, a mid-lithosphere discontinuity (MLD) is observed in receiver function data as a 5-7% reduction in shear wave velocities (Kumar et al., 2012). More regionally, seismic tomography data show a 2-4% reduction in shear wave velocities in the lower lithosphere beneath the SOA (Evanzia et al., 2014).

Explanations for MLDs at this depth suggest they may form as a result of metasomatic fluids/melts becoming frozen and crystallizing phlogopite upon encountering an increase in the solidus of peridotite found at depths less than 80-100 km, perhaps reflecting a paleo LAB (Rader et al., 2015; Hansen et al., 2015; Selway, 2018). Notably, phlogopite rich xenoliths are also often extracted from this depth (Aulbach, 2018; and references therein). The MATE software was used to model an MLD as a 10 km thick layer from 100-110 km with 10% phlogopite, in line with MLD thickness estimates by Rychert et al. (2010), and to match the observed seismic velocity reductions (Rader

et al., 2015). As with the SOAC, a fluorine concentration of 2 wt % fluorine was used for the phlogopite. The results show that resistivity values at the top of the LLC can be fit by this layer (Fig. 5.6B). The difference in resistivity between MT stations can be explained by varying the fluorine concentration from 0.5-2 wt %, which spans the range of values observed in the bulk of xenolith samples compiled by Li et al. (2016) (Fig. 5.6B).

Amphibole, as pargasite, stability extends up to a pressure of ~3 GPa, which corresponds to a depth of 100 km, and is coincident with the top of the LLC and MLD. This led Selway et al. (2015) to suggest that MLDs may be explained by significant amounts of amphibole that could have formed along a crystallization front at the maximum pressure stability. The authors show that 11-25% amphibole could produce a velocity reduction > 5%, similar to what is observed beneath the SOA (Figure. 11 in Selway et al., 2015). The modelling performed in Figure 5.5C shows that these percentages of amphibole cannot explain the resistivity values observed in the LLC. In fertile peridotite, paragasite stability can extend up to a pressure of 3.5 GPa (~115 km) (Mandler and Grove, 2016). The amphibole concentration of 11-25% in Figure 5.5C at a depth of 115 km would still produce resistivity values far higher than the LLC. As with the explanation for the resistivity of the SOAC, it is possible that fluorine will enhance the conductivity of amphibole. However, the mineral physics experiments to support this hypothesis have not yet been performed.

Below the MLD we note that the resistivity values of the LLC show limited variation. This could indicate a loss of data sensitivity due to depth and the combined effects of the overlying low resistivity layers (i.e., MLD layer and the sedimentary basins). To test this, we created a forward model that modifies the resistivity structure in Figure 5.4A with an MLD and a 100 ohm-m halfspace below it. The resulting inversion recovers the lower halfspace (Fig. A.13) showing the data is sensitive to the lithosphere below the MLD. As a result, the low resistivity values in this region could reflect the presence of widely disseminated phlogopite. To match the 2-4% shear wave velocity reductions (Evanzia et al., 2014) would require 4-8% phlogopite throughout the lithosphere. However, below 120 km this amount of phlogopite would produce resistivity values lower than observed (Fig. 5.6B), making phlogopite a less viable explanation.

The top of the LLC that corresponds to an observed seismic MLD is well explained by a ~10 km thick phlogopite layer that is potentially enriched in plume-derived fluorine acting as the primary charge carrier (Li et al., 2016; 2017). Amphibole offers a possible alternative interpretation (i.e. Selway et al., 2015), however, the mineral physics experiments needed to evaluate this have not yet been performed. Below 110 km phlogopite becomes a less likely explanation for the low resistivity, as the amount necessary to match observed seismic anomalies would produce resistivity values lower than observed.

5.4.3.2 Hydrogen in nominally anhydrous minerals (NAMs)

The remaining most viable conductivity mechanism for the LLC is from the enrichment of NAMs in water. Extending the modelling in Section 5.2.2. it can be shown that a concentration of hydrogen in the range 500 to 3000 ppm bulk hydrogen, 280-1000 ppm in olivine, could produce the resistivity values observed in the LLC (Fig. 5.6C). In the depth range 100 – 150 km the amount of water required is above the solubility limit of the minerals. However, below 150 km the solubility limit is large enough that water can produce the resistivity values with 300-1000 ppm bulk water, or 200-450 ppm in olivine, being sufficient (Fig. 5.6C).

As with the SOAC, metasomatic enrichment of the lithosphere in water likely occurred during rifting while also escaping late-stage partial melt depletion. Additionally, this type of lithosphere keel enrichment would be in line with similar SCLM keel enrichment observed in other plume impacted regions (e.g., Foley, 2008; Bedrosian, 2016; Aulbach et al., 2017; Foley and Fischer, 2017; Özaydın and Selway, 2022). Further, the compositional changes associated with keel enrichment can produce the small reductions in shear wave velocity observed in the region (Deen et al., 2006; Griffin et al., 2009; Evanzia et al., 2014). As a result, we find that hydrogen enrichment is a good candidate to explain LLC resistivity values in the lowermost lithosphere.

5.4.3.3 Summary of LLC conductivity mechanisms

Knowledge of the tectonic and magmatic history of the SOA, combined with constraints from regional seismic data, suggest that the low resistivity of the LLC is due to a combination of

conduction mechanisms. The first is the presence of a phlogopite layer from in the depth range 100 – 110 km that is possibly enriched in fluorine and which is coincident with a seismic MLD (Kumar et al., 2012). At greater depths, it is more difficult to explain the low resistivity with phlogopite. Conduction due to water enrichment of NAMs is the preferred explanation.

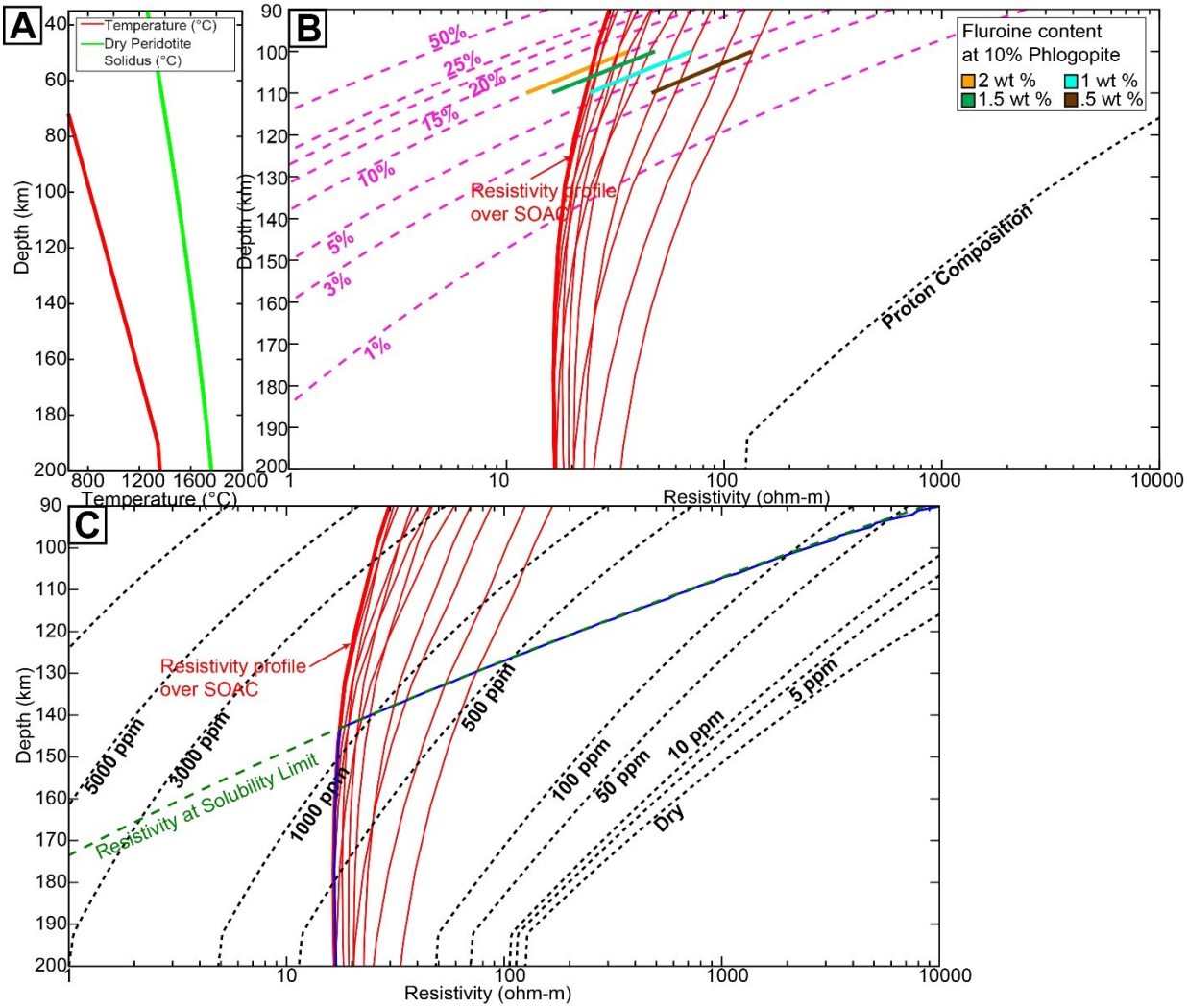

Figure 5.6: *A) The same geotherm from Fig. 5.5A. B-C, results of MATE analysis for the LLC and the lines are structured the same as Figure 5.5. B) Resistivity as a function of different percentages of the matrix being made up of phlogopite with 2 wt % fluorine. The various color-coded lines are the resistivity profiles for a fluorine enriched phlogopite-MLD with different wt % of fluorine. The yellow box denotes the combined minimum-maximum resistivity values that are 1 standard deviation from these main profiles. C) Resistivity as a function of different ppm bulk water content. The blue line is the resistivity profile that can be made though only water incorporation in peridotite while respecting the solubility limit. It shows that for a site central to the SOA water incorporation can explain the resistivity anomaly at depths >150 km.*

5.5 Implications

The MT data provide a new geophysical image of the lithosphere beneath the SOA. A summary of the interpretations for the resistivity anomalies can be found in Figure 5.4B. The newly imaged structure allows new insights in the tectonic history of the SOA and wider Midcontinent, which are discussed below.

5.5.1 The SOAC and involvement in the ARM

The ARM orogeny remains an enigmatic tectonic episode in the geological history of North Laurentia. The associated basement uplifts are discrete, widely separated, spread across a wide region of Laurentia, and are often far removed from the various plate boundaries invoked in tectonic models to explain the ARM (see Leary et al., 2017). Conversely, basement deformation and regional metamorphism along the suggested plate boundaries themselves is limited or nonexistent, suggesting weak collisional forces along the boundaries (Keller et al., 1989; Keller and Stephenson, 2007). This suggests that beneath the uplifts the lithosphere was uniquely relatively weak and prone to deformation.

What could have caused localized zones of weakness in the continental lithosphere? The strength of the continental lithosphere is thought to decrease with increasing lithosphere enrichment introducing hydrous (i.e., water) or Ti (as titanoclinohumite) point defects in Si vacancies of olivine (Peslier et al., 2010; O'Reilly and Griffin, 2013; Fei et al., 2013; Faul et al., 2016). Ti and water enrichment accompany each other, and both follow the enrichment state of the mantle, and Ti values are often high in rock impacted by plumes (Berry 2005; 2007; Rehgeldt et al., 2008; De Hoog et al., 2010; Padrón-Navarta and Hermann, 2017). Given the sensitivity of MT data to water content (e.g., Özaydın and Selway, 2022) resistivity anomalies can be used as a proxy for determining the location of associated rheological weakening.

The resistivity structure beneath the SOAC has been interpreted to reflect metasomatic enrichment of water during Cambrian rifting. As a result, the Cambrian metasomatism could have rheologically weakened the lithosphere, making the area susceptible to reactivation during the

ARM. Previous research has suggested that the ARM uplifts were localized along preexisting weaknesses (e.g., Kluth and Coney, 1981; Leary et al., 2017), particularly along paleo-rifts (Marshak et al., 2003). While the xenolith data necessary to confirm this interpretation is absent, it provides a possible mechanism for SOA participation in the ARM orogeny. Further study beneath other ARM uplifts unmodified by later tectonism (e.g., the Diablo Uplift and Central Basin Platform) will be useful to investigate the regional extent of this mechanism.

5.5.2 The LLC and SOA Lithosphere

5.5.2.1 Plume head accretion

The LLC resistivity anomaly suggests that the lower lithosphere was metasomatically enriched below 100 km during rifting. This type of keel enrichment has been observed elsewhere and is thought to be prevalent in regions impacted by plumes (Foley, 2008; O'Reilly and Griffin, 2013; Aulbach et al., 2017; Liu et al., 2018) and is often observed in MT data (e.g., Bedrosian, 2016; Özaydın et al., 2022; Bettac et al., 2023). Additionally, in nearby Arkansas to the east the region has experienced the same tectonic events as the SOA, and here the lithosphere shows strong metasomatic enrichment, with a major component related to SOA rifting (Griffin et al., 2004; 2011). However, the depths at which melts were generated to produce the olivine and quartz tholeiitic magmatic units in the SOA required a lithosphere no thicker than ~60-80 km during rifting (Green and Ringwood, 1967). The lithosphere today is 180-200 km thick (Priestly et al., 2016), implying that it has re-thickened since the Cambrian. Thickening by lithosphere stacking or orogenic compression (Lee et al., 2011) during the ARM orogeny (Lee et al., 2011) do not seem possible due to subduction polarity dipping to the southeast and the weak collisional forces likely limited the amount of lithosphere deformation (Kluth and Coney, 1981; Keller and Stephenson, 2007). Further, progressive cooling since rifting cannot rethicken the lithosphere to these depths (Dion et al., 1997).

The most viable remaining mechanism for lithosphere rethickening would be accretion of the plume head to the lower lithosphere. In this model, the plume may have been localized beneath the SOA due to the presence of (1) the thin lithosphere beneath the SOA and (2) a depleted

lithosphere to the east beneath Arkansas related to the Archean Sabine microcontinent (Griffin et al., 2004; 2011). This depleted layer may have shielded the Arkansas lithosphere from extensive modification, similar to plume and rift interactions occurring today beneath the Tanzanian craton (Nyblade and Brazier, 2002; Adams et al., 2018). The plume head may have been channeled into the region of thin lithosphere beneath the SOA, similar to the model proposed by Liu et al. (2021) for the rethickening of lithosphere beneath the Slave craton. However, this type of accretion typically produces depleted and dehydrated mantle residua (Lee et al., 2011; Pearson and Wittig, 2014), which would be electrically resistive. This appears to be the case beneath the plume-drive Midcontinent Rift (MCR) further north where the lithosphere is highly resistive (Bedrosian, 2016). The difference in resistivity structure may reflect the following: (1) the short duration of SOA magmatism (~10 My) vs the MCR (~30 My) resulting in less depletion of the plume source (Miller and Nicholson, 2013; Wall et al., 2021); (2) and the SOA plume sources being up to an order of magnitude more enriched than the MCR (Shirey et al., 1992; Lidiak et al., 2014; Brueseke et al., 2016), and by extension containing more water. As a result, the difference in the resistivity structure could reflect the accretion of more enriched, less dehydrated plume residual material beneath the SOA compared to the MCR. A more enriched plume composition alongside seismically slow hydrous mineral phases could also explain the 2-4% seismic velocity reduction beneath the SOA (Deen et al., 2006; Rader et al., 2015).

5.5.2.2 A shallow asthenosphere

An alterative model to plume accretion is that the regional lithosphere has remained thin (<150 km) since rifting and that the LLC represents an asthenosphere that has shallowed to a depth of 80-100 km beneath the SOA. To explain the low resistivity of the LLC observed in this study would require a damp asthenosphere containing up to a few hundred ppm of water (Naif, 2018). Modelling of seismic data led Evanzia et al. (2014) to suggest that the slow anomaly beneath the SOA may represent a conduit of asthenosphere flow from the Rio Grande Rift under the North American craton. In this scenario, the LLC would represent the electrical resistivity expression of this conduit, with the elevated water content causing the asthenosphere to be weakened and permit mantle flow (Hirth and Kohlstedt, 1996). However, seismic studies of LAB depth have shown that the lithosphere extends to a depth of 180-200 km in this region (Yuan and Romanowicz, 2010;

Priestly et al., 2018). It is possible that resolving the shallowing of the asthenosphere near the SOA in these seismic studies is difficult due a combination of the narrow width of the SOA and wide seismic station spacing (Evanzia et al., 2014). However, the top of the LLC is at a shallower depth than the seismic LAB estimates over the entire model space and the LLC has a lateral extent greater than the resolution scale of the seismic data (Fig. 5.4A). Additionally, the forward modelling results in this study suggest that the shallowing of the LLC beneath the SOA could be an artifact of the inversion process (Fig. A.8). On this basis, the plume accretion model is the preferred mechanism to explain the low resistivity of the LLC.

5.5.3 Mid-lithosphere discontinuities

The MLD beneath the SOA appears to be spatially associated with the LLC low resistivity feature. However this type of association is not always the case for MLDs (Selway, 2018). Beneath the Great Plains further north, a MLD is located at a similar depth but is not coincident with a conductor (Kumar et al., 2012). Variations in seismic radial anisotropy (Wirth and Long, 2014) or in the content of hydrous minerals like phlogopite (Hansen et al., 2015) have been invoked to explain the seismic anomaly associated with an MLD. Seismic anisotropy is not expected to produce substantial resistivity variations (Marti, 2014), whereas an increase in phlogopite concentration can increase conductivity. Unlike the SOA the seismic MLDs beneath the Great Plain lack a coincident conductor (Yang et al., 2015; Bedrosian, 2016). If phlogopite is an acceptable explanation for MLDs (e.g., Hansen et al., 2015) the variation in electrical responses could reflect variations in fluorine content, which is moderately incompatible in the lithosphere and is expected to be extracted and depleted during lithosphere stabilization (Rader et al., 2015; Joachim et al., 2017). In this model the MLDs of the Great Plains could reflect a fluorine depleted layer. In contrast, the SOA MLD may be re-enriched in fluorine by the fluids that ultimately produced the significant amount of fluorine-rich A-type felsic magmatism during rifting (Hogan et al., 1995; Martin, 2006; Bonin, 2007; Hanson et al., 2013; Price, 2014). Interestingly, near the plume driven MCR the MLDs of the Great Plains still lack coincident conductors. Notably, the MCR was mafic-dominated and contains little magmatism of the felsic fluorine-rich A-type affinity prevalent in the SOA (Green and Fitz, 1997; Vervoot et al., 2007; and references therein). This may reflect differences in the chemistry or evolution of the plume sources between the SOA

and MCR. Here, the MCR plume may have been depleted in fluorine content, or the tectonic evolution during rifting precluded introduction of fluorine into the lithosphere in the manner found in the SOA. The depletion hypothesis would be consistent with previous interpretations of a depleted lithosphere beneath the MCR (Bedrosian, 2016).

Prior work by Selway (2018) noted the variability in the resistivity signatures of MLDs. In regions of suspected phlogopite-related MLDs, enrichment in fluorine offers a potential explanation for these variations. It would also support the view of Li et al. (2016; 2017) that fluorine content is the critical parameter controlling phlogopite resistivity.

In the plume accretion model, the MLD could represent a layer of phlogopite-bearing metasomatic melts derived from the plume that froze to the base of the thinner lithosphere during rifting. This layer was then entombed during accretion of the plume head. This would be in line with suggestions that MLD represent paleo LABs (Rader et al., 2015; Hansen et al., 2015; Selway, 2018). We note that this model would be equally applicable to an amphibole layer (e.g., Selway et al., 2015) although mineral physics experiments required to show amphibole conductivity is enhanced by fluorine content have not been performed.

5.6 Conclusions

The south-central US provides valuable insights into the assembly and tectonic evolution of Laurentia. The area contains a variety of largely unmodified tectonic structures that are related to the breakup of Rodinia and assembly of Pangea. This study investigated one of these, the SOA, a Cambrian plume-driven failed-rift that was structurally inverted during the Paleozoic-Pennsylvanian ARM orogeny. Long-period MT data were used to produce a 2D resistivity model that was sensitive to the entire lithosphere. Two major low resistivity features are noted. The first is the SOAC, which is located in the crust and upper mantle lithosphere. The second is the LLC, which starts at a depth of 100 km and extends into the lower mantle lithosphere. The low resistivity of the SOAC is attributed to a combination of enrichment of NAMs with water and the formation of hydrous mineral phases like phlogopite via plume-lithosphere interactions during rifting metasomatism. Additional contributions to the low resistivity likely occurred during the ARM

orogeny where deformation led to olivine diminution and grain boundary alignment. This deformation may have also interconnected graphite possibly precipitated by early rift fluids, however, based on mineral physics experiments and the magmatic evolution of the SOA, the stability and presence of graphite appears tenuous. The upper part of the LLC at a depth of ~100 km is attributed to a fluorine-enriched phlogopite layer, which is coincident with an MLD imaged by seismic data. Below this region the remainder of the low resistivity of the LLC is attributed to a lower lithosphere of water enriched NAMs.

The rifting metasomatism would have likely resulted in the introduction of both water and Ti into the mantle peridotites of the SOAC. These phases would have rheologically weakened the lithosphere beneath the SOA, which permitted it to localize deformation during the ARM orogeny. This metasomatic rheological weakening model provides a possible mechanism for explaining how ARM deformation occurred only along discrete and spread-out features in the Laurentian intraplate that were far from the causative tectonic boundary forces. Evaluation of this mechanism via numerical modelling and additional geophysical sampling of the other tectonically unmodified ARM uplifts in the southern US would be useful.

The fluorine enrichment of the phlogopite MLD beneath the SOA provides a possible mechanism for explaining the variability in the electrical responses of phlogopite-derived MLDs. The enriched lower mantle lithosphere in the region represents a lithosphere that has been rethickened since rifting during the Cambrian. This would have been most readily accomplished via accretion of the plume head to the lithosphere upon rifting failure. Due to the enriched nature of the plume source and the short duration of SOA rifting, the accreted material could have remained more enriched, and therefore more electrically conductive, than typical plume accretion residua. In this model, the phlogopite MLD may reflect a melt layer deposited along a paleo lithosphere-asthenosphere boundary that was entombed during plume accretion.

The role of sulfides and graphite in lowering resistivity and explaining the crustal extension of the SOAC does not appear favorable due to the paucity of these phases in the rock record in addition stability issues with graphite films over geologic time. However, the other lithosphere conductivity

mechanisms have limited impact on resistivity values in the crust. Further evaluation is needed to explain the shallower resistivity values of the SOA.

Acknowledgments

We thank the variety of Oklahoma landowners who so graciously allowed us to place instruments on their lands. Micah Mayle, Curtis Carter, David Beckendorff, Dr. Folarin Kolawole, and Steven Johnson are thanked for their assistance in the field. We thank Sinan Özaydın for his assistance with answering technical questions regarding the MATE program. We thank Dr. Takashi Yoshino and, Dr. Richard Hanson, and Dr. William Griffin for answering questions regarding on graphite in the mantle, and in SOA geology/geochemistry, and Arkansas lithosphere, respectively. Conversations with Dr. Thomas Stachel and Dr. Graham Pearson helped to develop ideas in this paper regarding interpretation.

Data Availability Statement

The magnetotelluric dataset used in this study is available from the University of Alberta Education and Research Archive at https://era.library.ualberta.ca/items/3b884b44-882f-48c8-aaa0-4ad64c69a9a7. The MATE software can be accessed through https://github.com/sinanozaydin/MATE.

CHAPTER 6. MAGNETOTELLURIC EVIDENCE FOR THE FORMATION OF THE LAYERED SASK CRATON BY FLAT SLAB SUBDUCTION

B.F.W. Chase and M.J. Unsworth (2024)
Earth and Planetary Research Letters, Volume 647, 119027
https://doi.org/10.1016/j.epsl.2024.119027

Abstract

Long-period magnetotelluric (MT) data were collected at 56 locations over the Sask craton in 2021 and 2022. The data were combined with existing broadband data and inverted to produce a 3-D resistivity model of the Sask craton and Trans-Hudson Orogen (THO). The model reveals a number of northeast striking electrically conductive crustal structures that extend into the mantle lithosphere. In the mantle lithosphere, these conductors coalesce into a single large low resistivity anomaly in the depth range 70-85 km termed the Northern Sask craton (NSC) conductor. The resistivity of the NSC conductor is attributed to sulfides deposited along an interface between a flat slab that was accreted to the base of the pre-THO Sask craton lithosphere during closure of the Manikewan Ocean. Kimberlites have erupted along the margin of the NSC conductor. The boundary of the conductor likely represents deep-seated faults and mantle terrane boundaries formed during flat slab subduction that allowed the ascent of kimberlite melts. The resistivity of the northeast-trending conductors can be interpreted as due to graphite and sulfides precipitated by past fluid or melt flow during ocean closure and orogensis. A number of these conductors are located beneath known mineral districts and trends and may represent source pathways for regional base and precious metal deposits. Other conductors may represent possible, previously unknown, regions hosting mineralization. Many of these conductors are associated with major regional faults and shear zones, which may be deep-seated features that helped to guide both kimberlites and mineralizing fluids. Of the prominent northeast-trending conductors west of the Sask craton, one corresponds to the previously reported North American Central Plains (NACP) conductor. The new model shows that this conductor abruptly terminates at 54 °N and is not observed farther south in the model. This shows that the NACP is not as spatially continuous as previously suggested, suggesting that the tectonic processes that formed the THO were not as uniform along-strike as

shown in existing tectonic models. The connection of one of the northeast-trending anomalies to the NSC conductor suggests that a previously unrecognized phase of east-dipping subduction may have occurred beneath the Sask craton as the THO was formed.

Highlights

- A major mantle conductor underlies the northern Sask craton in the Trans-Hudson Orogen.
- The conductor formed due to flat slab accretion beneath the craton during Manikewan Ocean closure.
- The North American Central Plains conductor is not as continuous as previously suggested.
- A phase of east-dipping subduction may have occurred beneath the Sask craton.
- Kimberlites and mineralizing fluids may have ascended along conduits represented by conductors.

6.1 Introduction

Cratons are the oldest parts of the continents and record important information about the tectonic evolution of the Earth. They are also major repositories for both diamonds alongside minerals critical to the energy transition (Hoggard et al., 2020; Pearson et al., 2021). Mantle petrology and geophysical studies have demonstrated that thick lithosphere is present beneath most cratons (Griffin et al., 2004; Pearson and Wittig, 2013). However, there are aspects of craton structure and evolution that are not well understood. Craton formation is typically the result of multiple tectonic processes occurring over a long period of geological time resulting in complex lithospheric structure. However, data coverage for the study of cratons is often limited to regions where kimberlites are found. In addition, the processes that destroy or rejuvenate cratons are not well understood (Foley, 2008; Snyder et al., 2017). These limitations result in a partial view of the complex geologic history of cratons. This has complicated the development of regional tectonic models seeking to understand craton formation and evolution. Defining the lithosphere and its structure beneath cratons can also improve our understanding of craton-associated mineral systems, including those for diamondiferous kimberlites (McCuaig and Hronsky, 2014; Hoggard et al., 2020; Pearson et al., 2021; Özaydın and Selway, 2022).

The Sask craton in Canada is an excellent location in which to examine the lithospheric evolution of cratons, owing to the high degree of preservation of its complex geologic history (Ansdell, 2005; Czas et al., 2020). The Sask craton was formed in the Archean, but much of the lithospheric mantle was added during the tectonic processes that formed the Paleoproterozoic Trans-Hudson Orogen (THO) (Czas et al., 2018; 2020). During THO tectonics, the Sask craton moved northwards between the converging Hearne and Superior cratons (Ansdell, 2005; Bedrosian and Finn, 2021). During the final stages of collision, crust from the surrounding terranes was thrust over onto the Sask craton. Subsequent deposition of the Paleozoic Western Canadian Sedimentary Basin has buried the southern part of the THO and Sask craton (Ansdell, 2005). Tectonism also formed world-class mineral deposits along the length of the THO (Syme et al., 2011). Following THO formation, the only regional activity has been two phases of kimberlite eruptions at 417 ± 14 Ma and 115-92.5 Ma at Pikoo and Fort à la Corne (FALC), respectively (Kjarsgaard et al., 2017;

Smyth, 2020). The regional tectonic framework and distribution of kimberlites is shown in Figure 6.1.

Knowledge of the subsurface structure of the Sask craton has been restricted to either where kimberlites are found, or crustal-scale geophysical studies have taken place. As a result, uncertainties remain regarding the structure of the mantle lithosphere, and how the Sask craton was involved in the formation of the THO. Mantle resistivity is sensitive to a variety of conductive phases formed by metasomatism and fluid and melt flow related to tectonic activity during terrane assembly (Bedrosian and Finn, 2021; Chase et al., 2023; Murphy et al., 2023). Thus, MT is well suited to address these uncertainties, as it can provide 3-D images of mantle resistivity over a broad area. Prior MT data from the Sask craton (Fig. 6.1) have revealed a series of conductors in the crust. This included an extension of the North American Central Plains (NACP) conductor that extends along the THO for more than 2,200 km (Jones et al., 2005). However, despite a number of studies, the geometry, source, and relationship of the NACP conductor with the Sask craton and THO remain debated (Bedrosian and Finn, 2021 and references therein)

Previous MT studies have been limited by sparse MT station coverage, the use of 2-D modelling approaches, and the lack of long-period MT data. This has meant that the depth extent and geometry of these conductors remains poorly understood. In this study, a 3-D resistivity model of the northern THO in Saskatchewan is presented and provides new information about the lithospheric structure of the THO, NACP conductor, and Sask craton. In this article, the structure and evolution of the Sask craton is investigated in three-dimensions using magnetotelluric (MT) data. We interpret the resulting 3-D model with constraints from petrologic data using the MATE program (Özaydın and Selway, 2020).

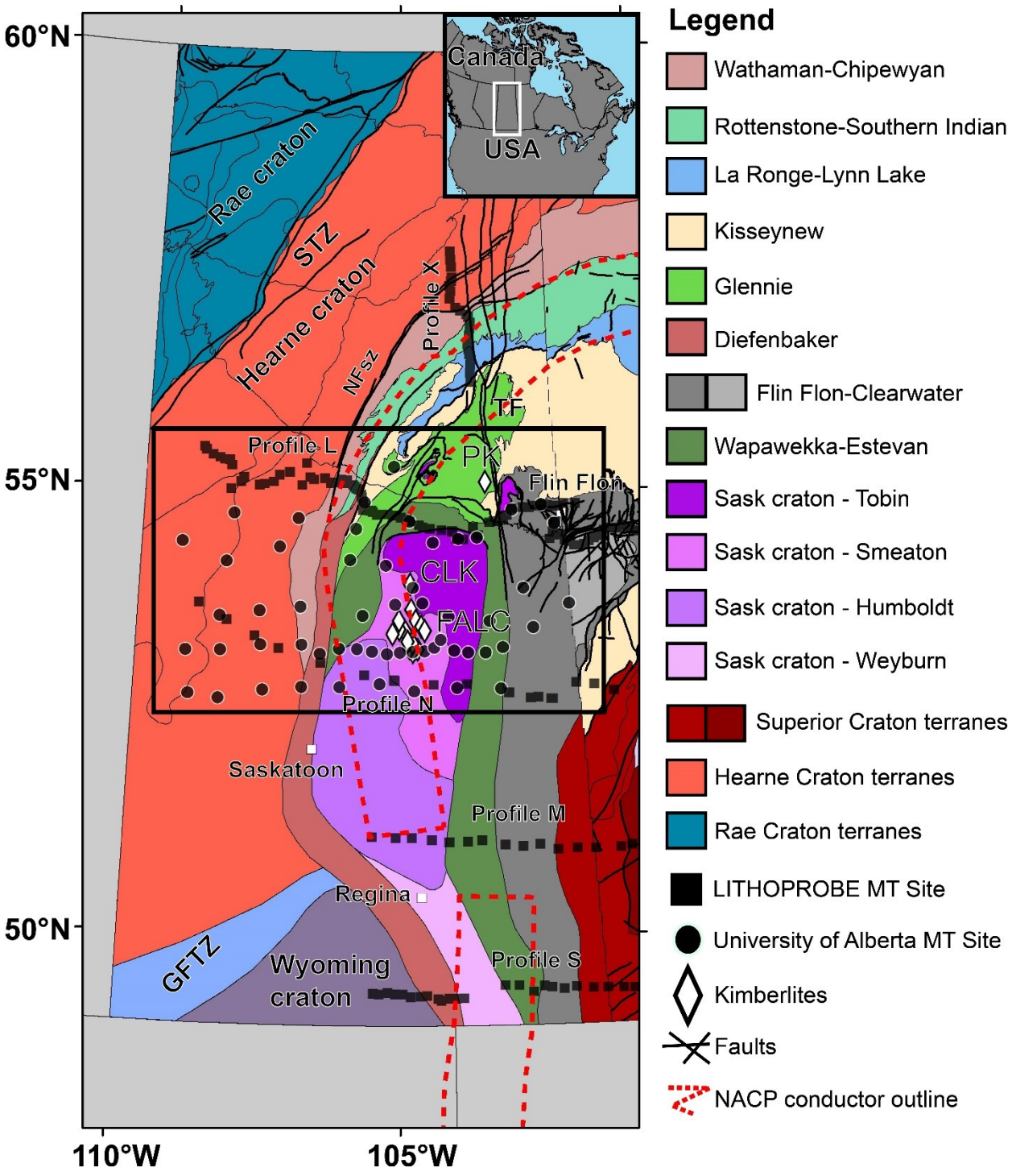

Figure 6.1: *Tectonic domain map of Saskatchewan and western Manitoba showing the coverage of magnetotelluric stations in the region. LITHOPROBE data is labelled by profile. The black box shows the area where data was selected for inversion. NACP conductor outline from Jones et al. (2005). Abbreviations: STZ, Snowbird Tectonic Zone; NFsz, Needle Falls shear zone; TF, Tabbernor fault; PK, Pikoo kimberlites; CLK, Candle Lake kimberlites; FALC, Fort à la Corne kimberlites; GFTZ, Great Falls Tectonic Zone.*

6.2 Methods and data

From 2021 to 2022 long-period MT data were recorded at 56 sites around the Sask craton (Fig. 6.1). Stations were spaced20-50 km and recorded data for 10-14 days, resulting in reliable data in the period range 1-10,000 s. Time series processing used the statistically robust multi-station method of Egbert (1997). These data were then combined with the previously collected LITHOPROBE data (Jones et al., 2005) to give an array of 106 MT stations. The phase tensors and induction vectors are plotted in the supplementary materials and show the regional resistivity structure is highly 3-D (Fig. B.1) and points to a major conductive feature beneath the northern Sask craton (Fig. B.2). A comparison of the LITHOPROBE and new MT data shows the two datasets are consistent (Figs. B.3-4). Selected examples of the long period MT data collected for this study are shown in Figure B.5.

The full MT impedance tensors were inverted using the ModEM inversion code of Kelbert et al. (2014). A range of inversions were undertaken, and a few are summarized in Table 1S of the Supplementary Material. The preferred inversion used a uniform 5 km horizontal cell size in the region of data coverage. The first vertical cell was 500 m thick and subsequent cell thickness increased by a geometric factor of 1.1. The model contained 1.06 million cells. No topography was implemented due to the flat terrane. The starting model was assigned a value of 100 Ωm. Error floors of 10% were assigned to both the diagonal and off-diagonal components of the impedance tensor. The root-mean-square data misfit was reduced from 9.88 to 1.22 after 204 iterations. Data misfit is displayed in Figure 6.2 and shows no systematic misfits in the spatial domain (Fig. 6.2A) or as a function of period (Fig. 6.2B-C).

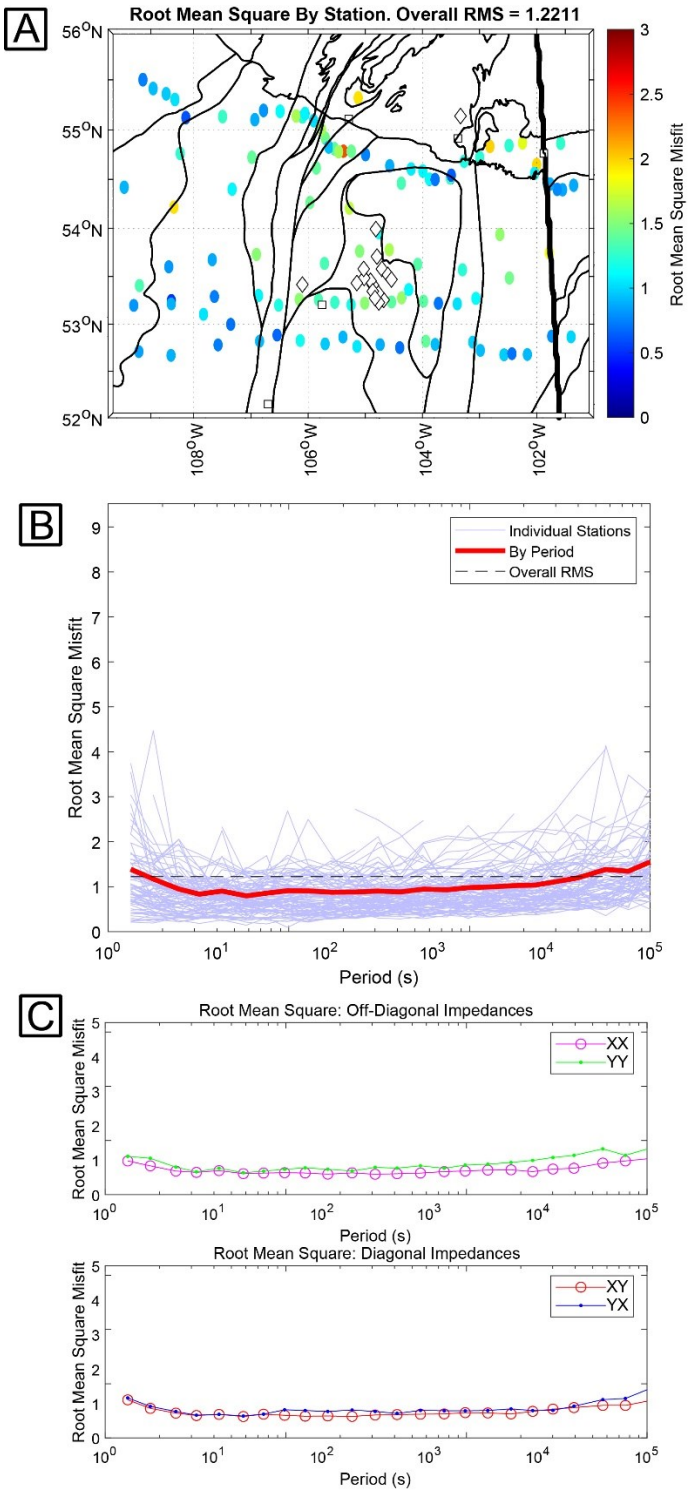

Figure 6.2: *Data misfit for the inversion model. (A) Data misfit at each station, represented as a colored circle. The thin black lines are the tectonic terrane from Fig. 6.1. The thick black line is the Manitoba-Saskatchewan border. (B) Data misfit as a function of period. (C) Overall data misfit as a function of period for the off-diagonal and diagonal impedances.*

The preferred inversion model is displayed in Figure 6.3 and in the supplemental materials. At depths less than 6 km, there are localized conductors associated with the Western Canadian Sedimentary Basin. From 6–30 km, a series of large conductors are observed along the edge of the Sask craton (Fig. 6.3A). The western conductors comprise two distinct northeast-striking lineaments (C1 and C2). Conductor (C2) is coincident with the boundary of the Hearne Craton (Fig. 6.3). An additional northeast-striking conductor (C3) is found east of the Sask craton and underlies the Flin Flon region (Fig. 6.3A, B and K). A number of additional discrete conductors can also be observed along the margin of the Sask craton (e.g., Fig. 6.3A, J, and L). The label C4 is given to the largest (Fig. 6.3B). Below a depth of 30 km the individual conductors begin to coalesce into single conductive anomaly in the depth range 70-85 km (Fig. 6.3). This conductor underlies most of the northern Sask craton and is named the northern Sask craton (NSC) conductor. Notably, the kimberlites at FALC, Pikoo, and Candle Lake are all located along the margin of the NSC conductor (Fig. 6.3). The conductance, which is the vertically integrated electrical conductivity and is a quantity that is well constrained by MT data, for the NSC from 70-150 km is shown in Figure B.6. The $>10^4$ (S) values associated with the NSC are comparable to the largest values measured in MT studies of the continents (Bedrosian and Finn, 2021 and references therein). Additionally, the NSC conductor attenuates the MT signal making its depth extent is unclear. It also reaches resistivity values as low as 0.1-0.01 Ωm, which are significantly lower than values typically observed in the lithospheric mantle. The reliability of the model was investigated using a number of resolution tests as follows:

(1) The first tests investigated the conductive anomalies by editing the preferred inversion model. The resistivity of crustal conductors was increased to 500 Ωm values and mantle conductors were raised to 100 Ωm. A forward calculation was then performed to determine how editing changed the RMS data misfit. The results are summarized in Figure B.7 and show that the removal of most conductive anomalies results in increased RMS data misfit at nearby stations, showing they are required by the data. The exceptions are the conductors in Figure B.7B and B.7L, which are located at both great depth and outside of the station grid, where reduced data sensitivity is expected.

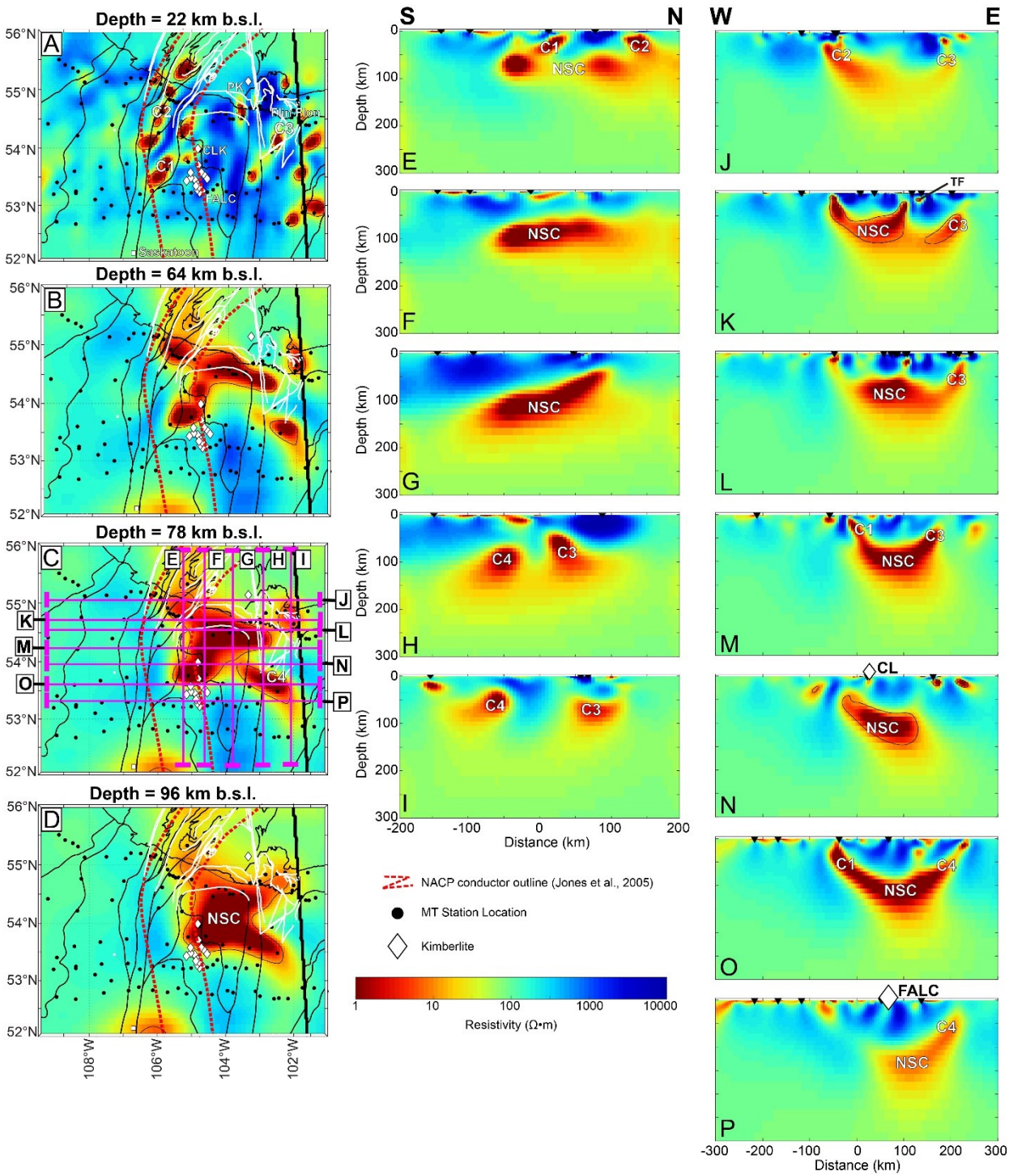

Figure 6.3: *(A-D) Horizontal depth slice for the resistivity model at depths of 22, 64, 78, and 96 km. (E-I) south to north vertical cross sections with profile locations shown on (C). (J-P) east to west vertical cross sections with purple profile locations shown on (B). See text for discussion of the conductive anomalies. Regional fault and shear zones shown by white lines. The thin black lines are the tectonic terrane from Fig. 6.1. The thick black line is the Manitoba-Saskatchewan border.*

(2) A second series of sensitivity tests applied a resistivity floor of 1, 5, 7, and 10 Ωm to the NSC conductor. The results in Figure B.8 show that station data misfit is not significantly affected until 5 Ωm values were used. The extremely low resistivity values may indicate that the inversion routine is underestimating resistivity values. The interpretation of the NSC conductor later in this paper will use a range of values from 0.01-1 Ωm but note that values closer to 1 Ωm may be more realistic.

(3) Finally, we examined the depth extent of the NSC conductor by iteratively replacing shallower layers with values of 100 Ωm. This showed that replacing portions of the conductor below 100 km has little effect on data misfit (Fig. B.9).

6.3 Resistivity model interpretation

The MATE program (Özaydın and Selway, 2020) was used to interpret the resistivity model. This software requires that the user define the physical and chemical properties of the lithosphere. A geotherm was calculated assuming a heat flow of 38 mW/m^2 obtained from FALC xenolith (Czas et al., 2018). The mantle composition was assumed to be a lherzolite down to 100 km and a mixture of 95% lherzolite and 5% eclogite from 100-210 km. The presence of eclogite is indicated by xenolith studies by Griffin et al. (2004) and Czas et al. (2018; 2020). A value of 5% eclogite is a rough middle value taken from the work of Schulze (1989), who estimated eclogite content in the upper mantle from multiple kimberlites. It is important to note that, by virtue of their involvement with kimberlites, xenoliths represent an inherently biased sample suite. However, they are the only way of directly sampling the lithospheric mantle. MATE also requires several secondary parameters to be defined and these are discussed in the supplementary materials. However, they had minimal effect on the results.

MATE was then used to model the effects of common mantle conductive phases, which included (1) hydration of nominally anhydrous mantle minerals (NAMs), (2) hydrous minerals such as phlogopite and (3) amphibole, (4) graphite, and (5) sulfides. These phases were considered as possible explanations for the conductors observed in the preferred model. Given their prominence, we focus the interpretation on the NSC and C1-C4 conductors.

6.3.1 Hydrous minerals

Amphibole was modelled throughout the lithosphere, as the K-richterite species can remain stable down to the LAB in cratonic settings (Konzett et al., 1997). Phlogopite was also modelled throughout the lithospheric mantle (Fig. 6.4B). A cementation exponent value of m = 1.3 was used, reflecting a well-connected system as both minerals are often deposited as veins or dikes (Tappe et al., 2008; Foley and Fischer, 2017). The results demonstrate that a lithospheric mantle composed of pure amphibole could not produce the observed resistivity values of the conductive anomalies (Fig. 6.4A). Similarly, a lithospheric mantle comprised of pure phlogopite could not produce the observed conductive anomalies (Fig. 6.4B). Partially explaining the NSC conductor with phlogopite is a particularly attractive explanation given its depth interval overlaps with global mid-lithosphere discontinuities (Rader et al., 2015). In this case, the NSC conductor could represent a layer of metasomatic phlogopite that crystallized where the peridotite solidus increases abruptly at depths of 80-100 km (Hansen et al., 2015; Rader et al., 2015). Chase et al. (2023) proposed a similar model for a mid-lithosphere discontinuity beneath the Southern Oklahoma Aulacogen. However, the Sask craton lacks any known seismic discontinuities or similar anomalies (Bank et al., 1998; Faure et al., 2011) and the percentage of phlogopite required is unrealistic (Fig. 6.4B). As a result, phlogopite and amphibole are not good candidates to explain the conductive anomalies beneath the Sask craton.

6.3.2 Hydration of nominally anhydrous minerals (NAMs)

The hydration of NAMs in the mantle is also not a good explanation for the conductors. Water contents > 1000 ppm would be necessary to produce the observed resistivity values at depths greater than 100 km (Fig. 6.4C). At shallower depths, even higher water contents > 5000 ppm would be required (Fig. 6.4C). This is far greater than the saturation limits of mantle minerals at depths < 80–100 km where the conductive anomalies are located (Fig. 6.4C) (Padrón-Navarta & Hermann, 2017).

6.3.3 Graphite

Graphite films are often invoked to explain low resistivity features in the crust and upper lithospheric mantle (e.g., Selway, 2014; Chase et al., 2023). It is an attractive explanation in regions affected by subduction or terrane suturing, where metamorphism is thought to mobilize sedimentary carbon into fluids that then deposit graphite along fractures, faults, and other conduits (Murphy et al., 2022). Graphite has been invoked to explain crustal conductors observed in the THO in the United States (Bedrosian and Finn, 2021). Mantle xenoliths provide evidence for the stability of these films in the mantle lithosphere in the 600-900 °C temperature range (Pineau and Mathez, 1990, and references therein). However, it is unclear if these films are widely disseminated due to the limited number of xenolith locations. The regional geotherm places the diamond-graphite transition at a depth of around 100 km (Czas et al., 2020), providing a maximum depth at which graphite can be present.

Graphite modelling in MATE was considered at depths less than 100 km and used a cementation exponent of m = 2, reflecting a poorly connected system. The results demonstrate that more than 500 ppm graphite are required to fit the data in the mantle lithosphere (Fig. 6.4D). Subducting slabs can contain more than 100,000 ppm, 500-600 ppm, and 700 ppm carbon in sediments, altered oceanic crust, and serpentinized peridotites, respectively, providing sufficient carbon to account for the values modelled with MATE (Kelemen and Manning, 2015; Plank and Manning, 2019).

There is no problem explaining crustal conductors with graphite. Fluid release during subduction at the blueschist-eclogite transition at < 2.5 GPa (80km) and 600 °C can allow for the mobilization of carbon from sediments and the crust (Peacock, 1993; Schmidt and Poli, 2013; Martin and Hermann, 2018; Plank and Manning, 2019). These fluids can precipitate graphite films while cooling (Huizenga and Touret, 2012; Murphy et al., 2022), and tectonic models and geochemical data show that subduction occurred around the Sask craton during the formation of the THO (Ansdell, 2005; Bedrosian and Finn, 2021). Additionally, graphite films could have been formed through fluid movement during late-stage orogenic metamorphism in the THO (Huizenga and Touret, 2012). At crustal levels, the lower temperatures could allow sufficiently thick graphite film networks to survive the process of film breakdown and still be present today (Yoshino and

Noritake, 2011; Zhang and Yoshino, 2017; Murphy et al., 2022). Drill core and field mapping from the Flin Flon belt, Kisseynew domain, and Wollaston domain (Fig. 6.1) provide direct evidence for graphite deposits in the region (Ansdell, 2005; Reid, 2018; Couëslan, 2022). As a result, graphite is likely a good explanation for the conductors in the crust (e.g., C1-C4 and the isolated conductors observed in Fig. 6.3L). However, it is more difficult to explain lithosphere mantle conductors with graphite films. Experimental results indicate that the higher temperatures will lead to film breakdown in as little as 20,000 years (Yoshino and Noritake, 2011; Zhang and Yoshino, 2017). While thicker films may survive, slab decarbonation is much more limited at depths greater than 60-80 km (2-2.5 GPa) (Schmidt and Poli, 2013). This would likely limit the amount of carbon available to form graphite films. Additionally, at depths of the NSC conductor, interactions between the predominately CO_2-rich fluids released via subduction and the mantle lithosphere of the Sask craton are likely to have occurred at redox conditions above the EMOD/G buffer, typically found at ~3 GPa (~100 km) in cratons (Frost and McCammon, 2008; Yaxley et al., 2017). The resulting reaction would precipitate crystalline carbonate over graphite (Stagno and Frost, 2010; Luth and Stachel, 2014)., and carbonate is not known to be electrically conductive.

Based on the geological history of the THO and Sask craton, graphite appears to be a viable explanation for the C1-C4 resistivity anomalies in the crust. However, given that mineral physics experiments show graphite films are unstable in the lithospheric mantle, graphite is an unlikely cause for the sub-crustal extensions of the C1-C4 conductors and NSC conductor.

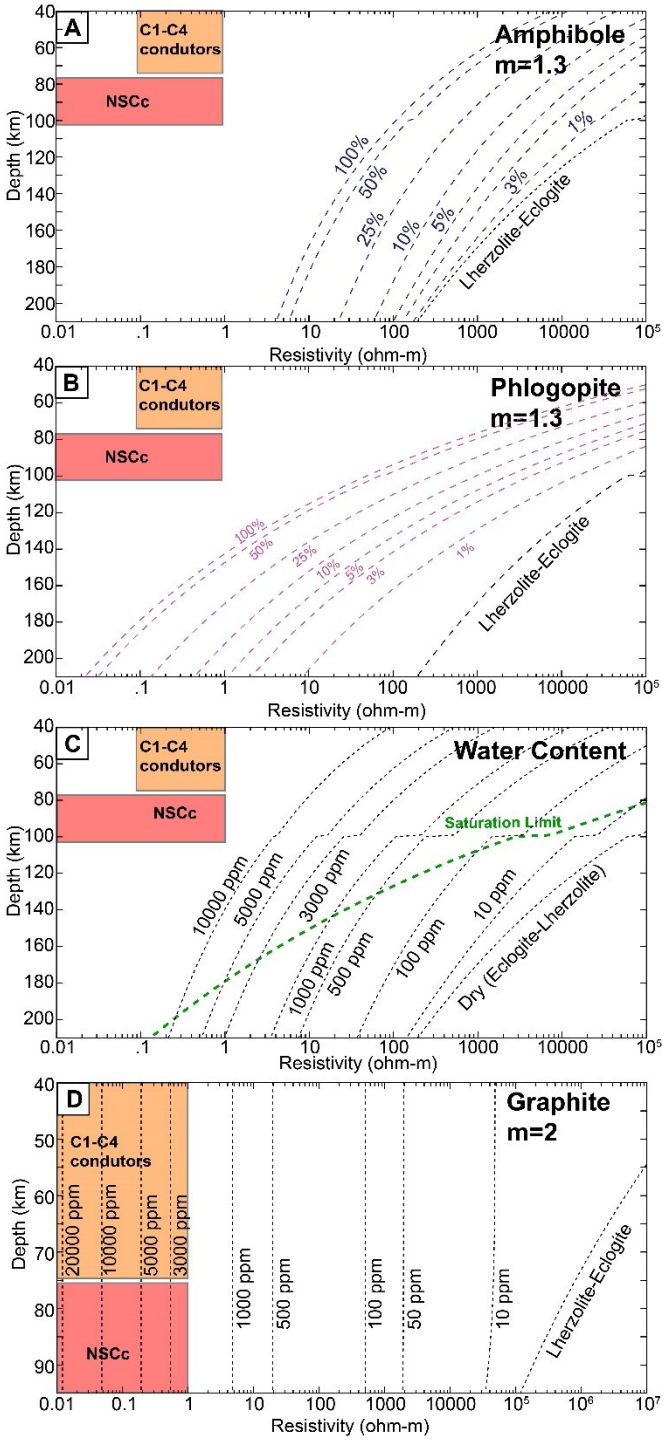

Figure 6.4: *MATE modelling results for (A) amphibole, (B) phlogopite, (C) water content (i.e., hydrogen in nominally anhydrous minerals, (D) graphite. Note the change in y-axis depth between (A) and (D) and (B) and (C). Orange and red boxes indicate the typical resistivity values for the main conductors observed in the resistivity model. The m values are the cementation exponents used for each conductive phase. The saturation limit in (D) is from Padrón-Navarta and Hermann (2017).*

6.3.4 Sulfide minerals

Saxena et al. (2021) showed that sulfide minerals could lower the bulk resistivity when the volume fraction was greater than ~5 %, and that volume fractions of 5-18.5 % would produce a bulk resistivity in the range 1-0.01 Ωm with cementation exponents in the range m = 3.9-5. These cementation exponent values are relatively high, and likely reflect that additional work is needed to better understand sulfide interconnection (Saxena et al., 2021). As a result, lower cementation exponents with values of m = 1-2 were also considered. A value of m = 1 represents well-connected sulfides in the form of films and this distribution is observed in some mantle xenoliths (e.g., Lorand et al., 2003) or deposited in a fluid-conduit model similar to the graphite model of Murphy et al. (2022). These parameters were modelled in MATE and the results are shown in Figures 6.5 and B.10. The results show that the volume fractions and cementation exponents obtained by Saxena et al (2021) could explain the resistivity values of the NSC and C1-C4 conductors (Fig. 6.5A), even those as low as 0.01 Ωm. The m = 1-2 scenarios can explain resistivity values as low as 0.01 Ωm with just a few hundred ppm to few volume percent (1 % volume fraction = ~14000 ppm) (Figs. 6.5B and B.10), predictably increasing with lower degrees of interconnection.

Sulfide minerals can produce regions of low resistivity in both the crust and mantle lithosphere (Selway, 2014). It is well established that subducting slabs release sulfur in the form of both reduced H_2S and HS^- (sulfides) or oxidized SO_4^{2-} and SO_2 (sulfate) melts or fluids, though fluid-generating dehydration reactions have dominated since ~2.5 Ga (Martin et al., 2005; Schmidt and Poli, 2013; Tomkins and Evans, 2015). Multiple episodes of subduction during the formation of the THO suggest that sulfides may be a realistic explanation for the anomalies observed in this study. The majority of fluid release during subduction occurs at depths less than 80 km (2.5 GPa), in agreement with the depth extent of the NSC conductor (Fig. 6.3). During ascent, these fluids or melts can precipitate electrically conductive sulfide minerals in the form of pyrite or pyrrhotite (Bataleva et al., 2016; Tomkins and Evans, 2015; Bérnard et al., 2018). In most subduction zones, sulfur-rich fluids are expected to precipitate sulfide minerals upon interacting with the more reduced mantle wedge (Walters et al., 2020). Here, these fluids would have precipitated sulfides upon interaction with the reduced overlying mantle lithosphere of the Sask craton (Frost and McCammon, 2008), forming a sulfide-rich layer like the NSC conductor itself. Slab signatures in

sulfur from arc magmas (Taracsák et al., 2023) attest to the mobility of sulfur during subduction, which would be necessary to form electrically conductive grain boundary networks. These factors make sulfides a possible explanation.

Based on the history of the THO, sulfide minerals derived from subduction related fluids appear to be a viable explanation for the resistivity of the NSC conductor. They are also a viable explanation for the lithospheric mantle extensions of C1-C4 conductors. The crustal extensions of the C1-C4 conductors are more likely to be explained by a combination of interconnected graphite and sulfides in metasedimentary rocks, similar to the interpretation by Bedrosian and Frost (2023).

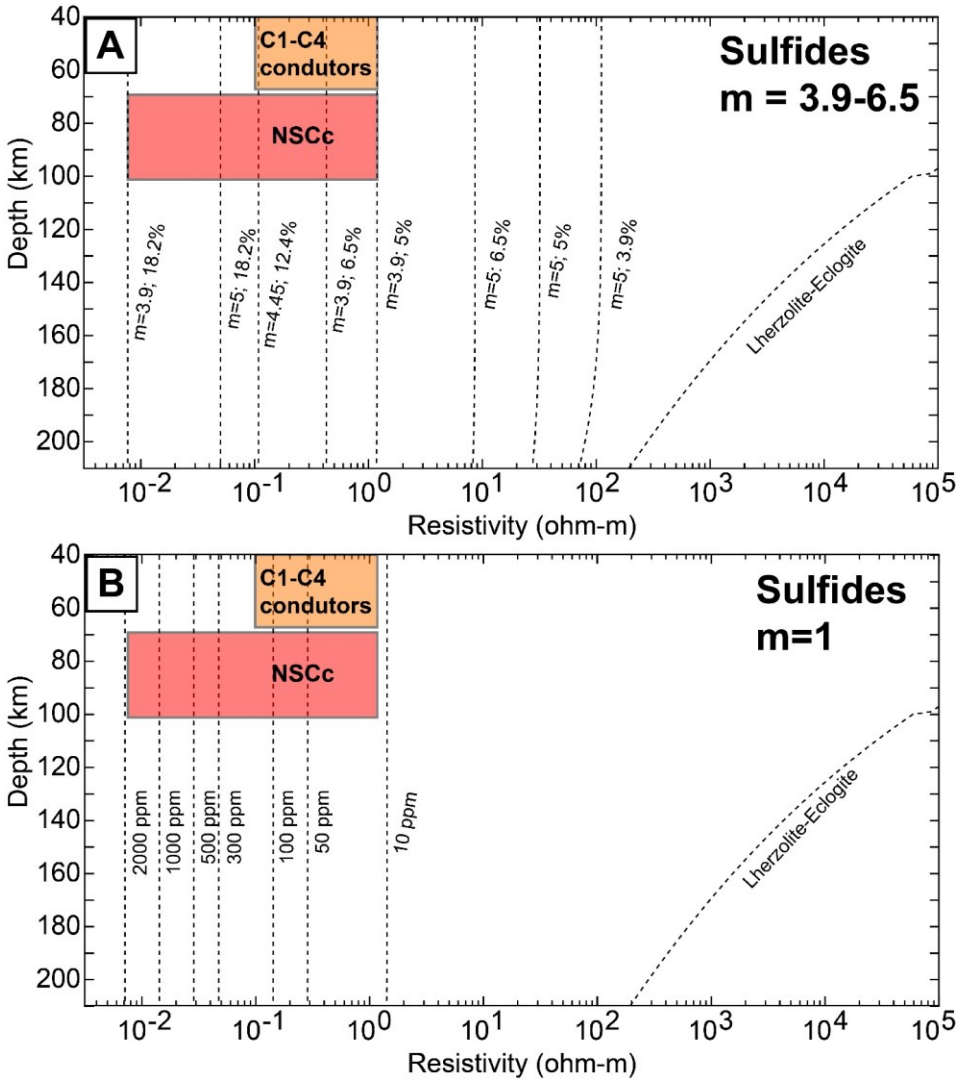

Figure 6.5: *MATE modelling results for sulfides using (A) the constraints offered by Saxena et al. (2021) and (B) a cementation exponent of 1.*

6.3.5 Garnet pyroxenites

Garnet pyroxenites have been suggested as explanations for low resistivity in the upper mantle (Ferrand and Chin, 2023). However, these are a unique rock type that is typically found in off-craton or intraplate settings (Gonzaga et al., 2010), have not been observed in Sask craton xenoliths records (Czas et al., 2018; Smyth, 2020), and would produce resistivity values ranging from 50-500 Ωm at the depths of the NSC conductor (Ferrand and Chin, 2003), which is far more resistive than observed (Fig. 6.3). This mechanism is not a likely explanation for this region but is explored more in the supplementary materials.

6.4. Discussion

6.4.1 Structure of the Sask craton and tectonic implications

The low resistivity of the NSC conductor is highly unusual compared to the moderate to high resistivity typically observed beneath most cratons. At certain locations, the connection between the NSC and C1-C4 conductors appears symmetric across the Sask craton (e.g., Fig. 6.3K, M and O). The geometry of the crustal conductors C1-C4 is reminiscent of the dipping conductors observed in suture zones that have been attributed to the presence of graphite and sulfides related to subduction (e.g., Bedrosian and Frost, 2023; Murphy et al., 2023). The along-strike spatially continuity of C1 and C2 (Fig. 6.3) is also typical of suture zone (e.g., Jones et al., 2005; Bedrosian and Finn, 2021). Given the ubiquity of subduction and terrane suturing during THO tectonics (Ansdell, 2005), this is the preferred interpretation for these conductors. Conversely, the C3 and C4 conductors are more isolated conductive anomalies and do not continue along strike of the Sask craton. This is not typical of a suture zone, and an alternative interpretation for these conductors is presented in section 4.3. The NSC conductor is similarly interpreted to be the result of sulfide minerals. Based on the continuity between the NSC and C1-C4 conductors, their similar interpretation as a result of sulfides, and the episodes of subduction that occurred during the formation of the THO (Ansdell, 2005), it is suggested that the NSC conductor represents a sulfide-enriched interval formed between a subducted oceanic crust that underwent flat slab subduction

beneath the northern Sask craton. This slab was accreted to the base of the Sask craton, and the sulfide-enriched interval now forms the top of the lower half of the lithosphere of the Sask craton (Fig. 6.6).

This hypothesis is supported by observations that the oceanic crust is the primary carrier of sulfur and sulfide minerals during subduction (Alt et al., 1989; Walters et al., 2020). These sulfide minerals and sulfur could have been remobilized and redistributed during fluid release (Peacock, 1993) and concentrated along the boundary between the overlying cratonic lithosphere and the down going plate. This could have deposited sufficient sulfide minerals to produce the NSC conductor over a relatively confined interval. This would avoid buoyancy instabilities in the lithosphere that would arise if a dense phase like sulfide minerals were added to significant portions of the lithosphere. Note that the sensitivity test presented earlier showed that the MT data are only sensitive to the upper part of NSC conductor. Additionally, this hypothesis is supported by the xenolith data, which show that eclogite first appears in the xenolith record at the depth of the NSC conductor and that the lower lithosphere formed during THO tectonism (Czas et al., 2018; 2020). Geochemical data from both the ecologite xenoliths and diamonds from FALC kimberlites also show that both were derived from subducted protoliths and organic carbon, respectively (Czas et al., 2018; Milne, 2024). Eclogites in the xenolith record at greater depths than the NSC conductor (Czas et al., 2018) may not be conductive because below 90-105 km (2.8-3.3 GPa) residual sulfur is thought to transform into electrically resistive sulfate (Walter et al., 2020). Conversely, sulfides have been observed in eclogite xenoliths from depths greater than 100 km in the Kaapvaal craton (e.g., Burness et al., 2021). If this applies at FALC, perhaps sulfides do not exist in sufficient quantities to conduct, or they are electrically screened by the low resistivity of the NSC conductor.

The east-west symmetry of the NSC conductor connecting with the C1-C4 conductors that dip along the boundaries of the Sask craton is striking (Fig. 6.3). The connection of C1 and C2 to the NSC conductor may indicate that a phase of east-dipping subduction occurred along the western margin of the Sask craton. The lack of horizontal continuation of the NSC conductor further west may be evidence that accretion occurred at a terminal phase in the formation of the THO. Alternatively, it could imply that the slab was deflected downwards or tore upon encountering the thick cratonic lithosphere of the Superior Craton east of the Sask craton, or that the sulfide-rich

oceanic crust was fully removed below the Sask craton and did not reach farther east. The latter two options are consistent with observations from numerical experiments on flat slab subduction systems (Liu and Currie, 2019). The termination of the C1-NSC conductor south of ~53.5 °N is also notable and implies that flat slab subduction only occurred under the northern Sask craton. A change in slab dip can occur when a slab encounters a thick, depleted, and rheologically strong cratonic lithosphere (Liu and Currie, 2019). In the resistivity model, the resistive, and thus depleted and unmodified, core of the Sask craton thickens to the south (Fig. 6.3F). Therefore, it may be that flat slab subduction was controlled by the original thickness and rheological strength of the Sask craton, and that the north Sask craton was originally thinner which permitted flat slab subduction (Fig. 6.6).

In light of the new 3-D resistivity model it is important to consider the polarity of subduction during THO tectonics. Prior geological and geophysical studies have favored west-dipping subduction along both margins of the Sask craton (e.g., Ansdell, 2005; Bedrosian and Finn, 2021). The interpretation of the C1, C2, and NSC anomalies as evidence for a possible east-dipping subduction zone along the western margin of the Sask craton requires a polarity that is the opposite of these prior models. It may be that the polarity inferred by previous studies reflects relatively thin-skinned features (e.g., Ye et al., 2019; Bedrosian and Finn, 2021). The seismic datasets used to support prior interpretations were largely limited to the crust (e.g., Lewry et al., 1994). However, the geologic data show that arc volcanic units are present along the Hearne margin, consistent with west-dipping subduction along that margin (Ansdell, 2005). Therefore, the C1, C2, and NSC anomaly may represent a previously unrecognized episode of subduction during the Manikewan Ocean closure phase of THO tectonics. The numerous conductive anomalies along the Manitoba border, including the C3 and C4 conductors, could reflect anomalies associated with the west-dipping subduction zone of the Superior margin or prior models (e.g., Ansdell, 2005; Bedrosian and Finn, 2021). However, the MT data coverage does not extend here and limits the analysis.

Visually, the NSC and C1-C4 conductors do appear to have similar geometry and structure to melt systems imaged by seismic data around the Tanzania craton (e.g., Mulibo and Nyblade, 2013). Given the kimberlite volcanism, the similar structure and geometry raises the possibility of melt as an explanation. However, this possibility is very unlikely given the lack of elevated regional

geothermal conditions and the fact that kimberlites are typically small-volume melts formed via decompression-induced redox melting, do not require deviations from ambient temperatures (Tappe et al., 2018), and so will have limited long-lived thermal impacts on the lithosphere. This possibility is dismissed here but is explored more in the supplemental materials.

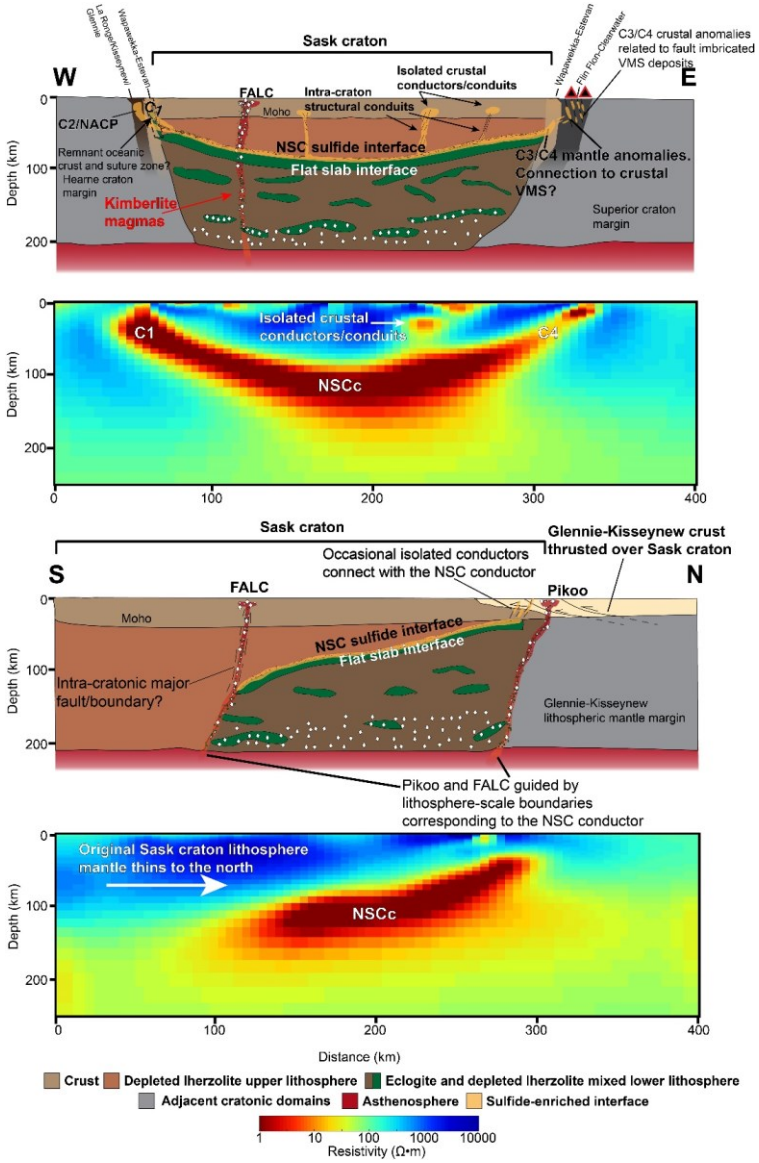

Figure 6.6: *Schematic cartoons summarizing the resistivity model interpretations and the observations of Czas et al. (2018; 2020) for the structure of the Sask craton in both the north-south and east-west directions. Below each cartoon is a representative vertical slice of the resistivity model from Figure 6.3 for comparison. Note that lithosphere depths for the Hearne and Superior margins are speculative. Abbreviations: NSC, North Sask craton; Moho, Mohorovičić discontinuity; FALC, Fort à la Corne kimberlite field; VMS, volcanogenic massive sulfide; NACP, North American Central Plaines Conductor.*

6.4.2 Relationship to the NACP anomaly and formation of the THO

The resistivity model presented in this study should be critically compared with previously published models of this region of the THO. On LITHOPROBE profile L (Fig. 6.1), Jones et al. (2005) identified a conductor as an extension of the previously reported ~1500 km long North American Central Plains (NACP) conductor. The length extent of the NACP conductor has previously been used to argue that tectonic processes were remarkably similar along the length of the THO (e.g., Jones et al., 2005; Bedrosian and Finn, 2021). This feature can be identified as conductor C2 in this study. Our resistivity model demonstrates that this conductor terminates abruptly at 54 °N, extends and dips east into the mantle lithosphere, and is organized en echelon with conductor C1. The original extension of the NACP conductor through much of southern Saskatchewan (e.g., Jones et al., 2005) was likely the result of LITHOPROBE profiles L and N (Fig. 6.1) being modelled in 2D while being sensitive to off-profile features such as the C1 and NSC conductors. Our model shows that there is an approximately 300 km gap in the NACP conductor from C2 to where it is located north of LITHOPROBE profile S (Fig. 6.1; Bedrosian and Finn, 2021). This suggests that tectonics in southern Saskatchewan may have been distinct from regions farther south in the US where the NACP conductor extends for hundreds of kilometers along strike of the THO (e.g., Bedrosian and Finn, 2021). Further, the NSC conductor may represent the mantle conductor suggested to exist in the region by Jones et al., (2005).

6.4.3 Relationship to kimberlite distribution

The factors that control kimberlite genesis and localization remain enigmatic. Kimberlites are often found in clusters and concentrated regionally. In recognition of this, kimberlite ascent models suggest controls by either lithosphere topography or major faults and terrane boundaries associated with craton assembly and evolution (Foley, 2008; Jelsma et al., 2009; Tappe et al., 2018, and references therein). Previous studies using MT data suggest kimberlites, and in particular diamondiferous kimberlites, are found adjacent to conductive mantle anomalies associated with metasomatic alteration (Özaydın and Selway, 2022). Indeed, the oxidation of CH_4 or reduction of carbonatitic CHO fluid species is likely to introduce hydrogen into mantle wall rock (Luth and Stachel, 2014), which could be electrically conductive. These same fluids may also precipitate

diamond via redox reactions or isobaric cooling (Stachel and Luth, 2015). Since MT data offer the ability to image these conductive zones as well as major lithosphere structures, it may offer insight into the genesis, localization, and diamond potential of kimberlites. Such analysis would feed into a Mineral Systems model (McCuaig and Hronsky, 2014) for diamond exploration, which seeks to understand mineral deposits from source to deposit in order to develop better exploration practices.

The resistivity model in Figure 6.3 reveals that the Candle Lake, FALC, and Pikoo kimberlite clusters all erupted along the margin of the NSC conductor (Fig. 6.3), suggesting a relationship between them and the subducted lithosphere beneath the north Sask craton. Within kimberlite ascent models (e.g., Jelsma et al., 2009; Tappe et al., 2018; and references therein), the NSC conductor represents a compositional heterogeneity of the Sask craton mantle lithosphere (Fig. 6.6). The well-defined borders of the NSC conductor suggest that this heterogeneity has a sharp boundary, likely reflecting a deep-seated fault or mantle terrane boundary. Such structures could have provided conduits for focusing kimberlite melts and aiding their ascent (e.g., Fig. 6.6). This could explain why the regional distribution of kimberlites tends to cluster around the outside of the NSC conductor. Major faults and shear zones hosted in the crust also likely played a role in kimberlite localization. Notably, the Pikoo kimberlite cluster occurs near the Tabbernor Fault zone, a major structure that separates lithotectonic domains and controlled igneous intrusions during THO tectonism (Davies, 1998). It is less clear if the FALC and Candle Lake kimberlites are associated with structures similar to the Tabbernor Fault as the extension of faults south beneath the Phanerozoic sedimentary cover (Fig. 6.3) is unclear. However, both FALC and Candle Lake overly the C1 conductor in the mantle lithosphere (Fig. 6.3), which corresponds to west-dipping minor crustal conductors connected to C1 (Fig. 6.3N and P). At crustal levels, C1 itself corresponds well to the southward extensions of either the Stanley fault, Hartley Lake shear zone, or Dowd Creek shear zone (Fig. 6.7). This suggests that these faults and associated splay structures, represented by the minor crustal conductors, may have acted as conduits and guided kimberlites during their ascent. This fluid and melt movement likely deposited minor conductive phases, similar to conductors observed in the Gawler craton (Heinson et al., 2018).

In summary, our model suggests that the NSC conductor could represent a compositional boundary in the lithosphere, and faults associated with it could have aided kimberlite localization and ascent

(Fig. 6.6). This may explain why the Candle Lake, FALC and Pikoo kimberlite clusters are located along the margins of the NSC conductor. The ultimate location for these kimberlites clusters was likely also guided by major structural faults and shear zones in the region, which correspond to structurally bound conductive anomalies in the crust.

6.4.4 Implications for metal exploration

A number of conductive elongated and narrow sub-vertical structures (e.g., C2-C4) and isolated conductors (e.g., Fig. 6.7) are present in the survey area and may be important to mineral potential. Notably, within the Flin Flon arc belt terrane (Fig. 6.1), there is a close spatial relationship between the C3 conductor and the prolific mining district centered on Flin Flon, Manitoba (Fig. 6.7). Mineralization in the Flin Flon belt is associated with volcanogenic massive sulfides (VMS) formed in an extensional arc-rifting environment that were imbricated within east-dipping thrust sheets developed during THO orogensis (Syme et al., 1999) (Fig. 6.3). The resistivity model reveals that the Flin Flon region overlies a crustal extension of the C3 conductor (Fig. 6.7). This crustal conductor could be explained as a layer of imbricated crustal sulfides minerals that originated as VMS deposits (Fig. 6.6). It is significant that the C3 conductor extends farther southwest along strike of the Namew Lake shear zone (Fig. 6.7). This suggests that sulfide mineralization is controlled by major faults and may extend beneath the Phanerozoic sedimentary cover southwest of Flin Flon. A number of similar conductive anomalies are located around Flin Flon and across the Manitoba-Saskatchewan border (Fig. 6.7). The MT data coverage in this study does not extend over many of these conductors, limiting resolution of their geometry. However, sensitivity tests reveal that they are required by the MT data (Fig. B.7). The number of conductors suggests that a system of additional, possibly mineralized, sulfides bodies are located under the sedimentary cover of the Kisseynew and Flin Flon-Clearwater terranes, which could be targets for future exploration.

The C2 conductor corresponds to the trace of the NACP conductor reported by Jones et al. (2005). The resistivity model presented here shows that the C2-NACP conductor corresponds to, and is structurally bound by, the Howard Lake shear zone (Fig. 6.7). The southward extension of C2 suggests the Howard Lake shear zone extends under the sedimentary cover until at least 54 °N.

Notably, the C2 conductor is parallel to and partially underlies a major trend of gold occurrences within the La Ronge terrane (Fig. 6.7). The current MT data coverage does not allow an investigation of how far north C2 extends. However, this suggests that regional gold potential may be related to the formation of the C2 conductor and may extend south under the Phanerozoic sedimentary cover. The connection of conductors C2 and C3 to the NSC conductor suggests that they may be related to the deep zone of sulfide minerals that account for the NSC conductor. In this model, the C1-C4 conductors may represent conduits that transported fluids and melts derived from the subducted flat slab. These fluids then moved upward along the edges of the Sask craton, where they were then guided by major terrane boundaries and faults, and ultimately fed into regional mineralization. Sulfide minerals in such fluids may be good carriers of economically important base and precious metals (e.g., Tomkins and Evans, 2015; Walters et al., 2020). In this respect, crustal regions near the conductive conduits may represent regions of enriched metal potential. The location of additional isolated conductors (e.g., Fig. 6.3J and L) in the crust are also of interest, as their depths are similar to crustal anomalies ultimately genetically linked to iron oxide-copper-gold deposits in Australia (e.g., Heinson et al., 2018). While our data cannot image how these deep conductors may move into the upper crust, much less at economically exploitable depths, we argue that where they are present in our model they may represent targets for future, more shallow-imaging exploration methods.

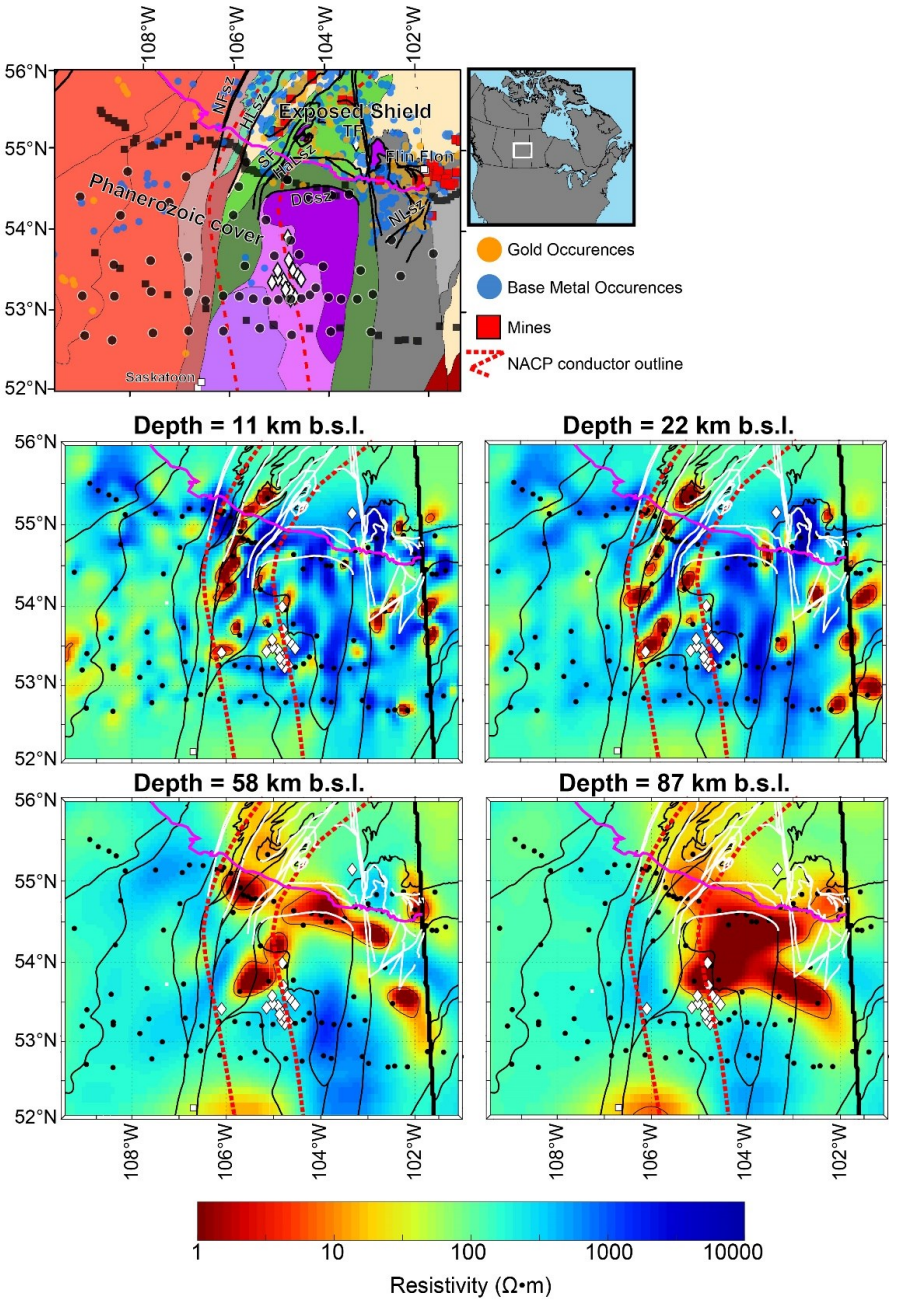

Figure 6.7: *(Top) Subset of Figure 6.1 showing mineral and metal occurrences and mines in the region of the resistivity model. Fault and shear zones are shown as thick black lines. Note that the majority of mineral, gold, and metal occurrences are located where the shield is exposed, where they are easiest to find. The boundary for where the shield is exposed is indicated by the purple line, south of which the basement is covered by Phanerozoic and younger sedimentary units. (Bottom) Depth slices are 11, 22, 58, and 87 km depth, showing the main conductors associated with mineralization in the region. White lines show faults and shear zones. Thin black lines are the tectonic terranes from Fig. 6.1. The thick black line is the Manitoba-Saskatchewan border. NACP conductor outline from Jones et al. (2005). Abbreviations: NFsz, Needle Falls shear zone; HLsz, Howard Lake shear zone; Sf, Stanley fault; HaLSz, Hartley Lake shear zone; DCsz, Dowd Creek shear zone; NLsz, Namew Lake shear zone; TF, Tabbenor fault.*

6.5 Conclusions

New long-period MT data have been combined with legacy datasets to produce the first fully 3D resistivity model of the THO and Sask craton. The results show:

- The northern Sask craton is underlain by a major conductor (NSC conductor) with an upper surface at a depth of 70-85 km. A number of northeast-trending conductors extend from the NSC conductor into the crust (C1-C4). The C2 conductor along western edge of the NSC conductor is the previously reported NACP conductor. Notably, the NACP-C2 conductor terminates abruptly south of 54 °N, showing it may not be as continuous along-strike as previously suggested. This suggests that THO tectonics may be more variable along strike than previously suggested.

- The low resistivity of the NSC conductor is best explained as a layer enriched in sulfide minerals that formed along the interface between subducted oceanic crust and overlying Sask craton lithosphere.

- The resistivity model suggests east-dipping flat slab subduction could have occurred along the western margin of the Sask craton during a previously unrecognized episode of tectonism during closure of the Manikewan Ocean, and in addition to west-dipping subduction of prior models. Prior studies also suggest westward subduction of the Superior craton margin beneath the Sask craton. A number of conductors east of the Sask craton may be evidence of this tectonic episode.

- The FALC, Candle Lake, and Pikoo kimberlites all erupted along the margins of the NSC conductor, suggesting a relationship between the two. The margins of the NSC conductor likely represent deep-seated faults or mantle terrane boundaries that acted as conduits that guided the ascent of kimberlite melts. Regional major crustal faults, such as the Tabbernor Fault zone associated with the Pikoo kimberlites, may represent such deep-seated conduits. The FALC and Candle Lake kimberlites are spatially associated with one of the major northeast-trending

conductors (C1) which may be associated with a number of prominent faults and shear zones that may extend south beneath the Phanerozoic sediment cover.

- The northeast-trending conductors alongside a variety of secondary conductive anomalies in the crust are interpreted as the results of sulfides and graphite deposited during past fluid or melt flow. One northeast-trending conductor (C3) is located around the prolific mining district at Flin Flon, Manitoba. Another (C2) occurs near a major concentration of gold occurrences in the La Ronge terrane of Saskatchewan. These conductive conduits may have transported sulfur-rich fluids or melts derived from the subducting slab and where they approach the surface, and they may have enriched the overlying shallow lithosphere and crust in base and precious metals. Many are located beneath the Phanerozoic sedimentary cover. These conductive anomalies may represent additional targets for mineral exploration. Additional work is needed to establish this connection.

Data Availability

The magnetotelluric data used in this study is available from the University of Alberta Education and Research Archive at https://doi.org/10.7939/r3-6ga7-pf05. The MATE software can be accessed at https://github.com/sinanozaydin/MATE.

Acknowledgments

We thank the variety of landowners who graciously allowed us to place our equipment on their land. Ken and Marion Laroque are especially thanked for allowing the field crew to use their farm as a staging area and place to sleep. We thank the Saskatchewan Ministry of Environment for allowing us access to regional provincial forestland. Kitsaki Management and Sakaw Askiy Management are thanked for providing their geospatial data on forest access, which considerably simplified fieldwork. Zoë Vestrum, Cedar Hanneson, Andrew Williamson, Keeya Beausoleil, Allyson Shewchuk, and Erich Slobodian are thanked for their help in the field. Conversations with Graham Pearson, Thomas Stachel, Sarah Milne, Claire Currie, and Sean Bosman helped to develop ideas in this paper regarding interpretation. This research was funded by an NSERC Discovery

Grant awarded to Martyn Unsworth and funding from the Saskatchewan Geological Survey. The LITHOPROBE MT data were collected by the Geological Survey of Canada, and permission to use them is gratefully acknowledged. Additional graduate research grants awarded to Brandon Chase from the Society of Economic Geologists, Society of Exploration Geophysicists, and Geological Society of America helped to fund the data collection. Sebastian Tappe and an anonymous reviewer are thanked for their comments that have significantly improved the paper.

CHAPTER 7. DEEP ELECTRICAL STRUCTURE OF THE BUFFALO HEAD HILLS AND BIRCH MOUNTAINS, NORTHERN ALBERTA: IMPLICATIONS FOR DIAMOND EXPLORATION

B.F.W. Chase, M.J. Unsworth, D.I. Pană and E. Wang (2024)

AER/AGS Special Report 117, 40 p.

https://ags.aer.ca/publication/spe-117

7.1 Introduction

Diamonds are formed in the deep lithospheric mantle where the pressure is high enough to allow carbon to turn into diamond. Diamonds are brought to the surface by the eruptions of kimberlites, which are small volume, volatile-rich melts that originate in the asthenosphere. As kimberlites ascend through the lithospheric mantle to the Earth's surface they entrain xenoliths, which can include diamonds if they are present (Russell et al., 2019). Although originally associated with Archean lithosphere, kimberlites and diamonds have recently been shown to frequently form and erupt within Proterozoic terranes (e.g., Liu et al., 2018; Czas et al., 2020). This has expanded the search area for kimberlite pipes that may contain economically significant quantities of diamonds. Kimberlite exploration is inherently challenging because pipes are usually less than 1 km in diameter and typical exploration areas are hundreds to thousands of kilometres in extent. As diamond exploration in Canada moves towards greenfield areas (i.e., unexplored regions) alongside more difficult targets in brownfields (i.e., previously developed or explored regions), additional criteria will be invaluable for area selection to help lower exploration costs.

Magnetotelluric (MT) data have been used to study the electrical resistivity structure of the lithosphere in regions containing diamondiferous kimberlites including in the Northwest Territories, Saskatchewan, and South Africa (e.g., Özaydın and Selway, 2022; Bettac et al., 2023). The interpretation of these MT data has proven useful for kimberlite exploration in two ways: (1) detecting upper mantle resistivity anomalies that may be correlated with diamondiferous kimberlites, and (2) providing information about the depth to the lithosphere-asthenosphere boundary (LAB).

Regarding the detection of anomalies, studies in a number of cratons have shown that diamondiferous kimberlites pipes are sometimes spatially associated with regions of low electrical resistivity (high conductivity) in the lithospheric mantle (e.g., Jones et al., 2005; Özaydın and Selway, 2022; Wang and Unsworth, 2022; Bettac et al., 2023). In particular, Özaydın and Selway (2022) showed that in various cratons kimberlites tend to be distributed along the margins of conductors and avoid the most resistive and most conductive regions. An early interpretation was that these conductors represented carbon in the form of graphite, which was identified as the carbon that led to diamond growth (e.g., Jones et al., 2005; Türkoğlu et al., 2009). Geochemical data and laboratory experiments have cast doubt on these interpretations, noting that graphite films are only stable at crustal depths and may be a transient feature, potentially lasting for only a few tens of thousands of years (Zhang and Yoshino, 2017). Additionally, the mantle is generally too oxidizing for graphite film formation, even at shallow depths, with the carbon producing carbonate minerals rather than graphite (Frost and McCammon, 2008). More recent interpretations have suggested that the low resistivity is due to metasomatism, a process where the lithosphere is modified by fluids. These studies have concluded that a degree of fluid or melt metasomatism is necessary to produce diamondiferous kimberlites (e.g., Özaydın and Selway, 2022), an interpretation that is consistent with geochemical results (Stachel and Luth, 2015).

The nature of this metasomatism and its genetic relationship with lithospheric mantle conductors and the diamond potential of kimberlites remains unclear. Northern Alberta is an excellent region to investigate this relationship. The region hosts two distinct kimberlite clusters known as the Birch Mountains and Buffalo Head Hills kimberlite fields (Fig. 7.1). Of the two, the Buffalo Head Hills kimberlite field has the best diamond potential, including the possibility that large ultradeep diamond sources exist in the asthenosphere (Banas et al., 2007; Eccles, 2011). In comparison, the Birch Mountains kimberlite field appears to have poor diamond potential (Eccles, 2011). Interestingly, the Birch Mountains kimberlite field is underlain by a low resistivity anomaly in the lithospheric upper mantle. In contrast, the Buffalo Head Hills kimberlite field is not underlain by a conductor (Wang and Unsworth, 2022). The conduction mechanisms and tectonic processes responsible for these contrasting mantle resistivity anomalies remains unclear, as does the relationship between the geophysical anomalies and the diamond potential of each kimberlite field.

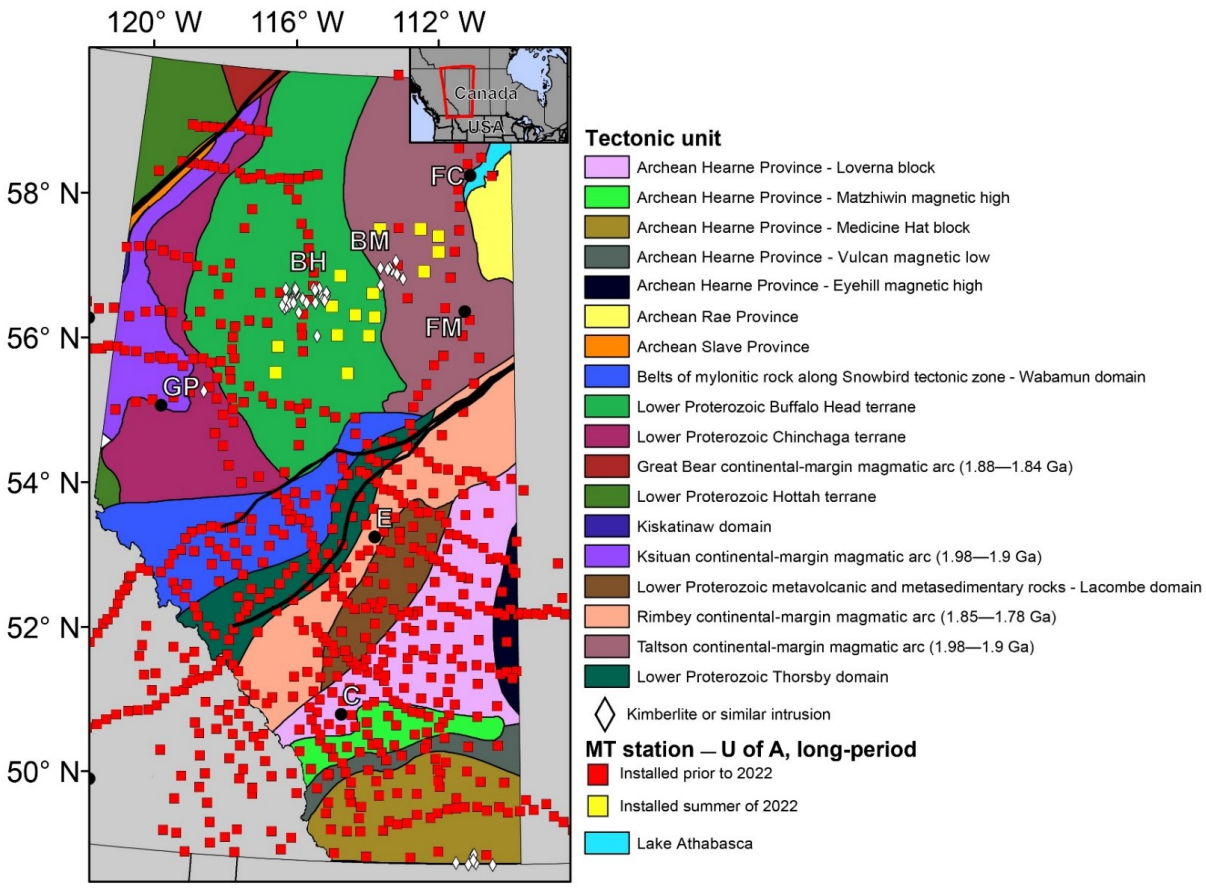

Figure 7.1: *Tectonic map of Alberta showing sites of the University of Alberta's (U of A) long-period magnetotelluric (MT) stations that collected data for this study. Sites shown with yellow symbols are those stations deployed in 2022 with Alberta Energy Regulator support. Thick black lines represent major shear zone boundaries and faults. Abbreviations: BH, Buffalo Head Hills kimberlite field; BM, Birch Mountains kimberlite field; C, Calgary; E, Edmonton; FC, Fort Chipewyan; FM, Fort McMurray; GP, Grand Prairie.*

Carbon is only stable in the form of diamond in the lower lithosphere at pressures greater than 3–5 GPa. This provides an upper limit on the depths at which diamonds can be formed. In settings with a colder geotherm, the diamond stability window begins at a shallower depth and has a greater depth extent. This may permit ascending kimberlites to encounter and entrain more diamonds, producing a greater diamond potential at the surface. The lower depth limit on diamond stability in the lithosphere is the depth of the LAB. Identification of minerals entrained by kimberlites can be used to produce geotherms useful for estimating the vertical extent of the diamond stability window. However, the depth distribution of these minerals is often nonuniform. An alternative approach uses geophysical data to estimate the depth of the LAB. As MT and seismic data are often sensitive to the change in rock properties at the LAB, they can be used to independently

estimate LAB depths over large areas (Eaton et al., 2009; Wang and Unsworth, 2022). This allows the depth extent of the diamond stability window to be determined in regions of interest. This can help to overcome limitations posed by kimberlites, which provide information over only a small area of the lithosphere or may not be accessible in certain exploration scenarios.

Continued development of the spatial and genetic relationship between lithospheric mantle conductors and diamondiferous kimberlites may have profound implications for diamond exploration. These deep mantle conductors could present much larger targets, useful for determining search areas during exploration. This, in combination with the ability of MT to image the LAB, makes MT a valuable reconnaissance tool when selecting target areas for exploration using more expensive techniques. In this report, new MT data collected in 2022 in the area around the Buffalo Head Hills and Birch Mountains kimberlite fields are discussed. These MT data were collected to improve upon the initial model of mantle resistivity structure in the region by Wang and Unsworth (2022). These new MT data will be used to determine (a) which conduction mechanisms caused the low resistivity zone detected in the mantle, (b) how these zones are related to regional tectonics, and (c) how the zones may be related to kimberlite diamond potential.

7.2 Geological setting

The surficial geology in the region is characterized by glacial deposits and a 1–2 km thick section of Phanerozoic sedimentary rocks of the Western Canada Sedimentary Basin (WCSB). The kimberlites have intruded into these sedimentary rocks and reached the near surface. Beneath the WCSB, the rocks consist of crystalline basement terranes that were accreted to the continent during the assembly of Laurentia in the Paleoproterozoic (Hoffman, 1988). These basement terranes will be discussed separately in relation to each kimberlite field.

7.2.1 Buffalo Head Hills kimberlite field

The Buffalo Head Hills kimberlite field is located in the Buffalo Head terrane (Fig. 7.1). This Paleoproterozoic terrane has an age of 2.3–2.0 Ga (Ross et al., 1994) and is interpreted to be a rifted sliver or accretionary terrane that first collided with the western Chinchaga domain during

the collision of the Rae and Slave cratons (Ross, 2002). During accretion, it was located between west- and east-dipping subduction zones to the west and east, respectively (Ross, 2002; Ross and Eaton, 2002). An alternative model suggests that the west-dipping subduction zone was east dipping (Chaco et al., 2000). Another alternative model proposed that the basement is composed of Archean crustal materials that were reworked during the Paleoproterozoic (Burwash et al., 2000). This model does not appear to apply to the lithospheric mantle, as a lack of subcalcic G10 peridotitic garnets argues against the presence of Archean lithosphere (Eccles, 2011).

Kimberlite magmatism occurred in the Buffalo Head Hills kimberlite field during the Late Cretaceous to Paleocene, from ca. 88 to 60 Ma (Kravchinsky et al., 2009; Eccles, 2011). The kimberlite magma sampled a depleted lithosphere during ascent (Eccles and Simonetti, 2008). In total 41 kimberlite pipes have been mapped in the Buffalo Head Hills kimberlite field. Of these, 28 are diamondiferous and the highest diamond grade was estimated at 55 carats per hundred tonnes (Eccles, 2011). The most economically attractive prospects are located in the northwestern portion of the field.

7.2.2 Birch Mountains kimberlite field

The Birch Mountains kimberlite field is located in the Taltson magmatic-arc terrane (or Taltson–Thelon orogenic belt; Fig. 7.1). The Taltson terrane was formed in the Proterozoic as either a plate-margin magmatic arc over a west-dipping subduction zone (Ross, 2002) or a hinterland where magmatism was triggered in response to crustal thickening from far-field convergence farther west (Chacko et al., 2000). Both of these models suggest that the Taltson terrane was formed during the assembly of Laurentia, but differ in the location of the terrane with respect to the plate boundary and the presence of subduction in the region.

Kimberlite magmatism occurred in the Birch Mountains kimberlite field during the Late Cretaceous, from ca. 78 to 70 Ma (Eccles, 2011). In comparison to the Buffalo Head Hills kimberlite field, the kimberlite magma sampled either remarkably thin lithosphere or an extensively re-enriched asthenosphere-type mantle (Eccles, 2011). A few of the intrusions appear to have sampled or originated in shallow levels of the mantle compared to other regional

kimberlites (Eccles, 2011). Of the eight known kimberlite bodies in the Birch Mountains kimberlite field, two do not fit the definition of kimberlites and instead appear similar to young (ca. 60 Ma) alkaline-ultrabasic intrusions in the Buffalo Head Hills kimberlite field (Eccles, 2011). Multiple kimberlites have been sampled for diamonds and have yielded diamond-poor scenarios with only a few micro- and macrodiamonds recovered (Eccles, 2011).

7.3 Previous geophysical surveys

Much of the geophysical data collected in northern Alberta remains in the private domain as part of hydrocarbon or mineral exploration and development efforts by industry. Publicly available data is limited and consists of gravity and aeromagnetic survey data of various vintages. Aeromagnetic data have been used extensively in diamond exploration. This is because the majority of kimberlites have a strong magnetic contrast with the surrounding sedimentary rocks (e.g., Pilkington et al., 2000; Ross and Eaton, 2002; Skelton et al., 2003). In cases where kimberlites are nonmagnetic, other geophysical methods are used in exploration. This includes electromagnetic, gravity, and seismic methods, which have helped to discover additional targets (Skelton et al., 2003). Investigations using aeromagnetic data to delineate regional deep-seated structures that controlled kimberlite emplacement have not yet been performed. However, seismic and gravity data have delineated the Peace River Arch, an east-northeast–trending basement-rooted structure that may have influenced kimberlite emplacement (Eccles, 2011).

Geophysical imaging at crustal and lithospheric mantle depths in the region has been performed using both MT and seismic data. The first major MT dataset was collected as part of the LITHOPROBE project in the 1990s. During LITHOPROBE, data were collected at 323 long-period MT stations in Alberta with the aim of studying the Paleoproterozoic basement terranes. This project included a number of MT stations near the Buffalo Head Hills kimberlite field. These data showed a one-dimensional (1D) resistivity structure in the upper 2–3 km that corresponded to the strata of the Western Canada Sedimentary Basin. The MT data also showed the presence of a two-dimensional (2D) resistivity structure at greater depths in the crystalline basement. A major crustal conductor, the Kiskatinaw conductor, was imaged near the Alberta–British Columbia border (Boerner et al., 2000).

For the past two decades, the University of Alberta has collected MT data at locations across the province with stations located near both the Buffalo Head Hills and Birch Mountains kimberlite fields (Fig. 7.1). The depth of investigation depends on the type of instrument used and the length of recording. For upper crustal studies, broadband MT data is collected for 18–24 hours and produces data in the frequency band of 1000–0.001 Hz. For studies of the lower crust and upper mantle, lower frequencies (longer periods) are needed. Long-period MT data typically requires recording for 2–3 weeks at each location and produces data in the frequency range 1–0.0001 Hz, which corresponds to periods of 1 to 10 000 seconds. Long-period MT data collected near the Buffalo Head Hills kimberlite field by Türkoğlu et al. (2009) showed additional conductors were spatially associated with terrane boundaries. The conductors were interpreted as zones where graphite films or sulphide minerals had been deposited by fluid movement during tectonism (Türkoğlu et al., 2009; Wang and Unsworth, 2022). The occurrence of graphite was significant because at upper mantle depths it could represent the carbon that resulted in diamond growth at greater depths (Türkoğlu et al., 2009). Wang et al. (2018) and Wang and Unsworth (2022) collected additional long-period MT data in the region and found additional conductors that they associated with terrane boundaries and faults. A recently published 3D resistivity model of the entire province produced by Wang and Unsworth (2022) shows that the lithospheric mantle is highly conductive beneath the Birch Mountains kimberlite field and highly resistive beneath the Buffalo Head Hills kimberlite field. The authors interpreted this difference to reflect more intense mantle enrichment and metasomatism beneath the Birch Mountains kimberlite field. This is in agreement with interpretations from regional seismic studies showing a low velocity seismic anomaly in the lithosphere beneath and around the Birch Mountains kimberlite field (Chen et al., 2020). The provincial MT dataset has also been used to interpret conductors related to the tectonic assembly of Alberta farther south (e.g., Nieuwenhuis et al., 2014) and for resource potential in specific areas (e.g., Liddell et al., 2016).

The study by Wang and Unsworth (2022) showed that additional long-period MT data collection was necessary near the kimberlite fields to improve resolution of upper mantle resistivity structure. Critically, the conductor beneath the Birch Mountains kimberlite field was constrained by only three MT stations, limiting the resolution of its geometry. Additionally, no MT data were available

from the region between the two kimberlite fields. As a result, the spatial relationship between the conductor beneath the Birch Mountains kimberlite field and region beneath the Buffalo Head Hills kimberlite field was unclear. The current study focused on collecting additional MT data in order to overcome these limitations of the previous work.

7.4 Magnetotelluric data collection in 2022

The MT survey was planned by the University of Alberta and Alberta Energy Regulator for 2022 in order to improve MT station coverage and address the concerns described above. The survey was conducted in two phases. The first phase aimed to collect MT data between the Birch Mountains and Buffalo Head Hills kimberlite fields where no long-period MT data had been previously collected. This phase aimed at determining if any conductors were present in the lithosphere between the two kimberlite fields or if the conductor beneath the Birch Mountains kimberlite field extended farther west. The second phase aimed to collect additional data around the Birch Mountains kimberlite field in order to improve the resolution of the Birch Mountains conductor (BMC; Wang and Unsworth, 2022), which was previously constrained by data from only a few MT stations (Fig. 7.1). Long-period MT data were collected because they can be used for imaging to the base of the lithosphere.

Over the two phases, 15 long-period MT stations were deployed with an interstation spacing of approximately 50 km (Fig. 7.1). At each location, the MT stations recorded data for 10–14 days. The MT data were recorded with Narod Geophysics Ltd.'s NIMS (Narod Intelligent Magnetotelluric System) long-period MT instruments, which are owned and operated by the University of Alberta. These MT instruments record two orthogonal electric field components and three magnetic field components as a function of time (Fig. 7.2) with an 8 Hz sampling rate. Following best practices for data collection, electrodes were buried 30–40 cm below the surface to avoid the effects of daily temperature variations and precipitation. Bentonite was placed in the electrode holes to improve electrical contact with the ground. Each station was time synchronized using GPS in order to allow for the comparison of the time series and noise removal. Despite extensive oil and gas production infrastructure in the region, cultural noise was minimal, and the

MT stations were always installed more than 500 m away from any major infrastructure. Each station produced approximately 150 MB of time-series data.

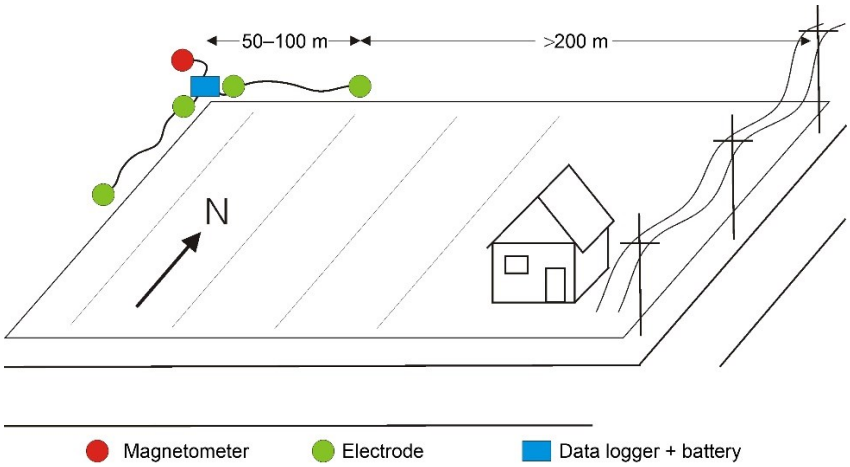

Figure 7.2: *Schematic cartoon showing the layout of a typical magnetotelluric (MT) site. Note that components are not to scale.*

7.5 Magnetotelluric data analysis

The MT method uses natural electromagnetic signals that penetrate the Earth to measure subsurface resistivity. At frequencies greater than 10 Hz, these signals are generated by global lightning activity, and below 1 Hz they are primarily generated by interactions between solar wind and the magnetosphere (Simpson and Bahr, 2005). The depth of signal penetration is proportional to the period (T; the reciprocal of frequency) of the signal and is represented by

$$\delta = 503\sqrt{\rho T} \tag{7.1}$$

where ρ is the electrical resistivity of the Earth measured in ohm•metres (Ω•m) and δ is the depth of signal penetration, called the skin depth, measured in metres. Figure 7.3 shows how the skin depth, as a function of period, decreases in mediums with lower electrical resistivity values. Typically, signals recorded by long-period MT systems are capable of imaging the entire lithosphere.

7.5.1 Time-series analysis

The electric and magnetic field data are recorded in the time domain. They are then transformed into the frequency domain using Fourier analysis to give spectra as a function of frequency. The magnetic field spectra are $H_x(\omega)$, $H_y(\omega)$, and $H_z(\omega)$ and the electric field spectra are $E_x(\omega)$ and $E_y(\omega)$, where ω is the angular frequency. These quantities can be related by

$$Z_{ij} = \frac{E_i(\omega)}{H_j(\omega)} \tag{7.2}$$

where Z is the impedance tensor, and i and j are the x, y, or z components of the respective orthogonal fields. For 3D analysis and modelling, the MT impedance is a complex-valued, full-rank, second-order tensor represented by

$$Z(\omega) = \begin{bmatrix} Z_{xx}(\omega) Z_{xy}\ (\omega) \\ Z_{yx}(\omega) Z_{yy}(\omega) \end{bmatrix} \tag{7.3}$$

Apparent electrical resistivity can be obtained from the impedance by

$$\rho_{ij}(T) = \frac{T}{2\pi\mu} \left| Z_{ij} \right|^2 \tag{7.4}$$

where μ is the magnetic permeability of free space. The apparent resistivity provides an estimate of the electrical properties of the subsurface. Regions of low resistivity can indicate the presence of water, melt, lithosphere modification, and hydrous mineral phases, which can be related to tectonic processes.

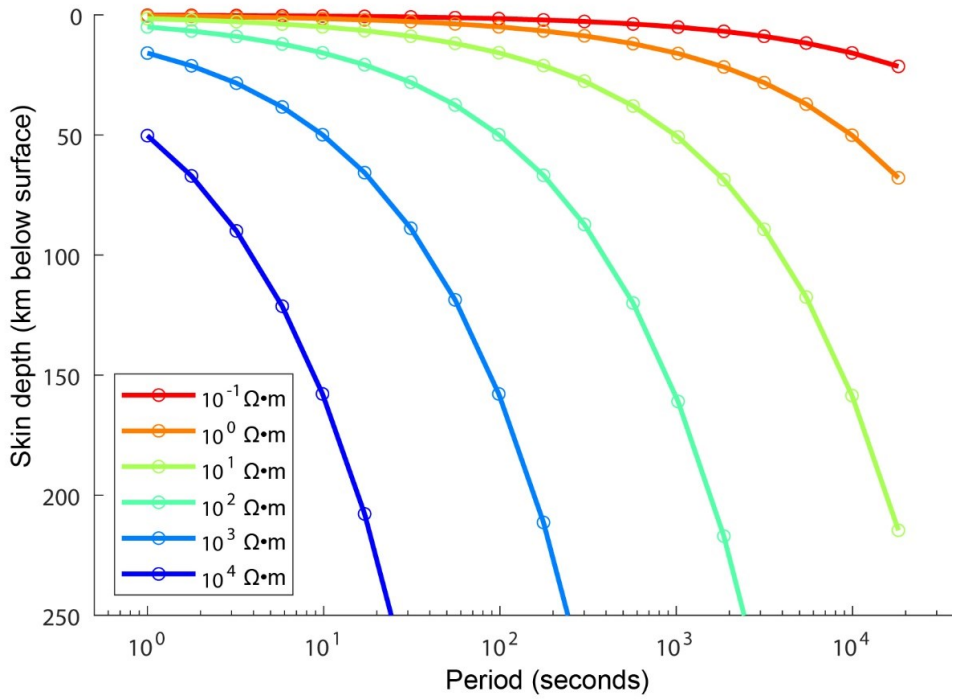

Figure 7.3: *Illustration of the skin depth concept. At higher resistivity values (on the left), the lowest frequency signals penetrate deeper than 250 km. At lower resistivity values (on the right), the lowest frequency signals are quickly attenuated within the upper 50 km of the lithosphere. Figure modified from Hanneson and Unsworth (2023). Abbreviation: Ω, ohm.*

7.5.2 Apparent resistivity, phase, and tipper curves

The apparent resistivity, phase, and tipper curves for each new site are shown in the appendix (Figs. C.1-15). In these figures, the red and blue curves in the apparent resistivity window correspond to the XY and YX components of the data, respectively. The XY component is computed from the north-south electric field and east-west magnetic field. The YX component is computed from the east-west electric field and the north-south magnetic field. If the two curves are coincident, this can indicate that the subsurface is characterized by a 1D resistivity structure. Differences between the curves can indicate the presence of a 2D or 3D resistivity structure. Determination of dimensionality requires that the apparent resistivity and phase are examined as a function of a coordinate system.

A common pattern in the northern Alberta data is that as period increases, the apparent resistivity rises then falls. This generally reflects a three-layer resistivity structure with

1) a near-surface, low resistivity layer that can be identified as the sedimentary rocks of the WCSB,

2) an underlying high resistivity layer that can be identified as the lithosphere, and

3) a deep, low resistivity layer that can be identified as the asthenosphere.

There are some systematic differences between the 15 sounding curves (Figs. C.1-15), generally in the degree to which the XY and YX data components are different at periods greater than 10–100 seconds. This indicates deviations from a simple 1D resistivity model. To determine a resistivity model, a formal inversion process is required, as described below (Section 0).

7.5.3. Phase tensors

The dimensionality of the MT data was evaluated using phase tensors. Phase tensors display the azimuthal variation of the impedance and give a graphical way, in the form of a coloured circle or ellipse, to determine if the subsurface has a 1D, 2D, or 3D resistivity structure (Caldwell et al., 2004). The direction of the major axis (i.e., long axis) of the ellipse is either parallel or perpendicular to the geoelectric strike, typically representing the conductive anomalies of interest. A parameter called the skew angle is also calculated, it indicates the dimensionality and is represented by the colour of the circle (Booker, 2014). A circular phase tensor with zero skew reflects a 1D resistivity structure, an elliptical tensor with zero skew indicates a 2D resistivity structure, and an elliptical tensor with non-zero skew indicates a 3D resistivity structure (Caldwell et al., 2004; Booker, 2014). An important aspect of the phase tensor is that it is not affected by near-surface galvanic distortions (Booker, 2014).

The phase tensors in Alberta are shown in Figure 7.4. At periods of less than 20 seconds, the data are 3D in nature, which reflects the low resistivity and structural complexity of the WCSB. For

periods from 20 to 200 seconds, the data are again 3D in nature around the Birch Mountains kimberlite field, which corresponds to the BMC noted by Wang and Unsworth (2022). Around the Buffalo Head Hills kimberlite field, the 3D dimensionality likely reflects a conductive structure east of the kimberlite field, as observed by Türkoğlu et al. (2009), Wang et al. (2018), and Wang and Unsworth (2022). In the period range of 200–2000 seconds, the dimensionality of the data becomes more 1D to 2D, likely reflecting a simpler lithosphere structure below the major conductors. At periods greater than 2000 seconds, the data again become 3D, likely reflecting the complexity of the asthenosphere and LAB in the region (Wang and Unsworth, 2022).

7.6 3D Inversion of magnetotelluric data

The MT data presented in Figures 7.4 and C.1-15 are shown as a function of frequency. To use these MT data to investigate the Earth's structure, the MT data must be converted into a resistivity model as a function of depth and horizontal position. This is done using a mathematical process called inversion, which produces a model of subsurface resistivity that fits the measured MT data curves to a specified statistical misfit. To do this, the inversion program represents the resistivity structure of the Earth as a set of layers or cells that each have an associated electrical resistivity. The predicted MT response of this model is compared to the measured MT data curves. The resistivity model is refined in a series of iterations until the predicted MT response of the model matches the measured MT data to within a specified tolerance. The inversion of MT data can use 1D, 2D, and 3D approaches. The 1D approach is the simplest and assumes a resistivity model with a set of horizontal layers (Simpson and Bahr, 2005). The 2D approach uses a model where resistivity varies with depth and distance along a profile of MT stations (Simpson and Bahr, 2005). A limitation of the 2D approach is that it assumes that the resistivity structure is invariant in the direction perpendicular to the profile. This may be approximately true in some cases, but in general the resistivity structure of the crust and upper mantle varies in three directions. The 3D inversion approach makes no assumptions about the subsurface structure but requires a much greater number of parameters than the 1D or 2D inversion approaches to define the subsurface structure. This means that the computational cost of a 3D inversion is far greater than for 1D or 2D inversions.

All inversions are subject to non-uniqueness, which means that many resistivity models can satisfy the measured MT data to the same statistical tolerance. Many inversion algorithms impose the requirement of spatial smoothness on the resistivity model. Thus, the inversion algorithm seeks the smoothest model that is consistent with the measured MT data. This reduces the number of artifacts introduced into the resulting model. Non-uniqueness can also be minimized by applying knowledge of regional geology and using other types of data as constraints during inversion or interpretation.

The 3D inversion approach was used because the survey collected data from a grid of stations (Fig. 7.1) and the phase tensors in Figure 7.4 showed that the resistivity structure of the subsurface is three dimensional. In this study, the 3D inversion approach was performed using the ModEM (Modular system for Electromagnetic inversion) code of Kelbert et al. (2014). This inversion process is computationally demanding, requiring the use of high-performance computer clusters. Two resistivity models were obtained by the inversion of the MT data and are compared in this report.

The 2022 resistivity model, published by Wang and Unsworth (2022), includes all of the long-period MT data collected across Alberta prior to 2022 (Fig. 7.1). The 2022 model was obtained by the following inversion procedure. The inversion began from a starting model that had a uniform resistivity of 100 Ω•m. The model was divided into cells that were 8 km wide in both the north-south and east-west directions. In the vertical direction, the first row of cells was assigned a thickness of 60 m and subsequent cell thicknesses increased geometrically by a factor of 1.2. This resulted in a total of 70 cells in the vertical direction. The starting model contained 198 by 136 by 70 cells. The inversion used data from 396 MT stations (in Alberta and southeastern British Columbia; Fig 7.1) and obtained a final root mean square (RMS) misfit value of 1.533 after 302 iterations (Fig 7.1). Topography was not included in this inversion. Error floors of 10% and 5% were applied to the diagonal and off-diagonal components of the impedance tensor, respectively, to handle noise in the data and avoid overfitting some data with small errors. Wang (2019) and Wang and Unsworth (2022) performed robust analyses of the sensitivity of the MT data to the various anomalies. The results of those studies showed the major conductors, including the BMC, were required to fit the measured MT data.

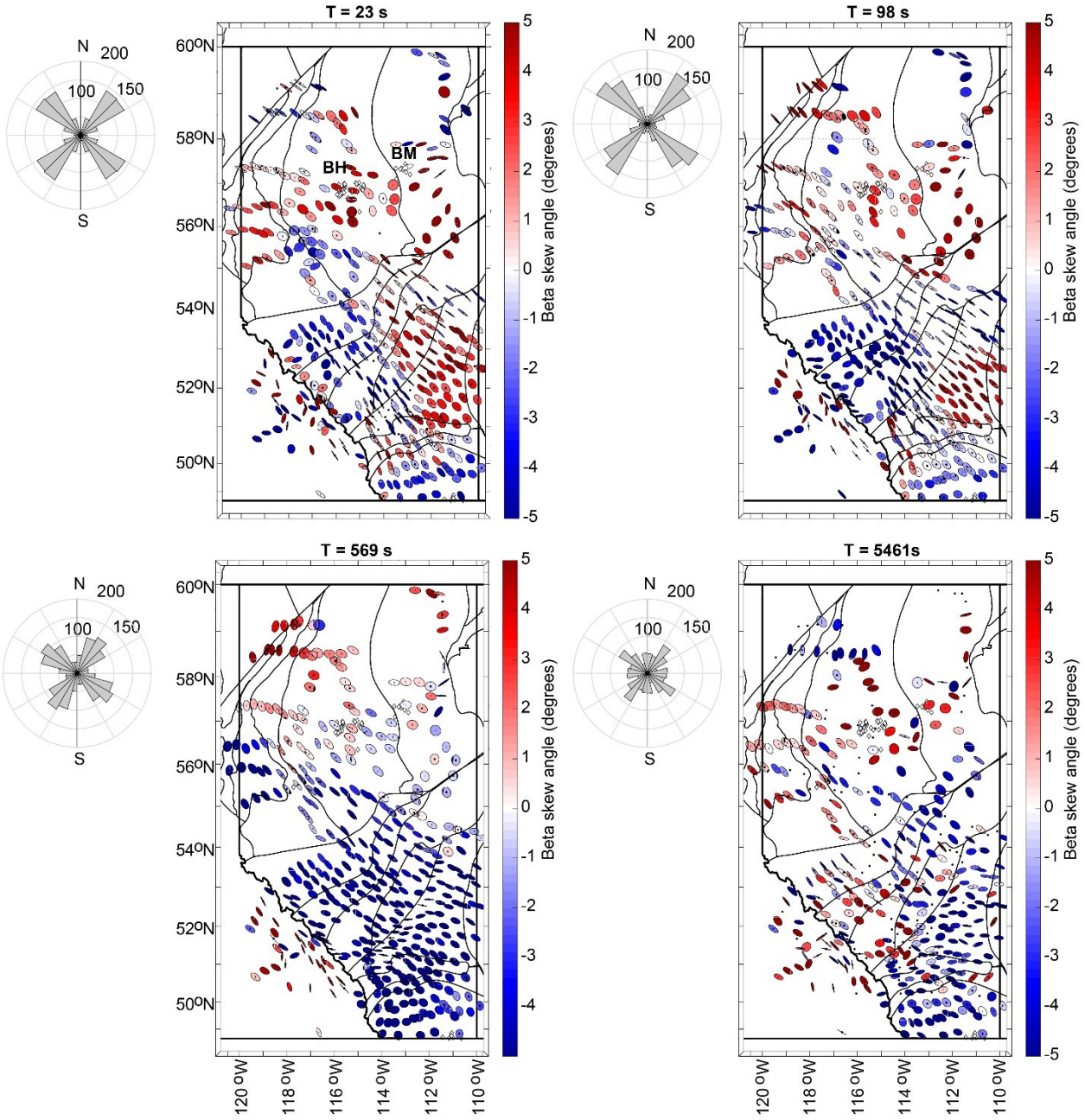

Figure 7.4: *Phase tensors in Alberta at periods (T) of 23, 98, 569, and 5461 seconds (s). The rose diagrams show trends in the orientations of the major and minor axes of the phase tensors. Black dots indicate sites of magnetotelluric stations and white diamonds indicate individual kimberlite and similar intrusions. Thin black lines represent tectonic terrane boundaries (see Figure 7.1). Thick black lines represent the provincial borders. Abbreviations: BH, Buffalo Head Hills kimberlite field; BM, Birch Mountains kimberlite field.*

The 2023 resistivity model was obtained by an inversion of the original MT data and the additional MT data collected in 2022, from a total of 411 stations (in Alberta and southeastern British Columbia; Fig. 7.1). The 2023 inversion used the same starting model and parameters as the 2022 model. The 2023 inversion obtained a final RMS misfit value of 1.4746 after 315 iterations (Fig. 7.5). Again, topography was not included in this inversion.

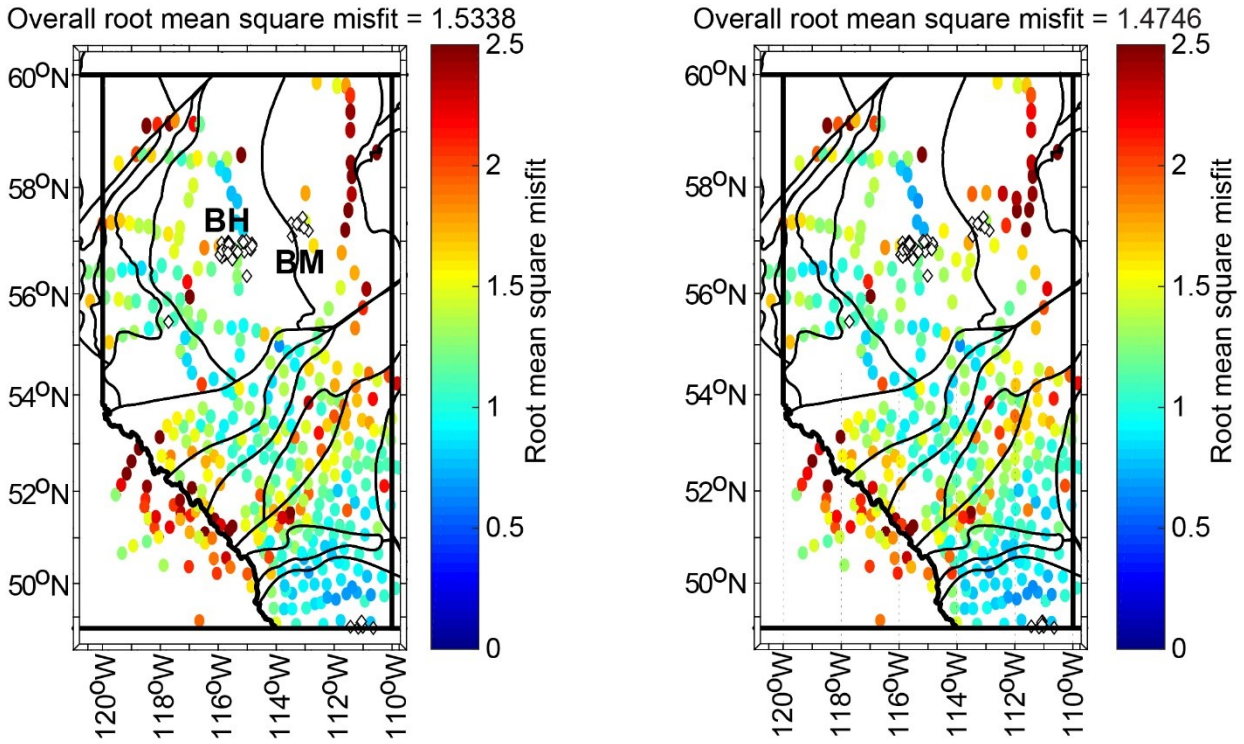

Figure 7.5: *Root mean square misfit maps for the 2022 model (left) and 2023 model (right). The value for each station is represented by a coloured ellipse. White diamonds indicate individual kimberlite and similar intrusions. Thin black lines represent tectonic terrane boundaries (see Figure 7.1). Thick black lines represent the provincial borders. Abbreviations: BH, Buffalo Head Hills kimberlite field; BM, Birch Mountains kimberlite field.*

A comparison of both resistivity models across all of Alberta is described below. However, given that the recently collected MT data focused on the Birch Mountains and Buffalo Head Hills kimberlite fields, this will remain the focus of the discussion in this report. Readers interested in the analysis and interpretation of the additional features and anomalies outside of this region are directed to Nieuwenhuis et al. (2014), Liddell et al. (2016), Wang et al. (2018), and Wang and Unsworth (2022).

7.6.1 Observations on the 2022 model of Wang and Unsworth (2022)

Slices from the 2022 model are shown in Figure 7.6 (with comparable 2023 slices shown in Fig 7.7), 7.Figure (with comparable 2023 slices shown in Fig. 7.9), 7.10, and 7.11 and show the following:

- In the depth range 0–1 km bsl, a series of shallow conductors are located around both kimberlite fields (Fig. 7.6). The features have resistivity values in the range of 1–30 Ω•m and can be identified as the sedimentary rocks of the WCSB. These WCSB conductors are more obvious farther south where the MT station coverage is denser. The WCSB is spatially continuous in both the north-south and east-west directions. However, it is not imaged as a horizontally continuous layer because of the relatively large distance between the MT stations. This phenomenon has been observed in the inversion models obtained in other MT studies, including the EarthScope project in the United States (Bedrosian, 2016).

- In the depth range 2–20 km bsl, the region around the Buffalo Head Hills kimberlite field is resistive with resistivity values in the range of 100–10 000 Ω•m (Fig. 7.6). This can be interpreted as representing the crystalline rocks that underlie the WCSB. In contrast, around the Birch Mountains kimberlite field, a series of discrete 1–10 Ω•m conductors are present in the crystalline basement (Fig. 7.6).

- In the depth range 20–70 km bsl, the same resistivity pattern as the 2–20 km bsl depth is observed. Beneath the Buffalo Head Hills kimberlite field, the crustal and upper mantle resistivity remains high. Beneath the Birch Mountains kimberlite field, the resistivity increases with depth but remains lower than beneath the Buffalo Head Hills region (Fig. 7.6).

- Between 100 and 200 km bsl, a major north-south trending region of low resistivity (1–50 Ω•m), termed the BMC, is observed east and northeast of the Birch Mountains kimberlite field (Fig. 7.8). North-south cross-sections of the model are displayed in Figure 7.10 and show that the BMC first appears at a depth of 100 km bsl. The southern edge dips steeply to the south of the Birch Mountains kimberlites (Fig. 7.10). The northern edge dips northwards at a gentler

angle until the boundary of the model (Fig. 7.10). Slightly east of the Birch Mountains kimberlite field, the BMC appears to connect upwards with the shallow conductors located in the crust near the Birch Mountains kimberlite field and farther north near Fort Chipewyan (Fig. 7.1, 7.10, and 7.11). Where MT station coverage is the densest, east of the Birch Mountains kimberlite field, a resistive block appears to interrupt these low resistivity structures. East-west cross-sections in Figure 11 show that the BMC appears as a conductive impingement on another otherwise resistive lithosphere. North of the Birch Mountains kimberlite field, this impingement rises to a depth of 100 km bsl; farther south it only rises to a depth of 180 km bsl.

- Starting at a depth of 150 km bsl, the BMC bends westwards until it underlies the Birch Mountains kimberlite field at a depth of 200 km bsl (Figs. 7.8 and 7.11). The resistivity increases with depth until 250 km bsl where it merges with a regional scale 20–30 Ω•m conductor underlying most of northern Alberta, which can be identified as the asthenosphere (Fig. 7.8). The lithospheric resistivity beneath the Buffalo Head Hills kimberlite field is the exact opposite of what is observed beneath the Birch Mountains kimberlite field. In fact, it distinctly remains the most resistive lithosphere in northern Alberta until the regional conductor at 250 km bsl is encountered (Fig. 7.8).

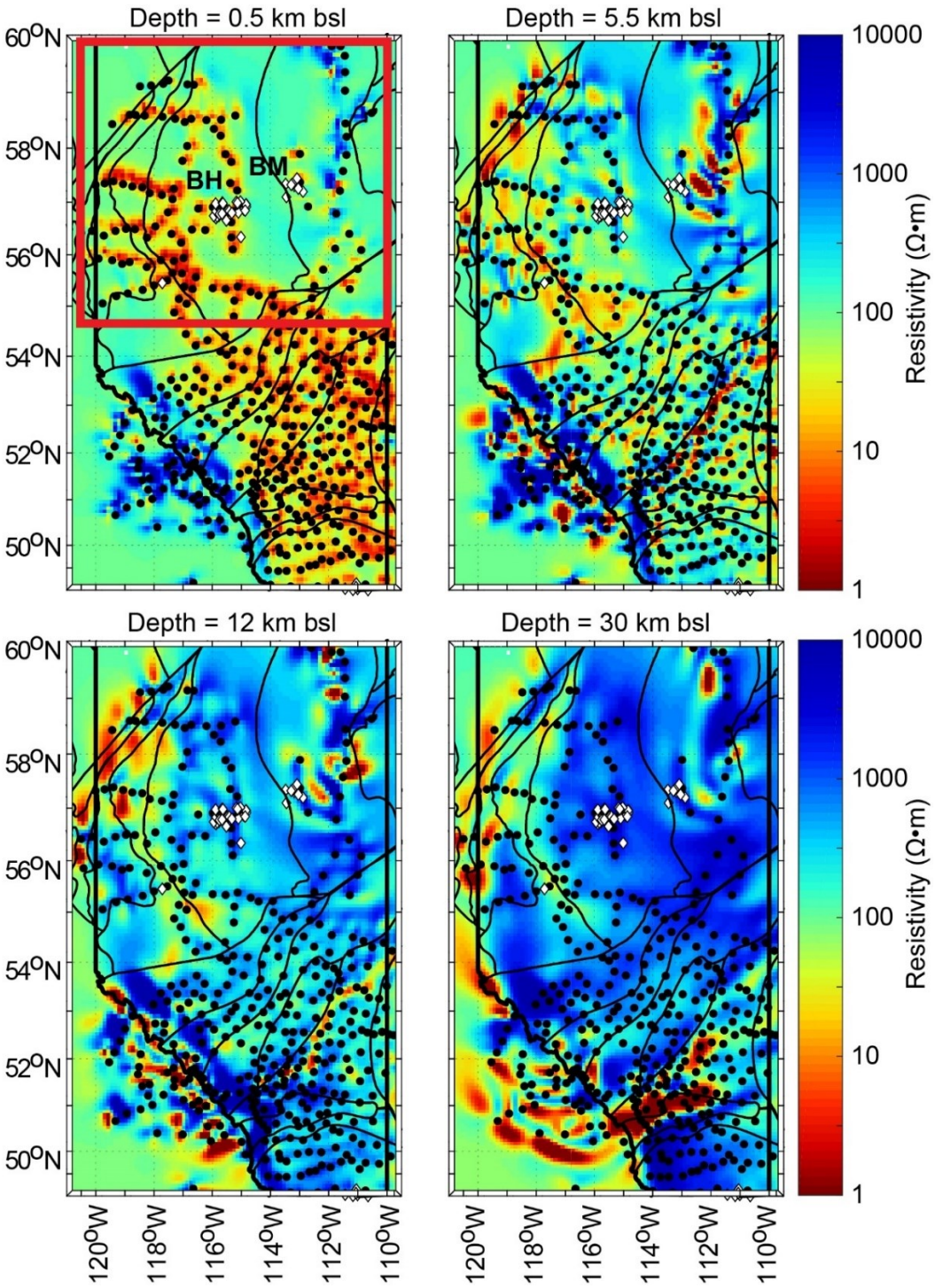

Figure 7.6: *Horizontal model slices from the 2022 resistivity model at depths of 0.5, 5.5, 12, and 30 km below sea level. The red box in the upper left panel is the area shown in Figures 7.10, 7.11, and 7.13. Black dots indicate sites of magnetotelluric stations and white diamonds indicate individual kimberlite and similar intrusions. Thin black lines represent tectonic terrane boundaries (see Fig. 7.1). Thick black lines represent the provincial borders. Abbreviations: Ω, ohm; BH, Buffalo Head Hills kimberlite field; BM, Birch Mountains kimberlite field.*

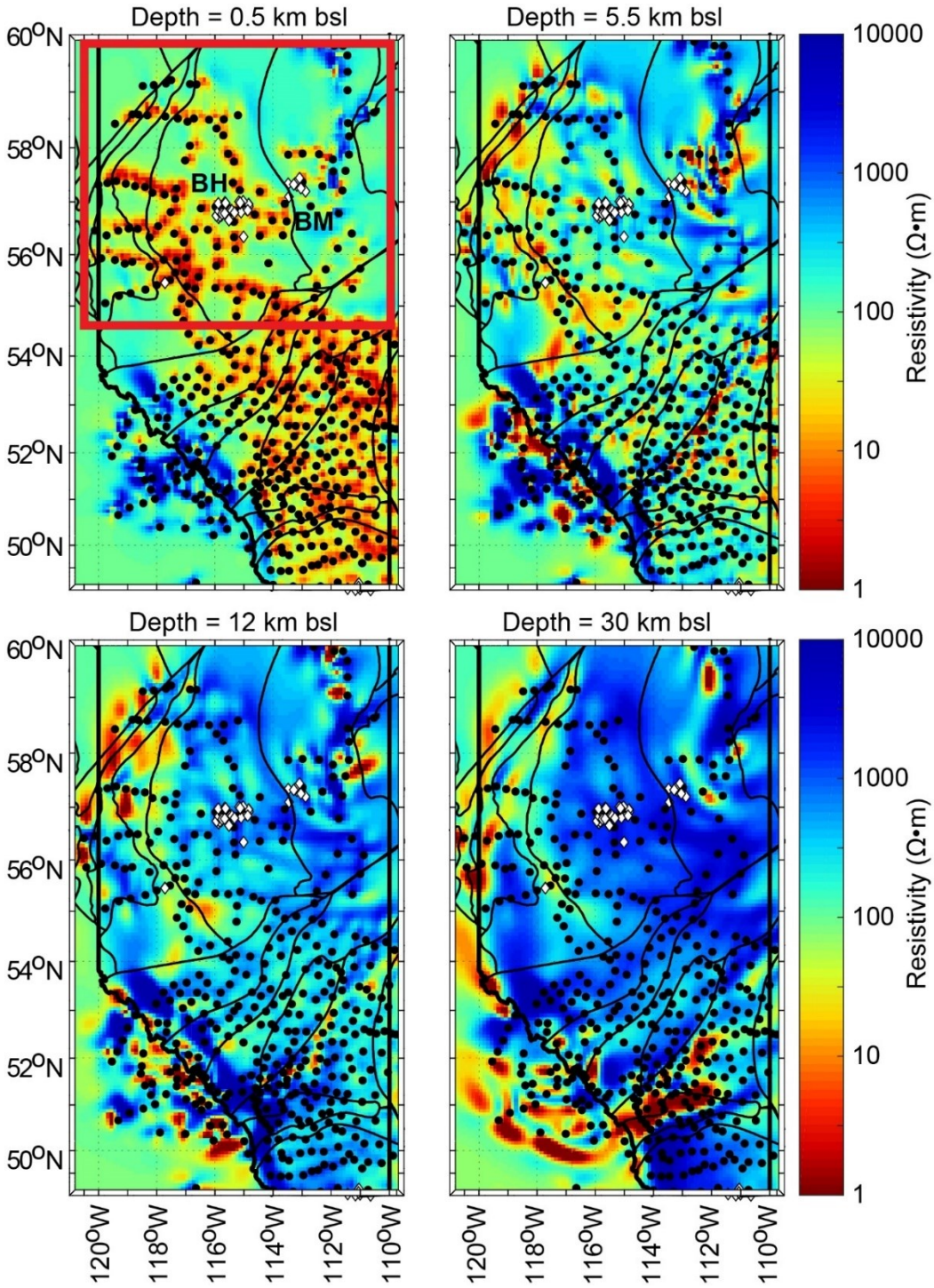

Figure 7.7: *Horizontal model slices from the 2023 resistivity model at depths of 0.5, 5.5, 12, and 30 km below sea level. The red box in the upper left panel is the area shown in Figures 7.10 and 7.11. Black dots indicate sites of magnetotelluric stations and white diamonds indicate individual kimberlite and similar intrusions. Thin black lines represent tectonic terrane boundaries (see Fig. 7.1). Thick black lines represent the provincial borders. Abbreviations: Ω, ohm; BH, Buffalo Head Hills kimberlite field; BM, Birch Mountains kimberlite field.*

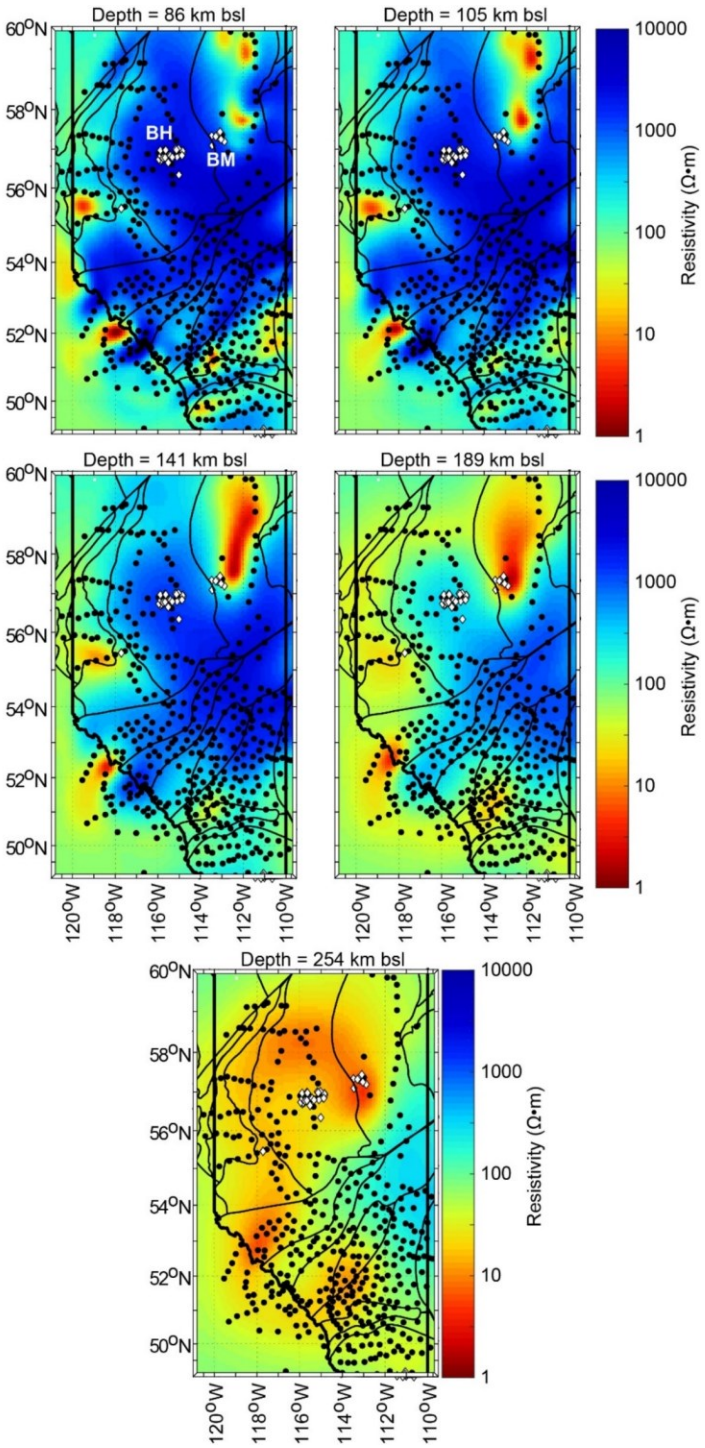

Figure 7.8: *Horizontal model slices from the 2022 resistivity model at depths of 86, 105, 141, 189, and 254 km below sea level. Black dots indicate sites of magnetotelluric stations and white diamonds indicate individual kimberlite and similar intrusions. Thin black lines represent tectonic terrane boundaries (see Fig. 7.1). Thick black lines represent the provincial borders. Abbreviations: Ω, ohm; BH, Buffalo Head Hills kimberlite field; BM, Birch Mountains kimberlite field.*

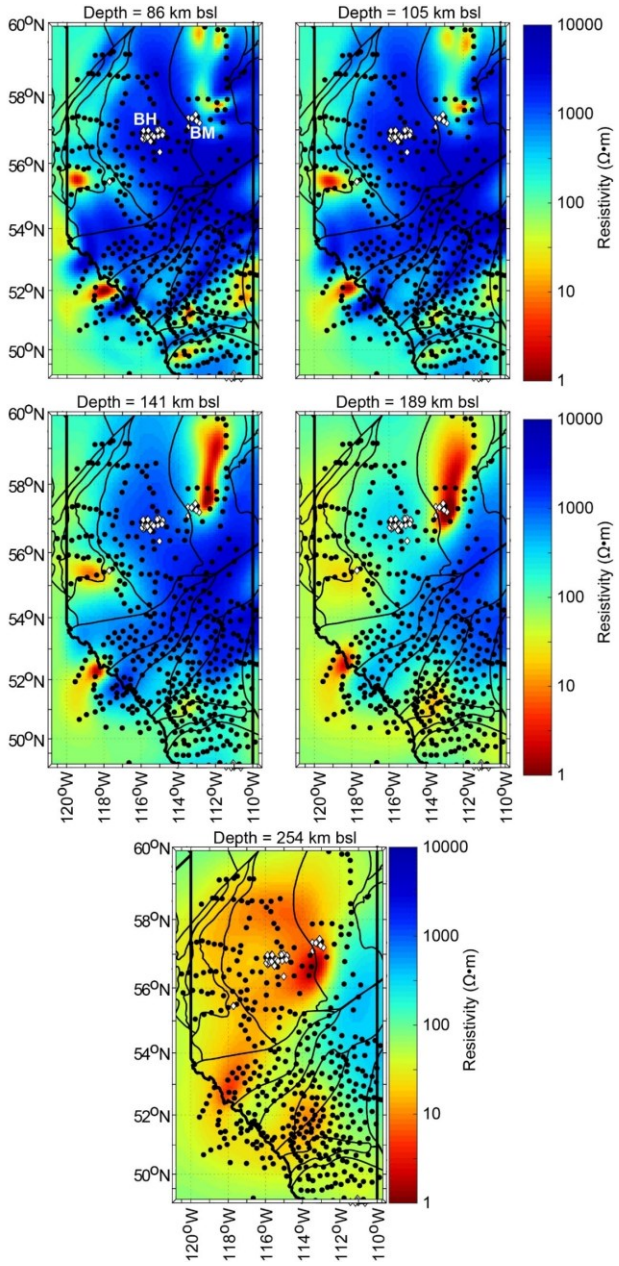

Figure 7.9: *Horizontal model slices from the 2023 resistivity model at depths of 86, 105, 141, 189, and 254 km below sea level. Black dots indicate sites of magnetotelluric stations and white diamonds indicate individual kimberlite and similar intrusions. Thin black lines represent tectonic terrane boundaries (see Fig. 7.1). Thick black lines represent the provincial borders. Abbreviations: Ω, ohm; BH, Buffalo Head Hills kimberlite field; BM, Birch Mountains kimberlite field.*

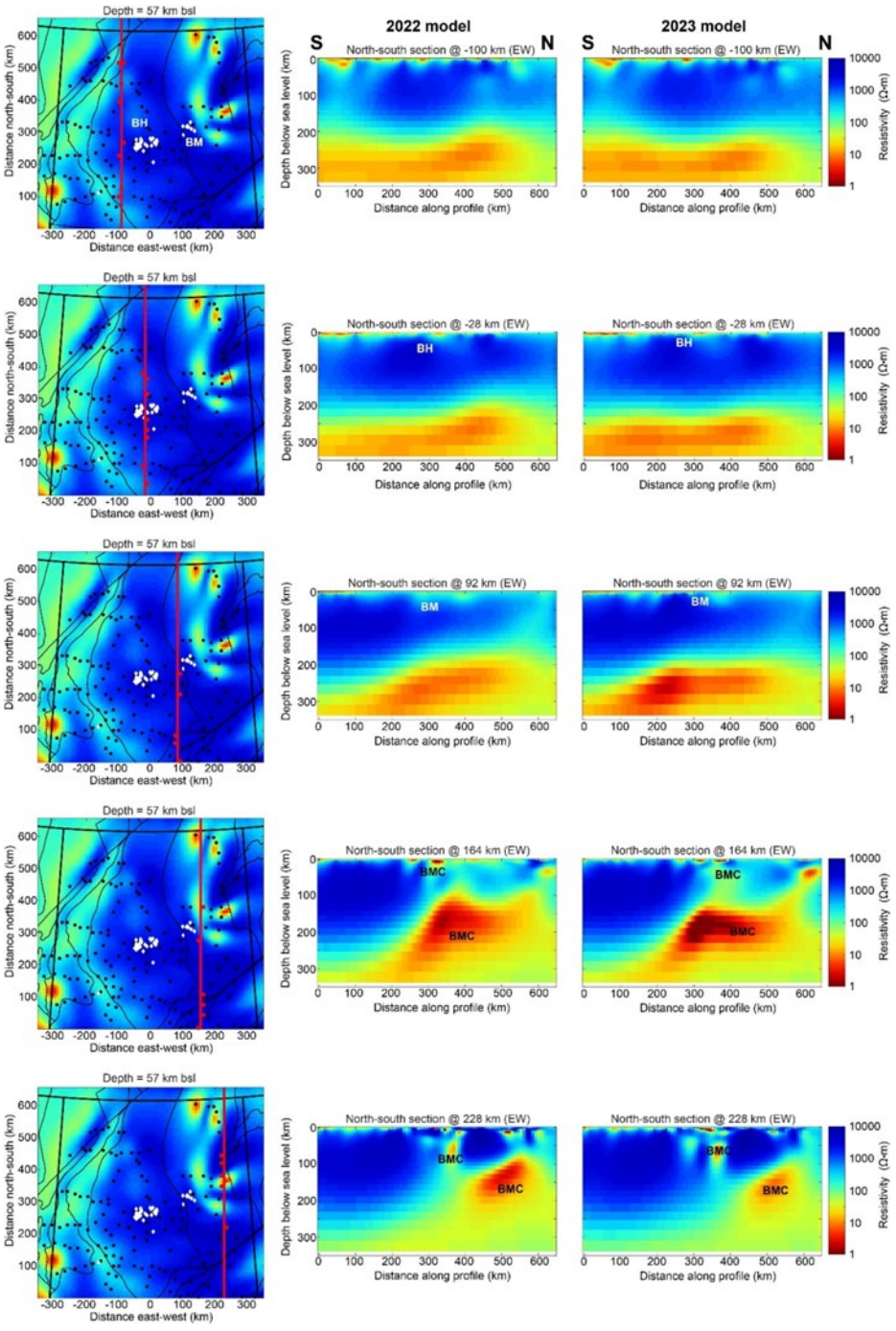

Figure 7.10: *North-south vertical depth slices of the northern portion of the model region (outlined in Fig. 7.6). The left column shows the model region, with the purple line showing the path of the slice. (black dots indicate sites of magnetotelluric stations and white diamonds indicate individual kimberlite and similar intrusions; thin black lines represent tectonic terrane boundaries [see Fig. 7.1]; thick black lines represent the provincial borders). The centre column shows the slice from the 2022 resistivity model, the right column shows the slice from the 2023 resistivity model. Abbreviations: Ω, ohm; BH, Buffalo Head Hills kimberlite field; BM, Birch Mountains kimberlite field; BMC, Birch Mountains conductor; EW, east-west.*

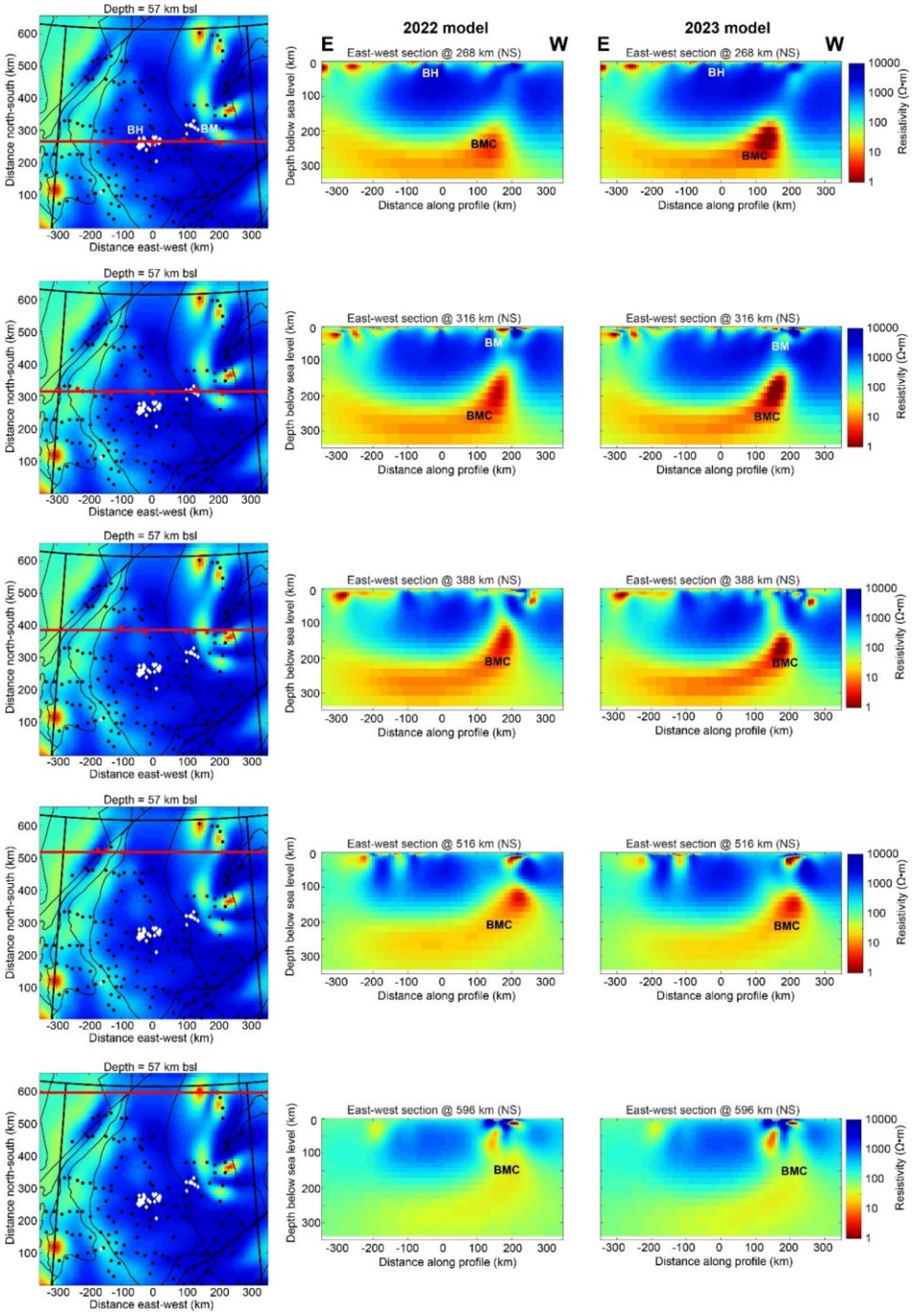

Figure 7.11: *East-west vertical depth slices of the northern portion of the model region (outlined in Fig. 7.6). The left column shows the model region, with the purple line showing the path of the slice (black dots indicate sites of magnetotelluric stations and white diamonds indicate individual kimberlite and similar intrusions; thin black lines represent tectonic terrane boundaries [see Fig 7.1; thick black lines represent the provincial borders). The centre column shows the slice from the 2022 resistivity model, the right column shows the slice from the 2023 resistivity model.*

Abbreviations: Ω, ohm; BH, Buffalo Head Hills kimberlite field; BM, Birch Mountains kimberlite field; BMC, Birch Mountains conductor; NS, north-south.

7.6.2. Observations on the new 2023 3D resistivity model

The new 3D resistivity model of Alberta generally shows the same features as those described in Section 0. This section will only discuss the differences observed between the two resistivity models.

At depths less than 6 km bsl, the new resistivity model shows that the shallow conductors east and northeast of the Birch Mountains kimberlite field are more numerous and smaller than in the 2022 model (Fig. 7.7). At depths down to 12 km bsl, the conductor just east of the Birch Mountains kimberlite field evident in Figure 7.6 is not longer evident (Fig. 7.7). Below a depth of 12 km bsl, the resistivity structure is very similar to the 2022 model, and the BMC is still present in the depth range 80–200 km bsl (Figs. 7.8 and 7.9). However, the spatial extent of the low resistivity anomaly has decreased, and the anomaly is narrower than in the 2022 model (compare Figs. 7.8 and 7.9). In the east-west and north-south cross-sections, there are limited differences between the two models (Figs. 7.10 and 7.11).

7.7 Interpretation

Summary Figure 7.12a–d displays the results of both models and a comparison of them to seismic anomalies in the region. The new 2023 3D resistivity model is generally similar to the model previously published by Wang and Unsworth (2022). The major change in the 2023 model is that the BMC is imaged as a sharper, narrower feature than in the 2022 model. Additionally, in the new model the BMC does not extend as far west towards the Buffalo Head Hills kimberlite field as in the 2022 model. The presence of the BMC beneath the Birch Mountains kimberlite field and the absence of a conductor beneath the Buffalo Head Hills kimberlite field is significant. Seismic data also show a similar difference in lithospheric structure, with a low velocity anomaly beneath the Birch Mountains kimberlite field and no anomaly beneath the Buffalo Head Hills kimberlite field (Fig. 7.12b; Chen et al., 2020). An isosurface plot of the BMC and asthenosphere conductors shows a remarkable correspondence between the low velocity anomaly of Chen et al. (2020) and

the resistivity model (Fig. 7.13). Wang and Unsworth (2022) noted that the kimberlites of the Birch Mountains kimberlite field either sampled warmer temperature zones or originated at shallower depths than kimberlites found in the Buffalo Head Hills kimberlite field (Eccles, 2011). Wang and Unsworth (2022) integrated their results with constraints from (1) the seismic study of Chen et al. (2020; Fig. 7.12c); (2) xenolith studies of Burwash et al. (2000); and (3) a petrological study of Eccles et al. (2004). Wang and Unsworth (2022) suggested that both the low resistivity and low velocity seismic anomalies associated with the BMC may reflect either (1) intense metasomatic modification that introduced hydrous minerals such as phlogopite or amphibole or (2) extensive enrichment of the lithosphere beneath the Birch Mountains kimberlite field. They also suggest that the resistive lithosphere beneath the Buffalo Head Hills kimberlite field reflects an absence of this modification or enrichment, and instead represents dry and depleted lithosphere.

Recent laboratory experiments allow a quantitative analysis of the lithospheric resistivity values determined from the MT data. The presence of hydrous minerals can produce both low resistivity and low velocity seismic anomalies (Selway, 2014, 2018; Rader et al., 2015). The seismic anomalies associated with the BMC correspond to an ~2% velocity reduction in shear wave velocity (Chen et al., 2018, 2020), which requires the presence of 5–7% phlogopite or 10% amphibole (Rader et al., 2015). Modelling of these hydrous phases in a mantle of a similar age and thermal structure, located farther east in Saskatchewan, showed that phlogopite can explain the resistivity values of the BMC in the upper mantle (Chase and Unsworth, 2022). Amphibole is not a viable explanation for the low resistivity anomaly because this mineral phase is not stable at pressures greater than 3 GPa, which occur at a depth of around 100 km and the BMC is deeper than this. At shallower depths, the modelling of Chase and Unsworth (2022) suggest phlogopite becomes less viable as an explanation for the low resistivity anomaly because 10–25% phlogopite by volume would be required to produce the resistivity of 1–10 Ω•m observed in the BMC. This amount of phlogopite would produce seismic anomalies greater than those observed in the region (Rader et al., 2015; Chen et al., 2018, 2020).

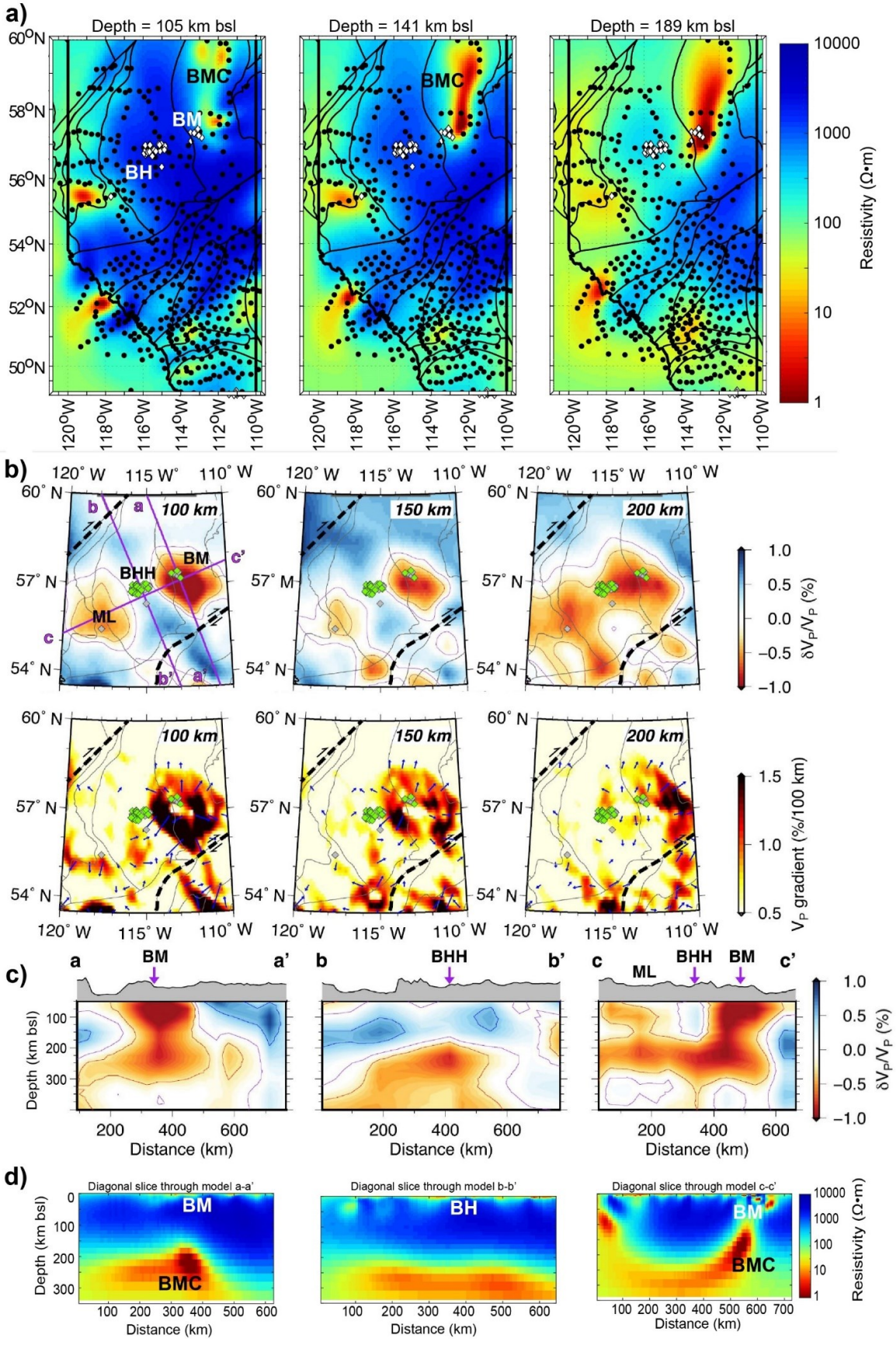
a)
Depth = 105 km bsl
Depth = 141 km bsl
Depth = 189 km bsl
BMC
BM
BH
Resistivity (Ω•m)
b)
100 km
150 km
200 km
BHH
ML
δVP/VP (%)
VP gradient (%/100 km)
c)
Depth (km bsl)
Distance (km)
d)
Diagonal slice through model a-a'
Diagonal slice through model b-b'
Diagonal slice through model c-c'

Figure 7.12: *(a) Horizontal model slices from the 2022 resistivity model showing the Birch Mountains conductor (BMC) at depths of 105, 141, and 189 km below sea level (bsl). Black dots indicate sites of magnetotelluric stations and white diamonds indicate individual kimberlite and similar intrusions. Thin black lines represent terrane boundaries (see Fig. 7.1). Thick black lines represent the provincial borders. (b) Horizontal model slices from the seismic model of Chen et al. (2020) at depths of 100, 150, and 200 km bsl, similar depths to those shown in (a). The slices show a low velocity anomaly beneath the Birch Mountains kimberlite field (BM) and no anomaly beneath Buffalo Head Hills kimberlite field (BH/BHH). Green and grey diamonds indicate diamondiferous and nondiamondiferous kimberlite fields, respectively; black dashed lines indicate the Great Slave Lake shear zone and Snowbird tectonic zone; blue arrows indicate the directions of the largest velocity gradients; grey lines represent terrane boundaries; and purple lines indicate the locations of profiles shown in (c). (c) Vertical model slices from the seismic model of Chen et al. (2020) showing the low velocity anomaly with depth. The locations of the profiles are shown in the upper left-hand model slice in (b). (d) Vertical model slices from the 2023 resistivity model taken over the same profile locations as (c). Note that the vertical scale of (c) is different from (d). Abbreviations: Ω, ohm; ML, Mountain Lake kimberlite field; Vp, seismic p-wave velocity.*

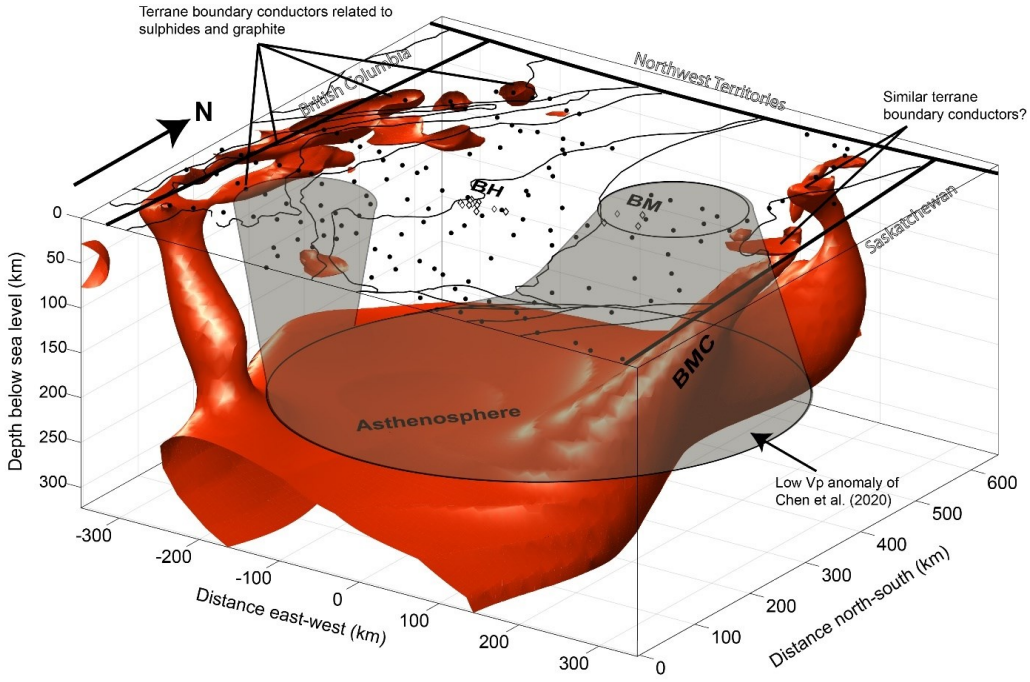

Figure 7.13: *Isosurface plot from the 2023 resistivity model at 30 ohm•metres (Ω•m) showing the geometry of the low resistivity anomalies in the study area (see Fig. 7.6 for location). The shallow conductors in the west were interpreted by Türkoğlu et al. (2009) and Wang et al. (2018). Black dots indicate sites of magnetotelluric stations and white diamonds indicate individual kimberlite and similar intrusions. Abbreviations: BH, Buffalo Head Hills kimberlite field; BM, Birch Mountains kimberlite field; BMC, Birch Mountains conductor; Vp, seismic p-wave velocity.*

The alternative hypothesis suggested by Wang and Unsworth (2022) to explain the low resistivity of the BMC was lithospheric enrichment. This would reduce seismic velocities (Deen et al., 2006)

and is consistent with the model of Chen et al. (2018, 2020). However, enrichment is unlikely to produce low resistivity anomalies unless the mantle minerals are also enriched in water in the form of H^+ (Selway, 2018). Wang and Unsworth (2022) modelled the resistivity effects produced by enrichment of olivine in water and concluded that the observed BMC resistivity values could not be explained with this conduction mechanism. Chase and Unsworth (2022), again farther east in Saskatchewan, showed that the resistivity values observed in the BMC could be reproduced in the lowermost lithospheric mantle via water enrichment if the lithosphere is modelled with a more complex multiphase mineralogy. However, similar to phlogopite, water enrichment becomes a less viable mechanism at depths shallower than 100–150 km because the water concentrations required would exceed the solubility limits of mantle minerals (Padrón-Navarta and Hermann, 2017; Chase and Unsworth, 2022). A direct assessment of the resistivity of the BMC using the updated techniques of Chase and Unsworth (2022) will be performed for the lithosphere beneath northern Alberta in the near future.

In the isosurface plot shown in Figure 7.13, the BMC and asthenosphere conductors connect to shallower upper crustal conductors located to both the east and west of the two kimberlite fields. The western series of shallow conductors has been previously interpreted as reflecting sulphides or graphite deposited during terrane assembly and associated metamorphism (Türkoğlu et al., 2009; Wang and Unsworth, 2022). The eastern conductors are offset from the Birch Mountains kimberlite field by 50–100 km (Figure 7.13), and their exact nature is unknown. However, many of the conductivity mechanisms that can help to explain low resistivity anomalies in the mantle have minimal effect on resistivity values in the crust (Chase and Unsworth, 2022). The notable exceptions to this are sulphides and graphite. As a result, it remains plausible that the genetic origin of the eastern conductors is similar to those found to the west (Figure 7.13). A direct assessment of these shallow conductors will also be performed in the near future.

In summary, the mechanisms suggested by Wang and Unsworth (2022) to explain BMC resistivity values in the lower lithospheric mantle remain plausible based on mantle resistivity modelling and constraints from seismic and xenolith data. However, rigorous mantle resistivity modelling has not been performed and will benefit from the additional data collected at MT stations in 2022 and discussed in this report. Further, as noted by Wang and Unsworth (2022), the connection of the

BMC to the asthenosphere, the northward extension of the BMC, and the vertical geometry of the BMC remains unexplained. The genetic relationship of the BMC and other regional conductors to the diamond potential of both the Buffalo Head Hills and Birch Mountains kimberlite fields has also not been investigated. Finally, the connection between the BMC, the asthenosphere conductor, and the shallow conductors east and west of the kimberlite fields remains unclear. In future research, analysis of these new MT data will be used to examine these unanswered questions.

7.8 Conclusions

In this study, a preliminary three-dimensional resistivity model has been developed for the Buffalo Head Hills and Birch Mountains kimberlite fields using long-period magnetotelluric (MT) data. The main objective of the study was to evaluate how the recently collected MT data have improved imaging of a large lithospheric mantle conductor beneath the Birch Mountains kimberlite field and the lack of a conductor beneath the Buffalo Head Hills kimberlite field. The existence, or lack of, an anomaly near or underneath a kimberlite field has previously been inferred to be related to the diamond potential of the kimberlites. This study shows the conductor beneath the Birch Mountains kimberlite field is narrower than previously imaged and does not extend significantly westward towards the Buffalo Head Hills kimberlite field. Further, the lithosphere beneath the Buffalo Head Hills kimberlite field is among the most resistive lithosphere in northern Alberta. Tentative modelling results suggest that interpretations by other authors that the Birch Mountains conductor (BMC) could represent a region of lithosphere enrichment or hydrous minerals remain valid. A more extensive investigation of the causes of the low mantle resistivity will be undertaken in order to fully evaluate which conductivity enhancing mechanisms could explain the low resistivity of the BMC. These results will be compared with regional xenolith analytical and mantle petrological data to determine if there is a genetic relationship between the anomalies and kimberlite diamond potential.

CHAPTER 8. SUMMARY

This thesis has described studies of three regions of the Laurentian craton using deep-sounding magnetotelluric data. Three separate study areas of the craton were investigated to understand their subsurface electrical resistivity structure. The first study was described in Chapter 5 and investigated the Southern Oklahoma Aulacogen (SOA). The SOA is a poorly understood feature on the southern margin of the Laurentian craton. A 2-D electrical resistivity model was produced using a profile of long-period MT (LMT) stations collected across the SOA. This resistivity model provided the highest resolution to date image of the whole lithosphere in this region and gave significant insights into lithosphere structure. The second study is described in Chapter 6, and was an investigation of the enigmatic Sask craton and surrounding areas of the Trans-Hudson Orogen. A grid of LMT stations was collected, combined with legacy MT datasets in the region, and inverted to produce a 3-D electrical resistivity model for the entire lithosphere. This 3-D electrical resistivity model mapped important tectonic and compositional boundaries as well as possible pathways taken by mineralizing fluids in the region. The third study was described in Chapter 7 and was an investigation of the Taltson Magmatic Zone and Buffalo Head terranes in northern Alberta, where two distinct yet similarly aged kimberlite fields with contrasting diamond potential are located. A grid of LMT stations was collected in the region to improve the resolution of the 3-D electrical resistivity model of Alberta previously published by Wang and Unsworth (2022). The improved electrical resistivity model removed uncertainty in the previous model about the lithospheric resistivity structure around these kimberlite fields. Each of these investigations is summarized in the following sections.

8.1 The lithosphere structure beneath the Southern Oklahoma Aulacogen

The 2-D inversion of LMT data across the SOA produced a resistivity model characterized by a conductive anomaly that was located in the crust and mantle lithosphere coincident with the north-south extent of the aulacogen, as defined by magnetic and seismic data (e.g., Brewer et al., 1983; Chase et al., 2022). This conductor was referred to as the Southern Oklahoma Aulacogen conductor (SOAC). A second, more regional conductor was located beneath the SOAC and was referred to

as the lower lithosphere conductor (LLC). The LLC extends to the edges of the new inversion model, and so its spatial extent is not fully known, but it extends north-south for at least 350 km.

Quantitative interpretation of the properties of two resistivity anomalies was performed separately. The resistivity of the SOAC anomaly was interpreted to be the result of a combination of conductive phases, including contributions from graphite, sulfides, and water enrichment. A change in the size of olivine grains may also contribute to the low resistivity anomaly through the process of diminution. The sulfides, water, and graphite could have been introduced via metasomatic fluid enrichment processes when rifting occurred along the SOA during the Cambrian. The olivine diminution could have occurred later in the Pennsylvanian-Permian when the SOA was involved in Ancestral Rocky Mountain deformation. Cambrian metasomatism likely would have mechanically weakened the lithosphere beneath the SOA. This mechanical weakening may explain why the Ancestral Rocky Mountain deformation along the SOA was so pronounced (e.g., Brewer et al., 1983; McConnell, 1989). It has previously been suggested that the various Ancestral Rocky Mountains uplifts within Laurentia were located along paleo-rifts such as the SOA (Marshak et al., 2003). The mechanical weakening mechanism proposed to have occurred beneath the SOA may also be applicable to other rift-related Ancestral Rocky Mountain uplifts. This could provide a plausible mechanism for the isolated and dispersed nature of Ancestral Rocky Mountain uplifts that are located exclusively within the interior of the Laurentian craton and not along the proposed tectonic margins. In other words, the Ancestral Rocky Mountain uplifts could represent anomalous, unique locations where the lithosphere was sufficiently weak and allowed for deformation.

The resistivity of the upper part of the LLC was interpreted to be due to the presence of a phlogopite mid-lithosphere discontinuity that is underlain by a water-enriched lower lithosphere. The percentage of phlogopite required to explain the resistivity anomaly is similar to the amount required to explain the seismic velocity of a mid-lithosphere discontinuity that is coincident with the top of the LLC (Kumar et al., 2012; Rader et al., 2015). This seismic mid-lithosphere discontinuity is present across much of the Laurentian craton in the Midwest United States (Kumar et al., 2012). However, over this larger area, the mid-lithosphere discontinuity is not electrically conductive (Bedrosian, 2016). Geochemical data from the Cambrian rift-related volcanics in the

SOA support the presence of fluorine-rich fluids (Hogan & Gilbert, 1998; Hanson et al., 2013; Price, 2014). Fluorine is suggested to be the primary charge carrier that makes phlogopite electrically conductive (Li et al., 2017). The low resistivity of the mid-lithosphere discontinuity beneath the SOA may reflect fluorine-bearing phlogopite that was enriched by fluorine-rich fluids associated with Cambrian rift-related magmatism in the SOA. The high resistivities associated with the mid-lithosphere discontinuities in the Midwest United States further north could then reflect phlogopite that has not been enriched with fluorine. The water-enriched lower lithosphere could have been formed by the accretion of the head of the enriched plume that was responsible for rifting and volcanism along the SOA during the Cambrian. The mid-lithosphere discontinuity may then reflect a paleo-lithosphere-asthenosphere boundary present prior to Cambrian rifting. This would be in agreement with prior suggestions that mid-lithosphere discontinuities may reflect paleo lithosphere-asthenosphere boundaries (Hansen et al., 2015; Rader et al., 2015; Selway, 2018).

8.2 The lithosphere structure around the Sask craton and Fort à la Corne

The 3-D inversion of MT data collected in the Sask craton, Trans-Hudson Orogen (THO), and Fort à la Corne (FALC) kimberlite field revealed a number of low resistivity anomalies in the region. The most striking anomaly is a major conductor located in the upper mantle lithosphere beneath the northern portion of the Sask craton. This conductor was referred to as the Northern Sask Craton (NSC) conductor. The NSC conductor was interpreted as a sulfide-rich layer located in the mid-lithosphere of the Sask craton. It is hypothesized that this sulfide-rich layer was formed as the result of a subducted slab undergoing flat slab subduction and then being accreted to the base of the northern Sask craton during the terminal phase of Manikewan Ocean closure. The sulfide-rich layer resulted from the mobilization of sulfur from the crust of the down-going slab, which precipitated sulfides upon interacting with the overlying depleted lithosphere of the Sask craton. This model proposes that much of the lithosphere of the northern Sask craton was added during the formation of the THO. This model is in line with eclogite (i.e., subducted oceanic crust) observed in xenolith data at the same depth as the NSC conductor (Czas et al., 2018). It is also consistent with xenolith data that supports the formation of a significant amount of the lithosphere of the Sask craton during the formation of the THO (Czas et al., 2020). The model also suggests

that a previously unrecognized east-dipping subduction zone may have been present along the western margin of the Sask craton.

An additional series of conductors was also observed in the resistivity model in the curst and upper lithospheric mantle. These conductors were referred to as C1-C4. These conductors all connect with the NSC conductor and extend upwards into the crust. The low resistivity of the C1-C4 conductors was interpreted to be due to the presence of a combination of sulfides and graphite, with graphite becoming more common in the crust where interconnected films may be stable. These conductors could have been formed by fluids being released from the downgoing flat slab, which then ascended upwards through the lithosphere and crust. Interestingly, two of these conductors are located beneath the Flin Flon and La Ronge areas of Saskatchewan, which are known centers of mineralization. These conductors could indicate source pathways for mineralizing fluids and may explain the prolific orogenic and volcanogenic massive sulfide metal resources in these areas. The other conductors are located further south below the Phanerozoic sedimentary cover in a region that is not known for mineralization. These conductors could represent additional targets for exploration that have been previously unrecognized due to their burial beneath the thin sedimentary cover in the area.

The movement of fluids in the region appears to have been influenced by the lithospheric structure Sask craton. The C1-C4 anomalies all ascend around the edge of the Sask craton. Similarly, the FALC, Pikoo, and Candle Lake kimberlites are also located around the edge of the Sask craton and the NSC conductor. It is likely that fluids and kimberlite melts were unable to move through the refractory and depleted pre-THO Sask craton lithosphere. Instead, the fluids ascended along compositional and terrane boundaries created along each side of the Sask craton during flat slab subduction and its interactions with adjacent terranes during THO formation. In this model, the localization of kimberlites and mineralization in the region was influenced by the formation of the NSC conductor and major tectonic structures and boundaries. Exploration around or along these features could yield additional economic deposits of minerals or kimberlites.

8.3 The contrasting lithosphere structure in northern Alberta and its relationship to diamond potential

The new long-period MT data were added to the Alberta resistivity model of Wang and Unsworth (2022) and improved resistivity model resolution within the Taltson magmatic zone and Buffalo Head terranes. Critically, the new LMT data filled in an approximately 200 km wide gap in the model of Wang and Unsworth (2022) that existed between the Buffalo Head Hills and Birch Mountains kimberlite fields. This dramatically improved model resolution in the region and eliminated ambiguity on whether any resistivity structures existed between the two kimberlite fields. The new data also improved the resolution of known resistivity anomalies in the region, particularly the Birch Mountains Conductor (BMC), which was previously constrained with only a few LMT stations arranged along profiles. The new resistivity model shows that the Birch Mountains kimberlite field is underlain by the most prominent conductive anomaly in the region, the BMC, located in the lower lithosphere, whereas the Buffalo Head Hills kimberlite field is clearly associated with the most resistive lithosphere in the region. The lowermost portion of the BMC at the base of the lithosphere can be explained by enriched water contents or phlogopite, as suggested by prior authors (e.g., Wang and Unsworth, 2022). However, with decreasing depth, realistic variations in water content cannot reproduce the observed resistivity values in the BMC. While phlogopite can partially explain the observed BMC resistivity values, this would require high phlogopite concentrations that would produce a major change in seismic velocity far in excess of those observed in the region (Chen et al., 2018; 2020). A paper describing the conductors in northern Alberta, including the BMC, is in progress.

8.4. The resistivity structure beneath kimberlites in Canada

Conductive anomalies in the mantle are often spatially associated with the locations of kimberlites (e.g., Türkoğlu et al., 2009; Özaydın and Selway, 2022; Bettac et al., 2023). This has motivated investigations into evaluating if there is a genetic relationship between these anomalies, kimberlite formation, and diamond potential. In some cases, resistivity anomalies at relatively shallow depths in the crust and upper mantle have been interpreted as graphite. In this interpretation, it is inferred that the carbon in the form of graphite at shallow depths implies that carbon is present and formed

diamonds at greater depths (e.g., Türkoğlu et al., 2009). Similarly, conductors in the deeper mantle lithosphere have been interpreted to reflect regions of metasomatized (i.e., enriched) lithosphere that aided kimberlite genesis and ascent by supplying volatiles and favorable conditions for melt ascent sustainability (e.g., Özaydın and Selway, 2022). The bulk of both the geophysical and xenolith data used to make these interpretations are from studies in Southern Africa. As a result, it is unclear if these models have global applicability or are more regionally limited. The work in this thesis provides new 3-D geophysical coverage over a number of additional kimberlite clusters. There is clearly a first-order spatial relationship between the distribution of kimberlites and the spatial extent of conductive mantle lithosphere features, as both are located near each other in FALC and Northern Alberta. Özaydın and Selway (2022) proposed that kimberlites and diamondiferous kimberlites can often be located near conductive (i.e., metasomatically modified or enriched) lithosphere but are generally not found within the most conductive and most resistive (i.e., depleted) regions. The authors proposed that regions near conductors provided a "Goldilocks zone" of volatiles and conditions for melt sustainability that allowed kimberlites to form and ascend. This interpretation appears to partially hold here, as the kimberlites in both Saskatchewan and Northern Alberta are located in close proximity to the conductive anomalies but not on top of them. However, the Buffalo Head Hills kimberlites, which have a substantial diamond potential, are located within some of the most resistive lithosphere in Northern Alberta. The results here suggest that the conductive anomalies in the study areas are related to major lithosphere structures and terrane boundaries that provided favorable conduits for localizing kimberlites. This same model probably applies to the Slave craton (e.g., Bettac et al., 2023), where a major conductor in the mantle lithosphere near kimberlites was interpreted as a relic feature related to an accreted subducted slab. However, it is unclear if this model applies to regions such as Southern Africa (e.g., Özaydın and Selway, 2022), but it likely does, as it seems reasonable to conclude that the centers of metasomatic modification linked to kimberlites there probably developed preferentially along major preexisting lithosphere structures or terrane boundaries. As a result, kimberlites, and possibly diamond potential, appear to be related to major conductive anomalies associated with major lithosphere structures. These structures acted to allow for both modification of the lithosphere and favorable conditions for kimberlite ascent. However, the applicability of this model more globally and in pursuit of a mineral systems model for kimberlites will require

additional xenolith and geophysical data collection over other regions where kimberlites are found.

8.5 Modification of the Laurentian lithosphere

The resistivity models from the three study areas show that the Laurentian craton has a complex internal structure that formed as the result of a protracted and multi-phase tectonic evolution. The resistivity model from the Sask craton and FALC demonstrates the important role that subduction played in the formation and stabilization of the oldest core region of the Laurentian craton during the Trans-Hudson Orogeny. Subduction also appears to have been critically important in the construction of the Slave craton further north in Laurentia (e.g., Bettac et al., 2023, and references therein). This argues that subduction during the first stages of craton assembly played a critical role in forming the various Archean cratonic nuclei. In turn, these nuclei then played an important role in the assembly of the overall Laurentian craton to produce the form observed today. The resistivity model from the SOA shows that the edges of the cratonic lithosphere can be extensively modified during tectonism. However, this modification does not always appear to have threatened the long-term survivability of the Laurentian craton. In fact, the accretion of the plume head to the lower lithosphere in the region shows that centers of extensive modification can be centers where thickened lithosphere is formed, ultimately resulting in further cratonization of the lithosphere. Curiously, the SOA results show that not all rifting-related modifications are created equal, as the Midcontinent Rift further north in Laurentia is not associated with electrically conductive lithosphere (e.g., Bedrosian, 2016). Finally, the resistivity model from Northern Alberta argues that the cratonic lithosphere can be extensively thinned without major changes (i.e., magmatic or deformation) occurring at the surface. Similar thinning of thick lithosphere was observed by Kim and Evans (2024) in the Northeastern United States. The thickness of the cratonic lithosphere is a dynamic, evolving process in response to tectonic activity that may not always have an expression at the surface. Combined, these results argue that the evolution of the Laurentian craton and its constituent terranes has been a dynamic and complex process. These results also demonstrate that a considerable amount of information on the interactions between major tectonic processes (i.e., subduction, orogenesis, plume impacts, and rifting) and the lithosphere can be preserved within

cratons. This preservation stores information vital for determining how present-day active tectonic processes have evolved and will continue to evolve with time.

8.6 Deep resistivity structure and mineralization

The low resistivity anomalies around the Sask craton and in northeastern Alberta appear to be spatially associated with either known mineralization, or regions with mineral potential. In the majority of cases, the low resistivity of these anomalies can be interpreted as being caused by sulfide minerals or graphite films deposited by past episodes of fluid flow. These low resistivity anomalies extend deep into the crust or lithosphere mantle and suggest a relationship between shallow economic mineralization and deep electrical structures associated with fluid flow. This relationship is not unique to the resistivity models presented here and has also been observed in resistivity models from the Slave craton and Olympic Dam (e.g., Heinson et al., 2018; Bettac et al., 2023). This relationship is becoming increasingly important in identifying and locating major centers of mineralization in Australia and China. However, it has not yet been applied to North America in any serious manner. The results from the Sask craton are especially striking, as the major conduit-like features are located beneath all of the major centers of known mineralization in the region where LMT data coverage is available. Much of this mineralization is located within volcanogenic massive sulfide deposits, which are largely thought to be features whose formation is largely confined to the crust with limited input from greater depths. The low-resistivity, conduit-like anomalies beneath regions such as Flin Flon make a compelling case that mineralization in these deposits could be related, at least in part, to past fluid movements, processes, and structures at greater depths than those proposed by current mineralization models. Additionally, while the main processes for mineralization in volcanogenic massive sulfides are predominately confined to crustal processes, perhaps these deeper features act to upgrade or enhance the mineralization of nearby deposits during their formation. It is highly unlikely that the presence of these deep low resistivity anomalies beneath known centers of prolific mineralization is purely coincidental. A current trend is that the exploration and mining industries are considering using new techniques and datasets to locate new economic prospects. It is my view that these deep conductive anomalies are likely related to mineralization and show that the processes related to mineralization operate on much larger spatial scales than are accounted for in most current exploration models. If this is

the case, these deep conductors could represent ideal targets for locating prospective centers of mineralization and mineral potential to target with higher-resolution methods. They may be especially important during the early stages of exploration, as their sheer size makes them easy to locate and identify.

8.7 Future Work

8.7.1 Regional structure around the Southern Oklahoma Aulacogen

At the time of data collection, the LMT data collected as part of the work in Chapter 5 were the only publicly available LMT data available in the region. Since that time, the national EarthScope LMT array in the United States has expanded station coverage throughout the southern United States, including Oklahoma and Texas. This new EarthScope data offers the opportunity to perform a 3-D inversion for the SOA region. This 3-D inversion can be used to evaluate the extent of the SOAC and LLC resistivity anomalies in a more robust way than possible with 2-D inversion. A 3-D inversion could answer questions regarding the total extent of the lithosphere modified by Cambrian rifting. A 3-D inversion would also be able to investigate if the SOA extends as far west as Colorado and New Mexico as has been previously suggested (e.g., Budnik, 1986; Brueke et al., 2016). This inversion could be better integrated with regional EarthScope teleseismic studies (e.g., Kumar et al., 2012; Evanzia et al., 2014; Porritt et al., 2014) to better interpret regional lithosphere structure. Ultimately, this model can be used to evaluate the structure beneath each of the Ancestral Rocky Mountain uplifts in order to determine the origin of the unique deformation associated with this orogeny.

8.7.2 The Trans-Hudson Orogen

3-D LMT data coverage and imaging of the THO in the United States have been made possible by the EarthScope array (e.g., Bedrosian and Finn, 2021). This type of study has helped to answer questions regarding the along-strike structure and complexity of the THO during its formation. In Canada, equivalent 3-D data coverage is lacking. Much of our knowledge of the THO in Canada comes from widely spaced 2-D MT profiles that we collected with predominantly broadband data,

which are largely limited to imaging only the crust. As a result, knowledge about the deep structure (i.e., whole lithosphere) and along-strike variability in the structure of the THO in Canada is lacking. To address this, an extension of the LMT data collected as part of the work in Chapter 6 is being planned. Figure 8.1 shows the regional existing MT data coverage by sounding type and also shows the future LMT survey being planned. 22 additional stations have already been collected in north-central Manitoba that will extend the resistivity model of Chapter 6 across the Superior craton margin and provide the first well-constrained 3-D LMT resistivity model across the entire THO. An additional survey of more than 70 LMT stations is being planned to expand LMT data coverage across the THO down to the United States–Canada border. Ultimately, these LMT data will be used to produce a resistivity 3-D resistivity model for the THO in southern Canada that will be linked to existing continental-scale resistivity models in the United States. These models will be extremely useful for the development of a 3-D model of the lithosphere architecture and tectonic evolution of the THO.

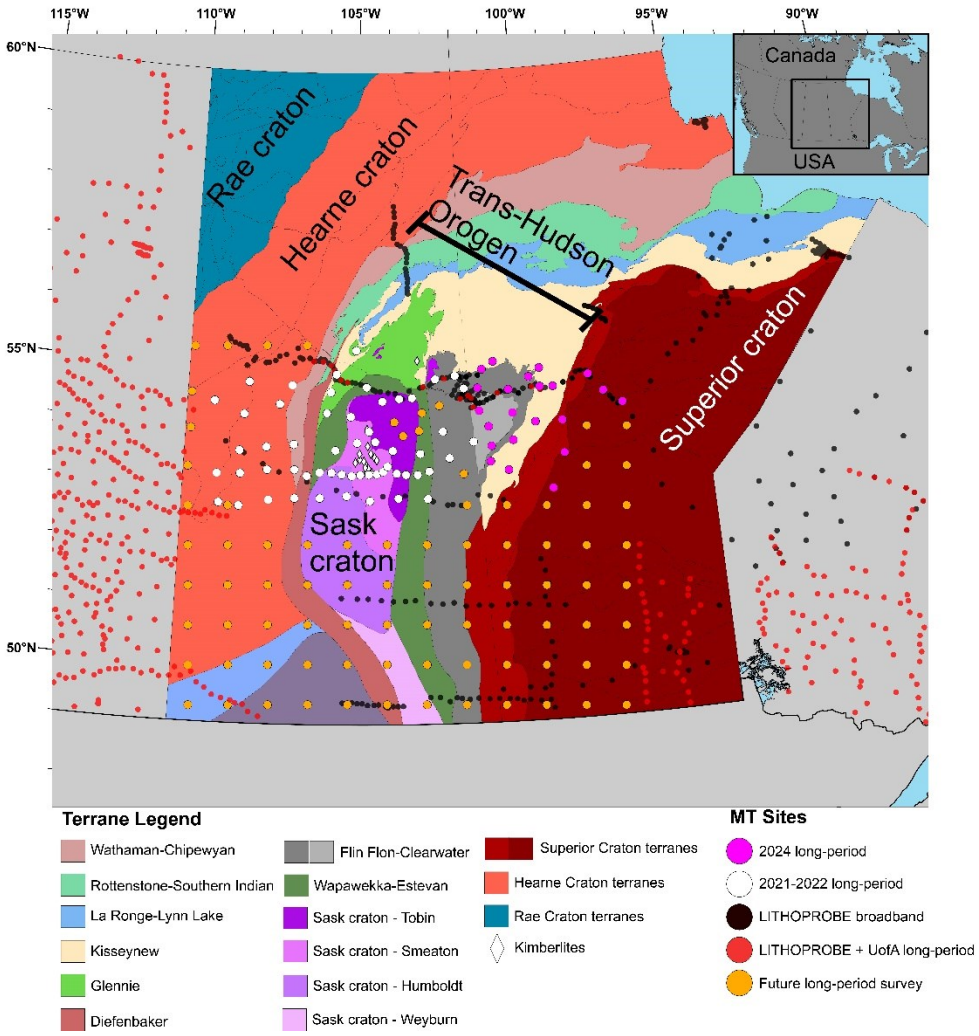

Figure 8.1*: Tectonic terrane map of the Trans-Hudson Orogen in Saskatchewan and Manitoba shows the extent of MT data in the region. The map also shows the locations of stations for a proposed long-period MT survey (orange dots) aimed at providing 3-D MT data coverage over a large section of the Trans-Hudson Orogen in Canada. This survey covers the area of the provinces that can be readily reached by roads. To go further north than this would require additional logistics (e.g., helicopters). The purple stations were recently collected in partnership with the Manitoba Geological Survey and will be added to the dataset in Chapter 6 to produce a new inversion to produce a new inversion model that reaches the Superior Craton margin.*

8.7.3 Northern Alberta

The BMC conductor appears to be connected with the underlying asthenosphere in northern Alberta. Additionally, the kimberlites at Birch Mountains show evidence that they originated in the mantle lithosphere in a region with elevated temperatures (Eccles, 2011). The presence of other non-kimberlite alkaline magmas in the Birch Mountain kimberlite field of a similar age would require melting to have occurred in the middle to upper lithosphere (Green and Ringwood, 1967).

This raises the possibility the low resistivity of the BMC could be due to the presence of partial melt. This could be evaluated in the future using the silicate and carbon-rich melt conductivity models of Sifré et al. (2014). This analysis will ultimately be used to understand the dramatic differences in diamond potential of the two kimberlite fields. Additionally, the exact nature of what triggered kimberlite magmatism in northern Alberta has been the subject of considerable debate (e.g., Currie and Beaumont, 2011; Kjarsgaard et al., 2017; Zhang et al., 2019). A number of models have been proposed involving the Farallon slab, edge-driven convection processes, and intraplate petit-spot volcanism resulting from intraplate flexure related to a west-dipping subduction zone (e.g., Curries and Beaumont, 2011; Kjarsgaard et al., 2017; Zhang et al., 2019). The relationship between the BMC and these various models should be investigated.

Finally, the resistivity models show a number of smaller conductors that are located in the upper lithospheric mantle and crust in the region immediately east of the BMC. The mineral potential of Alberta is poorly understood. However, the few regions with potential are in the area associated with these conductors. Given this, these shallow conductors may indicate regions of possible mineralization relevant to future exploration efforts. As a result, the relationship between these shallow conductors and potential mineralization will also be investigated. The collection of broadband MT data in the future would also be useful as it could provide higher-resolution models of these resistivity features, allowing for them to be related to major structural features and region of mineralization or mineral potential.

Beyond the study presented in this thesis, there are still many unanswered questions regarding the tectonics of northern Alberta. For example, the deep resistivity structure closer to the Northwest Territories border remains almost entirely unconstrained. In particular, the northward extent of the BMC is unclear. MT data coverage into the Northwest Territories in this area does not yet exist. Additionally, MT data coverage over the BMC north of 58°N is limited to a single profile of MT stations, which limits the ability to confidently resolve 3-D resistivity structures. The variety of shallow crustal conductors slightly east of the BMC are also of interest but are currently constrained only by a few LMT stations that are not well-suited for shallow crustal studies. Collecting broadband MT data in this region could be used to determine if and where these

conductors approach the near surface. If mineral exploration continues to develop in Alberta, the location of these shallow conductors could be ideal candidates for initial exploration activities.

REFERENCES

Abdelsalam, M. G., Liégeois, J. P., & Stern, R. J., 2002. The saharan metacraton. Journal of African Earth Sciences, 34, 119-136. https://doi.org/10.1016/S0899-5362(02)00013-1

Adams, A., Miller, J., & Accardo, N., 2018. Relationships between lithospheric structures and rifting in the East African Rift System: A Rayleigh wave tomography study. Geochemistry, Geophysics, Geosystems, 19, 3793-3810. https://doi.org/10.1029/2018GC007750

Aiuppa, A., Baker, D. R., & Webster, J. D., 2009. Halogens in volcanic systems. Chemical Geology, 263, 1-18. https://doi.org/10.1016/j.chemgeo.2008.10.005

Alard, O., Griffin, W.L., Pearson, N.J., Lorand, J.P. and O'Reilly, S.Y., 2002. New insights into the Re–Os systematics of sub-continental lithospheric mantle from in situ analysis of sulphides. Earth and Planetary Science Letters, 203, 651-663. https://doi.org/10.1016/S0012-821X(02)00799-9

Alt, J.C., Anderson, T.F., Bonnell, L., 1989. The geochemistry of sulfur in a 1.3 km section of hydrothermally altered oceanic crust, DSDP Hole 504B. Geochim. Cosmochim. Acta 53, 1011–1023. https://doi.org/10.1016/0016-7037(89)90206-8

Amsden, T.W., 1982. Early and Middle Paleozoic history of the Anadarko Basin. Geological Society of America Abstracts with Programs, 14, 105.

Ansdell, K.M., 2005. Tectonic evolution of the Manitoba-Saskatchewan segment of the Paleoproterozoic Trans-Hudson Orogen, Canada. Can. J. Earth Sci. https://doi.org/10.1139/e05-035

Archie, G.E., 1942. The electrical resistivity log as an aid in determining some reservoir characteristics. Transactions of the AIME, 146, 54-62. https://doi.org/10.2118/942054-G

Ardia, P., Hirschmann, M.M., Withers, A.C. and Tenner, T.J., 2012. H2O storage capacity of olivine at 5–8 GPa and consequences for dehydration partial melting of the upper mantle.

Earth and Planetary Science Letters, 345, 104-116. https://doi.org/10.1016/j.epsl.2012.05.038

Arth, J. G., 1976. Behavior of trace elements during magmatic processes—a summary of theoretical models and their applications. Journal of Research of the U.S Geological Survey, 4, 41-47.

Aubaud, C., Hauri, E. H., & Hirschmann, M. M. 2004. Hydrogen partition coefficients between nominally anhydrous minerals and basaltic melts. Geophysical Research Letters, 31. https://doi.org/10.1029/2004GL021341

Aulbach, S., 2012. Craton nucleation and formation of thick lithospheric roots. Lithos, 149, 16-30. https://doi.org/10.1016/j.lithos.2012.02.011

Aulbach, S., 2018. Cratonic lithosphere discontinuities: dynamics of small-volume melting, metacratonization, and a possible role for brines. Lithospheric Discontinuities, 177-203. https://doi.org/10.1002/9781119249740.ch10

Aulbach, S., Massuyeau, M. and Gaillard, F., 2017. Origins of cratonic mantle discontinuities: A view from petrology, geochemistry and thermodynamic models. Lithos, 268, 364-382. https://doi.org/10.1016/j.lithos.2016.11.004

Banas, A., Stachel, T., Muehlenbachs, K. and McCandless, T.E. 2007: Diamonds from the Buffalo Head Hills, Alberta: formation in a non-conventional setting; Lithos, 93, 199–213, doi:10.1016/j.lithos.2006.07.001.

Bank, C.G., Bostock, M.G., Ellis, R.M., Hajnal, Z., VanDecar, J.C., 1998. Lithospheric mantle structure beneath the Trans-Hudson Orogen and the origin of diamondiferous kimberlites. J. Geophys. Res. Solid Earth 103, 10103–10114. https://doi.org/10.1029/97jb03746

Bataleva, Y. V., Palyanov, Y.N., Borzdov, Y.M., Sobolev, N. V., 2016. Sulfidation of silicate mantle by reduced S-bearing metasomatic fluids and melts. Geology 44, 271–274. https://doi.org/10.1130/G37477.1

Bauer, A., 2017. Northwest Territories Mineral Sector Review and Benchmarking. Tabled document prepared for the Government of the Northwest Territories. Available at Northwest Territories Mineral Sector Review and Benchmarking (Accessed: 15 September 2024).

Bedrosian, P.A., 2016. Making it and breaking it in the Midwest: Continental assembly and rifting from modeling of EarthScope magnetotelluric data. Precambrian Research, 278, 337-361. https://doi.org/10.1016/j.precamres.2016.03.009

Bedrosian, P.A., Finn, C.A., 2021. When Wyoming Became Superior: Oblique Convergence Along the Southern Trans-Hudson Orogen. Geophysics Research Letters. https://doi.org/10.1029/2021GL092970

Bedrosian, P.A., Frost, C.D., 2023. Geophysical extent of the Wyoming Province, western USA: Insights into ancient subduction and craton stability. Bull. Geol. Soc. Am. 135, 725–742. https://doi.org/10.1130/B36417.1

Bell, D. R., & Rossman, G. R., 1992. Water in Earth's mantle: the role of nominally anhydrous minerals. Science, 255, 1391-1397. https://doi.org/10.1126/science.255.5050.1391

Bell, D.R., Ihinger, P.D., Rossman, G.R., 1995. Quantitative analysis of trace OH in garnet and pyroxenes. Am. Mineral. 80, 465–474. https://doi.org/10.2138/am-1995-5-607

Bénard, A., Klimm, K., Woodland, A.B., Arculus, R.J., Wilke, M., Botcharnikov, R.E., Shimizu, N., Nebel, O., Rivard, C., Ionov, D.A., 2018. Oxidising agents in sub-arc mantle melts link slab devolatilisation and arc magmas. Nat. Commun. 9. https://doi.org/10.1038/s41467-018-05804-2

Bercovici, D., & Ricard, Y., 2012. Mechanisms for the generation of plate tectonics by two-phase grain-damage and pinning. Physics of the Earth and Planetary Interiors, 202, 27-55. https://doi.org/10.1016/j.pepi.2012.05.003

Berry, A. J., Hermann, J., O'Neill, H. S., & Foran, G. J., 2005. Fingerprinting the water site in mantle olivine. Geology, 33, 869-872. https://doi.org/10.1130/G21759.1

Berry, A. J., Walker, A. M., Hermann, J., O'Neill, H. S. C., Foran, G. J., & Gale, J. D., 2007) Titanium substitution mechanisms in forsterite. Chemical Geology, 242, 176-186. https://doi.org/10.1016/j.chemgeo.2007.03.010

Bettac, S.P., Unsworth, M.J., Pearson, D.G. and Craven, J., 2023: New constraints on the structure and composition of the lithospheric mantle beneath the Slave craton, NW Canada from 3-D magnetotelluric data–origin of the Central Slave Mantle Conductor and possible evidence for lithospheric scale fluid flow; Tectonophysics, 851, 229760, doi:10.1016/j.tecto.2023.229760.

Bickford, M.E., Mock, T.D., Steinhart Iii, W.E., Collerson, K.D. and Lewry, J.F., 2005. Origin of the Archean Sask craton and its extent within the Trans-Hudson orogen: evidence from Pb and Nd isotopic compositions of basement rocks and post-orogenic intrusions. Canadian Journal of Earth Sciences, 42, 659-684. https://doi.org/10.1139/e04-064

Blackwell, D. D., Negraru, P. T., & Richards, M. C., 2006. Assessment of the enhanced geothermal system resource base of the United States. Natural Resources Research, 15, 283-308. https://doi.org/10.1007/s11053-007-9028-7

Bleeker, W., 1990. New structural-metamorphic constraints on Early Proterozoic oblique collision along the Thompson Nickel Belt, Manitoba, Canada. In The Early Proterozoic Trans-Hudson Orogen of North America. Edited by JF Lewry and MR Stauffer. Geological Association of Canada, Special Paper, 37, 57-73.

Boerner, D.E., Kurtz, R.D., Craven, J.A., Ross, G.M. and Jones, F.W., 2000: A synthesis of electromagnetic studies in the Lithoprobe Alberta Basement Transect: constraints on Paleoproterozoic indentation tectonics; Canadian Journal of Earth Sciences, 37, 1509–1534, https://www.doi.org/10.1139/e00-063.

Bonin, B., 2007). A-type granites and related rocks: evolution of a concept, problems and prospects. Lithos, 97, 1-29. https://doi.org/10.1016/j.lithos.2006.12.007

Booker, J. R., 2014. The magnetotelluric phase tensor: a critical review. Surveys in Geophysics, 35, 7-40. https://doi.org/10.1007/s10712-013-9234-2

Brewer, J. A., Good, R., Oliver, J. E., Brown, L. D., & Kaufman, S., 1983. COCORP profiling across the Southern Oklahoma aulacogen: Overthrusting of the Wichita Mountains and compression within the Anadarko Basin. Geology, 11, 109-114. https://doi.org/10.1130/0091-7613(1983)11<109:CPATSO>2.0.CO;2

Brueseke, M. E., Hobbs, J. M., Bulen, C. L., Mertzman, S. A., Puckett, R. E., Walker, J. D., & Feldman, J., 2016. Cambrian intermediate-mafic magmatism along the Laurentian margin: Evidence for flood basalt volcanism from well cuttings in the Southern Oklahoma aulacogen (USA). Lithos, 260, 164-177. https://doi.org/10.1016/j.lithos.2016.05.016

Brune, S., Williams, S. E., & Mueller, R. D., 2017. Potential links between continental rifting, CO2 degassing and climate change through time. Nature Geoscience, 10, 941-946.https://doi.org/10.1038/s41561-017-0003-6

Budnik, R. T., 1986. Left-lateral intraplate deformation along the Ancestral Rocky Mountains: implications for late Paleozoic plate motions. Tectonophysics, 132, 195-214. https://doi.org/10.1016/0040-1951(86)90032-6

Burness, S., Thomassot, E., Smart, K.A. and Tappe, S., 2021. Sulphur isotopes (δ34S and Δ33S) in sulphides from cratonic mantle eclogites: A glimpse of volatile cycling in ancient subduction zones. Earth and Planetary Science Letters, 572, 117118. https://doi.org/10.1016/j.epsl.2021.117118

Burwash, R.A., Krupička, J. and Wijbrans, J.R., 2000: Metamorphic evolution of the Precambrian basement of Alberta; The Canadian Mineralogist, 38, no. 2, 423–434, doi:10.2113/gscanmin.38.2.423.

Cai, J., Wei, W., Hu, X. and Wood, D.A., 2017. Electrical conductivity models in saturated porous media: A review. Earth-Science Reviews, 171, 419-433. https://doi.org/10.1016/j.earscirev.2017.06.013

Caldwell, T. G., Bibby, H. M., & Brown, C., 2004. The magnetotelluric phase tensor. Geophysical Journal International, 158, 457-469. https://doi.org/10.1111/j.1365-246X.2004.02281.x

Camfield, P.A. and Gough, D.I., 1977. A possible Proterozoic plate boundary in North America. Canadian Journal of Earth Sciences, 14, 1229-1238. https://doi.org/10.1139/e77-112

Cao, H., Wang, K., Wang, T. and Hua, B., 2018. Three-dimensional magnetotelluric axial anisotropic forward modeling and inversion. Journal of Applied Geophysics, 153, 75-89. https://doi.org/10.1016/j.jappgeo.2018.04.015

Chacko, T., De, S.K., Creaser, R.A. and Muehlenbachs, K., 2000: Tectonic setting of the Taltson magmatic zone at 1.9–2.0 Ga: a granitoid-based perspective; Canadian Journal of Earth Sciences, 37, 1597–1609, doi:10.1139/e00-029.

Chakraborty, S., 2008. Diffusion in solid silicates: a tool to track timescales of processes comes of age. Annual Reviews of Earth and Planetary Sciences, 36, 153-190. https://doi.org/10.1146/annurev.earth.36.031207.124125

Chang, W. F., McMechan, G. A., & Keller, G. R., 1989. Wave field processing of data from a large-aperture seismic experiment in southwestern Oklahoma. Journal of Geophysical Research: Solid Earth, 94, 1803-1816. https://doi.org/10.1029/JB094iB02p01803

Chase, B. F., Kolawole, F., Atekwana, E. A., Carpenter, B. M., Turko, M., Abdelsalam, M., & Finn, C., 2022. The 180-km-long Meers-Willow Fault System in the Southern Oklahoma Aulacogen: A potential US mid-continent seismic hazard. GSA Bulletin. https://doi.org/10.1130/B36363.1

Chase, B. and Unsworth, M.J., 2022: Results from a long-period magnetotelluric (MT) study of the Fort à la Corne kimberlite field and surrounding Trans-Hudson Orogen, Saskatchewan; AGU Fall Meeting 2022, Chicago, Illinois, December 12–16, 2022, Abstracts, 2022, GP35B-0355.

Chase, B.F.W, Unsworth, M.J., Pană, D.I. and Wang, E., 2024a. Deep electrical structure of the Buffalo Head Hills and Birch Mountains, northern Alberta: implications for diamond exploration; Alberta Energy Regulator / Alberta Geological Survey, AER/AGS Special Report 117, 40 p

Chase, B.F.W, Marks. J.A, Williamson, A., Maki, A., Moshtaghian, K., Unsworth, M.J., 2024b. Initial results from a long-period magnetotelluric survey in the Flin Flon, Snow Lake and The Pas area, west-central Manitoba (NTS 63F, G, J, K, parts of 63B, I, N) in Report of Activities 2024, Manitoba Economic Development, Investment, Trade and Natural Resources, Manitoba Geological Survey.

Chase, B.F.W. and Unsworth, M.J., 2024. Magnetotelluric evidence for the formation of the layered Sask craton by flat slab subduction. Earth and Planetary Science Letters, 647, 119027. https://doi.org/10.1016/j.epsl.2024.119027

Chase, B.F.W., Unsworth, M.J., Atekwana, E.A., Evans, R.L., Zhu, J., 2023. Magnetotelluric Imaging of the Lithospheric Structure of the Southern Oklahoma Aulacogen: Evidence for Long-Term Weakening Caused by Rifting. Journal of Geophysical Research: Solid Earth, 128. https://doi.org/10.1029/2023JB026555

Chave, A. D., & Thomson, D. J., 2004. Bounded influence magnetotelluric response function estimation. Geophysical Journal International, 157, 988-1006. https://doi.org/10.1111/j.1365-246X.2004.02203.x

Chave, A.D. and Jones, A.G. eds., 2012. The magnetotelluric method: Theory and practice. Cambridge University Press, Cambridge, United Kingdom, 604 p.

Chave, A.D. and Thomson, D.J., 1989. Some comments on magnetotelluric response function estimation. Journal of Geophysical Research: Solid Earth, 94, 14215-14225. https://doi.org/10.1029/JB094iB10p14215

Chave, A.D., 2017. Estimation of the magnetotelluric response function: the path from robust estimation to a stable maximum likelihood estimator. Surveys in Geophysics, 38, 837-867. https://doi.org/10.1007/s10712-017-9422-6

Chave, A.D., Thomson, D.J. and Ander, M.E., 1987. On the robust estimation of power spectra, coherences, and transfer functions. Journal of Geophysical Research: Solid Earth, 92, 633-648. https://doi.org/10.1029/JB092iB01p00633

Chen, C.W., Rondenay, S., Evans, R.L. and Snyder, D.B., 2009. Geophysical detection of relict metasomatism from an Archean (~ 3.5 Ga) subduction zone. Science, 326, 1089-1091. https://doi.org/10.1126/science.117847

Chen, Y., Gu, Y.J. and Hung, S.H., 2018: A new appraisal of lithospheric structures of the Cordillera-Craton Boundary Region in western Canada, Tectonics, 37, 3207–3228, doi:10.1029/2018TC004956.

Chen, Y., Gu, Y.J., Heaman, L.M., Wu, L., Saygin, E. and Hung, S.H., 2020: Reconciling seismic structures and Late Cretaceous kimberlite magmatism in northern Alberta, Canada; Geology, 48, 872–876, doi:10.1130/G47163.1.

Clemens, J. D., Holloway, J. R., & White, A. J. R., 1986. Origin of an A-type granite; experimental constraints. American Mineralogist, 71, 317-324.

Clifford, T.N., 1966. Tectono-metallogenic units and metallogenic provinces of Africa. Earth and Planetary Science Letters, 1, 421-434. https://doi.org/10.1016/0012-821X(66)90039-2

Clinton, G., 2024. Eyes Wide Open – Understanding the Effects of a Diminished Resource Economy in the NWT. Impact Economics Working Paper. Available at https://www.miningnorth.com/_rsc/site-content/library/economics/Eyes%20Wide%20Open%20(FINAL)%20with%20Addendum%20.pdf (Accessed: 15 September 2024).

Comeau, M.J., 2015. Electrical Resistivity Structure of the Altiplano-Puna Magma Body and Volcan Uturuncu from Magnetotelluric Data. Unpublished PhD thesis. University of Alberta. https://doi.org/10.7939/R3C24QW2S

Comeau, M.J., Becken, M. and Kuvshinov, A.V., 2022. Imaging the Whole-Lithosphere Architecture of a Mineral System—Geophysical Signatures of the Sources and Pathways of Ore-Forming Fluids. Geochemistry, Geophysics, Geosystems, 23, e2022GC010379. https://doi.org/10.1029/2022GC010379

Comiskey, C., 2013. Seismic anisotropy in Texas and Oklahoma and its relationship to tectonic events that shaped southern Laurentia. Unpublished PhD thesis. Baylor University.

Cordell, D.R., 2020. Magnetotelluric Investigation of the Laguna del Maule Volcanic Field, Central Chile. Unpublished PhD thesis. University of Alberta. https://doi.org/10.7939/r3-x17z-hv08

Corti, G., 2009. Continental rift evolution: From rift initiation to incipient break-up in the Main Ethiopian Rift, East Africa. Earth-Science Rev. 96, 1–53. https://doi.org/10.1016/j.earscirev.2009.06.005

Couëslan, C.G., 2022. Affinity and Petrogenesis of the Huzyk Creek Metal-Enriched Graphite Deposit: A Metamorphosed Metalliferous Black Shale in the Trans-Hudson Orogen Of Manitoba, Canada. The Canadian Mineralogist, 60, 853–880. https://doi.org/10.3749/canmin.2100001

Craddock, J. P., Jackson, M., van der Pluijm, B. A., & Versical, R. T., 1993. Regional shortening fabrics in eastern North America: Far-field stress transmission from the Appalachian-Ouachita Orogenic Belt. Tectonics, 12, 257-264. https://doi.org/10.1029/92TC01106

Crocker, C.H., Collerson, K.D., Lewry, J.F. and Bickford, M.E., 1993. Sm-Nd, U-Pb, and Rb-Sr geochronology and lithostructural relationships in the southwestern Rae province: constraints on crustal assembly in the western Canadian shield. Precambrian research, 61, 27-50. https://doi.org/10.1016/0301-9268(93)90056-8

Currie, C.A. and Beaumont, C., 2011. Are diamond-bearing Cretaceous kimberlites related to low-angle subduction beneath western North America? Earth and Planetary Science Letters, 303, 59-70. https://doi.org/10.1016/j.epsl.2010.12.036

Czas, J., Pearson, D.G., Stachel, T., Kjarsgaard, B.A., Read, G.H., 2020. A Palaeoproterozoic diamond-bearing lithospheric mantle root beneath the Archean Sask craton, Canada. Lithos 356–357. https://doi.org/10.1016/j.lithos.2019.105301

Czas, J., Stachel, T., Pearson, D.G., Stern, R.A., Read, G.H., 2018. Diamond brecciation and annealing accompanying major metasomatism in eclogite xenoliths from the Sask craton, Canada. Mineralogy and Petrology, 112, 311–323. https://doi.org/10.1007/s00710-018-0590-y

da Silva, F.J., de Assis Barros, R., Junior, G.W.C., da Costa Gomes, D.G., Bertolino, L.C. and Marques, E.D., 2022. Regional control structures of kimberlite emplacement in the southern São Francisco Craton basement: A multidisciplinary approach including a representative example from Junco diatreme (Divinópolis, MG, Brazil). Journal of South American Earth Sciences, 119, 104027. https://doi.org/10.1016/j.jsames.2022.104027

Dai, L. and Karato, S.I., 2009c. Electrical conductivity of wadsleyite at high temperatures and high pressures. Earth and Planetary Science Letters, 287, 277-283. https://doi.org/10.1016/j.epsl.2009.08.012

Dai, L., & Karato, S.-I., 2009a. Electrical conductivity of orthopyroxene: Implications for the water content of the asthenosphere. Proceedings of the Japan Academy, Series B, 85, 466-475. https://doi.org/10.2183/pjab.85.466

Dai, L., & Karato, S.-I., 2009b. Electrical conductivity of pyrope-rich garnet at high temperature and high pressure. Physics of the Earth and Planetary Interiors, 176, 83–88. https://doi.org/10.1016/j.pepi.2009.04.002

Dai, L., Li, H., Hu, H., Shan, S., Jiang, J. and Hui, K., 2012. The effect of chemical composition and oxygen fugacity on the electrical conductivity of dry and hydrous garnet at high

temperatures and pressures. Contributions to Mineralogy and Petrology, 163, 689-700. https://doi.org/10.1007/s00410-011-0693-5

Dall'Agnol, R., Scaillet, B., & Pichavant, M., 1999. An experimental study of a lower Proterozoic A-type granite from theEastern Amazonian Craton, Brazil. Journal of Petrology, 40, 1673-1698. https://doi.org/10.1093/petroj/40.11.1673

Dasgupta, R., & Hirschmann, M. M., 2010. The deep carbon cycle and melting in Earth's interior. Earth and Planetary Science Letters, 298, 1-13. https://doi.org/10.1016/j.epsl.2010.06.039

Davies, J.R., 1998. The origin, structural style, and reactivation history of the Tabbernor Fault Zone, Saskatchewan, Canada. PhD dissertation. McGill University.

Davies, R. S., Davies, M. J., Groves, D., Davids, K., Brymer, E., Trench, A., Sykes, J. P., & Dentith, M., 2021. Learning and expertise in mineral exploration decision-making: An ecological dynamics perspective. In: International Journal of Environmental Research and Public Health (Vol. 18, Issue 18). MDPI. https://doi.org/10.3390/ijerph18189752

Davis, H. G., Northcutt, R. A., & Johnson, K. S., 1988. The greater Anadarko basin: an overview of petroleum exploration and development. In Anadarko basin symposium (pp. 13-24).

Dawson, J.B. and Smith, J.V., 1977. The MARID (mica-amphibole-rutile-ilmenite-diopside) suite of xenoliths in kimberlite. Geochimica et cosmochimica acta, 41, 309-323. https://doi.org/10.1016/0016-7037(77)90239-3

Day, H.W., 2012. A revised diamond-graphite transition curve. American Mineralogist, 97, 52-62. https://doi.org/10.2138/am.2011.3763

De Hoog, J. C., Gall, L., & Cornell, D. H., 2010. Trace-element geochemistry of mantle olivine and application to mantle petrogenesis and geothermobarometry. Chemical Geology, 270, 196-215. https://doi.org/10.1016/j.chemgeo.2009.11.017

De Wit, M.C.J., 2010. Identification of global diamond metallogenic clusters to assist exploration. In South African Institute of Mining and Metallurgy, Conference Diamonds Source to Use, Botswana 23p.

De Wit, M.C.J., 2018. Prospecting history leading to the discovery of Botswana's diamond mines: from artefacts to Lesedi La Rona. Mineralogy and Petrology 112 (Supplement 1): 7-22. https://doi.org/10.1007/s00710-018-0556-0

Deen, T. J., Griffin, W. L., Begg, G., O'Reilly, S. Y., Natapov, L. M., & Hronsky, J., 2006. Thermal and compositional structure of the subcontinental lithospheric mantle: Derivation from shear wave seismic tomography. Geochemistry, Geophysics, Geosystems, 7. https://doi.org/10.1029/2005GC001120

DeLucia, M. S., Murphy, B. S., Marshak, S., & Egbert, G. D., 2019. The Missouri High-Conductivity Belt, revealed by magnetotelluric imaging: Evidence of a trans-lithospheric shear zone beneath the Ozark Plateau, Midcontinent USA?. Tectonophysics, 753, 111-123. https://doi.org/10.1016/j.tecto.2019.01.011

Demouchy, S., Bolfan-Casanova, N., 2016. Distribution and transport of hydrogen in the lithospheric mantle: A review. Lithos 240–243, 402–425. https://doi.org/10.1016/j.lithos.2015.11.012

Demouchy, S., Shcheka, S., Denis, C.M.M., Thoraval, C., 2017. Subsolidus hydrogen partitioning between nominally anhydrous minerals in garnet-bearing peridotite. Am. Mineral. 102, 1822–1831. https://doi.org/10.2138/am-2017-6089

Dobson, D.P., Jones, A.P., Rabe, R., Sekine, T., Kurita, K., Taniguchi, T., Kondo, T., Kato, T., Shimomura, O. and Urakawa, S., 1996. In-situ measurement of viscosity and density of carbonate melts at high pressure. Earth and Planetary Science Letters, 143, 207-215. https://doi.org/10.1016/0012-821X(96)00139-2

Doucet, L.S., Peslier, A.H., Ionov, D.A., Brandon, A.D., Golovin, A.V., Goncharov, A.G. and Ashchepkov, I.V., 2014. High water contents in the Siberian cratonic mantle linked to

metasomatism: An FTIR study of Udachnaya peridotite xenoliths. Geochimica et Cosmochimica Acta, 137, 159-187. https://doi.org/10.1016/j.gca.2014.04.011

Duba, A. G., & Shankland, T. J., 1982. Free carbon & electrical conductivity in the Earth's mantle. Geophysical Research Letters, 9, 1271-1274. https://doi.org/10.1029/GL009i011p01271

Eaton, D.W., Darbyshire, F., Evans, R.L., Grütter, H., Jones, A.G. and Yuan, X., 2009: The elusive lithosphere–asthenosphere boundary (LAB) beneath cratons; Lithos, 109, no. 1–2, p. 1–22, doi:10.1016/j.lithos.2008.05.009.

Ebinger, C., 2005. Continental break-up: The East African perspective. Astron. Geophys. 46, 2.16-2.21. https://doi.org/10.1111/j.1468-4004.2005.46216.x

Eccles, D.R., 2011. Northern Alberta kimberlite province: the first 20 years; Energy Resources Conservation Board, ERCB/AGS Bulletin 65, 116. Available at https://ags.aer.ca/publication/bul-065

Eccles, D.R. and Simonetti, A., 2008. A study of peridotitic garnet xenocryst compositions from selected ultramafic bodies in the northern Alberta kimberlite province: implications for mantle stratigraphy and garnet classification; Energy Resources Conservation Board, ERCB/AGS Earth Sciences Report 2008-01, 40. Available at https://ags.aer.ca/publication/esr-2008-01

Eccles, D.R., Heaman, L.M., Luth, R.W. and Creaser, R.A., 2004. Petrogenesis of the Late Cretaceous northern Alberta kimberlite province; Lithos, 76, 435–459, doi:10.1016/j.lithos.2004.03.046.

Egbert, G.D. and Booker, J.R., 1986. Robust estimation of geomagnetic transfer functions. Geophysical Journal International, 87, 173-194. https://doi.org/10.1111/j.1365-246X.1986.tb04552.x

Egbert, G.D. and Livelybrooks, D.W., 1996. Single station magnetotelluric impedance estimation: Coherence weighting and the regression M-estimate. Geophysics, 61, 964-970. https://doi.org/10.1190/1.1444045

Egbert, G.D., 1997. Robust multiple-station magnetotelluric data processing. Geophysical Journal International, 130, 475-496. https://doi.org/10.1111/j.1365-246X.1997.tb05663.x

Evans, R.L., Jones, A.G., Garcia, X., Muller, M., Hamilton, M., Evans, S., Fourie, C.J.S., Spratt, J., Webb, S., Jelsma, H., Hutchins, D., 2011. Electrical lithosphere beneath the Kaapvaal craton, southern Africa. Journal of Geophysical Research: Solid Earth, 116, 1–16. https://doi.org/10.1029/2010JB007883

Evanzia, D., Pulliam, J., Ainsworth, R., Gurrola, H., & Pratt, K., 2014. Seismic Vp & Vs tomography of Texas & Oklahoma with a focus on the Gulf Coast margin. Earth and Planetary Science Letters, 402, 148-156. https://doi.org/10.1016/j.epsl.2013.12.027

Faul, U. H., Cline II, C. J., David, E. C., Berry, A. J., & Jackson, I., 2016. Titanium-hydroxyl defect-controlled rheology of the Earth's upper mantle. Earth and Planetary Science Letters, 452, 227-237. https://doi.org/10.1016/j.epsl.2016.07.016

Faure, S., Godey, S., Fallara, F., Trépanier, S., 2011. Seismic Mantle Structure in Canada and Relationship to Kimberlites. Economic Geology, 106, 223–240. https://doi.org/10.2113/econgeo.106.2.223

Fei, H., Wiedenbeck, M., Yamazaki, D., & Katsura, T., 2013. Small effect of water on upper-mantle rheology based on silicon self-diffusion coefficients. Nature, 498, 213-215. https://doi.org/10.1038/nature12193

Ferrand, T.P., Chin, E.J., 2023. Garnet pyroxenites explain high electrical conductivity in the East African deep lithosphere. Lithos 462–463, 107405. https://doi.org/10.1016/j.lithos.2023.107405

Fitzpayne, A., Giuliani, A., Hergt, J., Phillips, D. and Janney, P., 2018. New geochemical constraints on the origins of MARID and PIC rocks: Implications for mantle metasomatism

and mantle-derived potassic magmatism. Lithos, 318, 478-493. https://doi.org/10.1016/j.lithos.2018.08.036

Foley, S., 1992. Vein-plus-wall-rock melting mechanisms in the lithosphere and the origin of potassic alkaline magmas. Lithos, 28, 435-453. https://doi.org/10.1016/0024-4937(92)90018-T

Foley, S. F., & Fischer, T. P., 2017. An essential role for continental rifts and lithosphere in the deep carbon cycle. Nature Geoscience, 10, 897-902. https://doi.org/10.1038/s41561-017-0002-7

Foley, S. F., Prelevic, D., Rehfeldt, T., & Jacob, D. E., 2013. Minor and trace elements in olivines as probes into early igneous and mantle melting processes. Earth and Planetary Science Letters, 363, 181-191. https://doi.org/10.1016/j.epsl.2012.11.025

Foley, S.F., 2008. Rejuvenation and erosion of the cratonic lithosphere. Nature Geoscience, 1, 503–510. https://doi.org/10.1038/ngeo261

Foley, S.F., Fischer, T.P., 2017. An essential role for continental rifts and lithosphere in the deep carbon cycle. Nat. Geosci. https://doi.org/10.1038/s41561-017-0002-7

Forst, B. R., & Lindsley, D. H., 1992. Equilibria among Fe-Ti oxides, pyroxenes, olivine, and quartz: Part II. Application. American Mineralogist, 77, 1004-1020.

Fortier, S., Nassar, N.T., Day, W.C, Hammarstrom, J.M., Seal, R.R., II., Graham, G.E., Lederer, G.W., 2022. USGS critical minerals review. Mining Engineering, 75, 30-44.

Fournier, D., Kang, S., McMillan, M.S. and Oldenburg, D.W., 2017. Inversion of airborne geophysics over the DO-27/DO-18 kimberlites—Part 2: Electromagnetics. Interpretation, 5, T313-T325. https://doi.org/10.1190/INT-2016-0140.1

Frezzotti, M. L., & Ferrando, S., 2018. The role of halogens in the lithospheric mantle. The role of halogens in terrestrial and extraterrestrial geochemical processes: surface, crust, and mantle, 805-845. https://doi.org/10.1007/978-3-319-61667-4_13

Frost, B.R., Fyfe, W.S., Tazaki, K. and Chan, T., 1989. Grain-boundary graphite in rocks and implications for high electrical conductivity in the lower crust. Nature, 340, 134-136. https://doi.org/10.1038/340134a0

Frost, D.J. and McCammon, C.A., 2008. The redox state of Earth's mantle; Annual Review of Earth and Planetary Sciences, 36, 389–420, doi:10.1146/annurev.earth.36.031207.124322.

Frost, D.J., 2006. The stability of hydrous mantle phases. Reviews in Mineralogy and Geochemistry, 62, 243-271. https://doi.org/10.2138/rmg.2006.62.11

Gaillard, F., Malki, M., Iacono-Marziano, G., Pichavant, M. and Scaillet, B., 2008. Carbonatite melts and electrical conductivity in the asthenosphere. Science, 322, 1363-1365. https://doi.org/10.1126/science.1164446

Gamble, T.D., Goubau, W.M. and Clarke, J., 1979. Magnetotellurics with a remote magnetic reference. Geophysics, 44, 53-68. https://doi.org/10.1190/1.1440923

Gardés, E., Gaillard, F., & Tarits, P., 2014. Toward a unified hydrous olivine electrical conductivity law. Geochemistry, Geophysics, Geosystems, 15, 4984-5000. https://doi.org/10.1002/2014GC005496

Gaudemer, Y., Jaupart, C., & Tapponnier, P., 1988. Thermal control on post-orogenic extension in collision belts. Earth and Planetary Science Letters, 89, 48-62. https://doi.org/10.1016/0012-821X(88)90032-5

Genge, M.J., Jones, A.P. and Price, G.D., 1995. An infrared and Raman study of carbonate glasses: implications for the structure of carbonatite magmas. Geochimica et Cosmochimica Acta, 59, 927-937. https://doi.org/10.1016/0016-7037(95)00010-0

Gilbert, M. C., 1983. Timing and chemistry of igneous events associated with the southern Oklahoma aulacogen. In Developments in Geotectonics (Vol. 19, pp. 439-455). Elsevier. https://doi.org/10.1016/B978-0-444-42198-2.50030-4

Giuliani, A. and Pearson, D.G., 2019. Kimberlites: from deep earth to diamond mines. Elements: An International Magazine of Mineralogy, Geochemistry, and Petrology, 15, 377-380. https://doi.org/10.2138/gselements.15.6.377

Giuliani, A., Fiorentini, M.L., Martin, L.A., Farquhar, J., Phillips, D., Griffin, W.L. and LaFlamme, C., 2016. Sulfur isotope composition of metasomatised mantle xenoliths from the Bultfontein kimberlite (Kimberley, South Africa): Contribution from subducted sediments and the effect of sulfide alteration on S isotope systematics. Earth and Planetary Science Letters, 445, 114-124. https://doi.org/10.1016/j.epsl.2016.04.005

Glover, P. W., 2010. A generalized Archie's law for n phases. Geophysics, 75, E247-E265. https://doi.org/10.1190/1.3509781

Glover, P. W., & Ádám, A., 2008. Correlation between crustal high conductivity zones and seismic activity and the role of carbon during shear deformation. Journal of Geophysical Research: Solid Earth, 113. https://doi.org/10.1029/2008JB005804

Glover, P.W., Hole, M.J. and Pous, J., 2000. A modified Archie's law for two conducting phases. Earth and Planetary Science Letters, 180, 369-383. https://doi.org/10.1016/S0012-821X(00)00168-0

Godel, B., Barnes, S. J., & Maier, W. D., 2006. 3-D distribution of sulphide minerals in the Merensky Reef (Bushveld Complex, South Africa) and the JM Reef (Stillwater Complex, USA) and their relationship to microstructures using X-ray computed tomography. Journal of petrology, 47, 1853-1872. https://doi.org/10.1093/petrology/egl029

Gonzaga, R.G., Lowry, D., Jacob, D.E., LeRoex, A., Schulze, D. and Menzies, M.A., 2010. Eclogites and garnet pyroxenites: similarities and differences. Journal of volcanology and geothermal research, 190, 235-247. https://doi.org/10.1016/j.jvolgeores.2009.08.022

Granath, J. W., 1989. Structural evolution of the Ardmore Basin, Oklahoma: Progressive deformation in the foreland of the Ouachita collision. Tectonics, 8, 1015-1036. https://doi.org/10.1029/TC008i005p01015

Green, D. H., & Ringwood, A. E., 1967. The genesis of basaltic magmas. Contributions to mineralogy and petrology, 15, 103-190. https://doi.org/10.1007/BF00372052

Green, J. C., & Fitz III, T. J., 1993. Extensive felsic lavas and rheoignimbrites in the Keweenawan Midcontinent Rift plateau volcanics, Minnesota: petrographic and field recognition. Journal of Volcanology and Geothermal Research, 54, 177-196. https://doi.org/10.1016/0377-0273(93)90063-W

Grégoire, M., Bell, D., & Le Roex, A., 2002. Trace element geochemistry of phlogopite-rich mafic mantle xenoliths: their classification and their relationship to phlogopite-bearing peridotites and kimberlites revisited. Contributions to Mineralogy and Petrology, 142, 603-625. https://doi.org/10.1007/s00410-001-0315-8

Griffin, W. L., Begg, G. C., & O'reilly, S. Y., 2013. Continental-root control on the genesis of magmatic ore deposits. Nature Geoscience, 6, 905-910. https://doi.org/10.1038/ngeo1954

Griffin, W. L., Begg, G. C., Dunn, D., O'Reilly, S. Y., Natapov, L. M., & Karlstrom, K., 2011. Archean lithospheric mantle beneath Arkansas: Continental growth by microcontinent accretion. Bulletin, 123, 1763-1775. https://doi.org/10.1130/B30253.1

Griffin, W. L., O'Reilly, S. Y., Afonso, J. C., & Begg, G. C., 2009. The composition and evolution of lithospheric mantle: a re-evaluation and its tectonic implications. Journal of Petrology, 50, 1185-1204. https://doi.org/10.1093/petrology/egn033

Griffin, W.L., O'Reilly, S.Y., Doyle, B.J., Pearson, N.J., Coopersmith, H., Kivi, K., Malkovets, V., Pokhilenko, N., 2004. Lithosphere mapping beneath the North American plate. Lithos 77, 873–922. https://doi.org/10.1016/j.lithos.2004.03.034

Groom, R.W. and Bailey, R.C., 1989. Decomposition of magnetotelluric impedance tensors in the presence of local three-dimensional galvanic distortion. Journal of Geophysical Research: Solid Earth, 94, 1913-1925. https://doi.org/10.1190/1.1443066

Groom, R.W. and Bailey, R.C., 1991. Analytic investigations of the effects of near-surface three-dimensional galvanic scatterers on MT tensor decompositions. Geophysics, 56, 496-518. https://doi.org/10.1190/1.1443066

Groves, D.I. and Santosh, M., 2021. Craton and thick lithosphere margins: The sites of giant mineral deposits and mineral provinces. Gondwana Research, 100, 195-222. https://doi.org/10.1016/j.gr.2020.06.008

Groves, D.I., Santosh, M., Müller, D., Zhang, L., Deng, J., Yang, L.Q. and Wang, Q.F., 2022. Mineral systems: Their advantages in terms of developing holistic genetic models and for target generation in global mineral exploration. Geosystems and Geoenvironment, 1, 100001. https://doi.org/10.1016/j.geogeo.2021.09.001

Guo, H. and Keppler, H., 2019. Electrical conductivity of NaCl-bearing aqueous fluids to 900 C and 5 GPa. Journal of Geophysical Research: Solid Earth, 124, 1397-1411. https://doi.org/10.1029/2018JB016658

Gupta, J.C., Kurtz, R.D., Camfield, P.A. and Niblett, E.R., 1985. A geomagnetic induction anomaly from IMS data near Hudson Bay, and its relation to crustal electrical conductivity in central North America. Geophysical Journal International, 81, 33-46. https://doi.org/10.1111/j.1365-246X.1985.tb01349.x

Ham, W. E., Denison, R. E., & Merritt, C. A., 1964. Basement rocks and structural evolution of southern Oklahoma. AAPG Bulletin, 48, 529-529. https://doi.org/10.1306/BC743C77-16BE-11D7-8645000102C1865D

Hammouda, T. and Laporte, D., 2000. Ultrafast mantle impregnation by carbonatite melts. Geology, 28, 283-285. https://doi.org/10.1130/0091-7613(2000)28<283:UMIBCM>2.0.CO;2

Hanneson, C. and Unsworth, M.J., 2023: Regional-scale resistivity structure of the middle and lower crust and uppermost mantle beneath the southeastern Canadian Cordillera and

insights into its causes; Geophysical Journal International, 234, 2032–2052, doi:10.1093/gji/ggad183.

Hansen, S.M., Dueker, K., Schmandt, B., 2015. Thermal classification of lithospheric discontinuities beneath USArray. Earth and Planetary Science Letters. 431, 36–47. https://doi.org/10.1016/j.epsl.2015.09.009

Hanson, R. E., Puckett Jr, R. E., Keller, G. R., Brueseke, M. E., Bulen, C. L., Mertzman, S. A., ... & McCleery, D. A., 2013. Intraplate magmatism related to opening of the southern Iapetus Ocean: Cambrian Wichita igneous province in the Southern Oklahoma rift zone. Lithos, 174, 57-70. https://doi.org/10.1016/j.lithos.2012.06.003

Hashin, Z.A. and Shtrikman, S., 1962. On some variational principles in anisotropic and nonhomogeneous elasticity. Journal of the Mechanics and Physics of Solids, 10, 335-342. https://doi.org/10.1016/0022-5096(62)90004-2

Hasterok, D., & Chapman, D. S., 2011. Heat production and geotherms for the continental lithosphere. Earth and Planetary Science Letters, 307, 59-70.https://doi.org/10.1016/j.epsl.2011.04.034

Hauri, E.H., Gaetani, G.A. and Green, T.H., 2006. Partitioning of water during melting of the Earth's upper mantle at H2O-undersaturated conditions. Earth and Planetary Science Letters, 248, 715-734. https://doi.org/10.1016/j.epsl.2006.06.014

Heinson, G., Didana, Y., Soeffky, P., Thiel, S., Wise, T., 2018. The crustal geophysical signature of a world-class magmatic mineral system. Sci. Rep. 8. https://doi.org/10.1038/s41598-018-29016-2

Hill, G.J., Caldwell, T.G., Heise, W., Chertkoff, D.G., Bibby, H.M., Burgess, M.K., Cull, J.P., Cas, R.A.F., 2009. Distribution of melt beneath Mount St Helens and Mount Adams inferred from magnetotelluric data. Nat. Geosci. 2, 785–789. https://doi.org/10.1038/ngeo661

Hirth, G. and Kohlstedt, D.L., 1996. Water in the oceanic upper mantle: implications for rheology, melt extraction and the evolution of the lithosphere. Earth and Planetary Science Letters, 144, 93-108. https://doi.org/10.1016/0012-821X(96)00154-9

Hoffman, P., Dewey, J. F., & Burke, K., 1974. Aulacogens and their genetic relation to geosynclines, with a Proterozoic example from Great Slave Lake, Canada. https://doi.org/10.2110/pec.74.19.0038

Hoffman, P.F., 1988: United plates of America, the birth of a craton: Early Proterozoic assembly and growth of Laurentia; Annual Review of Earth and Planetary Sciences, 16, 543–603, doi:10.1146/annurev.ea.16.050188.002551.

Hofmann, A. W, (1997. Mantle geochemistry: the message from oceanic volcanism. Nature, 385, 219-229. https://doi.org/10.1038/385219a0

Hofstra, A.H. and Kreiner, D.C., 2020. Systems-deposits-commodities-critical minerals table for the earth mapping resources initiative, US Geological Survey report No. 2020-1042. https://doi.org/10.3133/ofr20201042

Hogan, J. P., & Gilbert, M. C., 1995. The A-type Mount Scott Granite sheet: Importance of crystal magma traps. Journal of Geophysical Research: Solid Earth, 100, 15779-15792. https://doi.org/10.1029/94JB03258

Hogan, J. P., & Gilbert, M. C., 1998. The Southern Oklahoma aulacogen: A Cambrian analog for Mid-Proterozoic AMCG (anorthosite-mangerite-charnockite-granite) complexes?. Basement Tectonics 12: Central North America and Other Regions, 39-78. https://doi.org/10.1007/978-94-011-5098-9_3

Hoggard, M.J., Czarnota, K., Richards, F.D., Huston, D.L., Jaques, A.L., Ghelichkhan, S., 2020. Global distribution of sediment-hosted metals controlled by craton edge stability. Nature Geoscience, 13, 504–510. https://doi.org/10.1038/s41561-020-0593-2

Hornsby, K. T., Streig, A. R., Bennett, S. E., Chang, J. C., & Mahan, S., 2020. Neotectonic and paleoseismic analysis of the northwest extent of Holocene surface deformation along the

Meers Fault, Oklahoma. Bulletin of the Seismological Society of America, 110, 49-66.https://doi.org/10.1785/0120180148

Hu, H., Dai, L., Li, H., Sun, W. and Li, B., 2018. Effect of dehydrogenation on the electrical conductivity of Fe-bearing amphibole: Implications for high conductivity anomalies in subduction zones and continental crust. Earth and Planetary Science Letters, 498, 27-37. https://doi.org/10.1016/j.epsl.2018.06.003

Huizenga, J.M., Touret, J.L.R., 2012. Granulites, CO2 and graphite. Gondwana Res. 22, 799–809. https://doi.org/10.1016/j.gr.2012.03.007

Hunter, R.H. and McKenzie, D., 1989. The equilibrium geometry of carbonate melts in rocks of mantle composition. Earth and Planetary Science Letters, 92, 347-356. https://doi.org/10.1016/0012-821X(89)90059-9

Ionov, D.A., Ashchepkov, I. and Jagoutz, E., 2005. The provenance of fertile off-craton lithospheric mantle: Sr–Nd isotope and chemical composition of garnet and spinel peridotite xenoliths from Vitim, Siberia. Chemical Geology, 217, .41-75. https://doi.org/10.1016/j.chemgeo.2004.12.001

Jaireth, S. and Huston, D., 2010. Metal endowment of cratons, terranes and districts: Insights from a quantitative analysis of regions with giant and super-giant deposits. Ore Geology Reviews, 38 ,288-303. https://doi.org/10.1016/j.oregeorev.2010.05.005

Jansen, J. and Witherly, K., 2004. The Tli Kwi Cho kimberlite complex, Northwest Territories, Canada: A geophysical case study. In SEG Technical Program Expanded Abstracts 2004 (pp. 1147-1150). Society of Exploration Geophysicists. https://doi.org/10.1190/1.1839654

Jelsma, H., Barnett, W., Richards, S., Lister, G., 2009. Tectonic setting of kimberlites. Lithos 112, 155–165. https://doi.org/10.1016/j.lithos.2009.06.030

Joachim, B., Stechern, A., Ludwig, T., Konzett, J., Pawley, A., Ruzié-Hamilton, L., ... & Ballentine, C. J., 2017. Effect of water on the fluorine and chlorine partitioning behavior

between olivine and silicate melt. Contributions to Mineralogy and Petrology, 172, 1-15. https://doi.org/10.1007/s00410-017-1329-1

Jones, A.G., 1983. The problem of current channelling: a critical review. Geophysical surveys, 6, 79-122. https://doi.org/10.1007/BF01453996

Jones, A.G., 1987. MT and reflection: an essential combination. Geophysical Journal International, 89, 7-18.

Jones, A.G., 1988. Static shift of magnetotelluric data and its removal in a sedimentary basin environment. Geophysics, 53, 967-978. https://doi.org/10.1190/1.1442533

Jones, A.G., Chave, A.D., Egbert, G., Auld, D. and Bahr, K., 1989. A comparison of techniques for magnetotelluric response function estimation. Journal of Geophysical Research: Solid Earth, 94, 14201-14213. https://doi.org/10.1029/JB094iB10p14201

Jones, A.G., Ledo, J., Ferguson, I.J., 2005. Electromagnetic images of the Trans-Hudson orogen: The North American Central Plains anomaly revealed. Can. J. Earth Sci. https://doi.org/10.1139/e05-018

Jones, M.T., Jerram, D.A., Svensen, H.H. and Grove, C., 2016. The effects of large igneous provinces on the global carbon and sulphur cycles. Palaeogeography, Palaeoclimatology, Palaeoecology, 441, 4-21. https://doi.org/10.1016/j.palaeo.2015.06.042

Kaminski, E., & Jaupart, C., 2000. Lithosphere structure beneath the Phanerozoic intracratonic basins of North America. Earth and Planetary Science Letters, 178, 139-149. https://doi.org/10.1016/S0012-821X(00)00067-4

Kapp, P., Jepson, G., Carrapa, B., Schaen, A.J., He, J.J. and Wang, J.W., 2023. Laramide bulldozing of lithosphere beneath the Arizona transition zone, southwestern United States. Geology, 51,952-956. https://doi.org/10.1130/G51194.1

Karato, S.I., 1990. The role of hydrogen in the electrical conductivity of the upper mantle. Nature, 347, 272-273. https://doi.org/10.1038/347272a0

Katayama, I., Michibayashi, K., Terao, R., Ando, J.I. and Komiya, T., 2011. Water content of the mantle xenoliths from Kimberley and implications for explaining textural variations in cratonic roots. Geological Journal, 46, 173-182. https://doi.org/10.1002/gj.1216

Kelbert, A., Meqbel, N., Egbert, G.D., Tandon, K., 2014. ModEM: A modular system for inversion of electromagnetic geophysical data. Comput. Geosci. 66, 40–53. https://doi.org/10.1016/j.cageo.2014.01.010

Kelemen, P.B., Manning, C.E., 2015. Reevaluating carbon fluxes in subduction zones, what goes down, mostly comes up. Proceedings of the National Academy of Sciences, 112, E3997-E4006. https://doi.org/10.1073/pnas.1507889112

Keller, G. R., & Baldridge, W. S., 2006. The southern Oklahoma aulacogen. In Developments in geotectonics (Vol. 25, pp. 427-436). Elsevier. https://doi.org/10.1016/S0419-0254(06)80020-0

Keller, G. R., Braile, L. W., McMechan, G. A., Thomas, W. A., Harder, S. H., Chang, W. F., & Jardine, W. G., 1989. Paleozoic continent-ocean transition in the Ouachita Mountains imaged from PASSCAL wide-angle seismic reflection-refraction data. Geology, 17, 119-122. https://doi.org/10.1130/0091-7613(1989)017<0119:PCOTIT>2.3.CO;2

Keller, G.R., Stephenson, R.A., Hatcher, R.D., Carlson, M.P. and McBride, J.H., 2007. The southern Oklahoma and Dniepr-Donets aulacogens: A comparative analysis. Memoirs-Geological Society of America, 200, 127.

Kirkby, A.L., Musgrave, R.J., Czarnota, K., Doublier, M.P., Duan, J., Cayley, R.A. and Kyi, D., 2020. Lithospheric architecture of a Phanerozoic orogen from magnetotellurics: AusLAMP in the Tasmanides, southeast Australia. Tectonophysics, 793, 228560. https://doi.org/10.1038/s41598-022-11921-2

Kjarsgaard, B.A. and Levinson, A.A., 2002. Diamonds in Canada. Gems and Gemology, 38, 208-238. https://doi.org/10.5741/GEMS.38.3.208

Kjarsgaard, B.A., de Wit, M., Heaman, L.M., Pearson, D.G., Stiefenhofer, J., Janusczcak, N. and Shirey, S.B., 2022. A review of the geology of global diamond mines and deposits. Reviews in Mineralogy and Geochemistry, 88, 1-117. https://doi.org/10.2138/rmg.2022.88.01

Kjarsgaard, B.A., Heaman, L.M., Sarkar, C. and Pearson, D.G., 2017. The North America mid-Cretaceous kimberlite corridor: Wet, edge-driven decompression melting of an OIB-type deep mantle source. Geochemistry, Geophysics, Geosystems, 18, 2727-2747. https://doi.org/10.1002/2016GC006761

Kjarsgaard, B.A., Januszczak, N. and Stiefenhofer, J., 2019. Diamond exploration and resource evaluation of kimberlites. Elements: An International Magazine of Mineralogy, Geochemistry, and Petrology, 15, 411-416. https://doi.org/10.2138/gselements.15.6.411

Klimm, K., Holtz, F., Johannes, W., & King, P. L., 2003. Fractionation of metaluminous A-type granites: an experimental study of the Wangrah Suite, Lachlan Fold Belt, Australia. Precambrian Research, 124, 327-341. https://doi.org/10.1016/S0301-9268(03)00092-5

Kluth, C.F. and Coney, P.J., 1981. Plate tectonics of the ancestral Rocky Mountains. Geology, 9, 10-15. https://doi.org/10.1130/0091-7613(1981)9<10:PTOTAR>2.0.CO;2

Koch, A., Schilling, D., & Upton, D., 2015. Tackling the Crisis in Mineral Exploration. https://www.bcg.com/en-au/publications/2015/metalsmining-sustainability-tackling-the-crisis-in-mineral-exploration.aspx

Kong, W., Tan, H., Lin, C., Unsworth, M., Lee, B., Peng, M., Wang, M. and Tong, T., 2021. Three-Dimensional Inversion of Magnetotelluric Data for a Resistivity Model With Arbitrary Anisotropy. Journal of Geophysical Research: Solid Earth, 126, e2020JB020562. https://doi.org/10.1029/2020JB020562

Konzett, J., 1997. Phase relations and chemistry of Ti-rich K-richterite-bearing mantle assemblages: an experimental study to 8.0 GPa in a Ti-KNCMASH system. Contributions to Mineralogy and Petrology, 128, 385-404. https://doi.org/10.1007/s004100050316

Kravchinsky, V.A., Eccles, D.R., Zhang, R. and Cannon, M., 2009. Paleomagnetic dating of the northern Alberta kimberlites; Canadian Journal of Earth Sciences, 46, 231–245, doi:10.1139/E09-016.

Kumar, P., Kind, R., Yuan, X., & Mechie, J., 2012. USArray receiver function images of the lithosphere-asthenosphere boundary. Seismological Research Letters, 83, 486-491. https://doi.org/10.5194/se-3-149-2012, 2012.

Larsen, J.C., Mackie, R.L., Manzella, A., Fiordelisi, A. and Rieven, S., 1996. Robust smooth magnetotelluric transfer functions. Geophysical Journal International, 124(3), pp.801-819. https://doi.org/10.1111/j.1365-246X.1996.tb05639.x

Laske, G., Masters, G., Ma, Z. and Pasyanos, M., 2013. Update on CRUST1. 0—A 1-degree global model of Earth's crust. EGU General Assembly Geophysicla Research Abstracts, 15, 2658.

Laumonier, M., Farla, R., Frost, D.J., Katsura, T., Marquardt, K., Bouvier, A.S. and Baumgartner, L.P., 2017. Experimental determination of melt interconnectivity and electrical conductivity in the upper mantle. Earth and Planetary Science Letters, 463, 286-297. https://doi.org/10.1016/j.epsl.2017.01.037

Leary, R. J., Umhoefer, P., Smith, M. E., & Riggs, N., 2017. A three-sided orogen: A new tectonic model for Ancestral Rocky Mountain uplift and basin development. Geology, 45, 735-738. https://doi.org/10.1130/G39041.1

Lee, B., Unsworth, M., Finley, T., Kong, W. and Cordell, D., 2024. Electrically anisotropic structure of the Rocky Mountain Trench near Valemount, British Columbia inferred from magnetotellurics: implications for geothermal exploration. Canadian Journal of Earth Sciences. https://doi.org/10.1139/cjes-2023-0086

Lee, C. T. A., Luffi, P., & Chin, E. J., 2011. Building and destroying continental mantle. Annual Review of Earth and Planetary Sciences, 39, 59-90. https://doi.org/10.1146/annurev-earth-040610-133505

Lekić, V. and Fischer, K.M., 2014. Contrasting lithospheric signatures across the western United States revealed by Sp receiver functions. Earth and Planetary Science Letters, 402, 90-98. https://doi.org/10.1016/j.epsl.2013.11.026

Leseane, K., Atekwana, E.A., Mickus, K.L., Abdelsalam, M.G., Shemang, E.M., Atekwana, E.A., 2015. Thermal perturbations beneath the incipient Okavango Rift Zone, northwest Botswana Khumo. AGU J. Geophys. Res. Solid Earth 119, 3076–3095. https://doi.org/10.1002/2014JB011037.Received

Lewry, J.F., Hajnal, Z., Green, A., Lucas, S.B., White, D., Stauffer, M.R., Ashton, K.E., Weber, W. and Clowes, R., 1994. Structure of a Paleoproterozoic continent-continent collision zone: a LITHOPROBE seismic reflection profile across the Trans-Hudson Orogen, Canada. Tectonophysics, 232, 143-160. https://doi.org/10.1016/0040-1951(94)90081-7

Li, Y., Jiang, H., Yang, X., 2017. Fluorine follows water: Effect on electrical conductivity of silicate minerals by experimental constraints from phlogopite. Geochim. Cosmochim. Acta 217, 16–27. https://doi.org/10.1016/j.gca.2017.08.020

Li, Y., Yang, X., Yu, J. H., & Cai, Y. F., 2016. Unusually high electrical conductivity of phlogopite: the possible role of fluorine and geophysical implications. Contributions to Mineralogy and Petrology, 171, 1-11. https://doi.org/10.1007/s00410-016-1252-x

Li, Z.X.A., Lee, C.T.A., Peslier, A.H., Lenardic, A. and Mackwell, S.J., 2008. Water contents in mantle xenoliths from the Colorado Plateau and vicinity: Implications for the mantle rheology and hydration-induced thinning of continental lithosphere. Journal of Geophysical Research: Solid Earth, 113. https://doi.org/10.1029/2007JB005540

Liddell, M., Unsworth, M. and Pek, J., 2016. Magnetotelluric imaging of anisotropic crust near Fort McMurray, Alberta: implications for engineered geothermal system development; Geophysical Journal International, 205, 1365–1381, doi:10.1093/gji/ggw089.

Lidiak, E. G., Denison, R. E., & Stern, R. J., 2014. Cambrian (?) mill creek diabase dike swarm, Eastern arbuckles: A glimpse of Cambrian rifting in the southern Oklahoma aulacogen. Oklahoma Geological Survey, Guidebook, 38, 105-122.

Liu, H., Zhu, Q., Yang, X., 2019. Electrical conductivity of OH-bearing omphacite and garnet in eclogite: the quantitative dependence on water content. Contrib. to Mineral. Petrol. 174, 1–15. https://doi.org/10.1007/s00410-019-1593-3

Liu, J., Pearson, D. G., Wang, L. H., Mather, K. A., Kjarsgaard, B. A., Schaeffer, A. J., ... & Armstrong, J. P., 2021. Plume-driven recratonization of deep continental lithospheric mantle. Nature, 592, 732-736. https://doi.org/10.6084/m9.figshare.13789354

Liu, L., Morgan, J.P., Xu, Y. and Menzies, M., 2018. Craton destruction 1: cratonic keel delamination along a weak midlithospheric discontinuity layer; Journal of Geophysical Research: Solid Earth, 123, 10 040–10 068, https://doi.org/10.1029/2017JB015372

Liu, X., Currie, C.A., 2019. Influence of Upper Plate Structure on Flat-Slab Depth: Numerical Modeling of Subduction Dynamics. Journal of Geophysical Research: Solid Earth 124, 13150–13167. https://doi.org/10.1029/2019JB018653

Lorand, J.P., Alard, O., Luguet, A., Keays, R.R., 2003. Sulfur and selenium systematics of the subcontinental lithospheric mantle: Inferences from the Massif Central xenolith suite (France). Geochimica et Cosmochimica Acta, 67, 4137–4151. https://doi.org/10.1016/S0016-7037(03)00305-3

Luth, R.W., Stachel, T., 2014. The buffering capacity of lithospheric mantle: implications for diamond formation. Contrib. to Mineral. Petrol. 168, 1–12. https://doi.org/10.1007/s00410-014-1083-6

Manassero, M.C., Afonso, J.C., Zyserman, F., Zlotnik, S. and Fomin, I., 2020. A reduced order approach for probabilistic inversions of 3-D magnetotelluric data I: general formulation. Geophysical Journal International, 223(3), pp.1837-1863. https://doi.org/10.1093/gji/ggaa415

Mandler, B.E., Grove, T.L., 2016. Controls on the stability and composition of amphibole in the Earth's mantle. Contrib. to Mineral. Petrol. 171. https://doi.org/10.1007/s00410-016-1281-5

Marsh, S., & Holland, A., 2016. Comprehensive fault database and interpretive fault map of Oklahoma. Oklahoma Geol. Surv. Open-File Rep. OF2-2016, Oklahoma Geological Survey, Norman, OK.

Marshak, S., Nelson, W. J., & McBride, J. H., 2003. Phanerozoic strike-slip faulting in the continental interior platform of the United States: examples from the Laramide Orogen, Midcontinent, and Ancestral Rocky Mountains. Geological Society, London, Special Publications, 210, 159-184. https://doi.org/10.1144/GSL.SP.2003.210.01.10

Martin, H., Smithies, R.H., Rapp, R., Moyen, J.F., Champion, D., 2005. An overview of adakite, tonalite-trondhjemiten-granodiorite (TTG), and sanukitoid: Relationships and some implications for crustal evolution. Lithos 79, 1–24. https://doi.org/10.1016/j.lithos.2004.04.048

Martin, L.A.J., Hermann, J., 2018. Experimental phase relations in altered oceanic crust: Implications for carbon recycling at subduction zones. Journal of Petrology, 59, 299–320. https://doi.org/10.1093/petrology/egy031

Martin, R. F., 2006. A-type granites of crustal origin ultimately result from open-system fenitization-type reactions in an extensional environment. Lithos, 911, 125-136. https://doi.org/10.1016/j.lithos.2006.03.012

Mathez, E. A. (1987). Carbonaceous matter in mantle xenoliths: Composition and relevance to the isotopes. Geochimica et Cosmochimica Acta, 51, 2339-2347. https://doi.org/10.1016/0016-7037(87)90288-2

Mathez, E. A., Dietrich, V. J., & Irving, A. J., 1984. The geochemistry of carbon in mantle peridotites. Geochimica et Cosmochimica Acta, 48, 1849-1859. https://doi.org/10.1016/0016-7037(84)90038-3

Maxwell, J.C., 1873. A treatise on electricity and magnetism. Oxford University Press. London, United Kingdom. pp. 3408-3425.

McConnell, D. A., 1989. Determination of offset across the northern margin of the Wichita uplift, southwest Oklahoma. Geological Society of America Bulletin, 101, 1317-1332. https://doi.org/10.1130/0016-7606(1989)101<1317:DOOATN>2.3.CO;2

McConnell, D. A., & Gilbert, M. C., 1990. Cambrian extensional tectonics and magmatism within the Southern Oklahoma aulacogen. Tectonophysics, 174, 147-157. https://doi.org/10.1016/0040-1951(90)90388-O

McCuaig, C.T. and Hronsky, J.M.A. 2014: The mineral system concept: the key to exploration targeting; in Building Exploration Capability for the 21st Century, K.D. Kelly and H.C. Golden (ed.), Special Publication of the Society of Economic Geologists, 18, 153–175.

McCuaig, T.C., Beresford, S. and Hronsky, J., 2010. Translating the mineral systems approach into an effective exploration targeting system. Ore Geology Reviews, 38, 128-138. https://doi.org/10.1016/j.oregeorev.2010.05.008

McKenzie, D., 1985. The extraction of magma from the crust and mantle. Earth and Planetary Science Letters, 74, 81-91. https://doi.org/10.1016/0012-821X(85)90168-2

McNeice, G.W. and Jones, A.G., 2001. Multisite, multifrequency tensor decomposition of magnetotelluric data. Geophysics, 66, 158-173. https://doi.org/10.1190/1.1444891

McNicoll, V.J., McDonough, M., and Grover, T. 1994. U–Pb geochronology of the southern Taltson magmatic zone, northeastern Alberta. In Report of Lithoprobe Alberta Basement Transects Workshop. Edited by G.M. Ross. Lithoprobe Report No. 37, 270–273.

McNicoll, V.J., Thériault, R.J. and McDonough, M.R., 2000. Taltson basement gneissic rocks: U Pb and Nd isotopic constraints on the basement to the Paleoproterozoic Taltson magmatic zone, northeastern Alberta. Canadian Journal of Earth Sciences, 37, 1575-1596. https://doi.org/10.1139/e00-034

Miller, J. D., Nicholson, S. W., Easton, R. M., Ripley, E. M., & Feinberg, J. M., 2013. Geology and mineral deposits of the 1.1 Ga Midcontinent Rift in the Lake Superior region—An overview. Field guide to the copper-nickel-platinum group element deposits of the Lake Superior Region. Edited by Miller, J. Precambrian Research Center Guidebook, 13, 1-49.

Milne, S., 2024. Diamonds with unusual inclusions from unique cratonic settings. Unpublished PhD thesis. University of Alberta.

Milne, S.E., Timmerman, S., Read, G., Pearson, D.G., Banas, A. and Stachel, T., 2024, July. Mesoproterozoic diamond formation in the Sask craton mantle root: A far-field link to the Mackenzie large igneous event?. In International Kimberlite Conference: Extended Abstracts (Vol. 12).

Mookherjee, M., Karato, S., 2010. Solubility of water in pyrope-rich garnet at high pressures and temperature. Geophys. Res. Lett. 37. https://doi.org/10.1029/2009GL041289

Morelli, R.M. and MacLachlan, K., 2012. Saskatchewan Gold: Mineralization Styles and Mining History (Report 262). Saskatchewan Geological Survey, Saskatchewan Ministry of Energy and Resources.

Mulibo, G.D., Nyblade, A.A., 2013. The P and S wave velocity structure of the mantle beneath eastern Africa and the African superplume anomaly. Geochemistry, Geophys. Geosystems 14, 2696–2715. https://doi.org/10.1002/ggge.20150

Munch, F.D. and Grayver, A., 2023. Multi-scale imaging of 3-D electrical conductivity structure under the contiguous US constrains lateral variations in the upper mantle water content. Earth and Planetary Science Letters, 602, 117939. https://doi.org/10.1016/j.epsl.2022.117939

Murphy, B.S., Bedrosian, P.A., Kelbert, A., 2023. Geoelectric constraints on the Precambrian assembly and architecture of southern Laurentia, in: Memoir of the Geological Society of America. Geological Society of America, 203–220. https://doi.org/10.1130/2022.1220(13)

Murphy, B.S., Huizenga, J.M., Bedrosian, P.A., 2022. Graphite as an electrically conductive indicator of ancient crustal-scale fluid flow within mineral systems. Earth Planet. Sci. Lett. 594. https://doi.org/10.1016/j.epsl.2022.117700

Naif, S., Key, K., Constable, S. and Evans, R.L., 2013. Melt-rich channel observed at the lithosphere–asthenosphere boundary. Nature, 495, 356-359. https://doi.org/10.1038/nature11939

Naif, S., Selway, K., Murphy, B.S., Egbert, G. and Pommier, A., 2021. Electrical conductivity of the lithosphere-asthenosphere system. Physics of the Earth and Planetary Interiors, 313, 106661. https://doi.org/10.1016/j.pepi.2021.106661

Nesbitt, B.E., 1993. Electrical resistivities of crustal fluids. Journal of Geophysical Research: Solid Earth, 98, 4301-4310. https://doi.org/10.1029/92JB02576

Netto, A., & Pulliam, J., 2020. Upper mantle structure of the southern US continental margin from teleseismic traveltime tomography. Geophysical Research Letters, 47, e2019GL085482. https://doi.org/10.1029/2019GL085482

Nieuwenhuis, G., Unsworth, M.J., Pana, D., Craven, J. and Bertrand, E., 2014: Three-dimensional resistivity structure of southern Alberta, Canada: implications for Precambrian tectonics; Geophysical Journal International, 197, 838–859, doi:10.1093/gji/ggu068.

Novella, D., Frost, D.J., Hauri, E.H., Bureau, H., Raepsaet, C., Roberge, M., 2014. The distribution of H2O between silicate melt and nominally anhydrous peridotite and the onset of hydrous melting in the deep upper mantle. Earth and Planetary Science Letters, 400, 1–13. https://doi.org/10.1016/j.epsl.2014.05.006

NRCAN, 2019. Diamond facts. Available at: https://natural-resources.canada.ca/our-natural-resources/minerals-mining/mining-data-statistics-and-analysis/minerals-metals-facts/diamond-facts/20513 (Accessed: 20 December 2020).

Nyamwandha, C. A., Powell, C. A., & Langston, C. A., 2016. A joint local and teleseismic tomography study of the Mississippi Embayment and New Madrid Seismic Zone. Journal of Geophysical Research: Solid Earth, 121, 3570-3585. https://doi.org/10.1002/2015JB012761

Nyblade, A. A., & Brazier, R. A., 2002. Precambrian lithospheric controls on the development of the East African rift system. Geology, 30, 755-758. https://doi.org/10.1130/0091-7613(2002)030<0755:PLCOTD>2.0.CO;2

O'Reilly, S. Y., & Griffin, W. L., 2013. Mantle metasomatism. Metasomatism and the chemical transformation of rock, 471-533. https://doi.org/10.1007/978-3-642-28394-9_12

Okada, K., 2022. Breakthrough technologies for mineral exploration. In Mineral Economics (Vol. 35, Issues 3–4, pp. 429–454). Springer Science and Business Media Deutschland GmbH. https://doi.org/10.1007/s13563-022-00317-3

O'Neill, C.J., Lenardic, A., Griffin, W.L. and O'Reilly, S.Y., 2008. Dynamics of cratons in an evolving mantle. Lithos, 102, 12-24. https://doi.org/10.1016/j.lithos.2007.04.006

Özaydın, S., Selway, K. and Griffin, W.L., 2021. Are xenoliths from southwestern Kaapvaal Craton representative of the broader mantle? Constraints from magnetotelluric modeling. Geophysical Research Letters, 48, e2021GL092570. https://doi.org/10.1029/2021GL092570.

Özaydın, S., Selway, K., 2020. MATE: An Analysis Tool for the Interpretation of Magnetotelluric Models of the Mantle. Geochemistry, Geophysics, Geosystems 21. https://doi.org/10.1029/2020GC009126

Özaydın, S., Selway, K., 2022. The Relationship Between Kimberlitic Magmatism and Electrical Conductivity Anomalies in the Mantle. Geophysical Research Letters, 49. https://doi.org/10.1029/2022GL099661

Özaydın, S., Selway, K., Griffin, W. L., & Moorkamp, M., 2022. Probing the southern African lithosphere with magnetotellurics: 2. Linking electrical conductivity, composition, and

tectonomagmatic evolution. Journal of Geophysical Research: Solid Earth, 127, e2021JB023105. https://doi.org/10.1029/2021JB023105

Padrón-Navarta, J.A., Hermann, J., 2017. A Subsolidus Olivine Water Solubility Equation for the Earth's Upper Mantle. Journal of Geophysical Research: Solid Earth,122, 9862–9880. https://doi.org/10.1002/2017JB014510

Palacky, G.J., 1987. Resistivity characteristics of geologic targets. In M.N. Nabighian (Ed.), Electromagnetic Methods in Applied Geophysics: Volume 1. (pp. 52-129). Society of Exploration Geophysicists. https://doi.org/10.1190/1.9781560802631.ch3

Parker, R.L. and Booker, J.R., 1996. Optimal one-dimensional inversion and bounding of magnetotelluric apparent resistivity and phase measurements. Physics of the Earth and Planetary Interiors, 98, 69-282. https://doi.org/10.1016/S0031-9201(96)03191-3

Parkinson, W. D., 1959. Directions of rapid geomagnetic fluctuations. Geophysical Journal International, 2, 1-14. https://doi.org/10.1111/j.1365-246X.1959.tb05776.x

Peacock, S.M., 1993. The importance of blueschist-»eclogite dehydration reactions in subducting oceanic crust. Geol. Soc. Am. Bull. 105, 684–694. https://doi.org/10.1130/0016-7606(1993)105<0684:TIOBED>2.3.CO;2

Pearson DG, Wittig N., 2014. The formation and evolution of cratonic mantle lithosphere—evidence from mantle xenoliths. In Treatise on Geochemistry, ed. KK Turekian, HD Holland, 255–92.

Pearson, D.G., Scott, J.M., Liu, J., Schaeffer, A., Wang, L.H., van Hunen, J., Szilas, K., Chacko, T., Kelemen, P.B., 2021. Deep continental roots and cratons. Nature 596, 199–210. https://doi.org/10.1038/s41586-021-03600-5

Perry, W. J., 1989. Tectonic evolution of the Anadarko Basin region, Oklahoma (No. 1866). Department of the Interior, US Geological Survey.

Peslier, A. H., Woodland, A. B., Bell, D. R., & Lazarov, M., 2010. Olivine water contents in the continental lithosphere and the longevity of cratons. Nature, 467, 78-81. https://doi.org/10.1038/nature09317

Peslier, A.H., Woodland, A.B., Bell, D.R., Lazarov, M. and Lapen, T.J., 2012. Metasomatic control of water contents in the Kaapvaal cratonic mantle. Geochimica et Cosmochimica Acta, 97, pp.213-246. https://doi.org/10.1016/j.gca.2012.08.028

Peslier, A.H., Schönbächler, M., Busemann, H. and Karato, S.I., 2017. Water in the Earth's interior: distribution and origin. Space Science Reviews, 212, 743-810. https://doi.org/10.1007/s11214-017-0387-z

Pezzera, A., Nestola, F., Stachel, T., Stern, R.A., Perritt, S. and Pearson, D.G., 2024, July. Characterisation of sublithospheric and lithospheric diamond populations from the Candle Lake C29/30 kimberlite, Sask craton, Canada. In International Kimberlite Conference: Extended Abstracts (Vol. 12).

Pilkington, M., Miles, W.F., Ross, G.M. and Roest, W.R., 2000: Potential-field signatures of buried Precambrian basement in the Western Canada Sedimentary Basin; Canadian Journal of Earth Sciences, 37, 1453–1471, https://doi.org/10.1139/e00-020.

Pineau, F., Mathez, E.A., 1990. Carbon isotopes in xenoliths from the Hualalai Volcano, Hawaii, and the generation of isotopic variability. Geochim. Cosmochim. Acta 54, 211–227. https://doi.org/10.1016/0016-7037(90)90209-4

Plank, T., Manning, C.E., 2019. Subducting carbon. Nature. 574, 343-352. https://doi.org/10.1038/s41586-019-1643-z

Pommier, A., 2014. Interpretation of magnetotelluric results using laboratory measurements. Surveys in Geophysics, 35, 41-84. https://doi.org/10.1007/s10712-013-9226-2

Pommier, A., Kohlstedt, D. L., Hansen, L. N., Mackwell, S., Tasaka, M., Heidelbach, F., & Leinenweber, K., 2018. Transport properties of olivine grain boundaries from electrical

conductivity experiments. Contributions to Mineralogy and Petrology, 173, 1-13. https://doi.org/10.1007/s00410-018-1468-z

Porritt, R. W., Allen, R. M., & Pollitz, F. F., 2014. Seismic imaging east of the Rocky Mountains with USArray. Earth and Planetary Science Letters, 402, 16-25. https://doi.org/10.1016/j.epsl.2013.10.034

Power, M., Belcourt, G. and Rockel, E., 2004. Geophysical methods for kimberlite exploration in northern Canada. The Leading Edge, 23, 1124-1129. https://doi.org/10.1190/1.1825939

Pratt, T. L., Hauser, E. C., & Nelson, K. D., 1992. Widespread buried Precambrian layered sequences in the US mid-continent: Evidence for large Proterozoic depositional basins. AAPG bulletin, 76, 1384-1401. https://doi.org/10.1306/BDFF89FC-1718-11D7-8645000102C1865D

Price, J. D., 2014. The Mount Scott Intrusive Suite, Wichita Mountains, Oklahoma. Oklahoma Geological Survey Guidebook, 38, 299-318.

Price, J. D., Hogan, J. P., Gilbert, M. C., London, D., & Morgan, G. B., 1999. Experimental study of titanite-fluorite equilibria in the A-type Mount Scott Granite: Implications for assessing F contents of felsic magma. Geology, 27, 951-954. https://doi.org/10.1130/0091-7613(1999)027<0951:ESOTFE>2.3.CO;2

Priestley, K., McKenzie, D., & Ho, T., 2018. A lithosphere–asthenosphere boundary—A global model derived from multimode surface-wave tomography and petrology. Lithospheric discontinuities, 111-123. https://doi.org/10.1002/9781119249740.ch6

Puckett, R.E., Hanson, R.E., Eschberger, A.M., Brueseke, M.E., Bulen, C.L., Price, J.D. and Suneson, N., 2014. New insights into the early Cambrian igneous and sedimentary history of the Arbuckle Mountains area of the Southern Oklahoma aulacogen from basement well penetrations. Igneous and tectonic history of the Southern Oklahoma Aulacogen, 38, 61-94.

Puelles, P., Ábalos, B., & Fernández-Armas, S., 2014. Graphite and quartz petrofabrics: Examples from the Ediacaran black quartzites of the Ossa-Morena Zone (SW Iberia). Tectonophysics, 615, 53-68. https://doi.org/10.1016/j.tecto.2013.12.018

Rader, E., Emry, E., Schmerr, N., Frost, D., Cheng, C., Menard, J., Yu, C.Q., Geist, D., 2015. Characterization and Petrological Constraints of the Midlithospheric Discontinuity. Geochemistry, Geophys. Geosystems 16, 3484–3504. https://doi.org/10.1002/2015GC005943

Rankin, D. and Reddy, I.K., 1973. Crustal conductivity anomaly under the Black Hills: a magnetotelluric study. Earth and Planetary Science Letters, 20, 275-279. https://doi.org/10.1016/0012-821X(73)90167-2

Redden, J.A., Peterman, Z.E., Zartman, R.E., DeWitt, E., Lewry, J.F. and Stauffer, M.R., 1990. U-Th-Pb geochronology and preliminary interpretation of Precambrian tectonic events in the Black Hills, South Dakota. The Early Proterozoic Trans-Hudson Orogen of North America: Geological Association of Canada Special Paper, 37, 229-251.

Reed, L.E. and Witherly, K.E., 2007. 50 years of kimberlite geophysics: A review. In Proceedings of Exploration 07: Fifth Decennial International Conference on Mineral Exploration (pp. 679-689).

Refayee, H. A., Yang, B. B., Liu, K. H., & Gao, S. S., 2014. Mantle flow and lithosphere–asthenosphere coupling beneath the southwestern edge of the North American craton: constraints from shear-wave splitting measurements. Earth and Planetary Science Letters, 402, 209-220. https://doi.org/10.1016/j.epsl.2013.01.031

Rehfeldt, T., Foley, S. F., Jacob, D. E., Carlson, R. W., & Lowry, D., 2008. Contrasting types of metasomatism in dunite, wehrlite and websterite xenoliths from Kimberley, South Africa. Geochimica et Cosmochimica Acta, 72, 5722-5756. https://doi.org/10.1016/j.gca.2008.08.020

Reid, K.D., 2018. GS2018-4: Sub-Phanerozoic basement geology from drillcore observations in the Watts, Mitishto and Hargrave rivers area, eastern Flin Flon belt, west-central Manitoba (parts of NTS 63J5, 6, 11, 12, 13, 14). Manitoba Geological Survey Report of Activtieis 2018, 37–47.

Reitzel, J.S., Gough, D.I., Porath, H. and Anderson III, C.W., 1970. Geomagnetic deep sounding and upper mantle structure in the western United States. Geophysical Journal International, 19, 213-235. https://doi.org/10.1111/j.1365-246X.1970.tb06044.x

Revil, A., 2013. Effective conductivity and permittivity of unsaturated porous materials in the frequency range 1 mHz–1GHz. Water resources research, 49, 306-327. https://doi.org/10.1029/2012WR012700

Rodi, W., & Mackie, R. L., 2001. Nonlinear conjugate gradients algorithm for 2-D magnetotelluric inversion. Geophysics, 66, 174-187. https://doi.org/10.1190/1.1444893

Ross, G.M., 2002. Evolution of Precambrian continental lithosphere in Western Canada: results from Lithoprobe studies in Alberta and beyond; Canadian Journal of Earth Sciences, 39, 413–437, http://www.doi.org/10.1139/e02-012.

Ross, G.M. and Eaton, D.W., 2002. Proterozoic tectonic accretion and growth of western Laurentia: results from Lithoprobe studies in northern Alberta; Canadian Journal of Earth Sciences, 39, 313–329, https://www.doi.org/10.1139/e01-081.

Ross, G.M., Mariano, J. and Dumont, R., 1994. Was Eocene magmatism widespread in the subsurface of southern Alberta? Evidence from new aeromagnetic anomaly data; in 1994 LITHOPROBE Alberta basement transects workshop, LITHOPROBE Secretariat, University of British Columbia, LITHOPROBE Report No. 37, 240–249.

Rubingh, K.E., Lafrance, B. and Gibson, H.L., 2024. The Snow Lake Deposits in Manitoba, Canada: Formation of Metamorphosed Amphibolite Facies Orogenic Gold Deposits During a Progressive and Prograde Orogenic Event. Economic Geology, 119, 421-444. https://doi.org/10.5382/econgeo.5048

Russell, J.K., Sparks, R.S.J. and Kavanagh, J.L., 2019. Kimberlite volcanology: transport, ascent, and eruption; Elements, 15, 405–410, https://www.doi.org/10.2138/gselements.15.6.405.

Rychert, C. A., Shearer, P. M., & Fischer, K. M., 2010. Scattered wave imaging of the lithosphere–asthenosphere boundary. Lithos, 120, 173-185. https://doi.org/10.1016/j.lithos.2009.12.006

Safonov, O., Butvina, V., & Limanov, E., 2019. Phlogopite-forming reactions as indicators of metasomatism in the lithospheric mantle. Minerals, 9, 685. https://doi.org/10.3390/min9110685

Salters, V. J., Longhi, J. E., & Bizimis, M., 2002. Near mantle solidus trace element partitioning at pressures up to 3.4 GPa. Geochemistry, Geophysics, Geosystems, 3, 1-23. https://doi.org/10.1029/2001GC000148

Samrock, F., Kuvshinov, A., Bakker, J., Jackson, A. and Fisseha, S., 2015. 3-D analysis and interpretation of magnetotelluric data from the Aluto-Langano geothermal field, Ethiopia. Geophysical Journal International, 202, 1923-1948. https://doi.org/10.1093/gji/ggv270

Saxena, S., Pommier, A., Tauber, M.J., 2021. Iron Sulfides and Anomalous Electrical Resistivity in Cratonic Environments. Journal of Geophysical Research: Solid Earth, 126. https://doi.org/10.1029/2021JB022297

Schaeffer, A.J. and Lebedev, S., 2014. Imaging the North American continent using waveform inversion of global and USArray data. Earth and Planetary Science Letters, 402, 26-41. https://doi.org/10.1016/j.epsl.2014.05.014

Schmidt, M.W., Poli, S., 2013. Devolatilization During Subduction, in: Treatise on Geochemistry: Second Edition. Elsevier Inc., 669–701. https://doi.org/10.1016/B978-0-08-095975-7.00321-1

Schodde, R. (2019, October 30). MinEX consulting trends in mining up to 2019. International Mining and Resource Conference. Melbourne, Australia. Available at

https://minexconsulting.com/wp-content/uploads/2019/12/IMARC-Presentation-27-Oct-2019-FINAL.pdf

Schulze, D.J., 1989. Constraints on the abundance of eclogite in the upper mantle. Journal of Geophysical Research: Solid Earth, 94, 4205-4212. https://doi.org/10.1029/JB094iB04p04205

Selway, K., 2014: On the causes of electrical conductivity anomalies in tectonically stable lithosphere; Surveys in Geophysics, 35,219–257, doi:10.1007/s10712-013-9235-1.

Selway, K., 2018: Electrical discontinuities in the continental lithosphere imaged with magnetotellurics. *In:* Yuan H, Romanowicz B, eds. Lithospheric Discontinuities. Hoboken, NJ: John Wiley and Sons. 89–109

Selway, K., 2014. On the Causes of Electrical Conductivity Anomalies in Tectonically Stable Lithosphere. Surveys in Geophysics, 35, 219–257. https://doi.org/10.1007/s10712-013-9235-1

Shen, W., Ritzwoller, M. H., & Schulte-Pelkum, V. 2013. Crustal and uppermost mantle structure in the central US encompassing the Midcontinent Rift. Journal of Geophysical Research: Solid Earth, 118, 4325-4344. https://doi.org/10.1002/jgrb.50321

Shirey, S.B., klewin, K.W., Berg, J.H., Carlson, R.W., 1994. Temporal changes in the sources of flood basalts: Isotopic and trace element evidence from the 1100 Ma old Keweenawan Mamainse Point Formation, Ontario, Canada. Geochim. Cosmochim. Acta 58, 4475–4490. https://doi.org/10.1016/0016-7037(94)90349-2

Sifré, D., Gardés, E., Massuyeau, M., Hashim, L., Hier-Majumder, S. and Gaillard, F., 2014. Electrical conductivity during incipient melting in the oceanic low-velocity zone. Nature, 509, 81-85. https://doi.org/10.1038/nature13245

Simpson, F. and Bahr, K., 2005. Practical magnetotellurics; Cambridge University Press, Cambridge, United Kingdom, 270 p.

Sims, W.E., Bostick, F.X. and Smith, H.W., 1971. The estimation of magnetotelluric impedance tensor elements from measured data. Geophysics, 36, 938-942. https://doi.org/10.1190/1.1440225

Sinmyo, R. and Keppler, H., 2017. Electrical conductivity of NaCl-bearing aqueous fluids to 600 C and 1 GPa. Contributions to Mineralogy and Petrology, 172, 4. https://doi.org/10.1007/s00410-016-1323-z

Skelton, D., Clements, B., McCandless, T.E., Hood, C., Aulbach, S., Davies, R. and Boyer, L.P., 2003: The Buffalo Head Hills kimberlite province, Alberta; in Slave Province and Northern Alberta Field Trip Guidebook, B.A. Kjarsgaard (ed.), 8th International Kimberlite Conference, Victoria, Canada, June 22–27, 2003, 11–19.

Skulski, T., Francis, D., & Ludden, J. (1991). Arc-transform magmatism in the Wrangell volcanic belt. Geology, 19, 11-14. https://doi.org/10.1130/0091-7613(1991)019<0011:ATMITW>2.3.CO;2

Skulski, T., Francis, D., & Ludden, J., 1992. Volcanism in an arc-transform transition zone: the stratigraphy of the St. Clare Creek volcanic field, Wrangell volcanic belt, Yukon, Canada. Canadian Journal of Earth Sciences, 29, 446-461. https://doi.org/10.1139/e92-039

Sleep, N.H., 2003. Survival of Archean cratonal lithosphere. Journal of Geophysical Research: Solid Earth, 108(B6). https://doi.org/10.1029/2002JB001859

Smith, J. V., 1981. Halogen and phosphorus storage in the Earth. Nature, 289(5800), 762-765. https://doi.org/10.1038/289762a0

Smith, R.S., Annan, A.P., Lemieux, J. and Pedersen, R.N., 1996. Application of a modified GEOTEM® system to reconnaissance exploration for kimberlites in the Point Lake area, NWT, Canada. Geophysics, 61, 82-92. https://doi.org/10.1190/1.1443959

Smyth, D., 2020. Petrology, Geochemistry, and Geochronology of the Pikoo Kimberlites, Saskatchewan. Unpublished MSc thesis. University of Alberta. https://doi.org/10.7939/r3-94fn-cg71

Snyder, D.B., Humphreys, E., Pearson, D.G., 2017. Construction and destruction of some North American cratons. Tectonophysics. https://doi.org/10.1016/j.tecto.2016.11.032

Sodoudi, F., Yuan, X., Kind, R., Lebedev, S., Adam, J.M.C., Kästle, E. and Tilmann, F., 2013. Seismic evidence for stratification in composition and anisotropic fabric within the thick lithosphere of Kalahari Craton. Geochemistry, Geophysics, Geosystems, 14, 5393-5412. https://doi.org/10.1002/2013GC004955

Stachel, T., Luth, R.W., 2015. Diamond formation - Where, when and how? Lithos 220–223, 200–220. https://doi.org/10.1016/j.lithos.2015.01.028

Stagno, V., Frost, D. J., 2010. Carbon speciation in the asthenosphere: Experimental measurements of the redox conditions at which carbonate-bearing melts coexist with graphite or diamond in peridotite assemblages. Earth and Planetary Science Letters, 300, 72-84. https://doi.org/10.1016/j.epsl.2010.09.038

Stamm, N. and Schmidt, M.W., 2017. Asthenospheric kimberlites: volatile contents and bulk compositions at 7 GPa. Earth and Planetary Science Letters, 474, 309-321. https://doi.org/10.1016/j.epsl.2017.06.037

Syme, E.C., Lucas, S.B., Bailes, A.H., Stern, R.A., 1999. Contrasting arc and MORB-like assemblages in the Paleoproterozoic Flin Flon Belt, Manitoba, and the role of intra-arc extension in localizing volcanic-hosted massive sulphide deposits. Can. J. Earth Sci. 36, 1767–1788. https://doi.org/10.1139/e98-084

Tang, Y. J., Zhang, H. F., Santosh, M., & Ying, J. F., 2013. Differential destruction of the North China Craton: A tectonic perspective. Journal of Asian Earth Sciences, 78, 71-82. https://doi.org/10.1016/j.jseaes.2012.11.047

Tappe, S., Dongre, A., Liu, C.Z. and Wu, F.Y., 2018a. 'Premier' evidence for prolonged kimberlite pipe formation and its influence on diamond transport from deep Earth. Geology, 46, 843-846. https://doi.org/10.1130/G45097.1

Tappe, S., Foley, S.F., Kjarsgaard, B.A., Romer, R.L., Heaman, L.M., Stracke, A. and Jenner, G.A., 2008. Between carbontapatite and lamproite—diamondiferous Torngat ultramafic lamprophyres formed by carbonate-fluxed melting of cratonic MARID-type metasomes. Geochimica et Cosmochimica Acta, 72, 3258-3286. https://doi.org/10.1016/j.gca.2008.03.008

Tappe, S., Smart, K., Torsvik, T., Massuyeau, M. and de Wit, M., 2018b. Geodynamics of kimberlites on a cooling Earth: Clues to plate tectonic evolution and deep volatile cycles. Earth and Planetary Science Letters, 484, 1-14. https://doi.org/10.1016/j.epsl.2017.12.013

Taracsák, Z., Mather, T.A., Ding, S., Plank, T., Brounce, M., Pyle, D.M., Aiuppa, A., EIMF, 2023. Sulfur from the subducted slab dominates the sulfur budget of the mantle wedge under volcanic arcs. Earth Planet. Sci. Lett. 602. https://doi.org/10.1016/j.epsl.2022.117948

Tave, M. A., 2013. Imaging of the crust and Moho beneath Oklahoma using receiver functions and Pn tomography; with emphasis on the Southern Oklahoma Aulacogen. Unpublished MSc thesis. Texas Tech University. p. 191.

Ten Ten Grotenhuis, S. M., Drury, M. R., Peach, C. J., & Spiers, C. J., 2004. Electrical properties of fine-grained olivine: Evidence for grain boundary transport. Journal of Geophysical Research: Solid Earth, 109(B6). https://doi.org/10.1029/2003JB002799

Thomas, W. A. (2011). The Iapetan rifted margin of southern Laurentia. Geosphere, 7, 97-120. https://doi.org/10.1130/GES00574.1

Thomas, W. A., 2014. The southern Oklahoma transform-parallel intracratonic fault system. Oklahoma Geological Survey, Guidebook, 38, 375-388.

Tomkins, A.G., Evans, K.A., 2015. Separate zones of sulfate and sulfide release from subducted mafic oceanic crust. Earth Planet. Sci. Lett. 428, 73–83. https://doi.org/10.1016/j.epsl.2015.07.028

Tuncer, V., Unsworth, M.J., Siripunvaraporn, W. and Craven, J.A., 2006. Exploration for unconformity-type uranium deposits with audiomagnetotelluric data: a case study from the

McArthur River mine, Saskatchewan, Canada. Geophysics, 71, B201-B209. https://doi.org/10.1190/1.2348780

Turko, M., & Mitra, S. (2021). Structural geometry and evolution of the Carter-Knox structure, Anadarko Basin, Oklahoma. AAPG Bulletin, 105, 1993-2015. https://doi.org/10.1306/08212019114

Türkoğlu, E., Unsworth, M. and Pană, D., 2009: Deep electrical structure of northern Alberta (Canada): implications for diamond exploration; Canadian Journal of Earth Sciences, 46, 139–154, https://www.doi.org/10.1139/E09-009.

Vervoort, J. D., Wirth, K., Kennedy, B., Sandland, T., & Harpp, K. S., 2007. The magmatic evolution of the Midcontinent rift: New geochronologic and geochemical evidence from felsic magmatism. Precambrian Research, 157, 235-268. https://doi.org/10.1016/j.precamres.2007.02.019

Vozoff, K., 1972. The magnetotelluric method in the exploration of sedimentary basins. Geophysics, 37, 98-141.https://doi.org/10.1190/1.1440255

Wall, C. J., Hanson, R. E., Schmitz, M., Price, J. D., Donovan, R. N., Boro, J. R., ... & Toews, C. E., 2021. Integrating zircon trace-element geochemistry and high-precision U-Pb zircon geochronology to resolve the timing and petrogenesis of the late Ediacaran–Cambrian Wichita igneous province, Southern Oklahoma Aulacogen, USA. Geology, 49, 268-272. https://doi.org/10.1130/G48140.1

Walters, J.B., Cruz-Uribe, A.M., Marschall, H.R., 2020. Sulfur loss from subducted altered oceanic crust and implications for mantle oxidation. Geochemical Perspective Letters, 13, 36–41. https://doi.org/10.7185/geochemlet.2011

Wang, E., 2019. Multidimensional magnetotelluric studies of the Precambrian Alberta basement; Ph.D. thesis, University of Alberta, 397 p., https://www.doi.org/10.7939/r3-sctk-1z12.

Wang, E. and Unsworth, M., 2022. Three-dimensional crustal and upper-mantle resistivity structure of Alberta, Canada: implications for Precambrian tectonics; Geophysical Journal International, 230, no. 3, 1679–1698, doi:10.1093/gji/ggac128.

Wang, E., Unsworth, M. and Chacko, T., 2018: Geoelectric structure of the Great Slave Lake shear zone in northwest Alberta: implications for structure and tectonic history; Canadian Journal of Earth Sciences, 55, 295–307, https://www.doi.org/10.1139/cjes-2017-0067.

Wannamaker, P.E., Hohmann, G.W. and Ward, S.H., 1984. Magnetotelluric responses of three-dimensional bodies in layered earths. Geophysics, 49, 1517-1533. https://doi.org/10.1190/1.1441777

Wannamaker, P.E., Stodt, J.A. and Rijo, L., 1986. Two-dimensional topographic responses in magnetotellurics modeled using finite elements. Geophysics, 51, 2131-2144. https://doi.org/10.1190/1.1442065

Watson, E. B., & Brenan, J. M., 1987. Fluids in the lithosphere, 1. Experimentally-determined wetting characteristics of CO2H2O fluids and their implications for fluid transport, host-rock physical properties, and fluid inclusion formation. Earth and Planetary Science Letters, 85, 497-515. https://doi.org/10.1016/0012-821X(87)90144-0

White, D.J., Lucas, S.B., Bleeker, W., Hajnal, Z., Lewry, J.F. and Zwanzig, H.V., 2002. Suture-zone geometry along an irregular Paleoproterozoic margin: The Superior boundary zone, Manitoba, Canada. Geology, 308, 735-738. https://doi.org/10.1130/0091-7613(2002)030<0735:SZGAAI>2.0.CO;2

Whitmeyer, S. J., & Karlstrom, K. E. 2007. Tectonic model for the Proterozoic growth of North America. Geosphere, 3, 220-259. https://doi.org/10.1130/GES00055.1

Withers, A.C., Bureau, H., Raepsaet, C., Hirschmann, M.M., 2012. Calibration of infrared spectroscopy by elastic recoil detection analysis of H in synthetic olivine. Chem. Geol. 334, 92–98. https://doi.org/10.1016/j.chemgeo.2012.10.002

Wölbern, I., Rümpker, G., Link, K. and Sodoudi, F., 2012. Melt infiltration of the lower lithosphere beneath the Tanzania craton and the Albertine rift inferred from S receiver functions. Geochemistry, Geophysics, Geosystems, 13. https://doi.org/10.1029/2012GC004167

Yang, B., Egbert, G. D., Kelbert, A., & Meqbel, N. M., 2015. Three-dimensional electrical resistivity of the north-central USA from EarthScope long period magnetotelluric data. Earth and Planetary Science Letters, 422, 87-93. https://doi.org/10.1016/j.epsl.2015.04.006

Yang, B., Egbert, G.D., Zhang, H., Meqbel, N. and Hu, X., 2021. Electrical resistivity imaging of continental United States from three-dimensional inversion of EarthScope USArray magnetotelluric data. Earth and Planetary Science Letters, 576, 117244. https://doi.org/10.1016/j.epsl.2021.117244

Yang, X., Keppler, H., McCammon, C. and Ni, H., 2012. Electrical conductivity of orthopyroxene and plagioclase in the lower crust. Contributions to Mineralogy and Petrology, 163, 33-48. https://doi.org/10.1007/s00410-011-0657-9

Yaxley, G.M., Berry, A.J., Rosenthal, A., Woodland, A.B., Paterson, D., 2017. Redox preconditioning deep cratonic lithosphere for kimberlite genesis - Evidence from the central Slave Craton. Scientific Reports, 7. https://doi.org/10.1038/s41598-017-00049-3

Ye, G., Unsworth, M., Wei, W., Jin, S., Liu, Z., 2019. The Lithospheric Structure of the Solonker Suture Zone and Adjacent Areas: Crustal Anisotropy Revealed by a High-Resolution Magnetotelluric Study. J. Geophys. Res. Solid Earth 124, 1142–1163. https://doi.org/10.1029/2018JB015719

Yoshino, T., & Noritake, F., 2011. Unstable graphite films on grain boundaries in crustal rocks. Earth and Planetary Science Letters, 306, 186-192. https://doi.org/10.1016/j.epsl.2011.04.003

Yoshino, T., 2010. Laboratory electrical conductivity measurement of mantle minerals. Surveys in Geophysics, 31, 163-206. https://doi.org/10.1007/s10712-009-9084-0

Yoshino, T., Laumonier, M., McIsaac, E. and Katsura, T., 2010. Electrical conductivity of basaltic and carbonatite melt-bearing peridotites at high pressures: Implications for melt distribution and melt fraction in the upper mantle. Earth and Planetary Science Letters, 295, 593-602. https://doi.org/10.1016/j.epsl.2010.04.050

Yoshino, T., Matsuzaki, T., Shatskiy, A. and Katsura, T., 2009. The effect of water on the electrical conductivity of olivine aggregates and its implications for the electrical structure of the upper mantle. Earth and Planetary Science Letters, 288, 291-300. https://doi.org/10.1007/s10712-009-9084-0

Yoshino, T., Nishi, M., Matsuzaki, T., Yamazaki, D. and Katsura, T., 2008. Electrical conductivity of majorite garnet and its implications for electrical structure in the mantle transition zone. Physics of the Earth and Planetary Interiors, 170, 193-200. https://doi.org/10.1016/j.pepi.2008.04.009

Yuan, H., & Romanowicz, B., 2010. Lithospheric layering in the North American craton. Nature, 466, 1063-1068. https://doi.org/10.1038/nature09332

Yuan, H., French, S., Cupillard, P., & Romanowicz, B., 2014. Lithospheric expression of geological units in central and eastern North America from full waveform tomography. Earth and Planetary Science Letters, 402, 176-186. https://doi.org/10.1016/j.epsl.2013.11.057

Zhang, B. and Yoshino, T., 2017: Effect of graphite on the electrical conductivity of the lithospheric mantle; Geochemistry, Geophysics, Geosystems, 18, 23–40, doi:10.1002/2016GC006530.

Zhang, B.H., Guo, X., Yoshino, T. and Xia, Q.K., 2021. Electrical conductivity of melts: implications for conductivity anomalies in the Earth's mantle. National Science Review, 8, nwab064. https://doi.org/10.1093/nsr/nwab064

Zhang, W., Johnston, S.T. and Currie, C.A., 2019. Kimberlite magmatism induced by west-dipping subduction of the North American plate. Geology, 47, 395-398. https://doi.org/10.1130/G45813.1

Zhu, R., Zhang, H., Zhu, G., Meng, Q., Fan, H., Yang, J., Wu, F., Zhang, Z. and Zheng, T., 2017. Craton destruction and related resources. International Journal of Earth Sciences, 106, 2233-2257. https://doi.org/10.1007/s00531-016-1441-x

Zientek M.L., 2012. Magmatic ore deposits in layered intrusions - Descriptive model for reef-type PGE and contact-type Cu–Ni–PGE deposits. U.S. Geological Survey Open File, 2012-1010. Available at: https://pubs.usgs.gov/ of/2012/1010/contents/OF12-1010.pd

APPENDIX A: SUPPLEMENTAL MATERIALS FOR CHAPTER 5

A.1 Introduction

This is a supplementary file to the article *"Magnetotelluric Imaging of the Lithospheric Structure of the Southern Oklahoma Aulacogen: Implications for Ancestral Rocky Mountain."* This file provides the reader with additional information that is important in understanding the concepts and work in the main article but were not necessary to include in the main article. Here we provide information on: (1) the additional parameters used in MATE (Özaydın and Selway, 2020) calculations (2) data and other MT inversion work not depicted in the main article.

A.2 Experimental Parameters Chosen in MATE calculation

A series of experimental parameters were chosen for the MATE calculations in this study. Below, will discuss the parameters choices used. For a full discussion of the significance of each parameter, readers are referred to Özaydın and Selway (2020).

The peridotite composition used was the proton composition taken from Griffin et al. (2009) with volume fractions of 65.5 olivine, 16.5 orthopyroxene, 3.5 clinopyroxene, and 4.5 garnet. Ti contents in olivine was assigned a value of 70 ppm, this is a typical mantle value (Foley et al., 2013). The Moho was assigned a depth of 45 km from Tave (2013). The Lithosphere-Asthenosphere Boundary were assigned a maximum depth of 180-200 km from Yuan and Romanowicz (2010) and Priestly et al. (2018). The dependency of water partitioning between olivine and orthopyroxene on the aluminum content is orthopyroxene used the model of Novella et al. (2014). The additional conductivity models used for the mineral other than olivine are as follows: (1) Gardes et al. (2014) for olivine, (2) Dai and Karato (2009a) for orthopyroxene, Liu et al. (2019) for clinopyroxene, and Dai and Karato (2009b) for garnet. These mineral conductivity models were the defaults values for these minerals in MATE. The choice of model for these minerals is of secondary importance as they do not considerably affect bulk conductivity values in a proton composition compared to the effects of olivine (Özaydın and Selway, 2020). When phlogopite was incorporated the conductivity models of Li et al. (2016) and Li et al. (2017) were

used for phlogopite modelling without and with fluorine, respectively. Amphibole was modelled using the conductivity model of Hu et al (2018).

The water partitioning coefficients used are as follows: (1) partitioning between orthopyroxene/olivine and clinopyroxene/olivine used coefficients from Demouchy et al. (2017) as these were derived from experiments done at sub-solidus conditions; (2) partitioning between garnet/olivine used the conservative coefficient of Novella et al. (2014). Water calibrations corrections for the solubility and conductivity of olivine were set to the model of Withers et al. (2012). Water calibration corrections for the conductivity of the pyroxenes and garnet used the model of Bell et al. (1995). These parameters were all chosen following the work of Özaydın and Selway (2022) whose modelled water concentrations in similarly stable lithosphere environments.

Conductivity phases like graphite and sulfides were modelled using conductivity values of 0.00001 S/m, and this was taken from Yoshino and Noritake (2011) and Saxena et al. (2021), respectively.

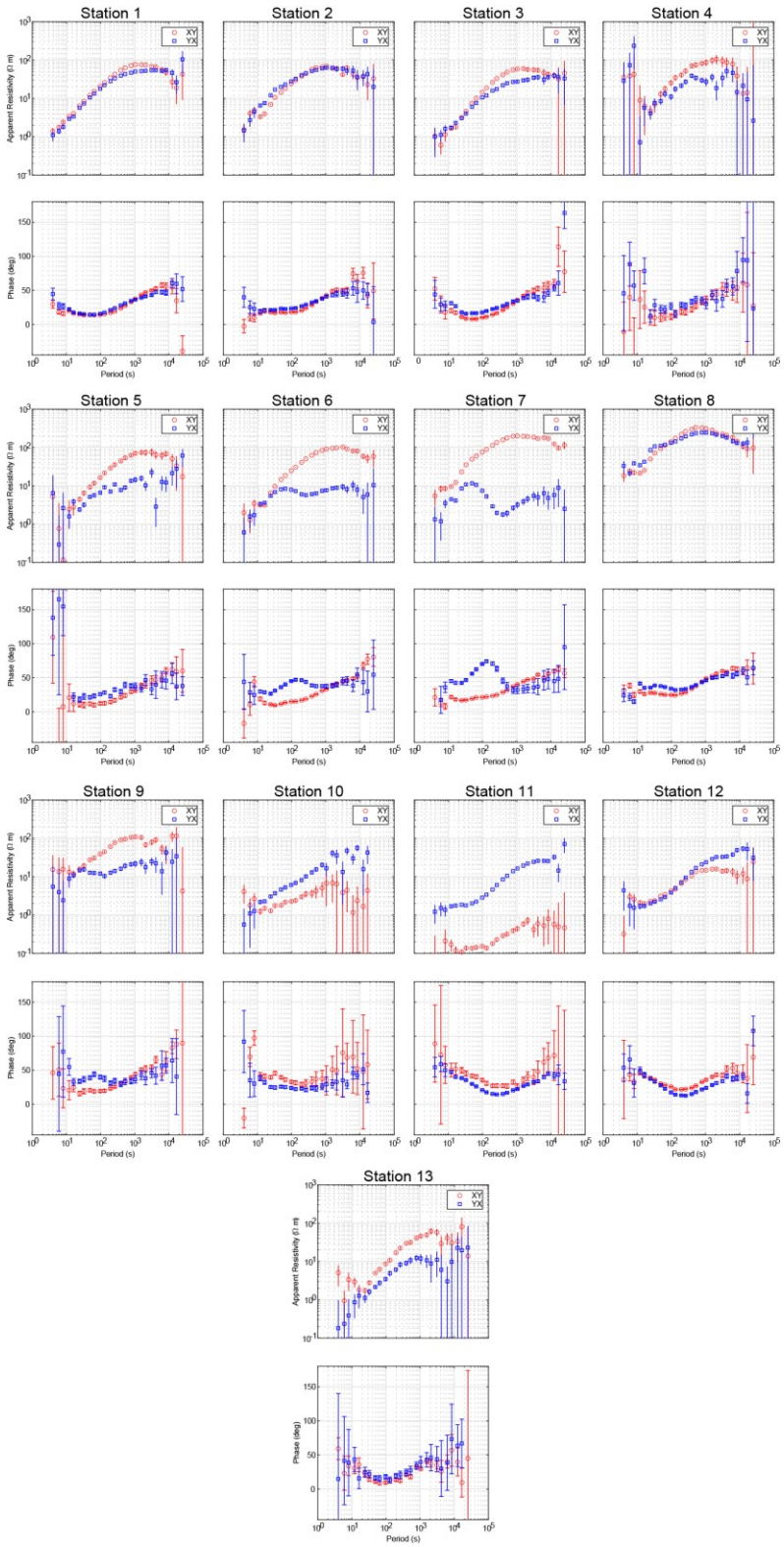

***Figure A.1*:** *Apparent resistivity and phase curves for each of the 13 stations collected across the SOA. The TE mode is shown in red. TM mode is shown in blue.*

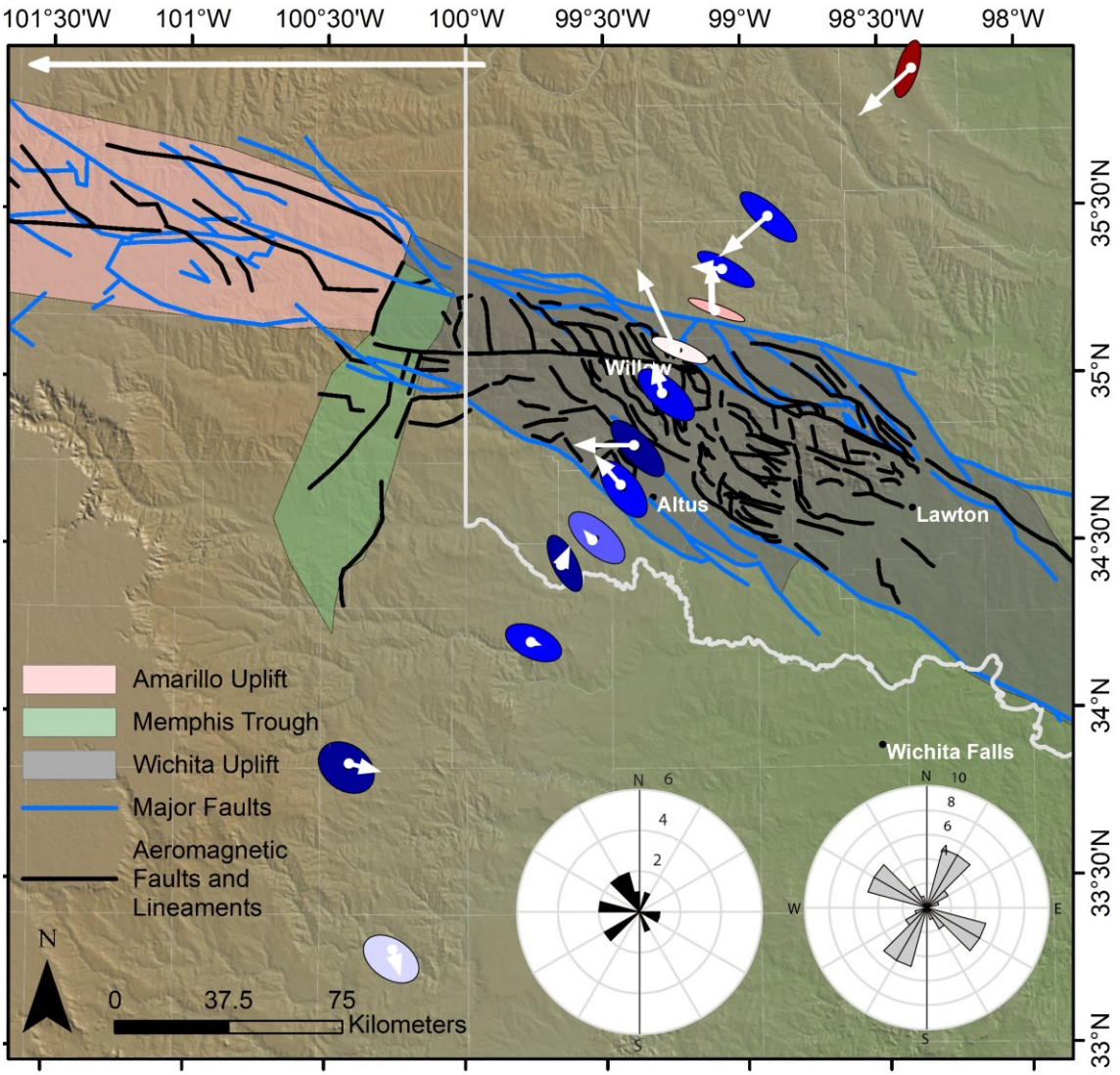

Figure A.2: *The real component of the induction vectors, shown in white, and displayed in the Parkinson's convention (i.e., arrows point towards conductors) for each site at the same period (4000 s) as phase tensors in Figure 5.2. The rose diagram in the lower right shows the orientation of the phase tensors in grey. The rose diagram to the left of this shows the orientation of the induction vectors in black. The white arrow in the upper left-hand corner is a unit vector of 3 units.*

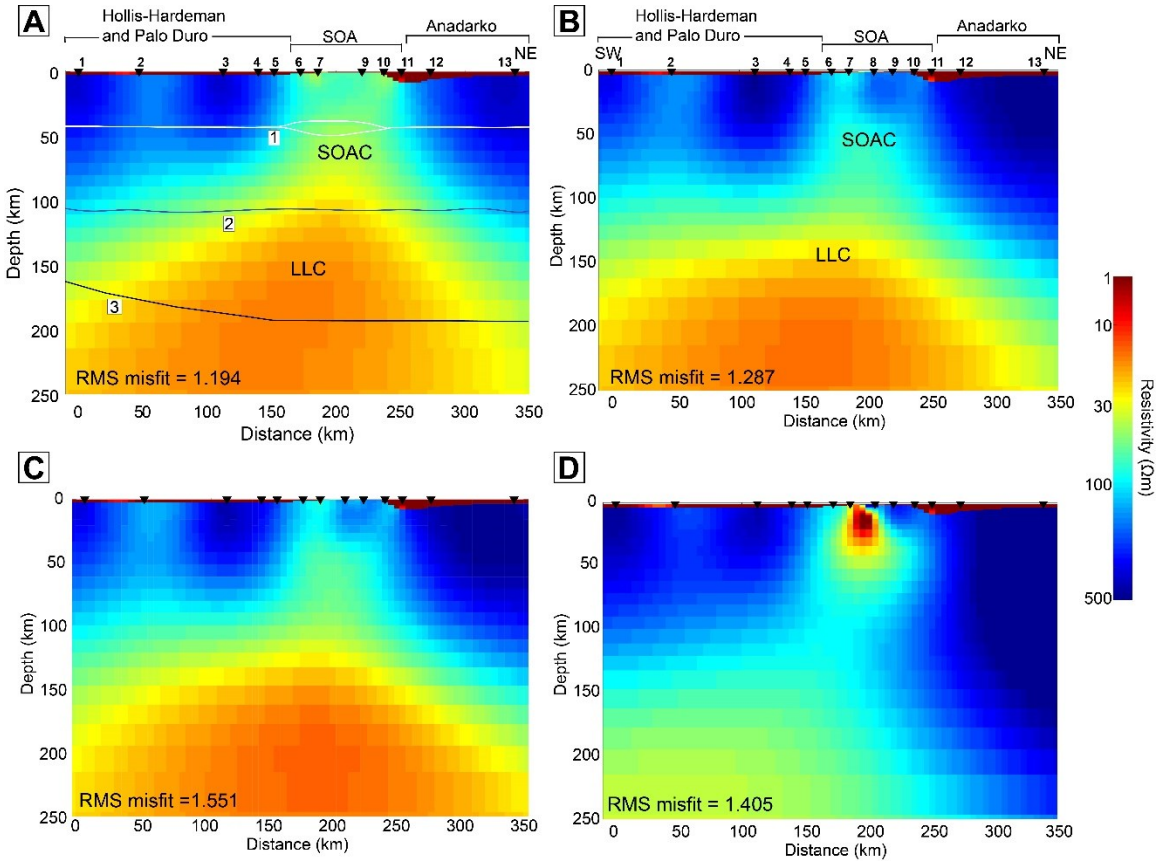

Figure A.3: *A) The final resistivity model from Figure 5.4A, for reference. B) An inversion that excludes Site 8, which was removed from Fig. 5.4A. C) The same inversion as Part B except the inversion routine was allowed to correct for the static shift at station 8 only. D) The same inversion as Part B, except here the static shift for station 8 was manually estimated based on the apparent resistivity curves of stations 6, 7 and 9.*

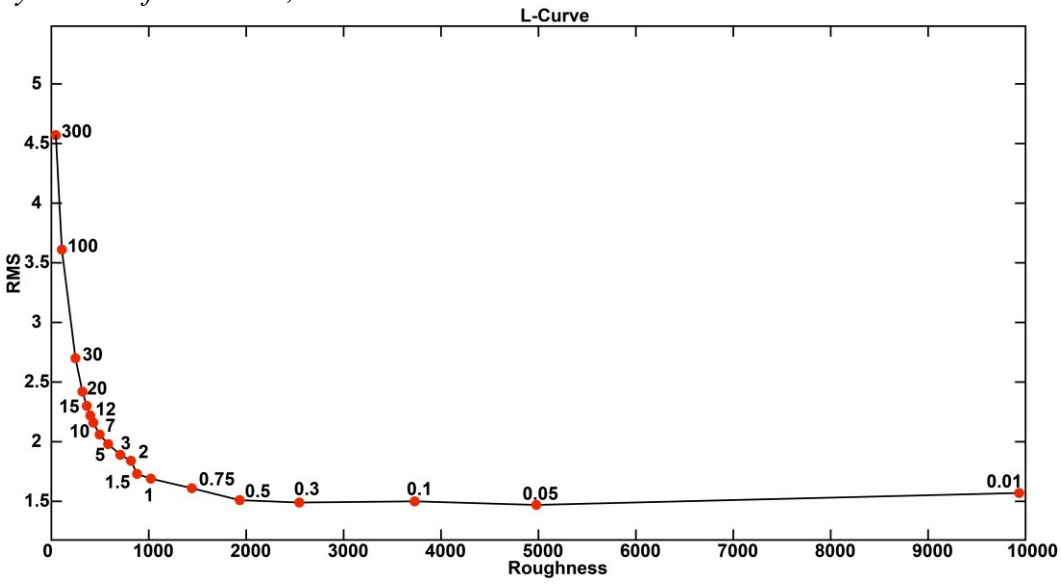

Figure A.4: *L-curve graph used to select the smoothing factor for Figure 5.1.*

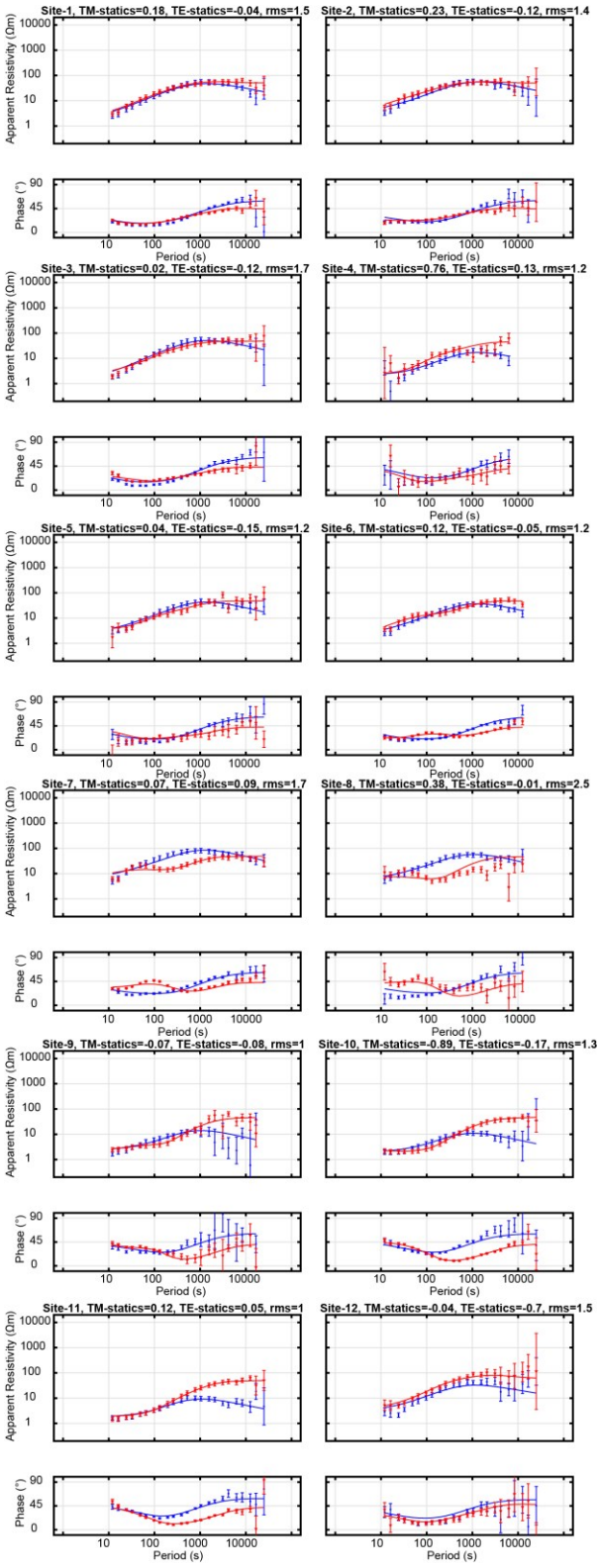

Figure A.5: *Apparent resistivity, phase curves, and fit (solid-colored lines) for the inversion using 12 stations and a 100 Ω-m starting model with no basin incorporated. The resulting inversion model is shown in Figure A.7.*

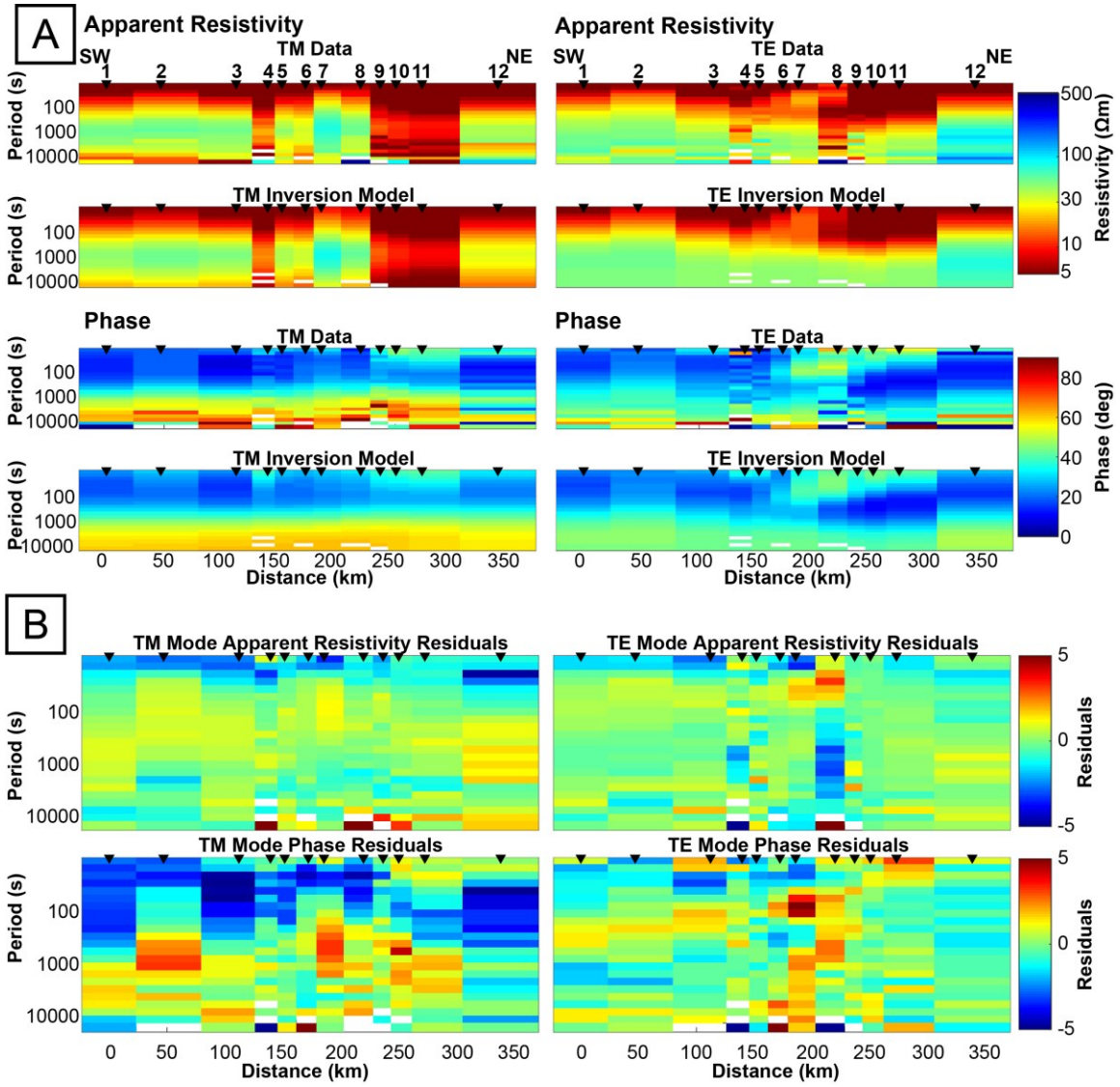

Figure A.6: *A) Pseudosections comparing the apparent resistivity and phase for the TM and TE modes between the data and the resulting inversion model using a 100 Ω-m starting model with no basin incorporated (Fig. A.7A). B) Pseudosections of the error residuals for the apparent resistivity and phase for the TM and TE modes after inversion.*

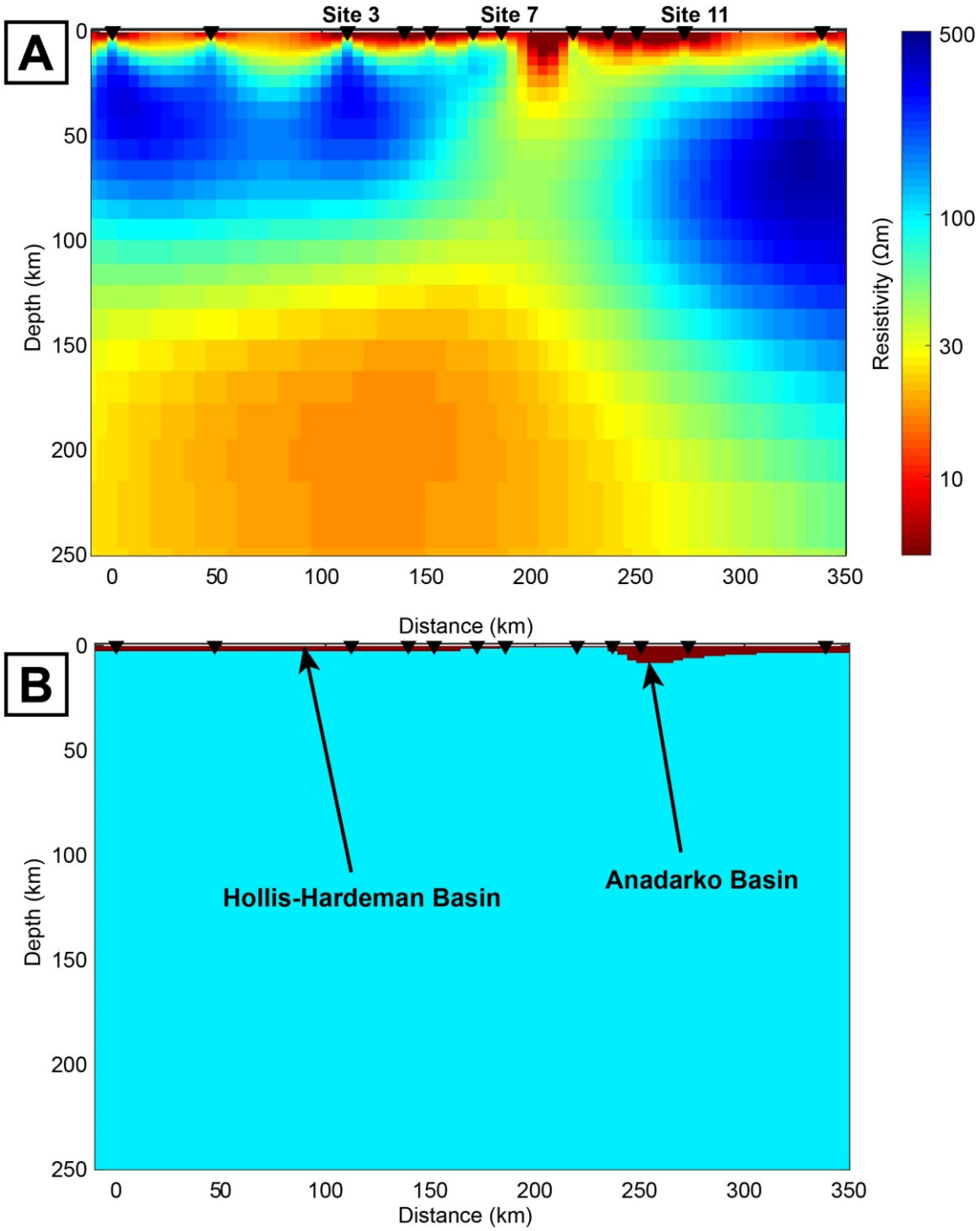

Figure A.7: *A) The inversion model resulting from a 100 Ω-m starting model, the low resistivity anomalies at the top of the model show the effects of the Anadarko and Hollis-Hardeman basins. B) Starting model for Figure 5.4A that incorporates the two basins as a 4 Ω-m discontinuity.*

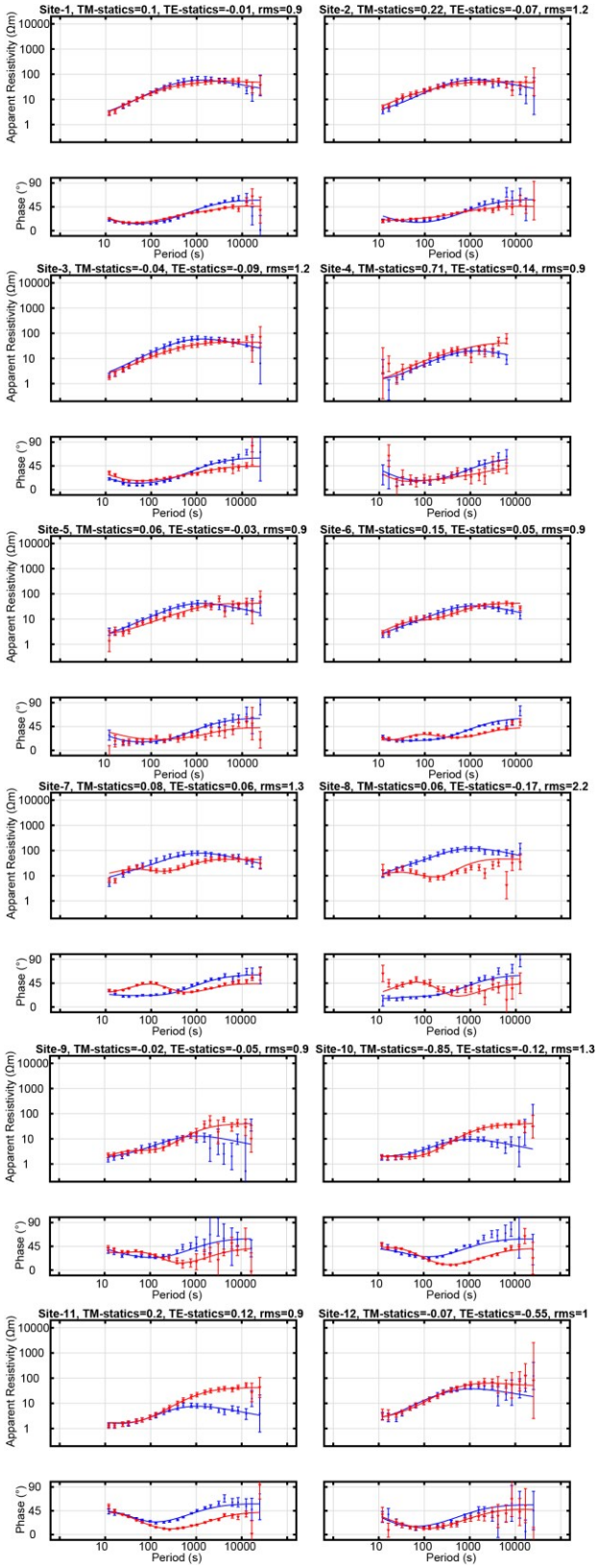

Figure A.8: *Apparent resistivity, phase curves, and fit (solid-colored lines) for the inversion using 12 stations and the modified starting model that incorporates the basin (Fig. A.7B).*

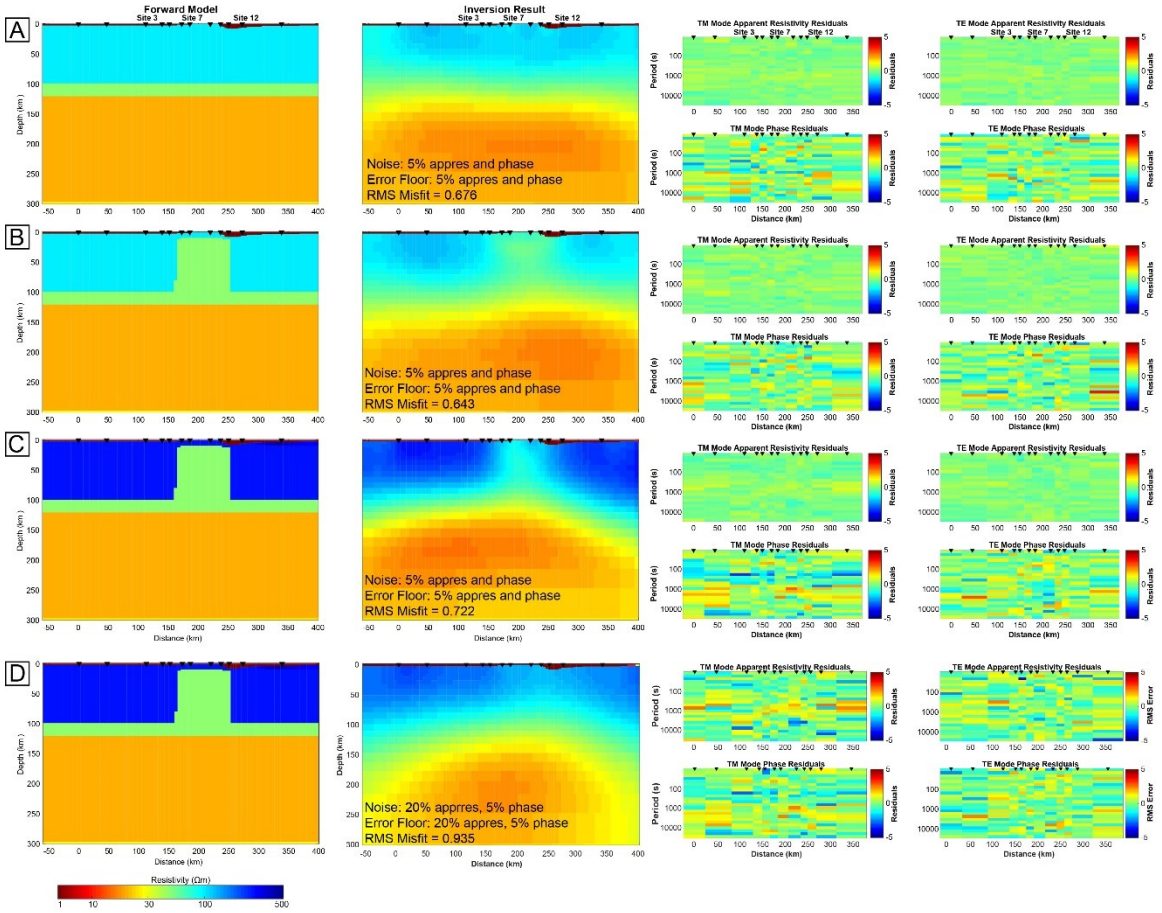

Figure A9: *Synthetic inversions to test the stability of the inversion. A) Incorporates the LLC and is from left to right, the forward model, resulting inversion model, TM and then TE data residuals for apparent resistivity and phase. B) Incorporates the SOAC. C) Incorporates the resistive crust and lithosphere. D) The same forward model as part C, but 20% and 5% noise were added to the apparent resistivity and phase data, respectively.*

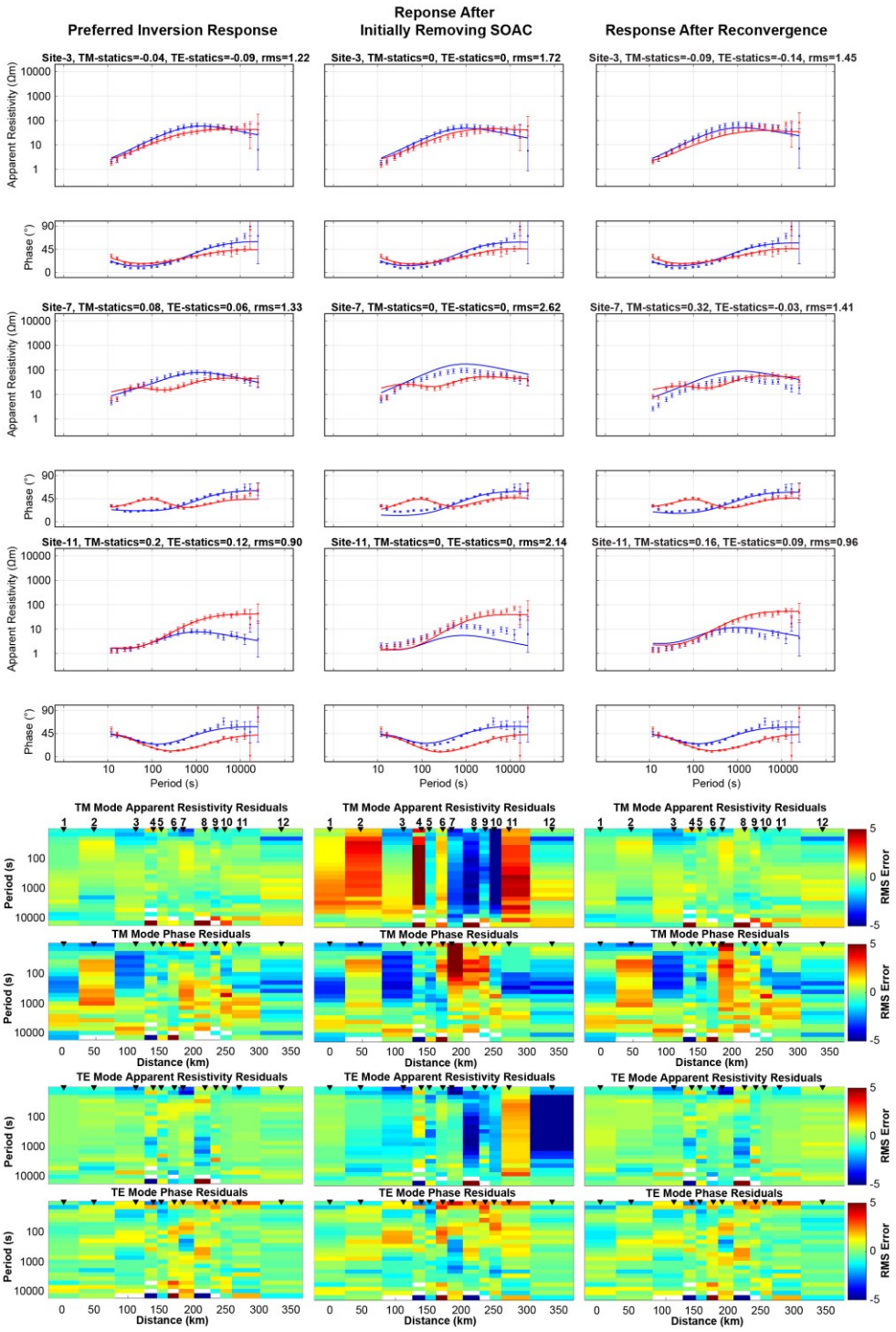

Figure A10: *Comparison of the resistivity and phases curves at 3 selected stations located southwest (Site 3), central to (Site 7), and northeast (Site 11) of the SOA in response to editing Figure 5.4 to remove the SOAC. The column on the left displays the responses from the preferred inversion model in Figure 5.4. The central column displays the responses created by removal of the SOAC. The column on the right displays the responses after the edited model is reinverted and converges. Pseudosections below each column display the error residuals for the TE and TM modes after inversion at all sites.*

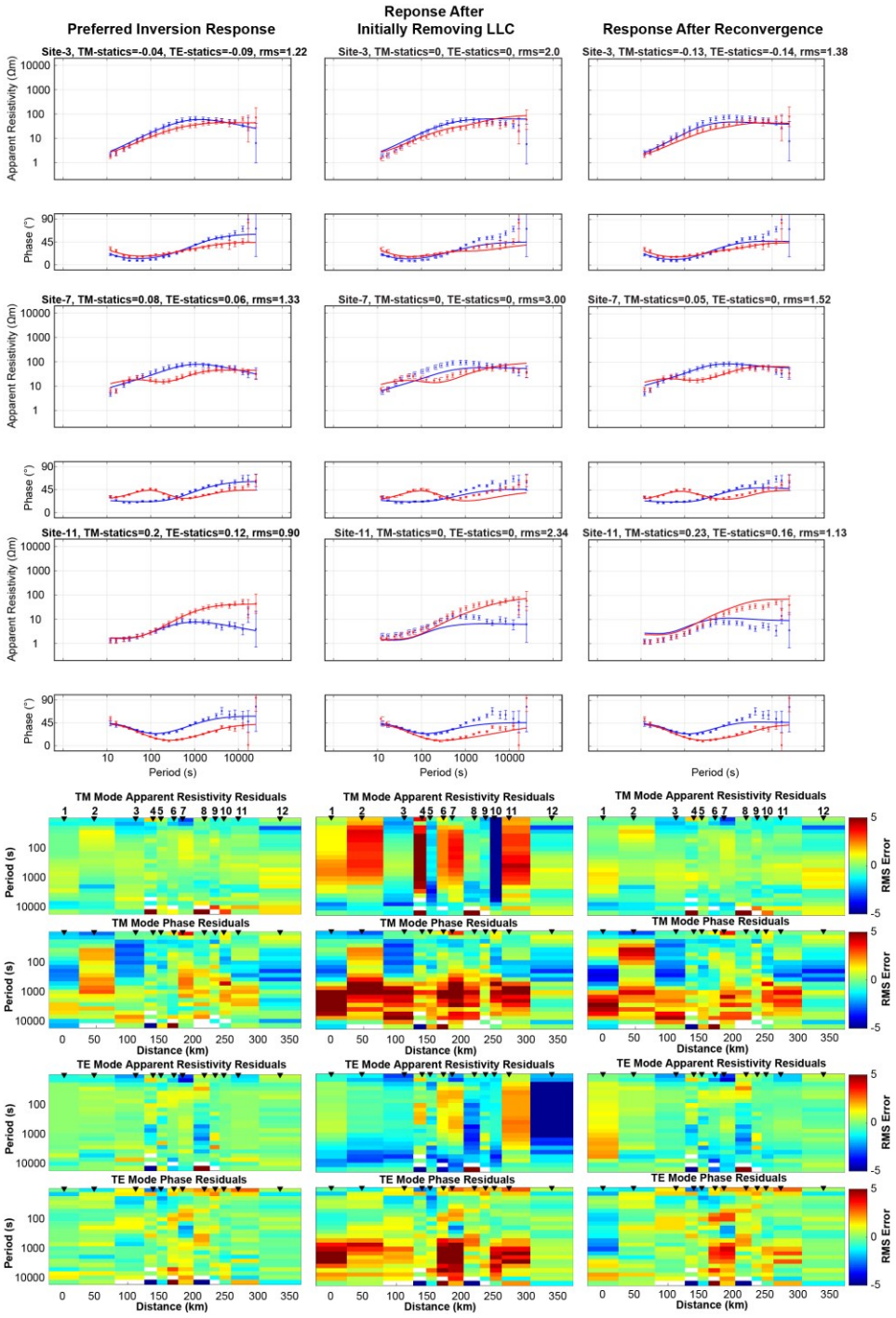

Figure A.11. *Comparison of the resistivity and phases curves at 3 selected stations located southwest (Site 3), central to (Site 7), and northeast (Site 11) of the SOA in response to editing Figure 5.4 to remove the LLC. The column on the left displays the responses from the preferred inversion model in Figure 5.4. The central column displays the responses created by removal of the LLC. The column on the right displays the responses after the edited model is reinverted and converges. Pseudosections below each column display the error residuals for the TE and TM modes after inversion at all sites.*

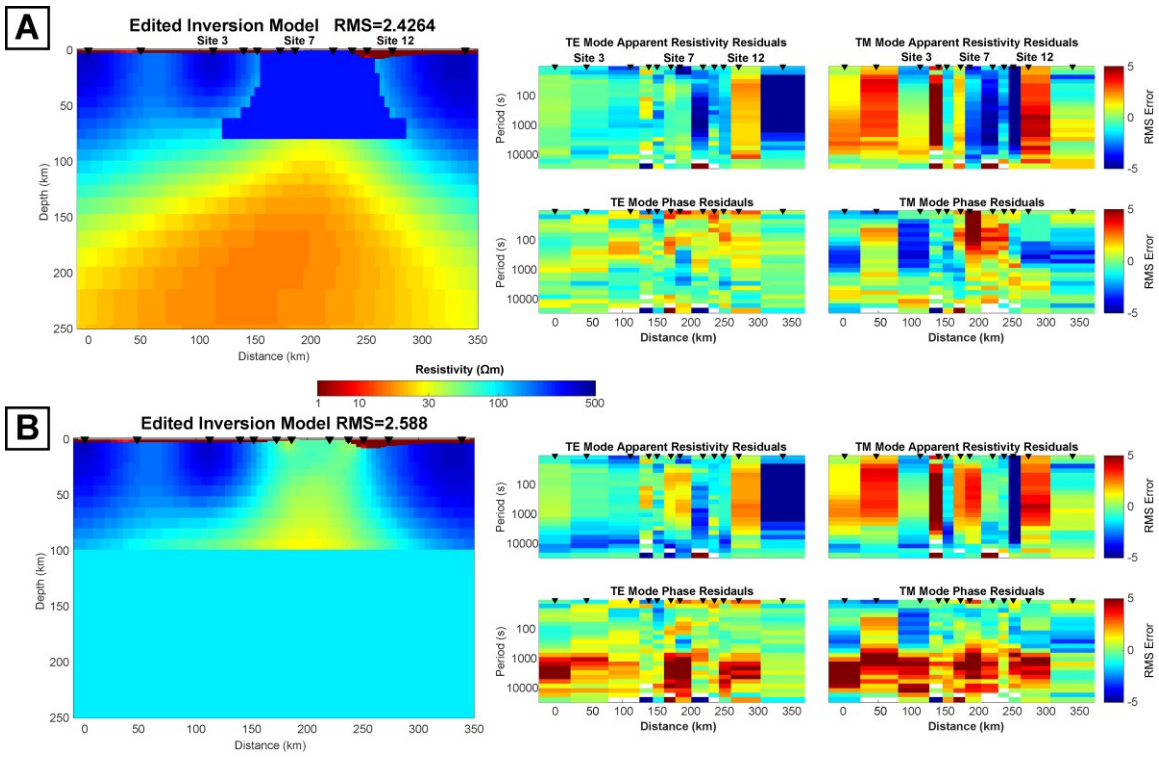

Figure A.12. *Models showing which regions were edited to remove the (A) SOAC and (B) the LLC during model sensitivity tests. The apparent resistivity and phase residuals are repeated from Figures A.9 and A.10. The RMS values are those produced after initially removing each resistivity feature.*

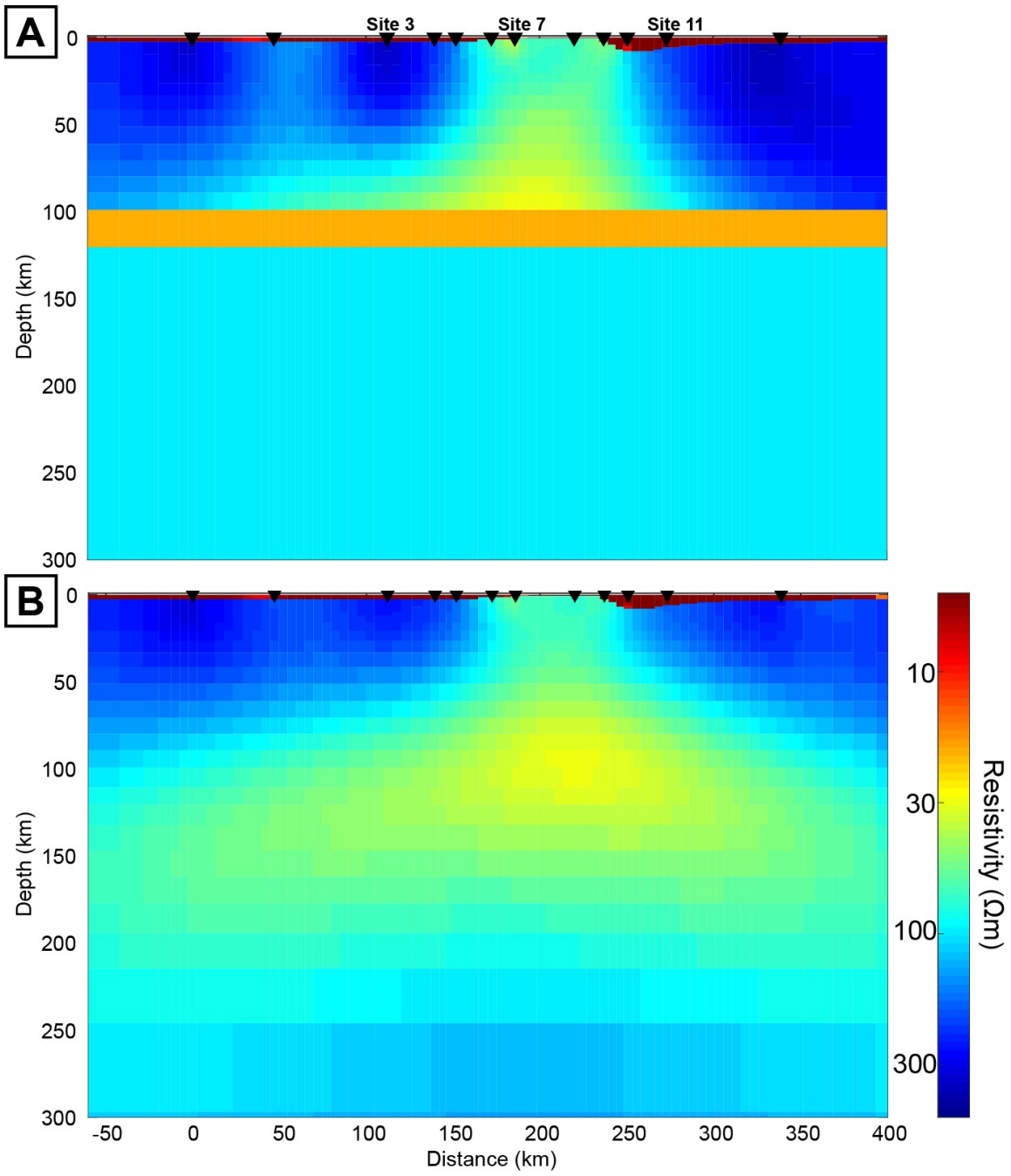

Figure A13. *Forward model test used to see if the data was sensitive to below the LLC at the MLD (~100-110 km). A) The forward model with the phlogopite-MLD shown as a 20 Ω-m orange conductor. Above this the model is the same as Figure 5.4. Below it the remainder of the model space is set to 100 ohm-m to see if those values are recovered. B) The resulting inversion model showing recovery of the 100 ohm-m layer, showing that the data is sensitive to below the initial LLC at the MLD.*

APPENDIX B: SUPPLEMENTAL MATERIALS FOR CHAPTER 6

B.1 Characteristics of phase tensors and induction vectors

Phase tensors and induction vectors at selected periods are shown in Figures B.1 and B.2, respectively. The phase tensors at all periods show skew angles that are non-zero, indicating the region has a significantly 3-D resistivity structure (Fig. B.1).

At short periods (e.g., T = 1 s) sites in the north show highly variable orientation of the major axis of the phase tensor ellipses (i.e., the geoelectric strike). This is as expected because the lack of sedimentary cover in this region means that the MT instruments are deployed directly on highly heterogeneous crystalline basement rocks. In the south, the ellipses are more circular and indicate the presence of a relatively 1-D resistivity structure. This is due to the presence of the up to 1 km thick layer of sedimentary rocks in this region.

At longer periods (T > 100 s), the phase tensors begin to elongate and their orientations rotate around the region surrounding 54.75°N, 104°W, indicating that a resistivity feature in this area is heavily influencing the regional geoelectric strike. The induction vectors also show the effects of this conductor around 54.75°N, 104°W. Starting at short periods (T < 25 s) and continuing through longer periods (T > 100 s) the induction vectors all point the region around 54.75°N, 104°W, indicating a major conductor is present in the area. Interestingly, at the longest periods (e.g., T = 5460 s) the inductor vectors points towards the Manitoba border, perhaps indicating that a major conductor is present along the Superior margin outside of the survey area.

B.2 Comparison with LITHOPROBE MT data

Pseudosections comparing the apparent resistivity and phase data of the LITHOPROBE MT sites and the new long-period MT data are shown in Figures B.3 and B.4. The comparison to profile N in the south of the survey area shows generally similar trends between the two datasets. For example, the off-diagonal XY component shows initially low resistivity values at the shortest periods that increase at mid and long periods. The phase data is also very similar, with 3 phase

features. These are (1) high phases at short period indicating low resistivity (2) low phases at mid periods indicating a higher resistivity layer, and (3) high phases at the longest period indicating a low resistivity layer. The main differences observed between the LITHOPROBE and long-period data is because of the different period bands present in each dataset. The LITHOPROBE data is predominately broadband MT data with a period range 0.001-1000 s, and so it is more sensitive to shallower features. The new long-period data is in the period band 1-10000 s and sensitive to deeper features than the LITHOPROBE broadband MT data. This is best illustrated in the plots showing the off-diagonal (XY and YX) components of the impedance in Figure B.3.The shallow conductive layer is only observed at the shortest measured periods in the long-period data. However, it is observed in a broader period band for the broadband data.

The comparison of the new long-period data and the northern Profile L (Fig. 6.1) LITHOPROBE data is shown in Figure B.4. As with the comparison with Profile L, the pseudosections shows similar trends including conductive (high phase) and resistive (low phase) features at roughly the same locations (e.g., the conductor at -50 km in the XY and YX impedances). The similarity between the two datasets indicates that no systematic errors are present in either dataset.

B.3 Sensitivity tests

The results of the first sensitivity test are shown in Figure B.6. In this test, conductors were replaced by values of 500 Ωm and 100 Ωm in the crust and mantle, respectively. These values were chosen based on average model values in regions without conductive anomalies. After the conductors were replaced a forward calculation was run to determine how editing the model changed the RMS data misfit. The new data misfit values were subtracted from those produced by the unedited preferred model and are plotted in Figure B.6. The results show that almost all of the conductors were required by the measured MT data. The only exceptions were Figure B.6B and S6L, where the conductors removed were at significant depth and were outside of the data coverage area, which is where reduced data sensitivity is expected.

The second series of sensitivity tests involve replacing the resistivity values of the north Sask craton (NSC) conductor with a resistivity floor of 0.1, 1, 3, 5, 7, and 10 Ωm (Fig. B.7). Essentially,

if model cell values were less than the resistivity floor values they were replaced. A forward calculation was then performed in order to determine if the imposed resistivity floor significantly affected the RMS data misfit. Only when a value 5 Ωm was used for the resistivity floor, did the RMS misfit change in a noticeable way. This suggests that the NSC conductor could be equally well explained by resistivity values in the range of 1-5 Ωm, which are much more reasonable values. The very low resistivity values observed in Figure 6.3 could be an artifact of the inversion process.

The final series of sensitivity tests involved removing iteratively shallower layers of the NSC conductor and replacing low resistivity model cells with a resistivity value of 100 Ωm (Fig. B.8). This was done as it was suspected that data sensitivity was lost within the NSC conductor given that is a major conductor at great depths. As a result, the vertical extent of the NSC conductor observed in Figure 6.3 was suspected to be an artifact of the inversion process vertically smoothing the conductor due to a loss of data sensitivity. The results demonstrated that replacing portions of the conductor up to 100 km has little effect on data misfit. This suggests that the NSC conductor may be a thinner feature than observed in resistivity model slices.

B.4. Parameters for quantitative interpretation of mantle resistivity anomalies

The MATE program requires a number of parameters to be defined in order to operate. Most are of second-order importance compared to inputs such as the geotherm, composition, and cementation exponents of various phases. The choice for each of these parameters is detailed below.

B.4.1 Water partitioning between minerals

Water partitioning calculations between orthopyroxene and olivine, clinopyroxene and olivine, and olivine and garnet used the models of Demouchy et al. (2017) and Mookherjee and Karato (2010). These were chosen as these experiments were made using samples of similar mineralogy and at pressure and temperature conditions close to what is expected beneath the Trans Hudson Orogen (THO). Water solubility calculations used the model of Padrón-Navarta and Hermann

(2017) as this was performed on subsolidus peridotite. Water content calibrations for olivine conductivity and solubility used the results of Withers et al. (2012) and those for pyroxene-garnet conductivity used the results of Bell et al. (1995), since they are discussed to be the most reliable calibrations by Demouchy and Bolfan-Casanova (2016).

B.4.2 Mineral conductivity

The mineral conductivity model of Gardes et al. (2014) was used to calculate the olivine conductivity. A variety of olivine mineral conductivity experiments have been published in the past at a range of temperature and pressuring conditions and often produced differing results. The model of Gardes et al. (2014) accounted for these variations as well as errors in previous experiments in order to propose a unified model for olivine conductivity. The model of Liu et al. (2019) was used for garnet and clinopyroxene, as it was performed on eclogitic samples, matching the mantle mineralogy observed from xenoliths in the study area in the Trans-Hudson Orogen (Czas et al., 2018; 2020). The model of Dai and Karato (2009) was used for orthopyroxene, following the work of Özaydın and Selway (2022). Amphibole used the results of Hu et al. (2018), as these experiments were performed at similar pressure and temperature conditions. Finally, the model of Li et al. (2017) was used for phlogopite as it incorporates the resistivity-enhancing effects of fluorine, which is thought to be the primary charge carrier in phlogopite.

B.4.3 Additional parameters

The effects of aluminum content on the water partitioning between orthopyroxene and olivine used the results of Novella et al. (2014) as it was developed from data spanning typical mantle lithosphere pressure conditions. Phase-mixing was modelled using the generalized multi-phase Archie's Law of Glover (2010).

B.5 Viability of garnet pyroxenites as a conductive phase

Garnet has been proposed to explain resistivity anomalies in the lithospheric mantle of the Kaapvaal craton (e.g., Evans et al., 2011). Recent experiments have suggested that garnet

pyroxenites networks can produce resistivity values as low as 1–5 Ωm towards the base of the lithosphere (Ferrand and Chin, 2023). At the depth of the NSC conductor and shallower, these networks will produce resistivity values in the range 50-500 Ωm (Ferrand and Chin, 2023), far more resistive than observed. While the eclogite beneath the Sask craton could provide the additional garnet needed for such networks, these types of networks appear to be specific to the particular pyroxene-dominated mineralogy of pyroxenites, which are associated with off-craton or intraplate settings (Gonzaga et al., 2010) and are not observed in the regional xenolith record of the Sask craton (Czas et al., 2018; Smyth, 2020). It is unclear is such networks could be produced in eclogites. As a result, garnet pyroxenites are not a good candidate to explain the low resistivity of the NSC.

B.6 An alternative melting model explanation for the NSC and C1-C4 conductors

The geometry and structure of the NSC and C1-C4 conductors appears similar to conductors imaged by seismic data collected at volcanic and rifting centers (e.g., Hill et al., 2009; Mulibo and Nyblade, 2013). An alternative explanation for the conductivity structure of the Sask craton is that the NSC and C1-C4 conductors reflect partial melt that is ascending through the lithosphere. A possible analog would be what is observed beneath the Tanzanian craton and adjacent East African rift segments, which has a similar geophysical structure in seismic data (e.g., Mulibo and Nyblade, 2013). There are a number of significant challenges for this model. First, if C1-C4 conductors are interpreted as partial melt, it seems likely that either surface volcanism or extension should be present, as is observed in the East African Rift around the Tanzanian craton (Mulibo and Nyblade, 2013). Similarly, other rifts, such as the incipient Okavango, well-developed Ethiopian, and failed Midcontinent rifts all showed some combination of extension or magmatism well before thermal or melt anomalies reach depths of the NSC or C1-4 conductors (Shirey et al., 1994; Ebinger, 2005; Corti, 2009; Leseane et al., 2015). No corresponding elevated geothermal conditions, extension, or surface magmatism is observed on the Sask craton. Second, it also seems unlikely that any partial melts beneath the Sask craton are relict features from the 112-94 Ma kimberlite magmatism, since kimberlites are small volume melts and it would be difficult for them to produce such thermal anomalies sufficiently large to persist for 90 My. Additionally, kimberlites are formed via decompression induces redox melting and do not require deviations from ambient lithospheric

mantle temperatures (Tappe et al., 2018). Finally, thermal anomalies would produce thermal conditions antithetical to the cold geotherms needed for diamond stability. While a melt model cannot be explicitly ruled out by the MT data, the lack of corresponding surface thermal anomalies, magmatism, or deformation make it highly unlikely.

Inversion Name	**Main Property Changed From Prior Inversions**	**Starting λ**	**Ending λ**	**Starting RMS misfit**	**Final RMS misfit**	**Iterations**
FALC_INV46	Data editing to remove outliers.	1.0	1.49E-08	10.441	1.425	164
FALC_INV47	Added topography data	1.0	1.49E-08	10.209	1.3	172
SASLITHO_INV13	Added LITHOPROBE data to model (109 total stations vs 56 originally)	1.0	1.00E+00	9.974	1.547	118
SASLITHO_INV15	Included tipper data.	1.0	1.49E-08	11.439	7.238	115
SASLITHO_INV18	Removal of 3 sites with consistently high RMS in prior inversions	1.0	1.49E-08	9.832	1.365	161
SASLITHO_INV19	Cut all data at 1 Hz to speed up inversion process and focus on deep structure.	1.0	1.49E-08	9.842	1.224	174
SASLITHO_INV23 (preferred inversion)	Removal of topography to speed up the inversion process by removing excess model cells.	1.0	1.49E-08	9.802	1.221	204

SASLITHO_INV30	10 Ωm starting model.	1.0	1.49E-08	5.853	1.299	165
SASLITHO_INV31	1000 Ωm starting model.	1.0	1.49E-08	32.688	1.810	192
SASLITHO_INV32	30 Ωm starting model.	1.0	1.49E-08	6.532	1.315	128
SASLITHO_INV33	300 Ωm starting model.	1.0	1.49E-08	17.157	1.444	195

Table B.1: *A summary of some of the inversions performed, demonstrating a variety of properties changed during the course of data modeling and the resulting RMS data misfit changes.*

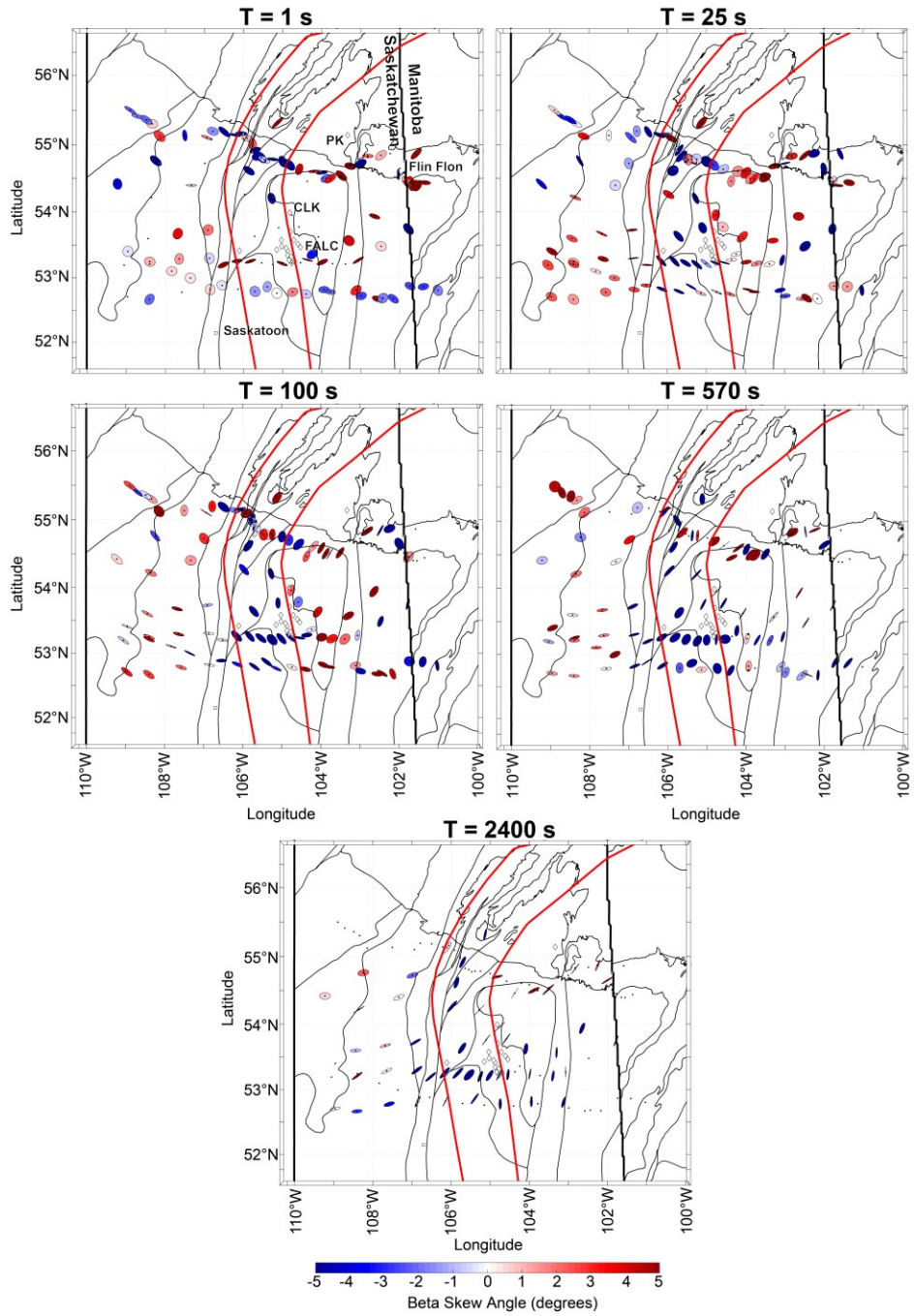

Figure B.1: *Phase tensors at 1, 25, 100, 570 and 2400 seconds for each site. The direction of the major (long) axis of the ellipse is either parallel or perpendicular to the regional geoelectric strike. The color of the circle or ellipse corresponds to the skew angle and indicates the dimensionality, with a non-zero skew indicating 3-D resistivity structure (Booker, 2014). The phase tensors show local geoelectric strikes (e.g., 54.75°N, 104°W at 100 s), but overall the structure in the region is highly 3-D as evidenced by the highly variable skew angle. The outline of the NACP conductor is shown in red, from Jones et al. (2005). Thin black lines are the tectonic terranes from Fig. 6.1. The thick black line is the border between Saskatchewan and Manitoba.*

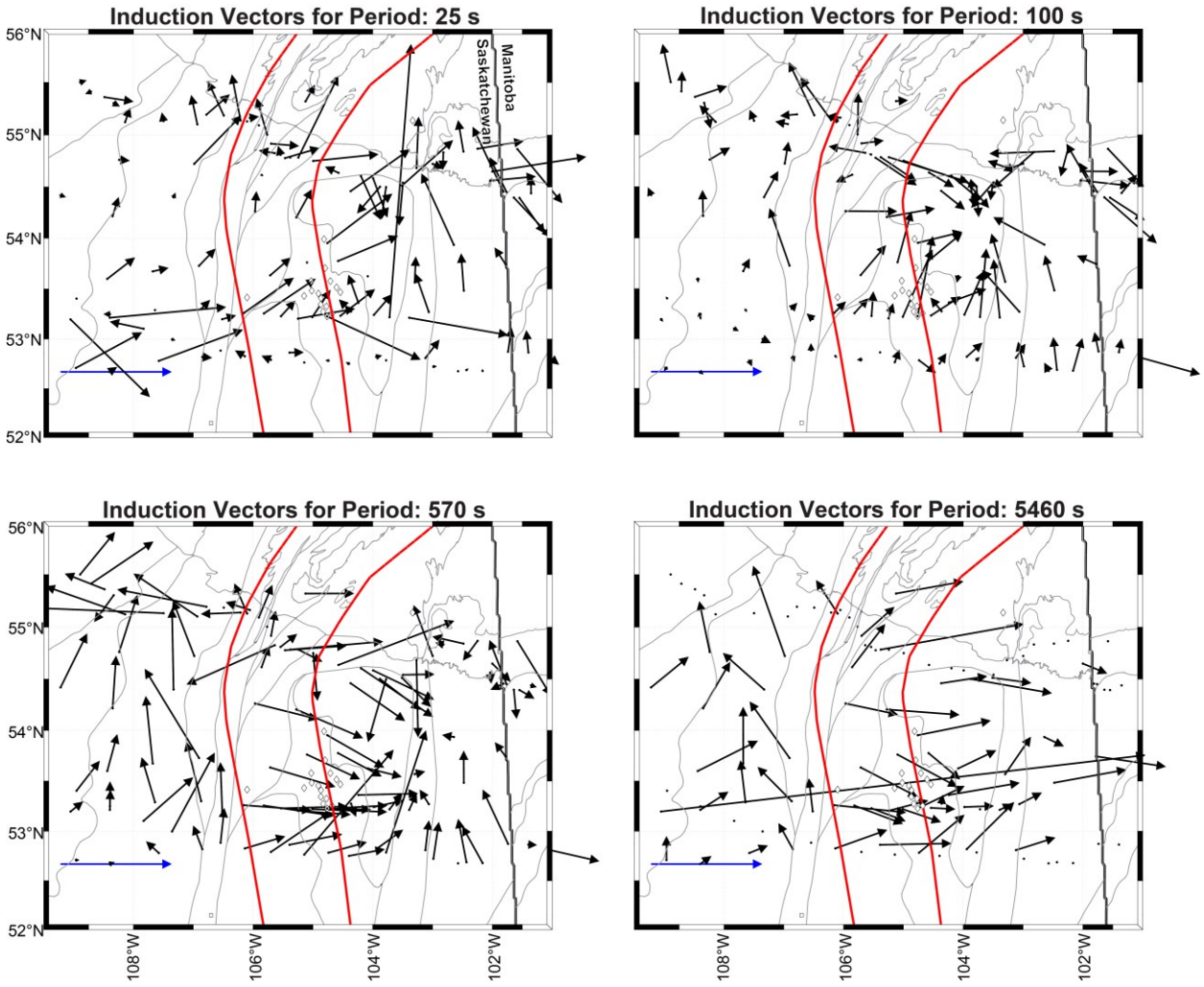

Figure B.2: *Map of induction vectors at 25, 100, 570 and 5460 seconds for each site. The induction vectors are plotted using the Parkinson convention with arrowing pointing towards conductors. The induction vectors at 25, 100, and 570 seconds predominately point toward the region around 54°N, 103°W, indicating that a major conductor is present in that area. The outline of the NACP conductor is shown in red, from Jones et al. (2005). Thin grey lines are the tectonic terranes from Fig. 6.1. The thick black line is the border between Saskatchewan and Manitoba. The blue vector is the unit vector.*

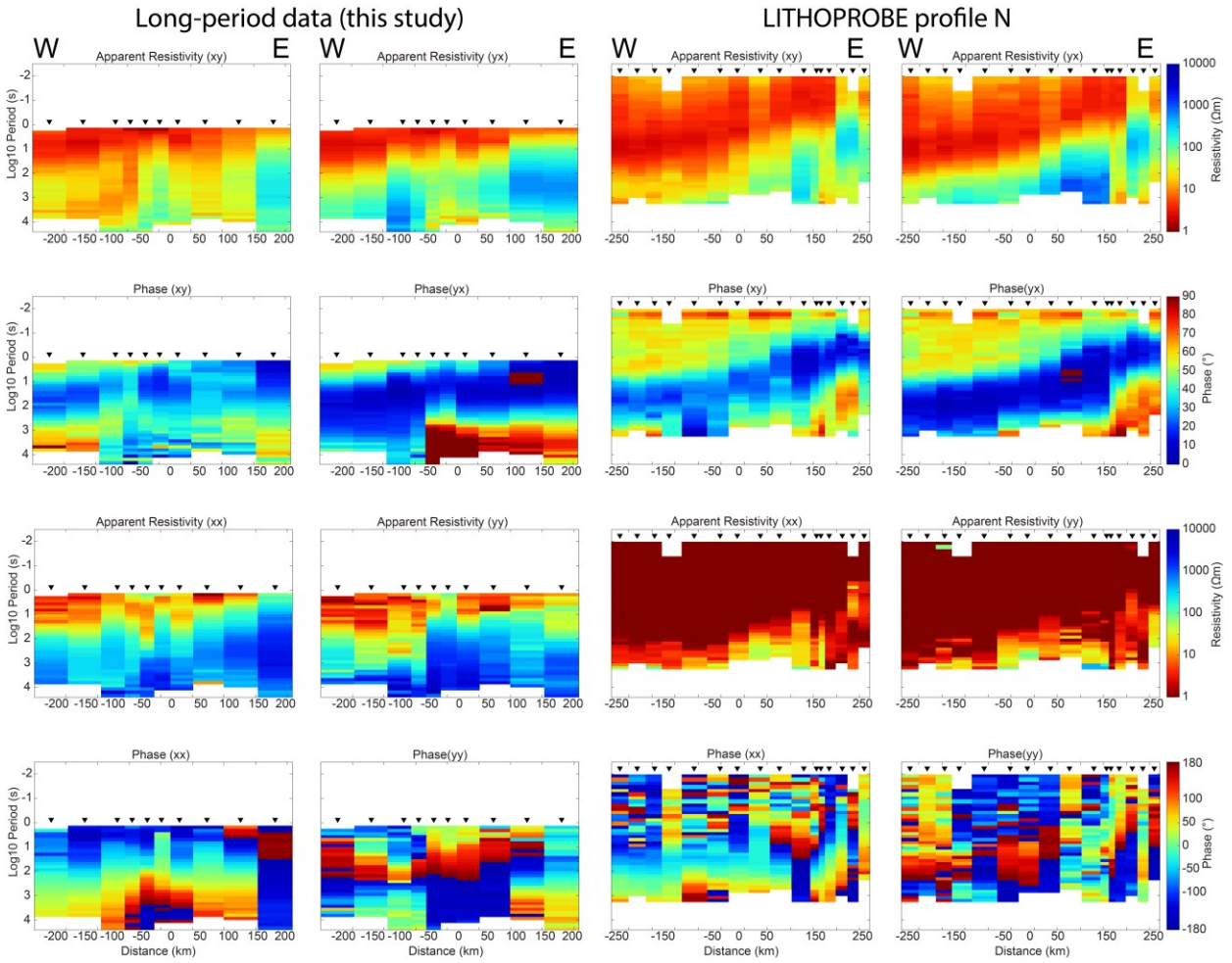

Figure B.3: *Pseudosections comparing the apparent resistivity and phase for the four impedances components. The left columns show data collected during this study. The right column shows coincident data from the LITHOPROBE profile N (see Fig. 6.1 for profile location). Note that the period ranges for long-period data and broadband data are different. The pseudosections are very similar where periods are present in each dataset X = geographic north; Y = geographic east.*

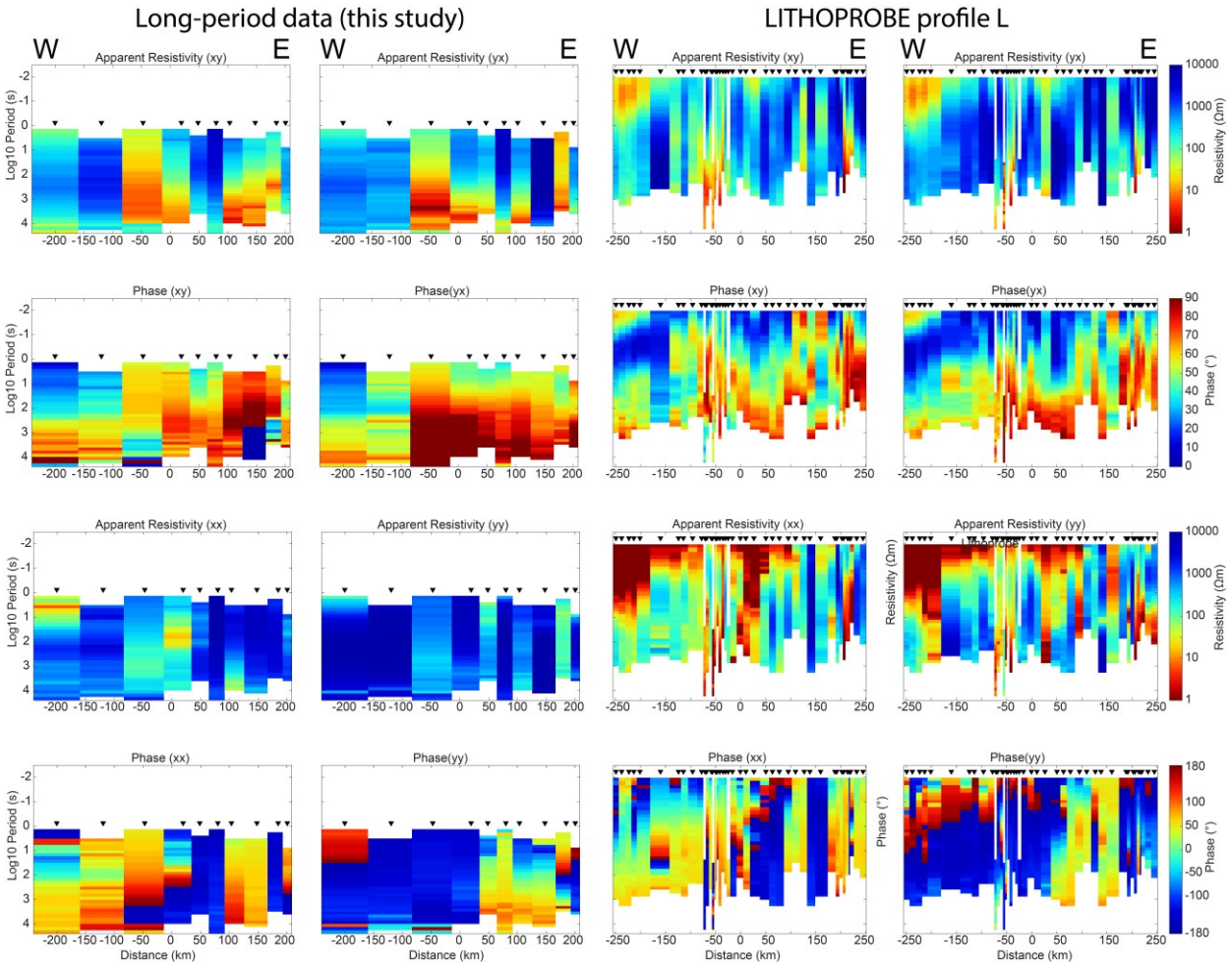

Figure B.4: *Pseudosections comparing the apparent resistivity and phase for the four impedances components. The left columns show data collected during this study. The right column shows coincident data from the LITHOPROBE profile L (see Fig. 6.1 for profile location). Note that the period ranges for long-period data and broadband data are different. The pseudosections are very similar where periods are present in each dataset X = geographic north; Y = geographic east.*

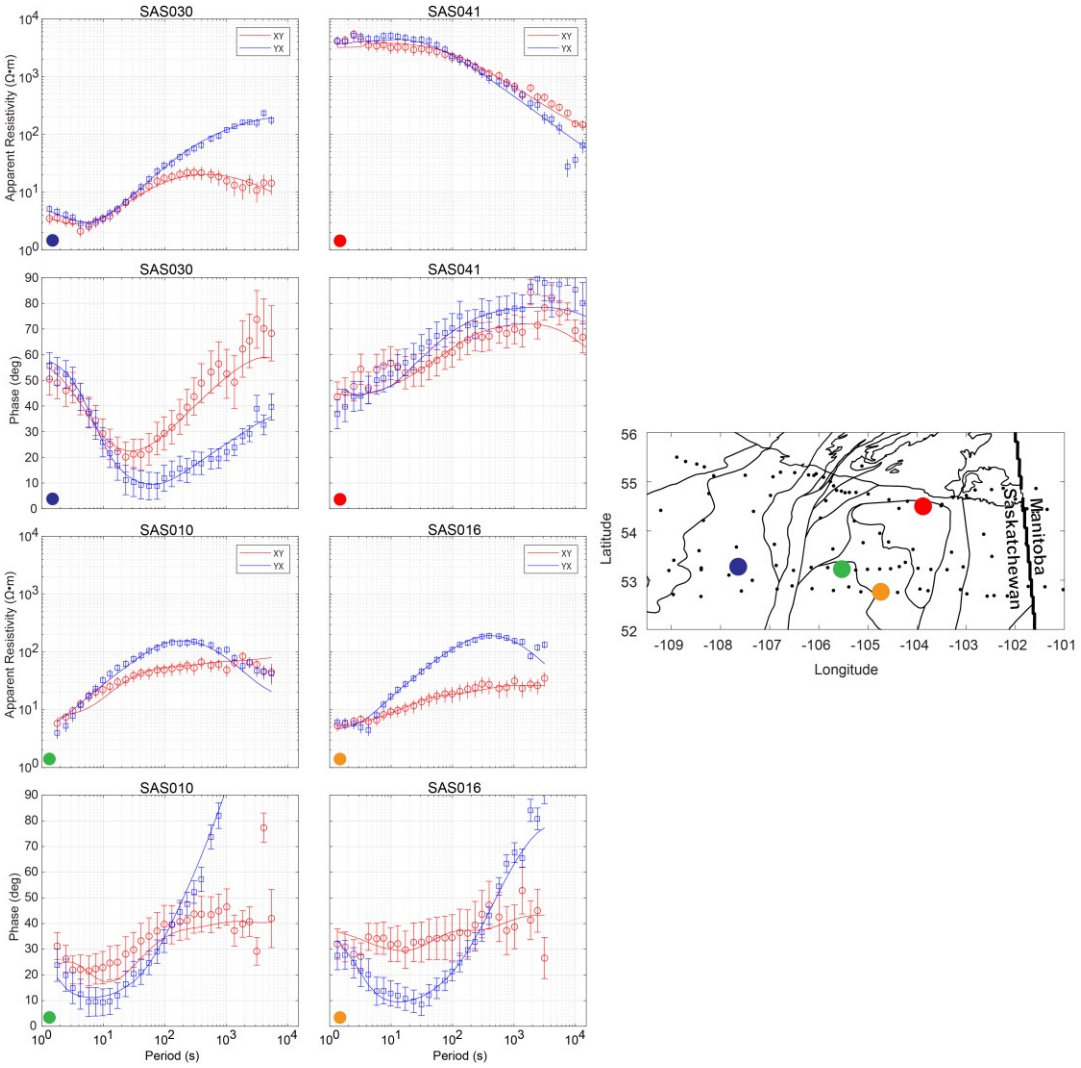

Figure B.5: *Example apparent resistivity and phase curves for four long period MT sites. The map on the right shows the location of each station as a color-coded dot. The thick black line is the border between Saskatchewan and Manitoba.*

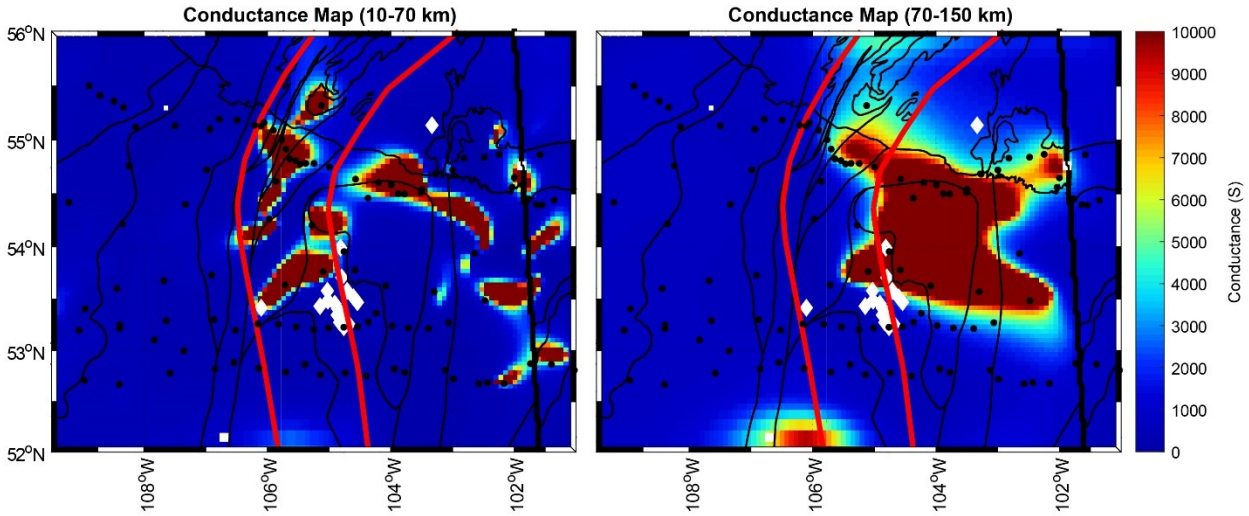

Figure B.6: *Conductance plots for 10-70 km and 70-150 km showing the conductance values for the C1-C4 and NSC resistivity anomalies, respectively. The red outline is the trace of the NACP conductor from Jones et al. (2005).*

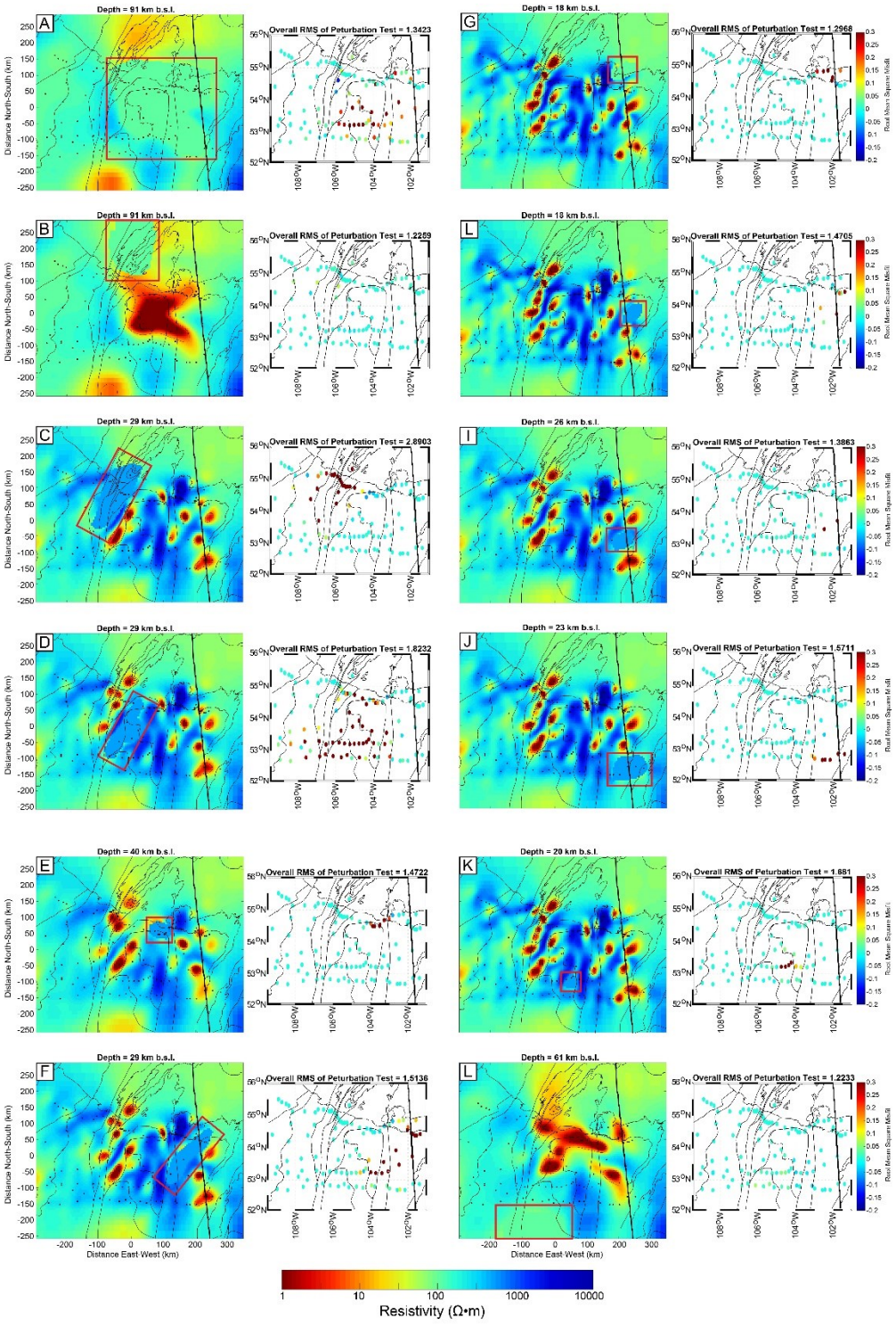

Figure B.7: *Sensitivity tests for various the conductors observed in the resistivity model. The resistivity model panel on the left shows the representative area for each conductor removed. Red boxes show the specific region where the conductor was removed. The panel on the right shows the resulting RMS misfit change at each station as a result of removing the conductor.*

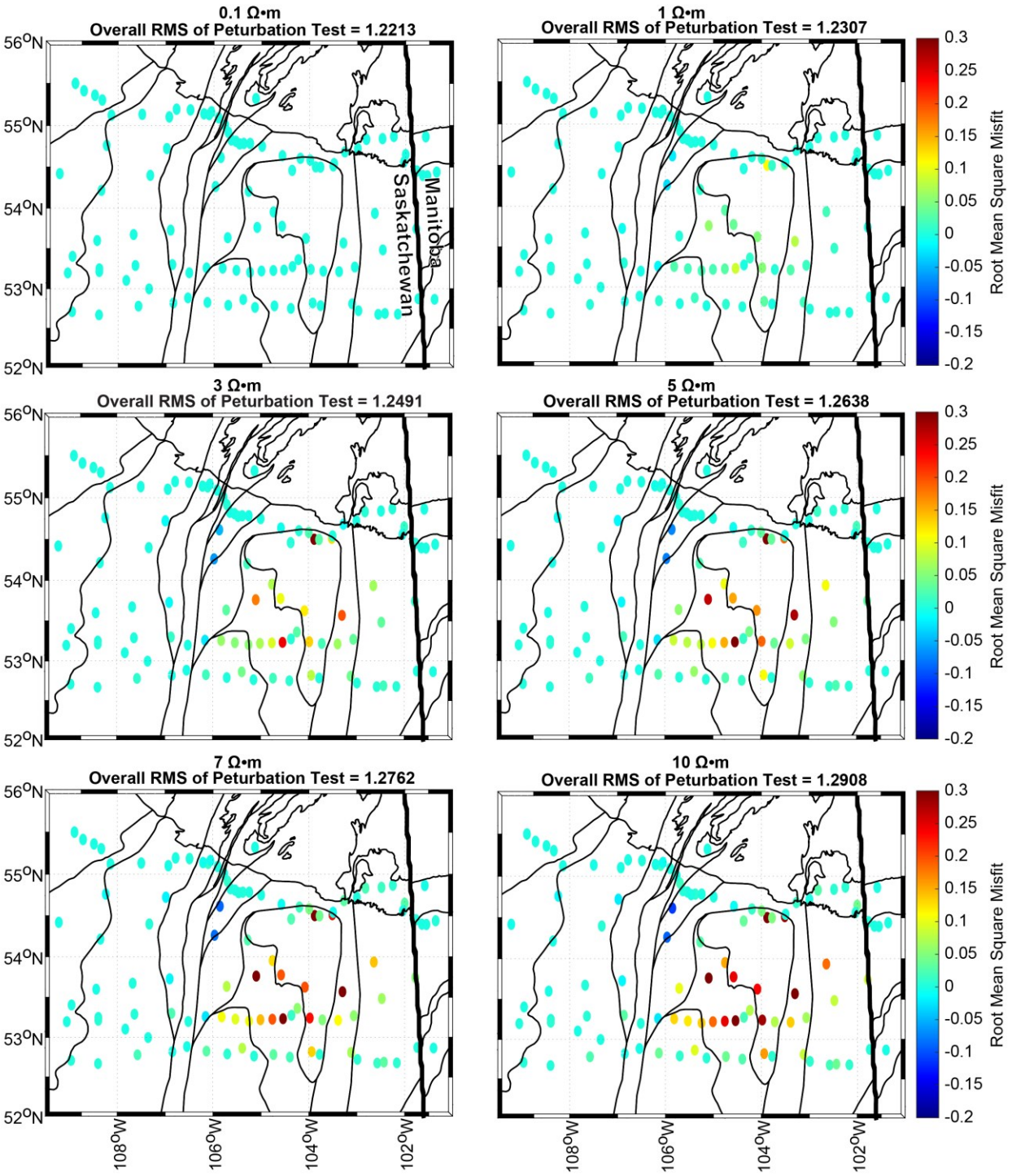

Figure B.8: *The resulting change in RMS misfit if resistivity values of the NSC conductor lower than 0.1, 1, 3, 5, 7, and 10 were replaced by these values. The thick black line is the border between Saskatchewan and Manitoba.*

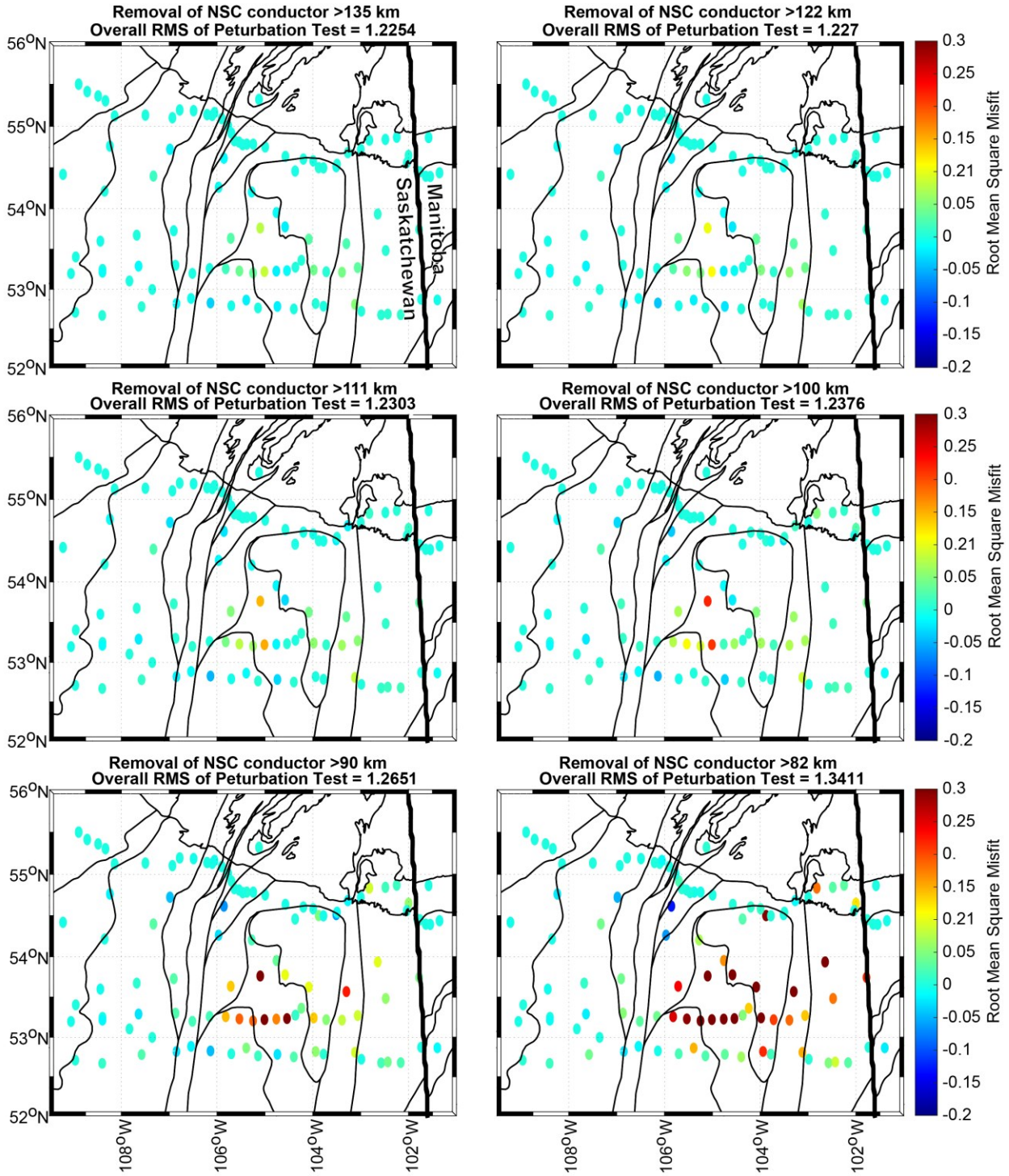

Figure B.9: *RMS data misfit change as a result of removing sequentially shallower layers of the NSC conductor. For example, the first panel is the removal of the conductor at depth of 135 km or more, and the fourth panel is the removal of conductor at depths of 100 km or more. The thick black line is the border between Saskatchewan and Manitoba.*

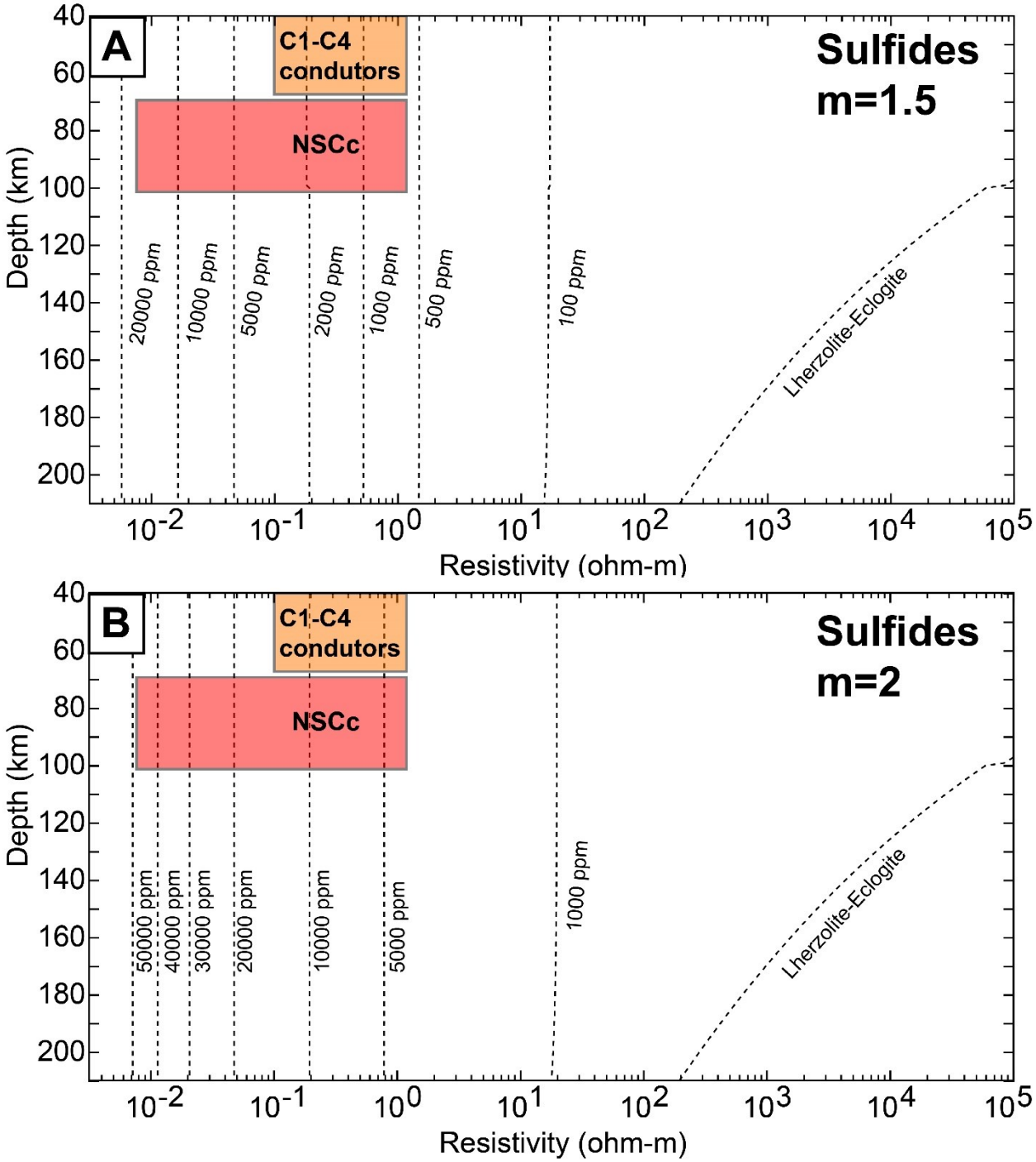

Figure B.10: *MATE modelling results for sulfides using (C) a cementation exponent of 1.5 and (D) a cementation exponent of 2.*

APPENDIX C: SUPPLEMENTAL MATERIALS FOR CHAPTER 7

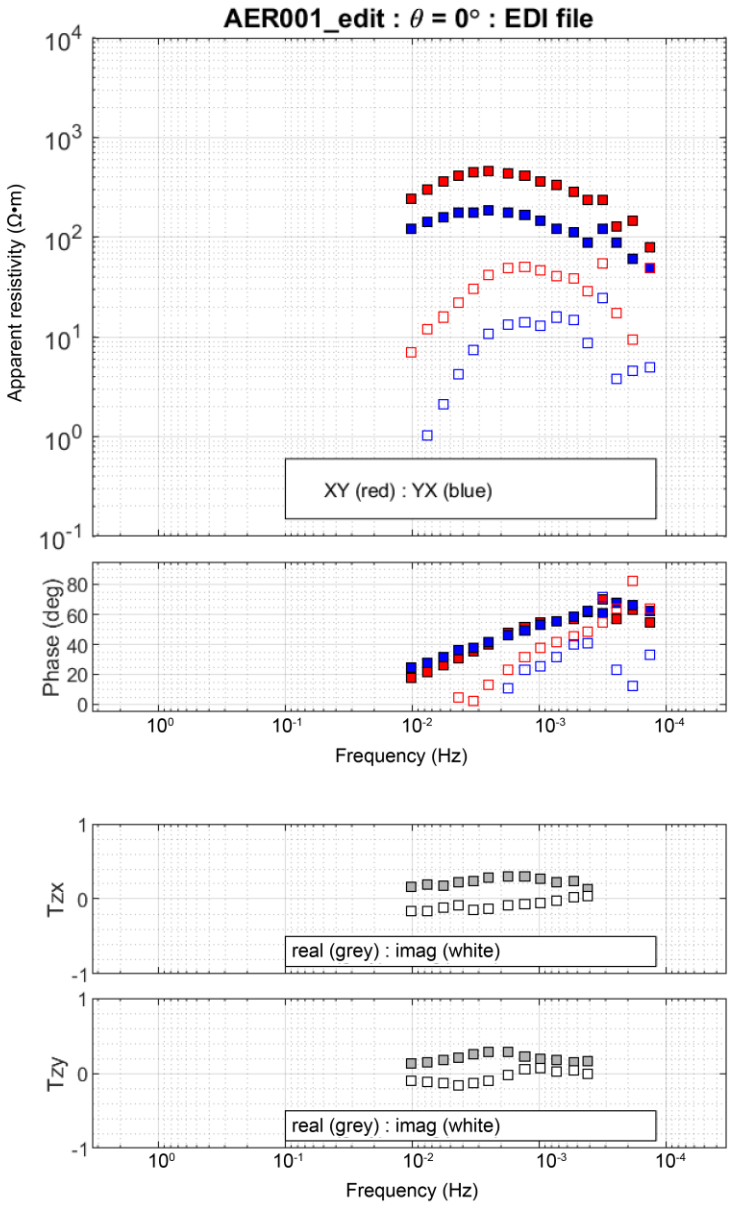

Figure C.1*: Data from station AER 001 (lat. 55.83°N, long. 114.16°W). In the top two panels, the solid red boxes are the XY component of the impedance tensor, solid blue boxes are the YX component, open red boxes are the XX component, and open blue boxes are the YY component. In the bottom two panels, the grey and white boxes are the real (in-phase) and the imaginary (imag; out-of-phase) components of the tipper (T), respectively. Abbreviations: Ω, ohms; deg, degrees.*

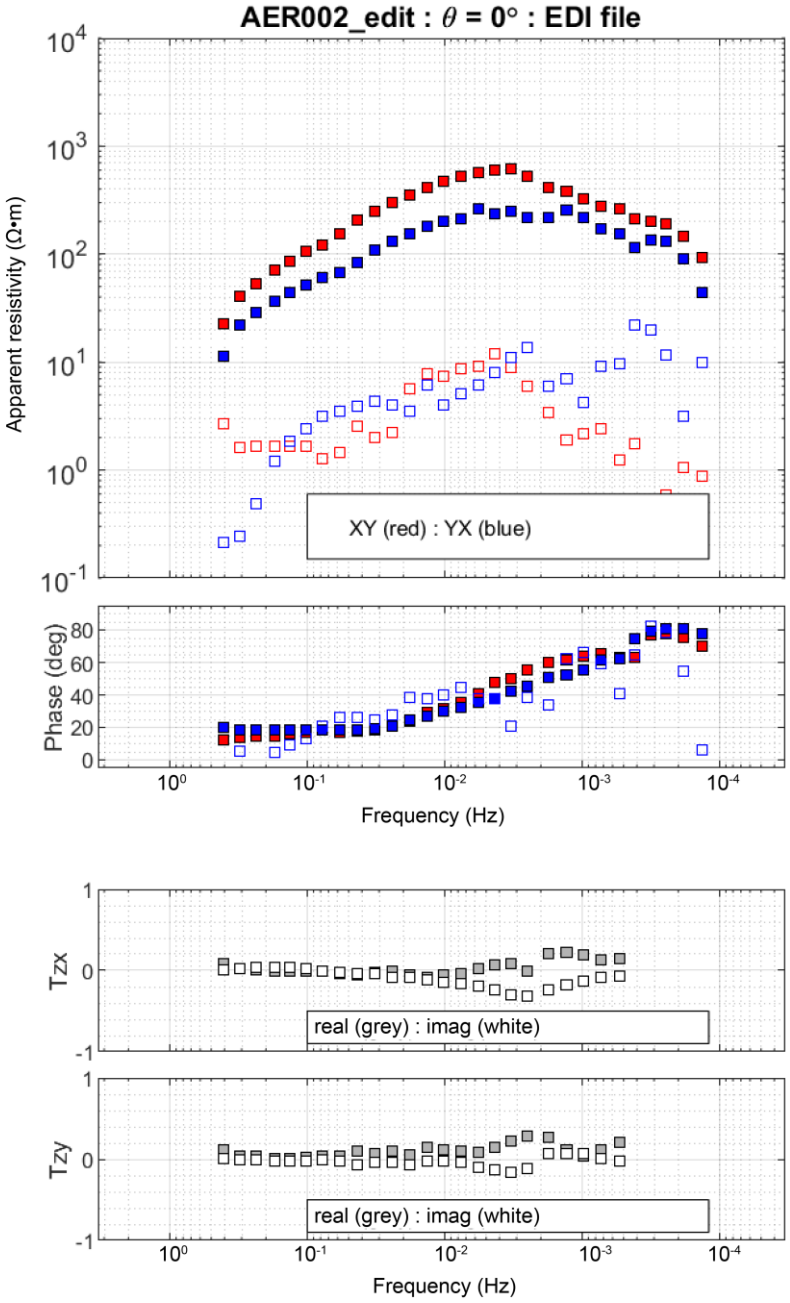

Figure C.2: *Data from station AER 002 (lat. 56.96°N, long. 113.60°W). In the top two panels, the solid red boxes are the XY component of the impedance tensor, solid blue boxes are the YX component, open red boxes are the XX component, and open blue boxes are the YY component. In the bottom two panels, the grey and white boxes are the real (in-phase) and the imaginary (imag; out-of-phase) components of the tipper (T), respectively. Abbreviations: Ω, ohms; deg, degrees.*

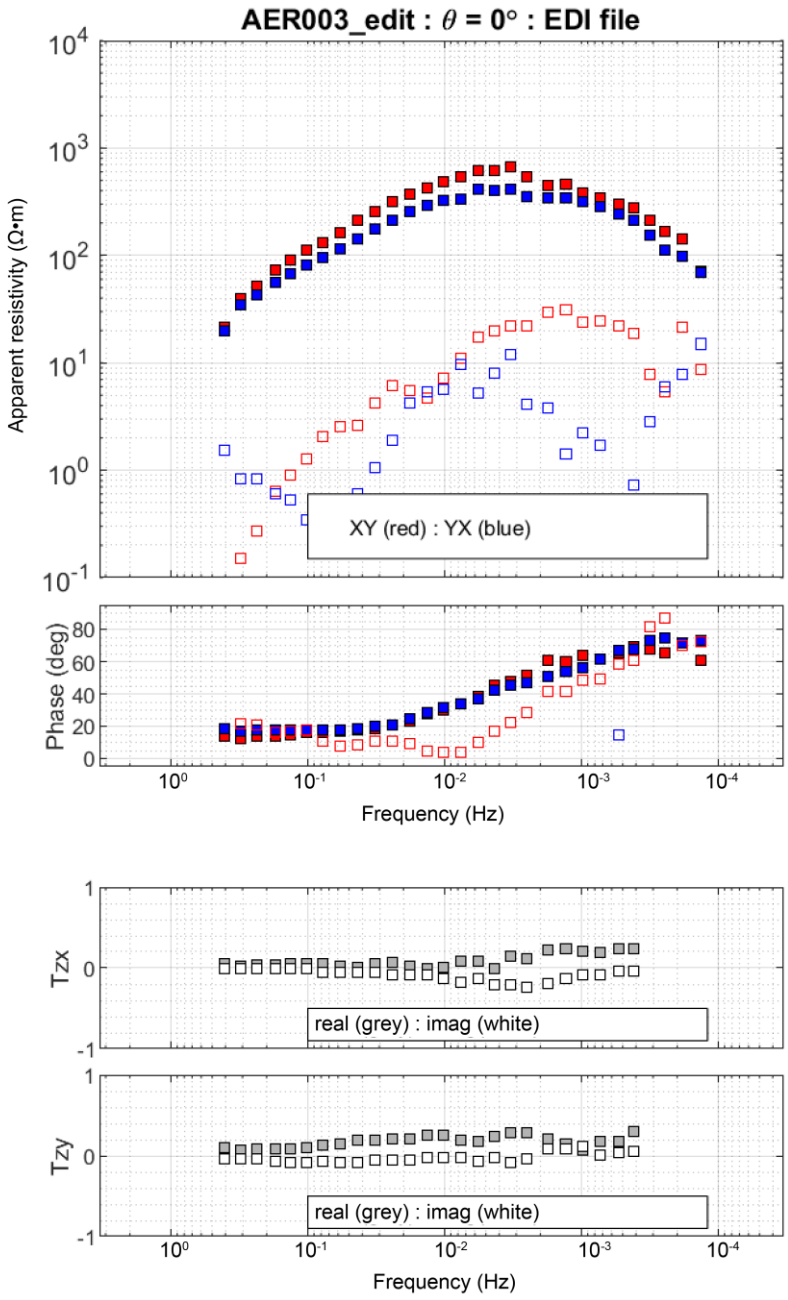

Figure C.3: *Data from station AER 003 (lat. 56.63°N, long. 113.53°W). In the top two panels, the solid red boxes are the XY component of the impedance tensor, solid blue boxes are the YX component, open red boxes are the XX component, and open blue boxes are the YY component. In the bottom two panels, the grey and white boxes are the real (in-phase) and the imaginary (imag; out-of-phase) components of the tipper (T), respectively. Abbreviations: Ω, ohms; deg, degrees.*

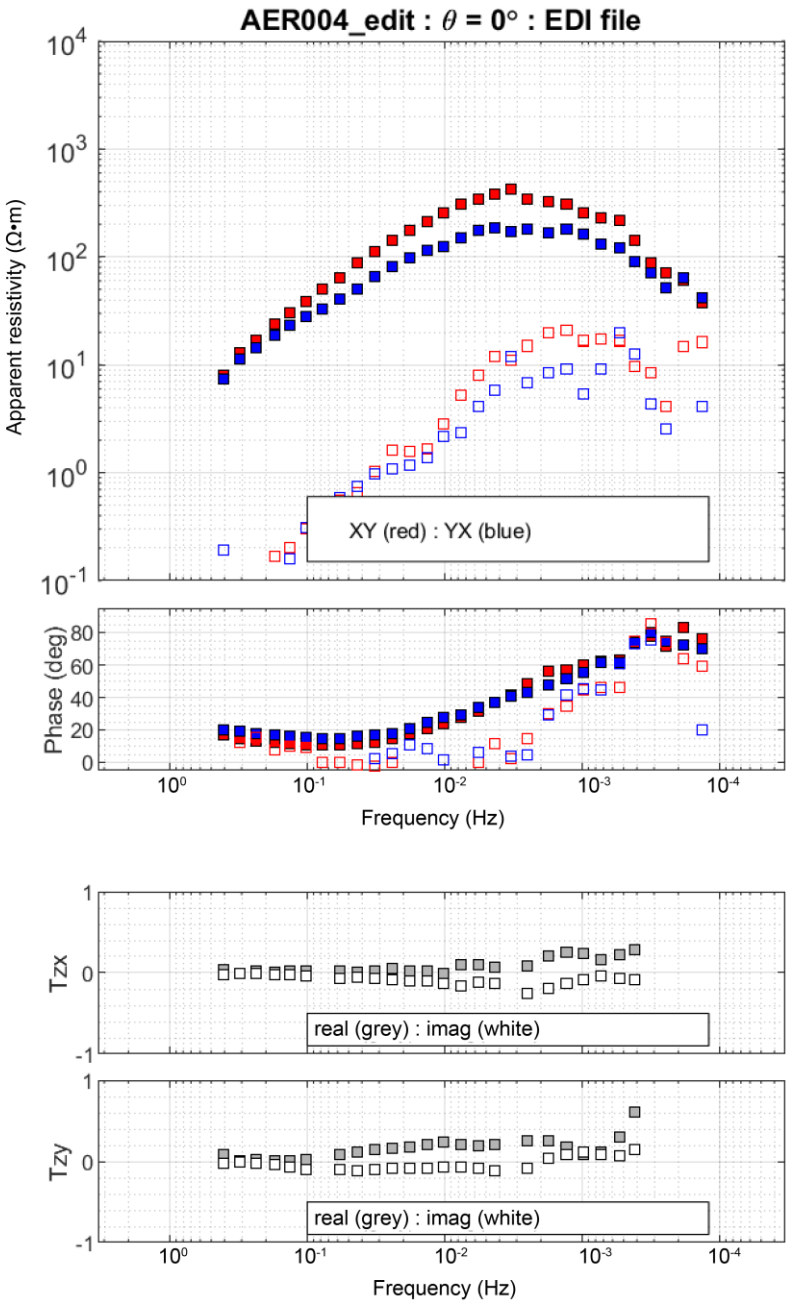

Figure C.4: *Data from station AER 004 (lat. 56.65°N, long. 114.03°W). In the top two panels, the solid red boxes are the XY component of the impedance tensor, solid blue boxes are the YX component, open red boxes are the XX component, and open blue boxes are the YY component. In the bottom two panels, the grey and white boxes are the real (in-phase) and the imaginary (imag; out-of-phase) components of the tipper (T), respectively. Abbreviations: Ω, ohms; deg, degrees.*

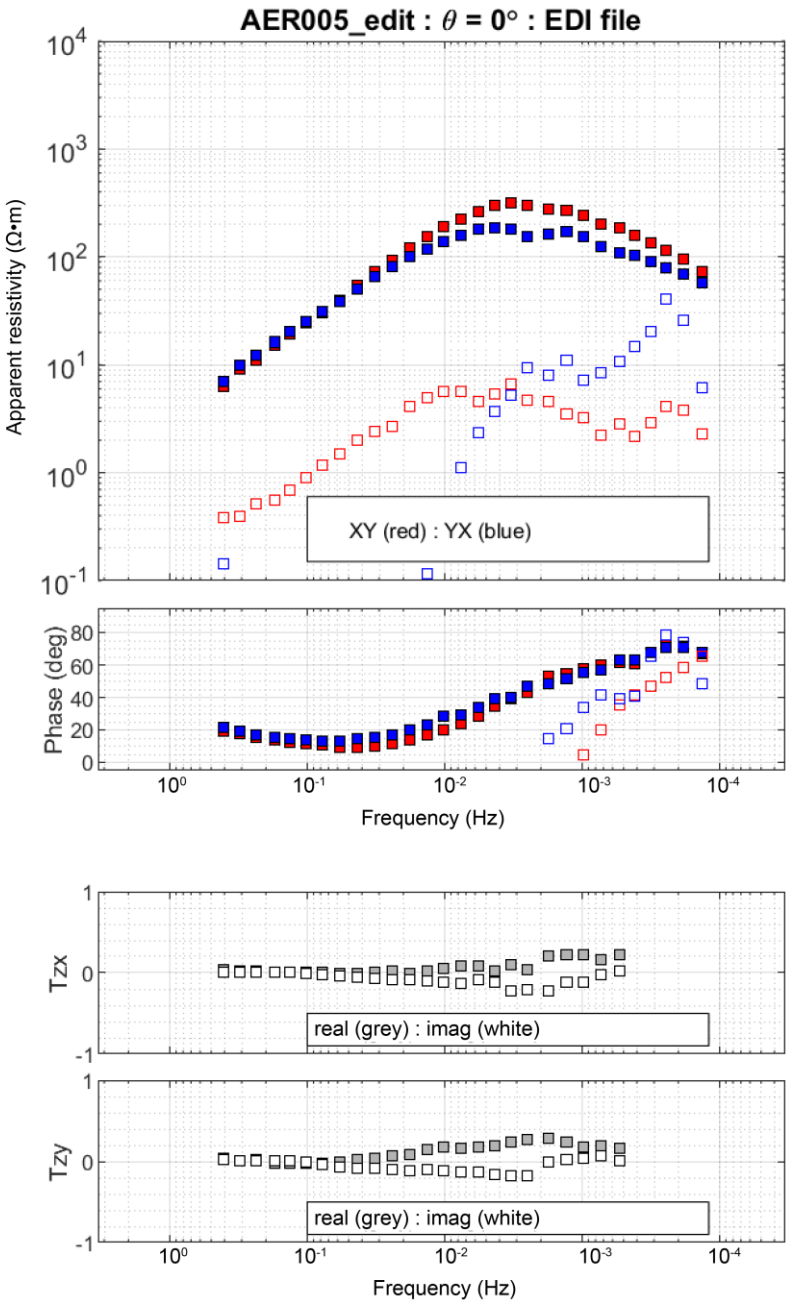

Figure C.5: *Data from station AER 005 (lat. 56.36°N, long. 114.46°W). In the top two panels, the solid red boxes are the XY component of the impedance tensor, solid blue boxes are the YX component, open red boxes are the XX component, and open blue boxes are the YY component. In the bottom two panels, the grey and white boxes are the real (in-phase) and the imaginary (imag; out-of-phase) components of the tipper (T), respectively. Abbreviations: Ω, ohms; deg, degrees.*

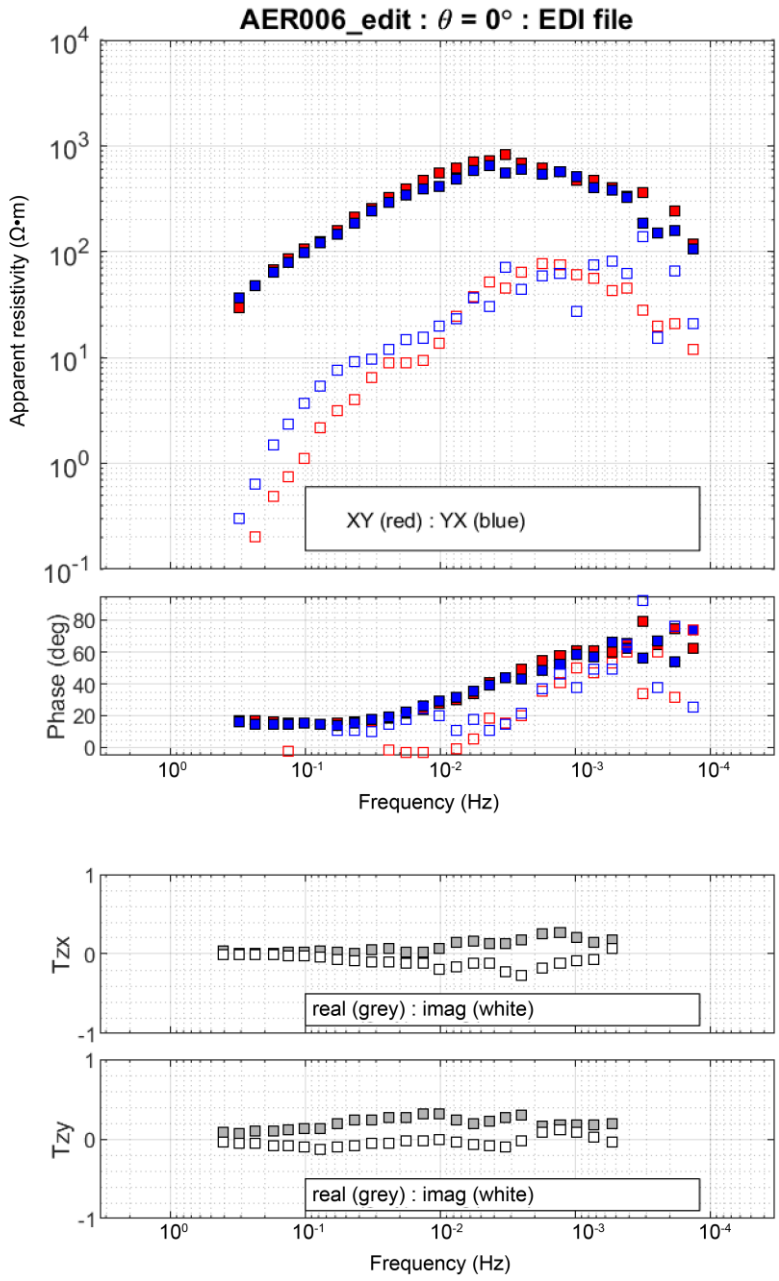

Figure C.6: *Data from station AER 006 (lat. 56.37°N, long. 113.66°W). In the top two panels, the solid red boxes are the XY component of the impedance tensor, solid blue boxes are the YX component, open red boxes are the XX component, and open blue boxes are the YY component. In the bottom two panels, the grey and white boxes are the real (in-phase) and the imaginary (imag; out-of-phase) components of the tipper (T), respectively. Abbreviations: Ω, ohms; deg, degrees.*

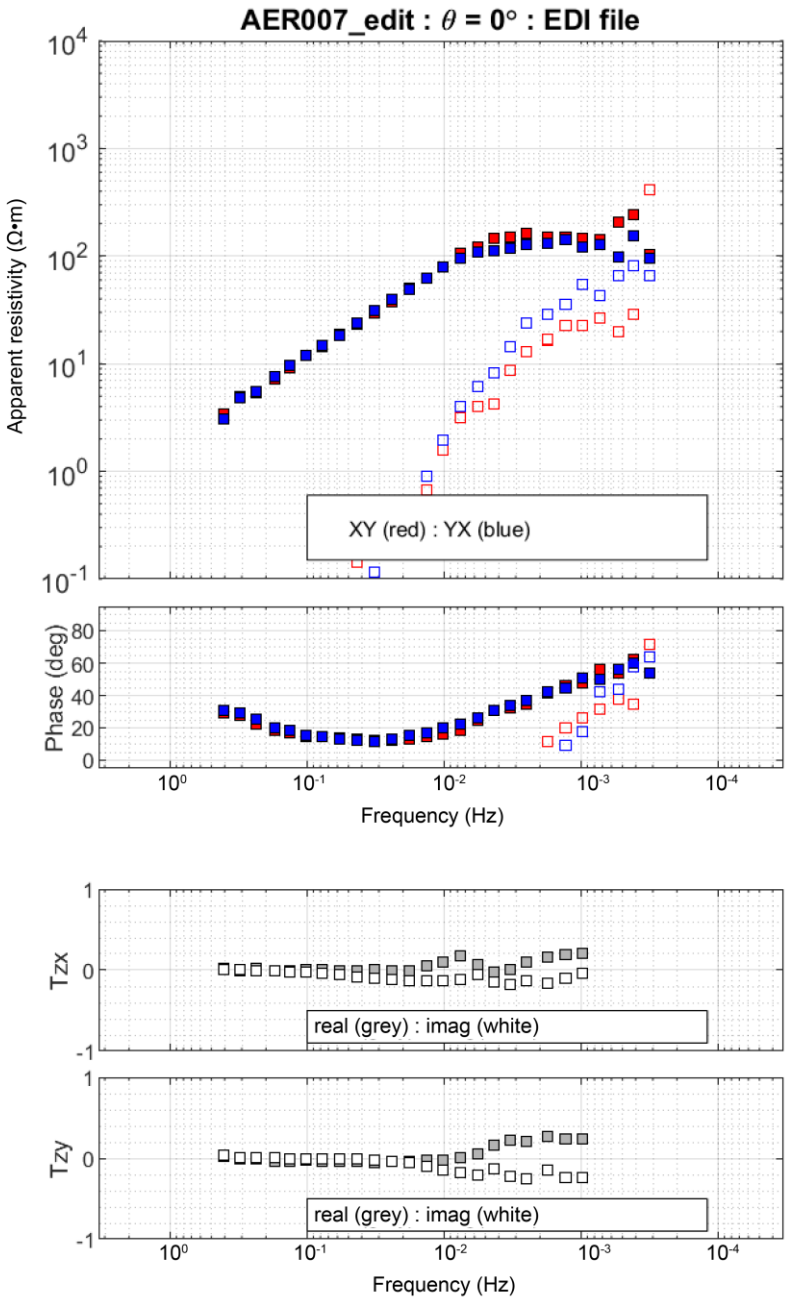

Figure C.7: *Data from station AER 007 (lat. 55.78°N, long. 115.95°W). In the top two panels, the solid red boxes are the XY component of the impedance tensor, solid blue boxes are the YX component, open red boxes are the XX component, and open blue boxes are the YY component. In the bottom two panels, the grey and white boxes are the real (in-phase) and the imaginary (imag; out-of-phase) components of the tipper (T), respectively. Abbreviations: Ω, ohms; deg, degrees.*

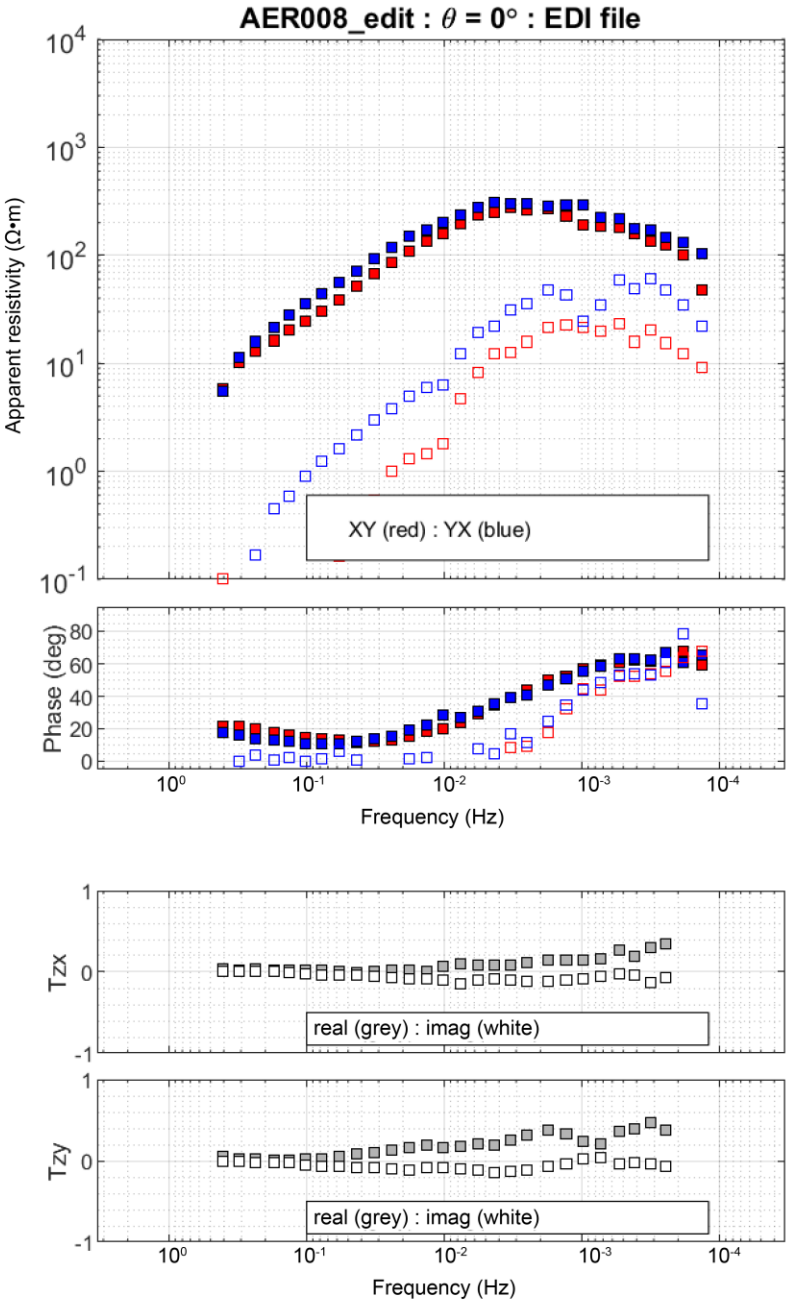

Figure C.8*: Data from station AER 008 (lat. 56.76°N, long. 114.63°W). In the top two panels, the solid red boxes are the XY component of the impedance tensor, solid blue boxes are the YX component, open red boxes are the XX component, and open blue boxes are the YY component. In the bottom two panels, the grey and white boxes are the real (in-phase) and the imaginary (imag; out-of-phase) components of the tipper (T), respectively. Abbreviations: Ω, ohms; deg, degrees.*

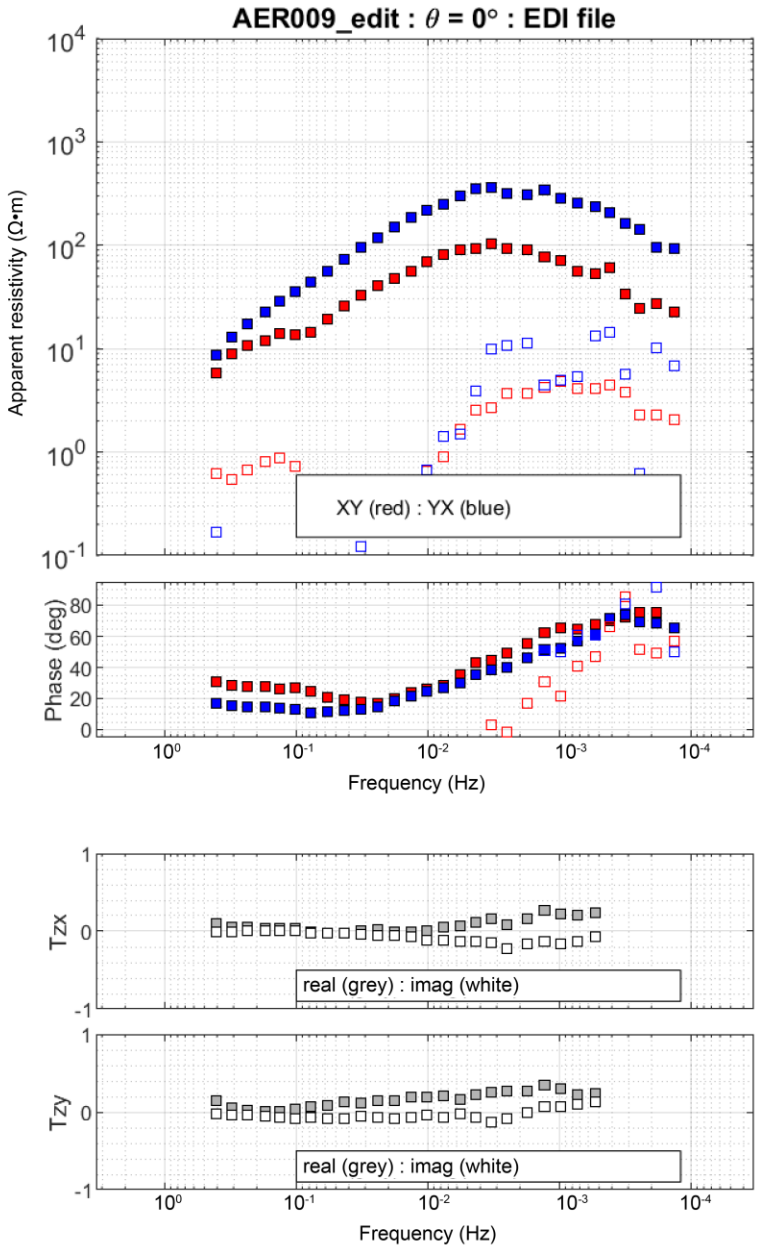

Figure C.9: *Data from station AER 009 (lat. 57.19°N, long. 114.46°W). In the top two panels, the solid red boxes are the XY component of the impedance tensor, solid blue boxes are the YX component, open red boxes are the XX component, and open blue boxes are the YY component. In the bottom two panels, the grey and white boxes are the real (in-phase) and the imaginary (imag; out-of-phase) components of the tipper (T), respectively. Abbreviations: Ω, ohms; deg, degrees.*

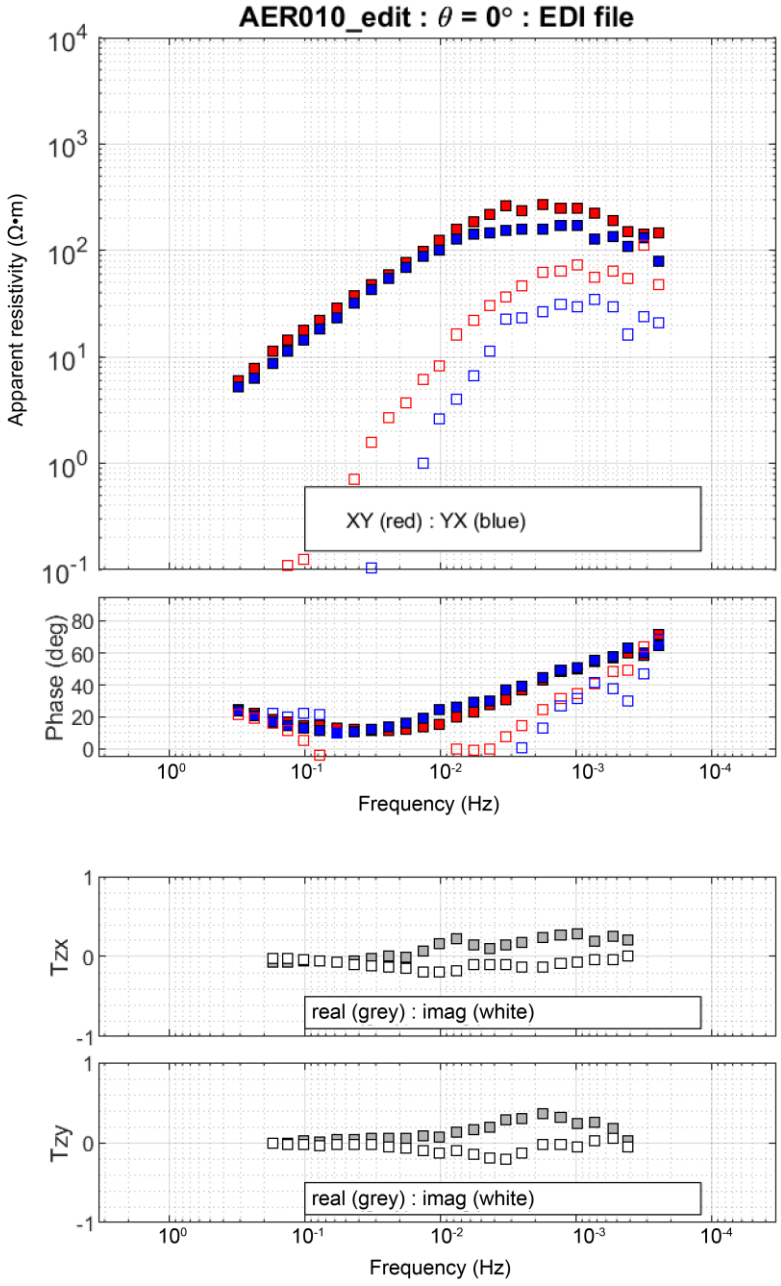

Figure C.10: *Data from station AER 010 (lat. 56.15°N, long. 115.93°W). In the top two panels, the solid red boxes are the XY component of the impedance tensor, solid blue boxes are the YX component, open red boxes are the XX component, and open blue boxes are the YY component. In the bottom two panels, the grey and white boxes are the real (in-phase) and the imaginary (imag; out-of-phase) components of the tipper (T), respectively. Abbreviations: Ω, ohms; deg, degrees.*

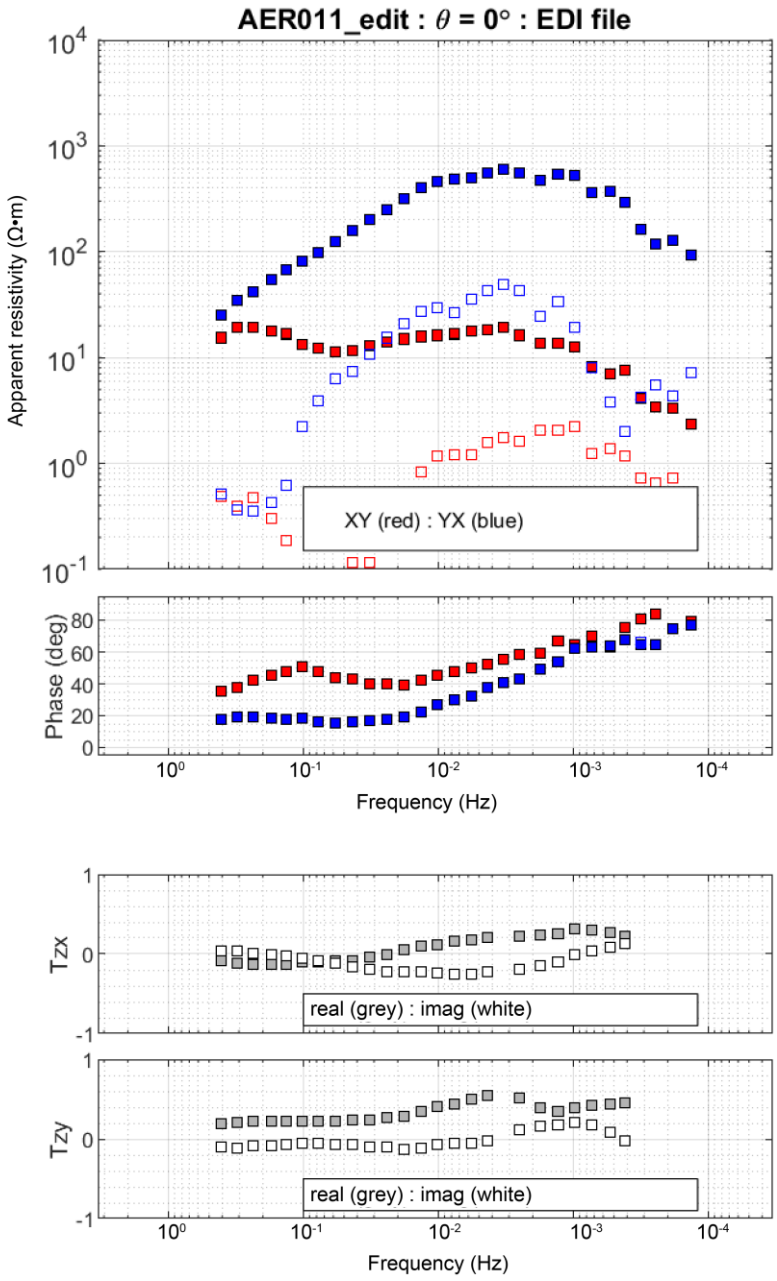

Figure C.11: *Data from station AER 011 (lat. 57.57°N, long. 111.93°W). In the top two panels, the solid red boxes are the XY component of the impedance tensor, solid blue boxes are the YX component, open red boxes are the XX component, and open blue boxes are the YY component. In the bottom two panels, the grey and white boxes are the real (in-phase) and the imaginary (imag; out-of-phase) components of the tipper (T), respectively. Abbreviations: Ω, ohms; deg, degrees.*

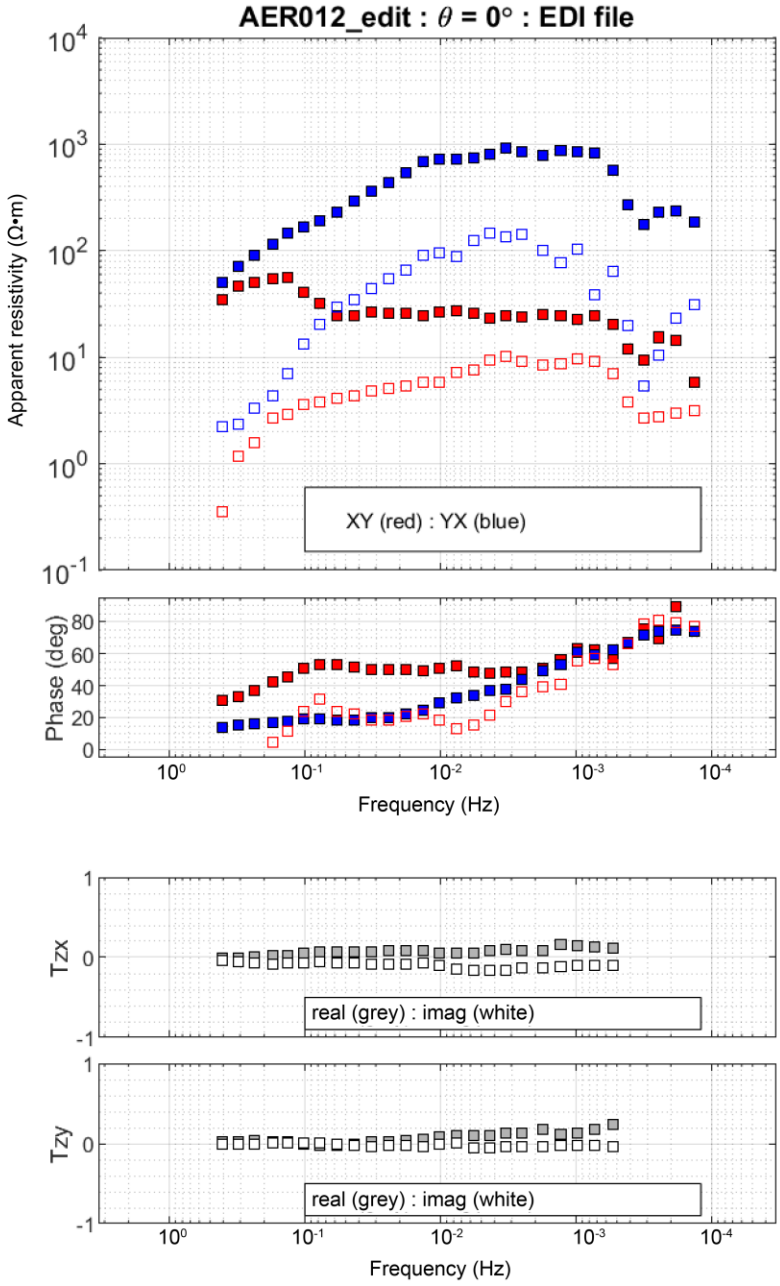

Figure C.12: *Data from station AER 012 (lat. 57.88°N, long. 112.42°W). In the top two panels, the solid red boxes are the XY component of the impedance tensor, solid blue boxes are the YX component, open red boxes are the XX component, and open blue boxes are the YY component. In the bottom two panels, the grey and white boxes are the real (in-phase) and the imaginary (imag; out-of-phase) components of the tipper (T), respectively. Abbreviations: Ω, ohms; deg, degrees.*

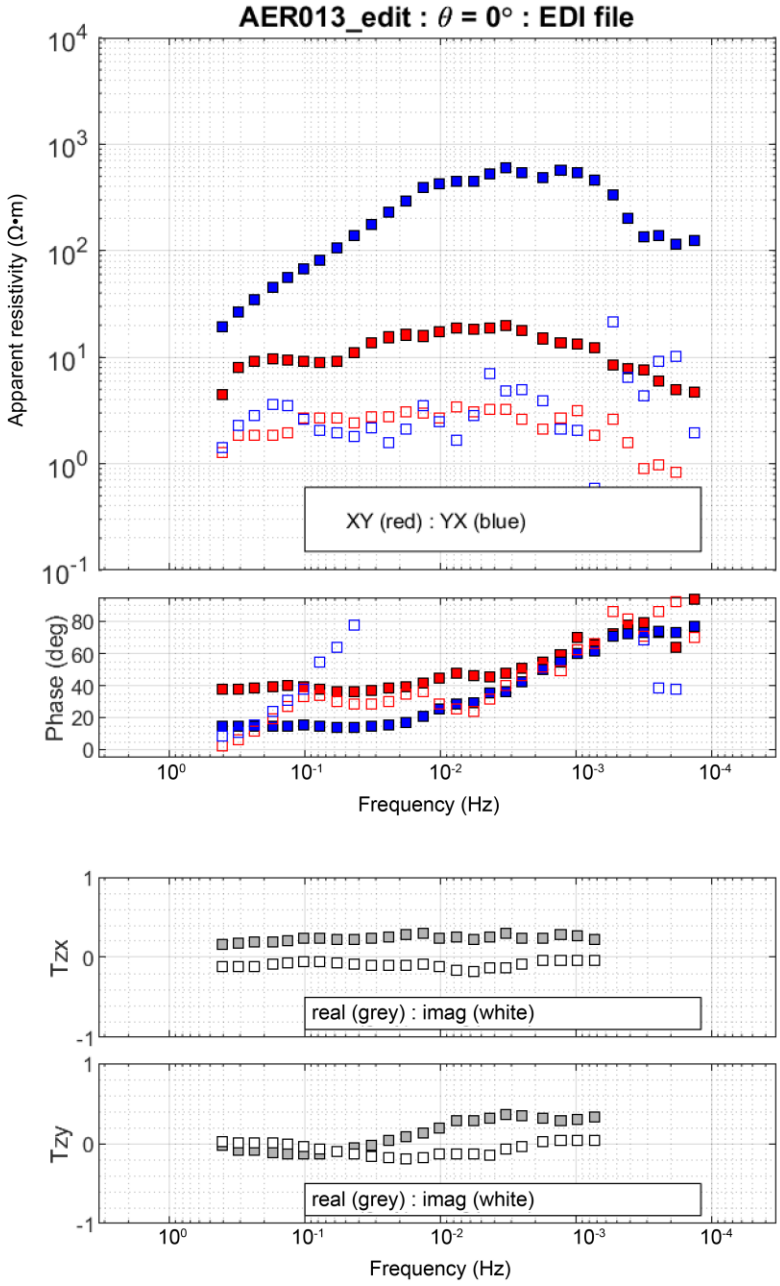

Figure C.13: *Data from station AER 013 (lat. 57.79°N, long. 111.94°W). In the top two panels, the solid red boxes are the XY component of the impedance tensor, solid blue boxes are the YX component, open red boxes are the XX component, and open blue boxes are the YY component. In the bottom two panels, the grey and white boxes are the real (in-phase) and the imaginary (imag; out-of-phase) components of the tipper (T), respectively. Abbreviations: Ω, ohms; deg, degrees.*

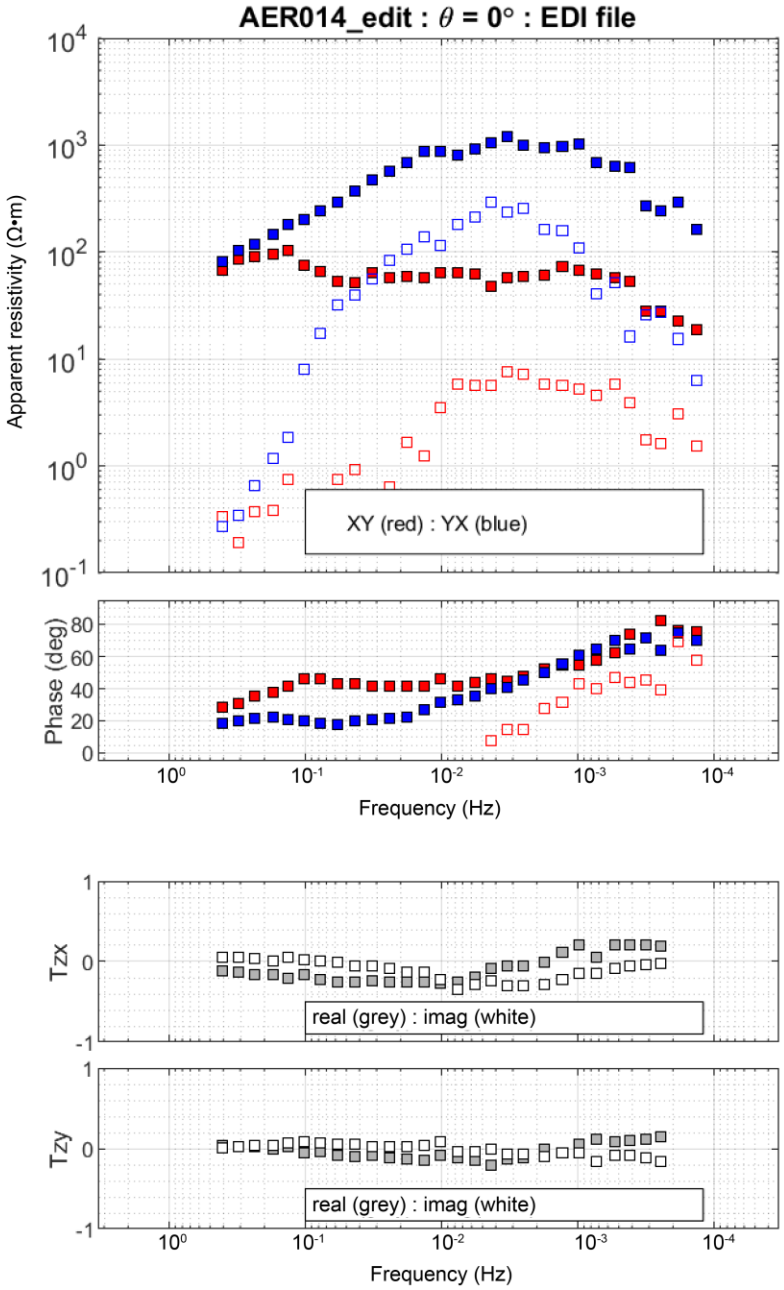

Figure C.14: *Data from station AER 014 (lat. 57.29°N, long. 112.30°W). In the top two panels, the solid red boxes are the XY component of the impedance tensor, solid blue boxes are the YX component, open red boxes are the XX component, and open blue boxes are the YY component. In the bottom two panels, the grey and white boxes are the real (in-phase) and the imaginary (imag; out-of-phase) components of the tipper (T), respectively. Abbreviations: Ω, ohms; deg, degrees.*

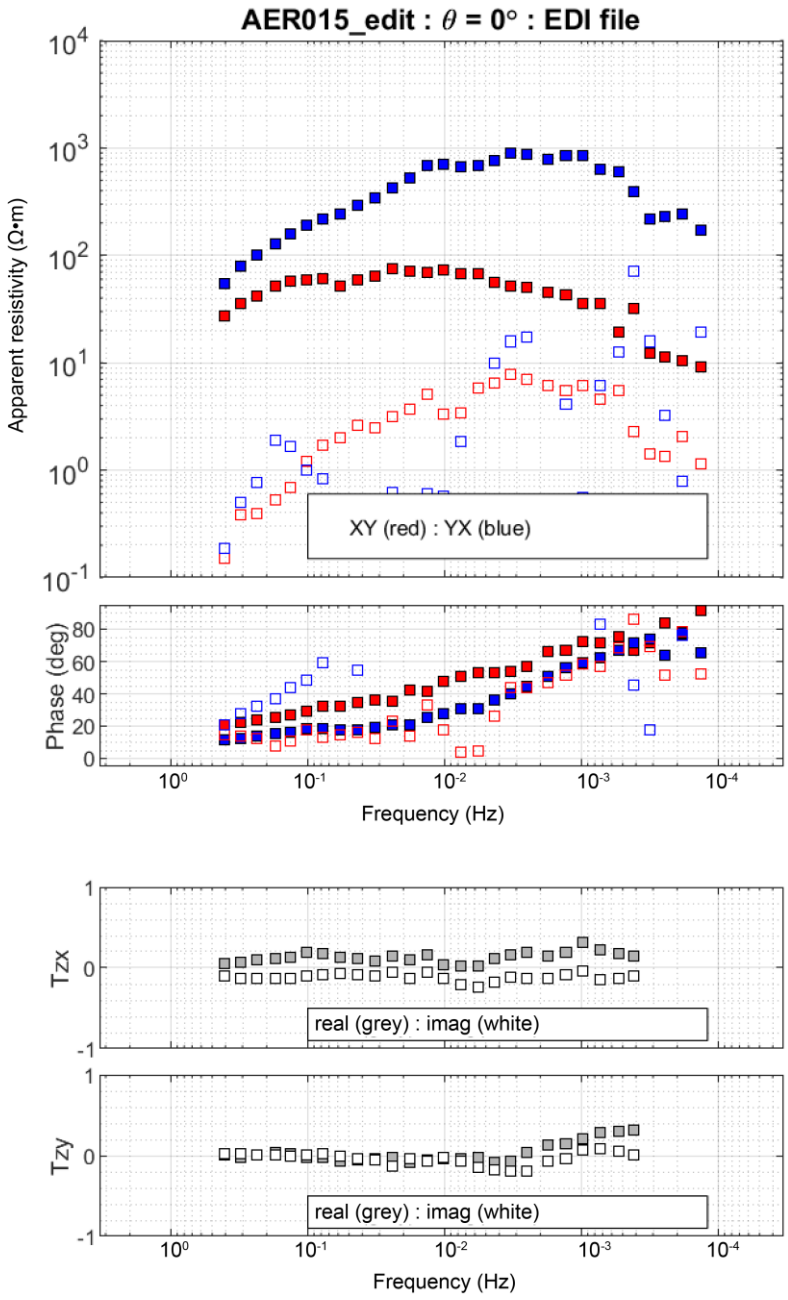

Figure C.15: *Data from station AER 015 (lat. 57.87°N, long. 113.48°W). In the top two panels, the solid red boxes are the XY component of the impedance tensor, solid blue boxes are the YX component, open red boxes are the XX component, and open blue boxes are the YY component. In the bottom two panels, the grey and white boxes are the real (in-phase) and the imaginary (imag; out-of-phase) components of the tipper (T), respectively. Abbreviations: Ω, ohms; deg, degrees.*